PSL UNIVERSITÉ PARIS

THÈSE DE DOCTORAT
DE L'UNIVERSITÉ PSL

Préparée à Mines Paris – PSL

Effect of welding on stress relaxation cracking of the austenitic stainless steel AISI 316L(N)

Soutenue par
Baptiste PY-RENAUDIE
Le 03 Février 2023

École doctorale n°621
Ingénierie des Systèmes, Matériaux, Mécanique, Energétique

Spécialité
Mécanique

Composition du jury :

Eric ANDRIEU Professeur émérite, ENCIASET	*Rapporteur*
Tomas MARTIN Senior lecturer, Uni Bristol	*Rapporteur*
Sabine DENIS Professeure émérite, Institut Jean Lamour	*Examinatrice*
Diogo GONCALVES Ingénieur de recherche, CEA	*Examinateur*
Vladimir ESIN Chargé de recherche, Mines Paris - PSL	*Co-directeur*
Thilo F. Morgeneyer Maître de recherche, Mines Paris - PSL	*Directeur de thèse*

MINES PARIS | PSL

Contents

Introduction

316L(N) austenitic stainless steels have been chosen as structural material for primary and secondary circuits components of 4^{th} generation nuclear power plants, including Sodium-cooled Fast Reactor (SFR) [1]. During the nuclear power plant life-time, such structural materials are continuously exposed to temperatures between 345 and 600 °C and non-negligible mechanical loads. The 316L(N) steel is also foreseen to be used as structural material for the International Thermonuclear Experimental Reactor (ITER) project [2]. Although mechanical and chemical properties of the 316L(N) steel are well-known, the available data are not sufficient to confidently predict the durability of the material for long period of time. Typically, 60 years of life-time service is considered for the 4^{th} nuclear reactor generation. Therefore, long-term experimental tests and numerical simulations must be conducted in order to assess the material performance and predict any probability of mechanical failure.

In this context, the welded joints of structural materials are of high interest as they present mechanical and microstructural discontinuities within the structural material due the successive torch passes during the welding process. Consequently, these weld regions are more prone to damage issues and particularly to a phenomenon called stress relaxation cracking. This issue has been observed since the 1950s and affects several industrial fields, notably the nuclear industry.

Stress relaxation cracking in industry

The production of energy via steam, nuclear or solar power plants requires the use of materials capable of operating at high temperatures and internal pressures [3]. Components necessary for the completion of such structures are usually assembled by welding, aiming for both mechanical integrity and proper sealing during the exploitation of the plant. The welding process and further use of the welded components may result in numerous cases of failures, which presents new challenges for fabricators and operators [4]. One of the main issues associated to welded components is the cracking of the welds, later distinguished into three main groups of cracking: (i) hot cracking, (ii) warm cracking (solid state cracking) and (iii) cold cracking [5] (Figure 1). Hot cracking refers to cracks in welds in the presence of liquid films. This regroups solidification cracking and liquation cracking issues. Warm cracking failures specifically refer to solid state cracking with an exposure to elevated temperatures. Finally, cold cracking is distinguished from the two others as occurring at room temperature. It is mainly associated to the hydrogen cracking phenomenon and the presence of brittle microstructure. The present work is exclusively focused on phenomena belonging to the second group of failures, warm cracking.

Warm cracking includes different phenomena as well as different designations of the same phenomenon, according to the literature: stress relaxation cracking (SRC) [9–11], strain relaxation cracking [7], stress relief cracking [4], stress-induced cracking [11], stress-rupture cracking [4], strain-age cracking (SAC) [5], reheat cracking (RC) [6], post-weld heat treatment (PWHT) cracking [9], underbead cracking and underclad cracking [7].

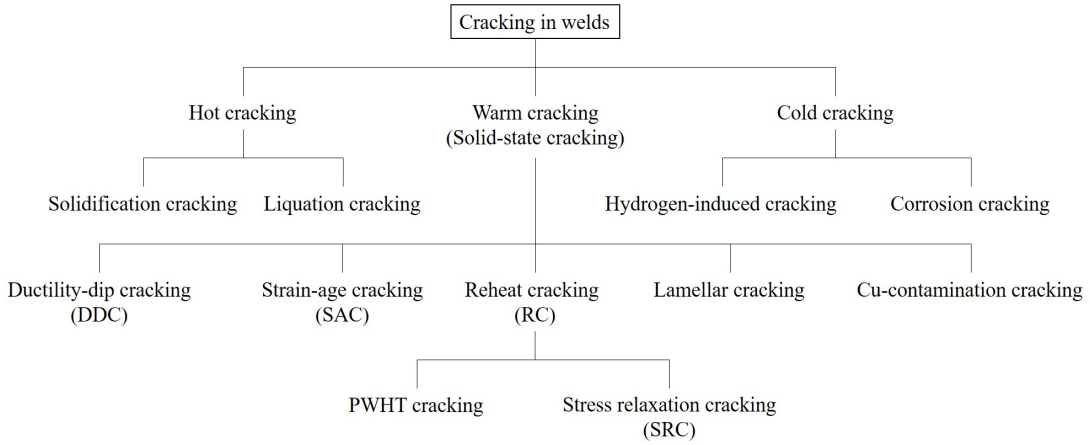

Figure 1: Classification of main cracking phenomena in welds, according to [6–8].

Sometimes, these mechanisms are also associated to ductility dip cracking (DDC) [5]. Also, some of these failures were misidentified as stress corrosion cracking (SCC) mechanism [12], which can actually act as a secondary mechanism to warm cracking [13]. Lastly, some authors mentioned that the failure mechanism is the same as type IV [14] or type III [15] cracking. Type III is associated to cracks initiated in the heat affected zone (HAZ) of weld microstructure close to the fusion zone, thus generally in the coarse-grained region of the heat affected zone, while type IV cracks initiate away from the fusion line in the fine grain region of the HAZ [15]. Most of these phenomena are highly related to each others because of their similar mechanisms and driving factors, however the exact definition and use of each of these names widely differs from one author to another. Nevertheless, a differentiation is proposed here according to most common usages:

- DDC mainly occurs during the reheat or upon cooling of an anterior weld pass during a multipass welding process. Because ductility dips of steels are most often observed between 700 and 1400 °C, DDC is generally used to refer to cracks appearing in this temperature range [5].
- PWHT cracking, sometimes called stress relief cracking, is by definition exclusively related to cracking occurring during short heat treatments (several hours) conducted at high temperatures (>750 °C) after the welding process to remove/reduce the residual stresses or to temper martensitic microstructures. Strain-age cracking is often described as a type of PWHT cracking, specific to Ni-base precipitation-strengthened alloys which can also occur during multipass welding, similarly to DDC [5].
- SRC in contrast is used to refer to cracking occurring at temperatures between 500 and 775 °C during service, for relatively long duration (several weeks to years) [5].

The term reheat cracking is generally used to either refer to PWHT or SRC [6]. Finally, the terms "underbead" or "underclad" cracking simply refer to the type of components and cracks localization, however it should not be confused with hydrogen-induced cracking occurring in the same region but at room temperature [6]. Since most warm cracking present similar mechanisms and driving factors [16], they will be discussed all together under the term of stress relaxation cracking, or SRC, for simplification.

The earliest observations of relaxation cracking were reported by Poole in 1953 [4], who investigated failures of welded 347 (niobium-stabilized) stainless steel, following numerous welding difficulties encountered by major stainless steels fabricators. Out of all failed welds, 22% of cracking occurred after a PWHT. Later in 1957, Curran *et al.* [17]

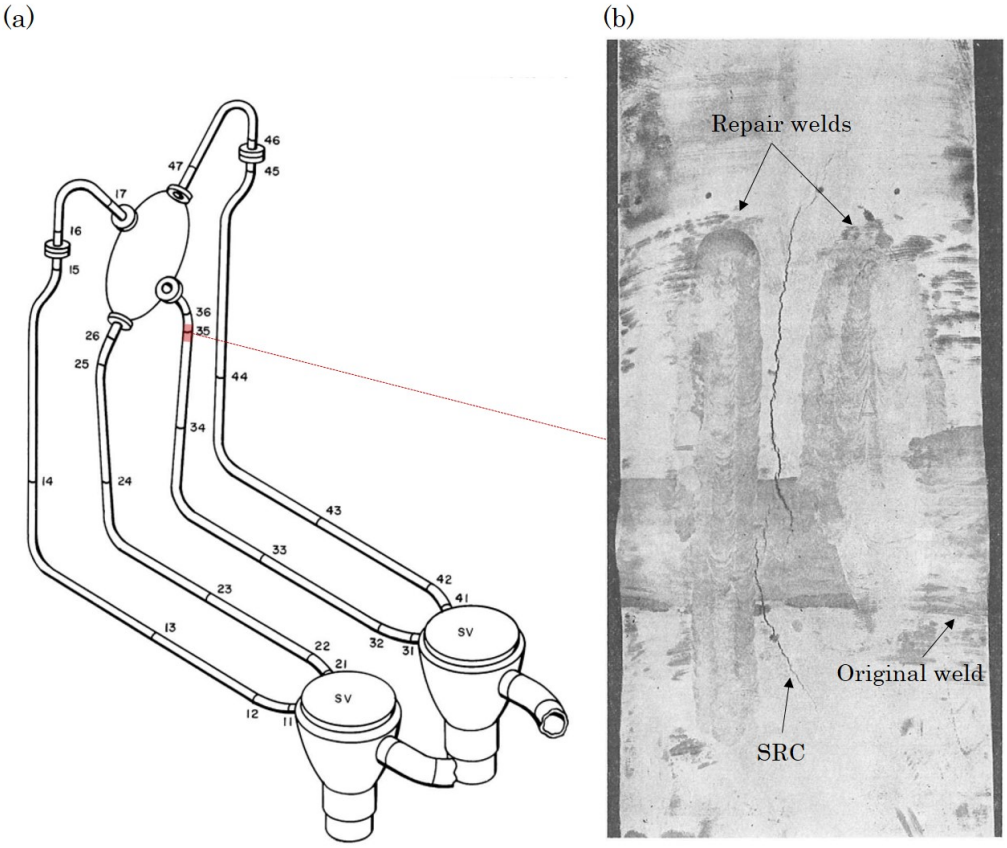

Figure 2: Occurrence of stress relaxation cracks between two repair welds of a 347H steel pipe after 47 months of service at 565 °C. (a) Location of the failed weld in the schematic drawing of the turbine main steam piping system, (b) micrograph of cracks and welds [17].

published a review of damaged piping systems joints of a steam turbine. These damages were observed after periods of 6 months up to more than 5 years of service at 565 °C in pressurized environment. Analyses showed that failures were induced by the nucleation of cracks near welded joints made of 347 and 321 (titanium-stabilized) steels. Curran *et al.* [17] even reported cracks detected after 34 months of service being repaired by grinding and additional welding, followed 47 months later by new cracking between the repair welds (Figure 2). Following the Phénix nuclear power plant shutdown in 1989 after 90000 h of service, similar defects were also observed in welded 321 steel joints [18]. More recently, occurrences of stress relaxation cracking were reported in welds of molten salt hot tanks made of 347H steel after operating at 565 °C in a concentrating solar power plant [19].

These examples of failures imply that SRC is a serious concern for power industries, an issue that is still not completely understood, despite the numerous studies carried out on the phenomenon. The ongoing interest regarding relaxation cracking is illustrated in Figure 3, showing the number of referenced journal articles related to SRC since 1964. Note that earlier academic works on SRC are not included in Figure 3 as SRC had not been identified as such before this date; industrial reports are not included either as most of them are confidential.

Throughout the years, similar failures were observed during the industrial use of many other austenitic steels and nickel-based alloys, as in the 304, 304H, 316, 316H, 321H, 601, 617, 625, 740H, 800, 800H, 800H(T) and 803 steels [7, 17, 20–29]. These appeared either in service after 15 days to 20 years of operation at temperatures comprised between 500 and 775 °C, or directly after PWHTs performed at solutionizing temperatures (750 to

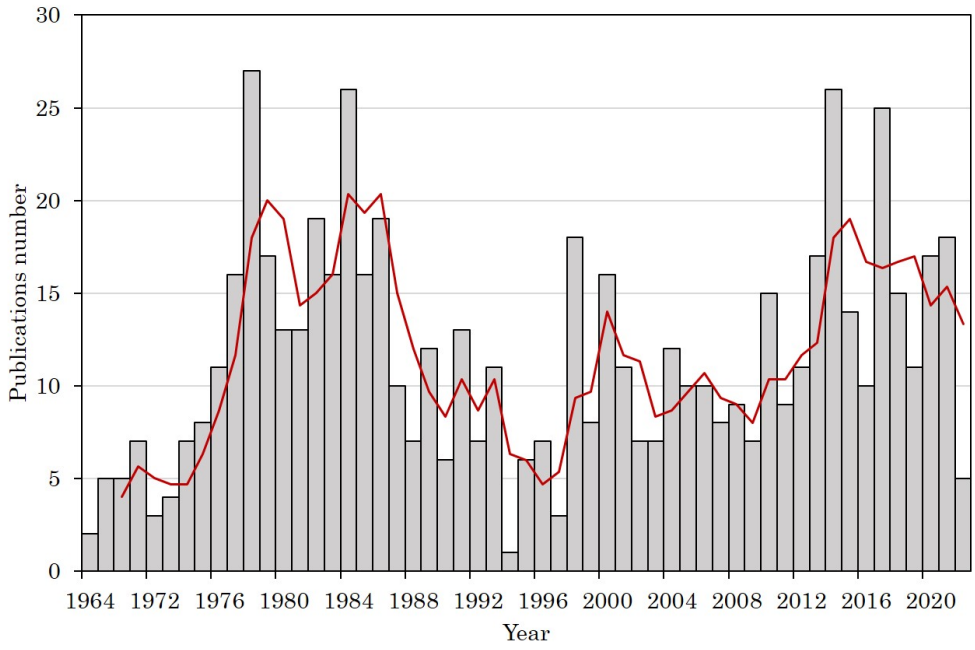

Figure 3: Number of scientific documents related to SRC as a function of years. Data gathered from Scopus website, for reports containing "reheat cracking", "stress relaxation cracking", "stress relief cracking", "post weld heat treatment cracking" in the title, abstract or keywords.

1400 °C) [30]. After repair, SRC is susceptible to occur again in even shorter times [12]. High carbon steels were found to be particularly subjected to SRC, while no industrial case of SRC was reported for low carbons steels to this day. Characteristic features of the cracks observed in the failed welds were described by many authors, which are summarized thereafter.

Main features of stress relaxation cracks

Stress relaxation cracks were found to form at grain boundaries, mostly located just below the fusion zone (FZ), in the coarse-grained heat-affected zone (CGHAZ) of the weld and generally initiated at the toe of the weld bead from the outer surface as illustrated in Figure 4 (a) [7, 12, 15, 21, 31–43]. In some cases, cracks are initiated in the inner side of pipes [18]. Cracks propagation are in majority parallel to the FZ/CGHAZ boundary [33,37, 42], even though Lancaster *et al.* [7] have also reported cracks penetrating the heat-affected zone and then propagating into the base metal as in Figure 4 (a). SRC was also observed to form in the FZ, however, these represent rare cases and are generally more associated to DDC failures [6,7,28,38]. Intergranular cracks observed in the FZ were typically associated to columnar grains normal to the weld surface and to thin ferritic layer on grain boundaries (GBs), increasing strain localization in these areas [6]. Observations of regions affected by SRC revealed the presence of GB cavities similar to those forming during creep (Figure 4 (b) to (d)), near the crack tips [3]. These cavities were often observed on grain boundary precipitates, and mostly on GBs with a perpendicular direction to the principal direction of residual stresses induced by welding [11, 23, 25, 34, 41, 44]. In some cases, crack faces were covered by Cr and Fe oxides and filled with a metallic filament rich in Fe and Ni, as illustrated in Figure 4 (b) [10–12, 23, 25, 26, 35, 41]. The exact chemical composition of the filament is dependent on the alloy [12]. The presence of the filament in only some of

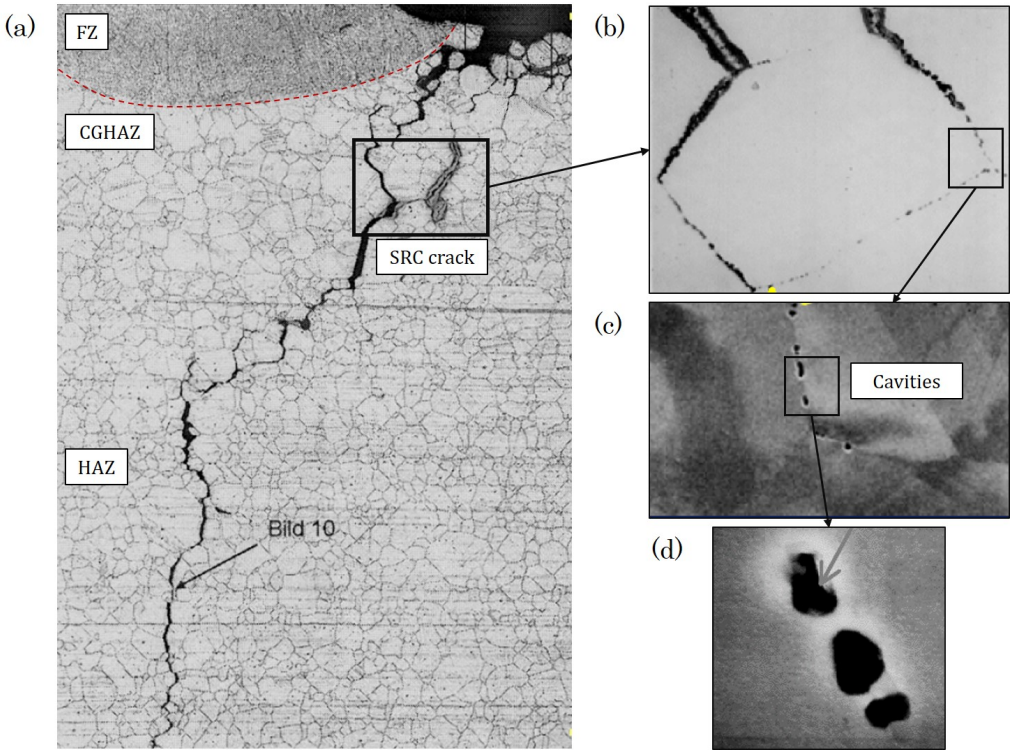

Figure 4: Stress relaxation crack in a failed 800H vessel after 2000 h of service at temperatures between 600 to 650 °C with (a) micrograph image, (b) close-up showing Cr-rich oxide layer (in black) along the intergranular crack and Ni-rich filament within the crack, (c) and (d) close-ups of the grain boundary cavities responsible for cracks initiation [22]. Scale was not indicated by the author, however for reference a common 800H grain size is of 65 μm in average.

the cracks showed that oxidation is a non-necessary secondary mechanism for SRC [13]. Chabaud-Reytier [18] also mentioned cracks were found to be in chromium-rich regions. Finally, some authors reported that cracks were only present in areas where the Vickers hardness exceeds 200 HV10 [12,13]. Note that the presence of high residual tensile stresses can offset this statement since they may significantly decrease hardness, as suggested by Pommier [45]. As a result, the measure of hardness is not considered to be a good indicator of SRC-susceptible regions.

These numerous works allowed identifying factors which can potentially influence the initiation of damage during stress relaxation (Figure 5). Typically, it was found that the chemical composition, the microstructure and mechanical properties of the steel can affect its resistance to SRC. The welding process itself induces changes of the microstructure (precipitation, phase transformation) but is also responsible for the rise of residual stresses. During service, temperature and time will affect the material sensitivity to cavity nucleation, eventually leading to stress relaxation cracking. In order to better understand the phenomenon, some of the main factors such as the effect of sample geometry, residual stress, pre-hardening (cold-rolling), grain size, welding (microstructure, precipitation), stress relaxation time and temperature will be investigated in this study.

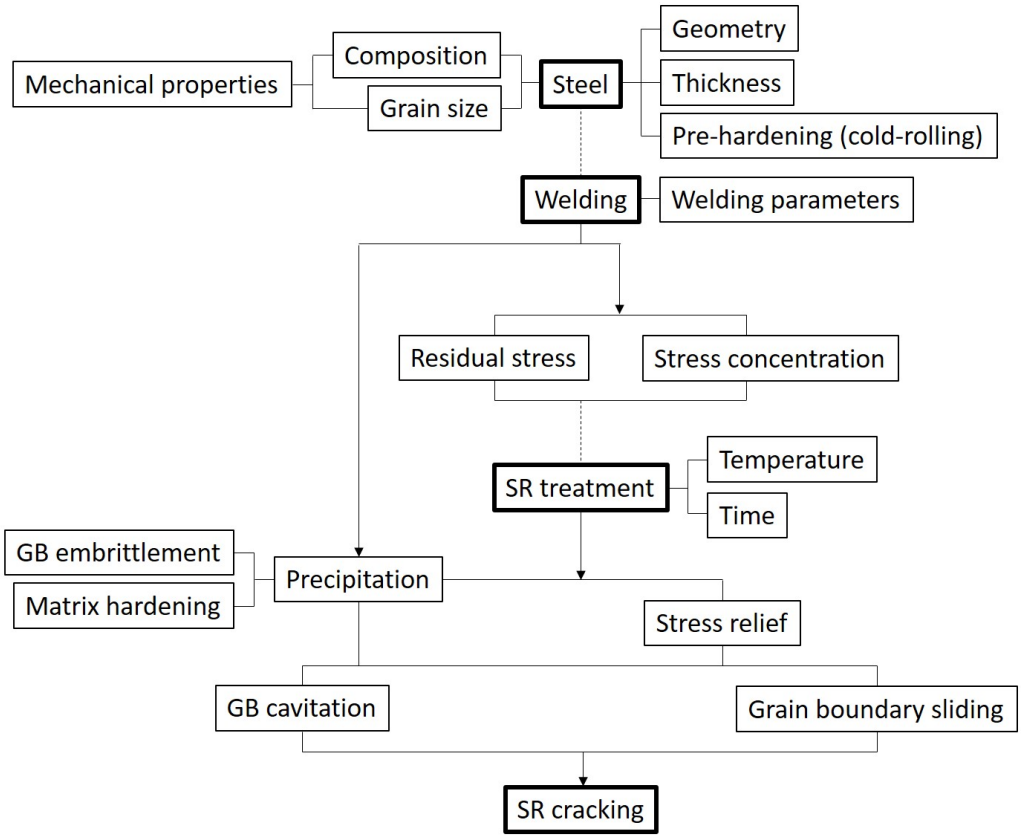

Figure 5: Factors associated to stress relaxation cracking mechanism, summarized from Ito *et al.* [46] and Lippold [5] works. "SR" stands for stress relaxation.

Objectives of the present work

The majority of previous works investigating SRC on different steels were carried out by experimental testing using homogeneous materials, with microstructure and mechanical properties representative of heat affected zones [13, 45, 47], which were considered as most prone to SRC. While this relatively simple approach allows straightforward interpretation of obtained results, particularly for mechanical simulations and damage characterization, it does not capture the complex behavior of a heterogeneous microstructure regarding stress relaxation of stainless steels. Specifically, although industrial observations found in technical reports [9, 48, 49] often describe the coarse-grained region of the HAZ as the most prone to SRC, data found in the literature do not provide clear explanations for this sensitivity, especially for austenitic steels. In addition, there are few scientific journal articles that indicate the crack location and even less that provide an explanation for the preferential location. Therefore, this work aims investigating SRC in a highly SRC-resistant steel, by introducing controlled levels of residual stresses and plastic strain, subjecting all weld zones to similar mechanical conditions. The use of the Turski compression approach [47] is necessary since SRC cannot be expected to occur in a welded 316L steel, especially in laboratory conditions. This will then allow studying the resistance of each weld zone to SRC and further understand the effect of weld microstructure on SRC.

The main objective of this work is thus to study stress relaxation cracking in welded 316L(N) steel, by accounting for the effect of microstructure heterogeneity on SRC. For this purpose, experiments and simulations were used in order to:

(i) develop an approach to characterize the SRC susceptibility of the welded 316L(N)

steel employing mechanical tests and simulations as well as microscopic characterizations;

(ii) characterize the influence of welding on SRC by identifying the weakest region of the weld microstructure and comparing the results to homogeneous material states (without welding). From industrial observations, the coarse-grained region of the HAZ is expected to be more prone to SRC. However, due to the new approach used here exposing all weld zones to similar levels of residual stresses, conclusions might be different;

(iii) evaluate the mechanical and microstructural factors influencing the phenomenon.

Approach

To meet these objectives, stress relaxation cracking tests in this work will be carried out following an approach consisting in four main steps, listed as follows:

(i) **Prior thermo-mechanical treatments** will be applied to as-received plates to introduce different SRC factors, thereby producing several material states. Specifically, welding (without filler material) will be applied to the material to produce heterogeneous microstructures. SRC tests will also be carried out on the as-received material without prior treatment for comparison.

(ii) **Introduction of residual stresses** will be achieved using a self-restrain method as initially proposed by Turski *et al.* [47], consisting in a pre-compression at room temperature using specimen geometries similar to the CT (Compact Tension) ones. As shown by Turski *et al.* [47], the unloading following the compression results in high residual tensile stresses and plastic strain fields near the notch root of the specimens. The estimation of the post-compression residual stresses and plastic strain will be performed by finite element method (FEM) simulations.

(iii) **Relaxation of residual stresses** will be carried out applying heat treatments at 575 and 600 °C at ambient air for 580 h (about 1 month) and 1470 h (about 3 months) to the specimens after the Turski compression. These specific conditions were chosen as they were found by Pommier [45] to be favorable to SRC for a 316L(N) steel of composition similar to the one studied in this work. These relaxation treatments will be followed by cooling at room temperature in ambient air.

(iv) For **characterization of damage**, the reheated samples will be cut into sections in the regions presenting highest post-Turski compression residual stresses and polished for microscopical analyses to characterize both the microstructure and stress relaxation damage.

Thesis outline

The present manuscript is divided into six chapters. In the Chapter 1, a literature review is proposed where the composition, the microstructure of 316L(N) steel as well as the microstructural and mechanical effects of welding on steels are reported. Then, the mechanism of SRC, the influencing factors as well as the most commons SRC testing methods found in the literature are discussed.

The experimental methods used to perform the SRC tests using the studied 316L(N) steel are presented in the Chapter 2. In particular, the different material states tested for SRC and the process employed to produce them are presented. Besides, the different

methods used for the characterisation of microstructures, mechanical properties and stress relaxation damage are described.

In the Chapter 3, the microstructure of each material state produced for this work is characterised, allowing to reveal the microstructural features expected to influence their resistance to SRC. In addition, microstructure evolution with temperature is characterized without the effect of the residual stresses and plastic strain introduced by the compression test used further for the SRC test, and thus better understand the SRC mechanism for each material state.

Then, the Chapter 4 presents the Turski compression allowing the controlled introduction of residual stress and plastic strain, necessary for SRC. In this chapter, the experimental and numerical methods used to predict the mechanical fields are presented, concluding with predictions of stress relaxation damage hazard for each tested condition.

In Chapter 5, the actual SRC tests of each material state are presented. Characterisation of the nature, levels and distributions of damage are described for each condition and microstructure. The results for each microstructure are then compared to conclude on its effect on SRC, particularly the effect of heterogeneous microstructures.

Finally, Chapter 6 proposes an analysis of different SRC influencing factors to better understand the sensitivity of weakest microstructures. Conclusions of this work and perspectives for further researches are presented at the end of the document.

Chapter 1

Literature review

Contents

1.1 Introduction

Stress relaxation cracking (SRC) is an intergranular type of cracking occurring during the reheating of welded steels, induced by the relaxation of welding residual stresses at high temperature in presence of welding-induced hardening and grain boundary precipitates. Such cracks were observed to be initiated by the coalescence of grain boundary cavities similarly to creep. This type of failure, firstly observed in the 1950s, is a complex combination of several mechanical and microstructural factors acting from the macroscopic to the nanometric scale. The study of the SRC phenomena is a challenge, since it requires good knowledge about the material metallurgy and mechanical properties, the welding process and obviously the SRC mechanism itself. To this end, a literature review on the metallurgy of austenitic steels, welding of austenitic steels and finally stress relaxation cracking is proposed in the following.

The first section presents in general terms the austenitic stainless steels, then more specifically the 316L(N) alloy. The chemical composition, microstructure and properties of austenitic stainless steels are discussed. The chemical composition of steels, influencing the microstructure, is of high interest as it also affects the material mechanical properties, especially for long duration mechanical issues. The second section presents the welding methods used for stainless steels and their impact. Specifically, the evolution of the microstructure, mechanical properties and the generation of residual stress due to welding are discussed. A short review of simulating welding is proposed. The third section is devoted to the review of SRC, considering the mechanism of the phenomenon, the associated necessary and influencing factors and finally the experimental method available to test SRC.

1.2 Metallurgy of austenitic steels

1.2.1 Generalities on the 316L(N) steel

In this work, SRC of 316L(N) stainless steels is investigated. In the following, the metallurgy and properties of this alloy are presented. Comparisons with other stainless steel grades are also proposed, allowing a more complete overview of this material.

1.2.1.1 Microstructure

Steels are specific iron alloys with a maximum of 2.1% wt. of C [50]. Stainless steels were specifically created adding 11 to 26% wt. of Cr to these alloys [51, 52]. The presence of Cr in stainless steel allows the formation of a chromium-oxide Cr_2O_3 passive layer on the surface of the material when exposed to oxygen, creating a natural protection to corrosion issues [53]. However, at high temperature the addition of Cr is also susceptible to allow the precipitation of undesirable secondary phases, such as chromium carbides, which are detrimental to mechanical strength performances. For these reasons, carbon content must be limited. The stainless steels group is divided into five different categories, depending on their microstructure: austenitic, ferritic, martensitic, duplex and precipitation hardened stainless steels [54, 55] (Figure 1.1). Austenitic stainless steels are used for many applications, especially for structural components, particularly in the energy sector [56]. Despite their higher initial cost, austenitic stainless steels, known as the 300 series, are used because of their better performance regarding corrosion resistance, formability and good properties at high temperatures. This make them particularly interesting for nuclear applications, where the safety and integrity of the structures must be ensured for long duration service at high temperature, with generally little to no possibility of repairing in case of failure.

Austenitic steels are characterized by an austenitic matrix, meaning it is largely composed of the Face Centered Cubic (FCC) austenite phase [55]. This differs from the other types of stainless steels, with ferritic steels being composed of a Body Centered Cubic (BCC) ferrite matrix, and martensitic steels of a tetragonal body centered martensite matrix [55]. Duplex steels are composed of both ferrite and austenite phases, in comparable proportions. Precipitation hardening steels can either be martensitic, martensitic-austenitic or austenitic. These are hardened through thermal treatments carried out between 400 and 700 °C, allowing age strengthening.

The microstructure of stainless steels is the direct result of both the chemical composition and the elaboration process. Particularly, austenitic phase is stabilized by the addition of elements such as Ni, N and Mn even though ferrite stabilizing elements such as C, Cr, Mo, Si and Nb can also be present in austenitic steels. These are either additions to improve the material performances or can be simply impurities resulting from the elaboration process. The numerous different grades of the 300 austenitic stainless steels series are usually described as being variants of the most common austenitic grade, the 304 steel, by changing the constituting elements and their contents to better fit the aimed application (Figure 1.1). The role of major elements present in stainless steels are described in Table 1.1.

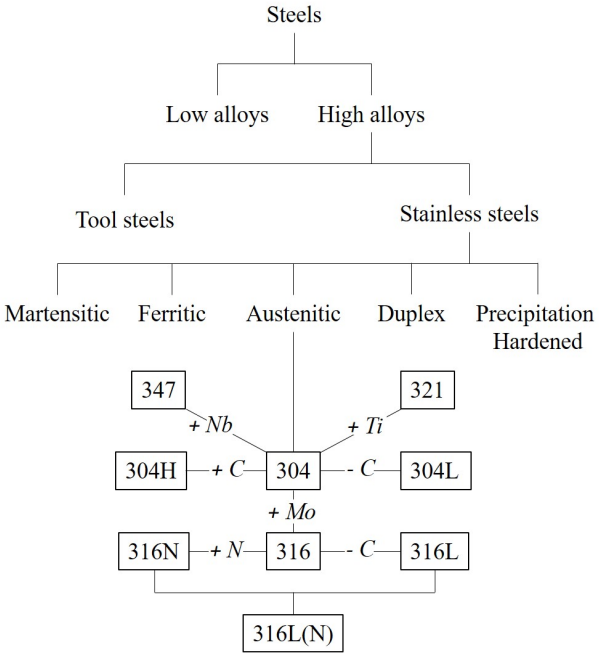

Figure 1.1: Simplified classification of steels with the main variants of 300 austenitic stainless steels, according to [18, 54–56].

Addition of carbon (from 0.04 to 0.10% wt.) improves mechanical strength, as in the 304H and 316H steels. However, the high carbon content favors the precipitation of undesirable chromium carbides. This precipitation weaken the grain boundary and can cause a local depletion in chromium. This phenomenon, called sensitization, results in regions more susceptible to corrosion issues [53]. A way to avoid chromium carbides precipitation is to force the carbon atoms to form other types of carbides, without affecting the chromium content. This approach is employed in the stabilized steels. In 347 stainless steels for instance (Figure 1.1), the addition of niobium is performed, leading to the formation of NbC and Nb_4C_3 carbides when exposed to thermal treatments, preventing chromium carbides precipitation. In 321 steels (Figure 1.1), an addition of titanium is

Table 1.1: Alloying elements in austenitic steels, their effect on ferrite (BCC) or austenite (FCC) stabilization and impact on the material properties [18, 57].

Element	Stabilized structure	Impact on properties
Chromium	BCC	Prevents corrosion issues through Cr_2O_3 oxide layer formation. Susceptible to form carbides which alter mechanical strength and corrosion performances.
Nickel	FCC	Increases the corrosion resistance and improves welding properties.
Molybdenum	BCC	Highly increases the corrosion resistance and material strength at high temperatures, making it a suitable alloy for welding process and nuclear applications.
Carbon	FCC	Improves thermal and mechanical properties (material strength). Responsible for intergranular carbide precipitation, and facilitates corrosion issues through sensitization.
Nitrogen	FCC	Improves material strength through solid solution hardening.

carried out in order to form preferentially TiC carbides [18]. Another approach is to decrease the carbon content to limit carbide precipitation, then called low carbon alloys, such as the 304L and 316L (Figure 1.1). These were specifically developed to decrease intergranular corrosion sensitivity and improve $Cr2O_3$ passive layer development as more chromium content is available. However, compared to high carbon steels the low carbon content degrades the mechanical strength.

The addition of molybdenum can also be carried out to improve the mechanical strength of low carbon steels, and more specifically creep resistance. Molybdenum also slows down carbides precipitation at temperature below 700 °C, especially for low carbon steels (less than 0.03% wt.) [57]. This led to the development of the 316 type steels (Figure 1.1). In low carbon steels, an addition of nitrogen can also be performed to improve the steel mechanical strength through solid solution hardening, as for 316L(N) type steels (Figure 1.1). The chemical composition requirements for 316L(N) steels as described by the RCC-MRx (2012) are reported in Table 1.2. Chemical compositions of industrial 316L(N) used by the CEA as reference are also given as examples.

Table 1.2: Chemical composition (%wt.) requirement for 316L(N) steel alloy, according to RCC-MRx (2012) [58], as well as composition for K46-T9, EDF-SQ and AVESTA indutrial alloys.

Element	C	Si	Mn	P	Cr	Mo	Ni	N	Co	Cu
RCC-MRx										
Min	0.000	0.00	1.60	0.000	17.00	2.30	12.00	0.060	0.00	0.00
Max	0.030	0.50	2.00	0.035	18.00	2.70	12.50	0.080	0.25	1.00
K46-T9	0.025	0.19	1.7	0.019	17.38	2.39	12.12	0.069	0.04	0.16
EDF-SQ	0.030	0.44	1.88	0.028	17.54	2.48	12.46	0.077	0.15	0.175
AVESTA	0.026	0.31	1.74	0.025	17.27	2.54	12.13	0.069	0.09	0.29

Austenitic stainless steels may also contain some ferrite additionally to the austenitic matrix, then called residual ferrite or δ-ferrite. It is important to account for the presence of ferrite: while it can increase the weldability of austenitic steels, it can also deteriorate the steel thermal and mechanical properties. For instance, ferrite can lower the resis-

tance to stress corrosion cracking [59]. Limiting the content of residual ferrite in steels is thus necessary, which can be achieved by adjusting the heat treatment used to obtain an austenitic material. To produce the austenite phase, an isothermal treatment of a few hours at temperatures between 1000 and 1200 °C is usually carried out [60]. This specific heat treatment is commonly called austenitization, solution treatment or annealing treatment. Such treatment also allows the dissolution of undesirable secondary phases such as the σ-phase or carbides [57], detrimental to the steel mechanical properties. The final fraction of austenite phase depends on the austenitization time, temperature and cooling rate. Usually, the thermal treatment does not allow to obtain a fully austenitic microstructure and residual ferrite is often observed as a result, as shown in Figure 1.2. A way to predict the final ferrite content is by calculating nickel equivalent and chromium equivalent contents such as proposed by Schaeffler [61] and Long *et al.* [62].

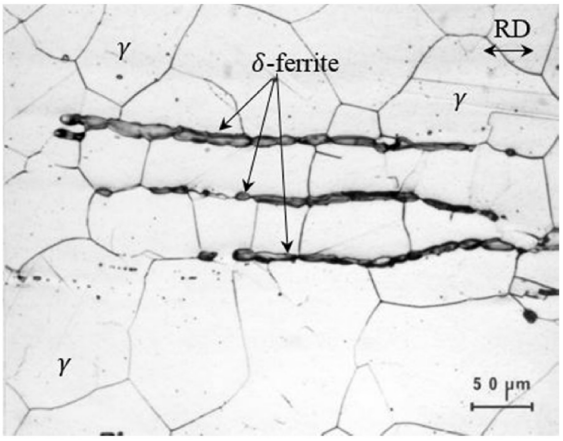

Figure 1.2: Optical micrograph of a 316L steel annealed at 1070 °C for 1 h, showing δ-ferrite bands (or "islands") in the austenitic (γ) matrix [63]. "RD" stands for the rolling direction.

1.2.2 Precipitation in austenitic stainless steels

Phase precipitation in austenitic stainless steels is a fundamental industrial problem, since it influences mechanical properties, especially crack initiation and propagation in service. During mechanical and thermal loading, undesirable precipitates in the material can induce local concentrations of stress, and can particularly weaken the material if these are located at grain boundaries [64]. Chromium carbides are very often cited in the literature [45] as preferential sites for the initiation of stress relaxation cracks. For these reasons, the study of the SRC sensitivity of a steel requires a proper knowledge of the phases prone to precipitate during the processing of the material (austenitization, welding) or during its service. In addition, it is important to identify the factors influencing this precipitation.

Despite the low carbon content, reducing the susceptibility for the precipitation of undesirable secondary phases, carbides can still be observed in 316L(N) steels. From their processing to application in nuclear reactors, components made of austenitic stainless steels can be subjected to phase precipitation at four different stages. They can either be formed during the elaboration, during the welding process (see Section 1.3), post-welding heat treatment or later during service. These correspond to different time/temperature ageing treatments, which may be favourable to the precipitation of carbides and intermetallic phases, as summarized below:

- welding process induces high temperature gradients in the material (from 25 to more than 1400 °C) and thus induces important microstructure transformations.

Precipitates with fast nucleation kinetics can then nucleate and grow in the heat affected zones of the welded component [13, 18];

- post-welding heat treatment is not foreseen for 316L(N) steels by the RCC-MRx [65], even though dimension stabilization treatment may be applied to relax welding residual stresses. It usually consists in a rapid thermal treatment (a few hours) at temperatures varying from 400 to 800 °C [66]. Particularly for the 316L(N) steel, the RCC-MRx [65] suggests a treatment at 650 °C for 50 h to relax residual stresses, which constitute favorable conditions for carbides precipitation [67];

- service temperature and time depend on the application. Typically, for the 4^{th} generation of nuclear reactors, the life-time is expected to be at least 60 years for a service at temperatures near 550 °C. These long ageing times are also favorable to the formation of precipitates with very low precipitation kinetics.

During thermal treatment of austenitic stainless steels, numerous secondary phases may form. In the literature, these phases are often discussed under different names and groups. To clarify this, a classification of the most common phases observed in the austenitic stainless steels is proposed in Figure 1.3, according to data reported by different authors [67–73]. Characteristics of the main phases of interest are detailed in Table 1.4. Precipitating phases are generally found to be intermetallics, carbides, nitrides, borides and sulphides. The intermetallics group includes the σ-phase, Laves phases, χ-phase, G-phase, R-phase and μ-phase [69, 71]. Laves phases, often reduced to the hexagonal C14 (η phase), actually also include the cubic C15 and hexagonal C36 compounds [72, 73]. Most of intermetallics (σ, μ, M, P and R phases) and Laves phases along with A15 phases constitute the most common members of the larger Frank-Kasper (FK) phases group [74]. It is worth noting that the χ-phase does not belong to the FK group while being an intermetallic [75] as it does not follow the FK phases rules. The carbides group includes MC, M_6C (also called η-carbide), M_7C_3 and $M_{23}C_6$ phases. MX carbonitrides, such as NbN, NbC, TiC, TiN or the Z-phase can also be found [69]. Borides and sulphides are less often observed in austenitic stainless steels [67].

Knowing the chemical composition of a steel, thermodynamics simulations can be carried out to make predictions about the most stable phases for different temperatures and determine what secondary precipitating phase to expect during the material exposure to thermal treatments. Typically, for a 316L steel such computation predict the stability of austenite, ferrite, $M_{23}C_6$, σ and χ phases for temperatures between 500 and 1000 °C accounting for the effect of elements contents, such as carbon as illustrated in Figure 1.5.

These phases can thus be expected to be observed after welding or after stress relaxation heat treatment which will be carried out to test the 316L(N) resistance to SRC.

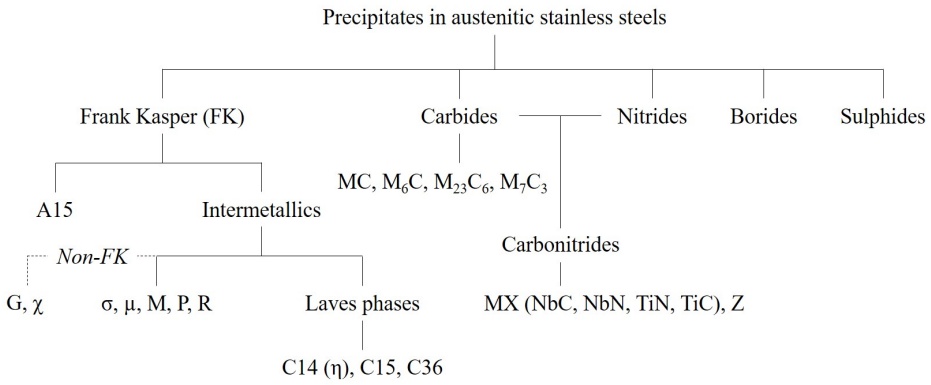

Figure 1.3: Classification of major precipitating phases found in austenitic stainless steels, according to [67–73]. Note that not all intermetallics are part of the FK group, such as the G and χ phases.

Phase	Unit cell	Atoms per cell	Space group	Lattice parameters (nm)	Composition
			Carbides		
$M_{23}C_6$	fcc	116	Fm3m	a = 1.057-1.068	$(Cr, Fe, Mo)_{23}C_6$; $(Cr_{16}Fe_5Mo_2)C_6$
MC	ord fcc	8	Fm3m	a = 0.4131-0.4698	(Ti,Nb,V)C
M_6C	fcc	112	Fd3m	a = 1.085-1.128	$(Fe, Mo, Nb,Cr,Si)_6C$
M_7C_3	pseudo hex.	40	Pnma	a = 1.398 c = 0.4523	$(Cr,Fe)_7C_3$
			Intermetallic phases		
Sigma (σ)	bct	30	$P4_2/mnm$	a = 0.87-0.92 c = 0.4554-0.48	$(Fe,Ni)_x(Cr,Mo)_y$
Chi (χ)	bcc	58	I43m	a = 0.881-0.895	$Fe_{36}Cr_{12}Mo_{10}$; $(Fe,Ni)_{36}Cr_{18}Mo_4$
Laves (η)	hex.	12	$P6_3/mmc$	a = 0.473-0.483 c = 0.772-0.786	Fe_2Mo; Fe_2Nb; Fe_2Ta; Fe_2Ti; Fe_2W
G	fcc	116	Fd3m	a = 1.115-1.120	$Ni_{16}Nb_6Si_7$; $Ni_{16}Ti_6Si_7$; $(Ni,Fe,Cr)_{16}(Nb,Ti)_6Si_7$
R	hex.	53 (159)	R3	a = 1.090; c = 1.934	$Fe_{22}Mo_{18}Cr_{13}$; $(Fe,Ni)_{10}Cr_5Mo_3Si_2$
Mu (μ)	rhombohedral	13	R3m	a = 0.4762; c = 2.5015	$(Fe,Co)_7(Mo,W)_6$; $(Cr,Fe)_7(Mo)_2(Cr,Fe,Mo)_4$

Figure 1.4: Crystal structure and composition of the main secondary phases found in austenitic stainless steels [68, 70, 71].

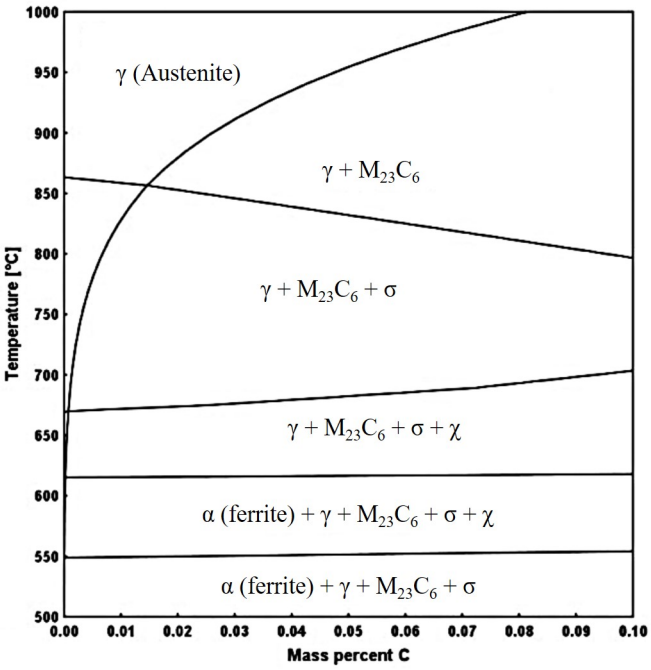

Figure 1.5: Equilibrium pseudobinary Fe-C phase diagram for a 316L steel for temperatures between 500 °C and 1000 °C, computed with Thermo-Calc software [76].

1.3 Welding of austenitic stainless steels

Stress relaxation cracking issues reported since the 1950s in industry mostly affected welded steel components [18]. In order to properly understand the causes of stress relaxation damage during service, shortly or long after the welding process, it is fundamental to first understand the impact of welding on the microstructure and properties of a steel.

Large structural components, as used in nuclear applications, are assembled by welding process, necessary to ensure the integrity of the structure. Whether it is to manufacture steels joints or to repair failed components, it exist numerous welding methods for structural materials. Figure 1.6 shows the classification of most common welding methods. These are divided into two main families, pressure and fusion welding. The fusion welding family includes the gas, arc and power beam welding.

The most common methods used for stainless steel welding are the Gas Tungsten Arc Welding (GTAW) and Gas Metal Arc Welding (GMAW) [77], both are part of the larger groups of gas shielded arc welding and more widely fusion welding. GMAW, which includes Metal Inert Gas (MIG) and Metal Active Gas (MAG) methods, is widely used in industry because of its high production rate, facility and versatility of usage [57]. GMAW is particularly used for thick components while GTAW is more suited for thin materials, from about 0.5 to 3 mm thick, and less accessible components for repairs [78]. GTAW, also called Tungsten Inert Gas (TIG), can be performed with or without filler metal and has the advantage of producing high quality, clean and reliable joints, which makes it suitable for crucial components as used in aeronautics or nuclear applications. However, GTAW requires higher experience of the operator and has a lower productivity rate than GMAW because of a lower speed, inducing a higher overall cost.

For the 316 grade, it was found that GTAW allowed higher tensile strength, toughness and fracture energy values in impact test than welds obtained by GMAW [79]. Quality and mechanical properties of weld joints manufactured by GTAW are then often considered over the cost for structures requiring high safety in the long term, justifying why only the GTAW is proposed in the RCC-MRx [65] specifications for welding of nuclear reactor components. Regardless of the arc wielding method, such processes induce thermal cycles of high amplitudes, affecting the microstructure of the material and, hence, its mechanical behavior. Particularly in the case of GTAW, these thermal cycles are generally numerous, since the process often requires several welding passes to manufacture a joint. In order to understand the mechanism of stress relaxation cracking in weld joints and identify weak zones, the GTAW process, its influence on both the microstructure and mechanical properties are presented in the next sections.

1.3.1 Gas Tungsten Arc Welding

The GTAW process, as the other fusion welding processes, allows assembling thermally conductive materials such as metals and alloys, through the partial fusion of the different parts. The integrity of the resulting component or structure is then ensured by the solid joint between both parts, produced from the solidification of the filler metal, then called weld metal [80].

In order to join the parts, materials are exposed to a high current via a tungsten electrode (Figure 1.7), inducing an electric arc. When ignited, the electron arc forces the electrons to migrate from the negative pole to the positive one; however, ions traveling in the opposite direction result in collisions with electrons. These collisions release high energy, allowing the fusion of the base metal in regions close to the surface and/or the fusion of the filler metal. The GTAW equipment is constituted of several parts. A power source is used to produce the high current transmitted to the GTAW torch, which creates the electrical arc. Even though the GTAW torch can be controlled manually, its displacement

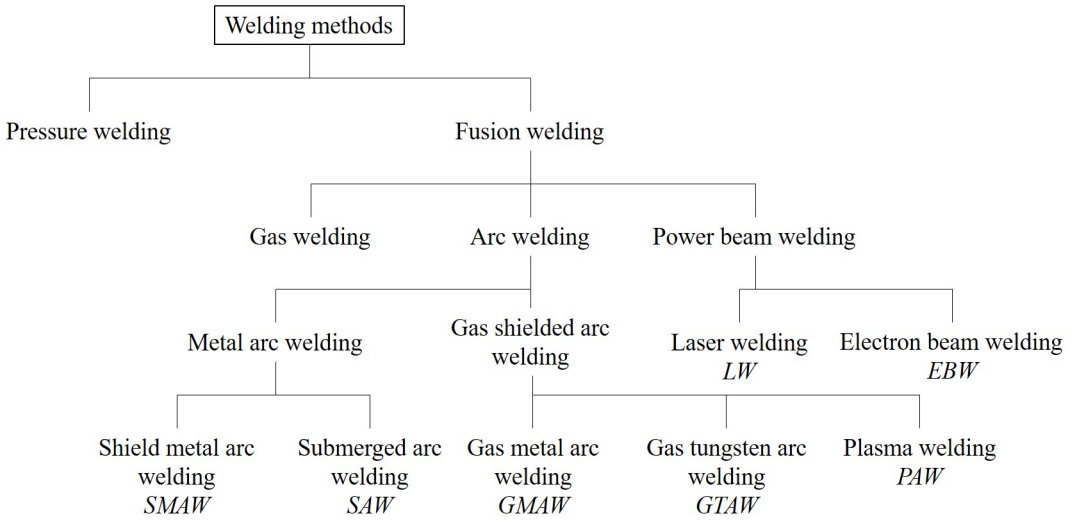

Figure 1.6: Schematic presentation of the most common modern welding methods, according to Weman [78].

is usually automatized via mechanical monitoring to ensure continuous and homogeneous treatment. The welding parameters such as the current, voltage, torch velocity and gas flow are currently controlled via a numerical monitor. A gas tank connected to the control unit provides the shielding gas used during the welding process. The choice of the inert gas is primordial as it prevents the interaction between ambient air and the weld pool, avoiding oxidation issues. Additionally, it can also improve current conduction and heat convection in the arc [78]. The choice of inert gas depends on the studied material, the welding method, the component geometry, accessibility and the foreseen cost for production. In the case of stainless steels, argon (Ar) shielding gas is the most used, but Ar/H_2 and Ar/He mix are also commonly used [80, 81].

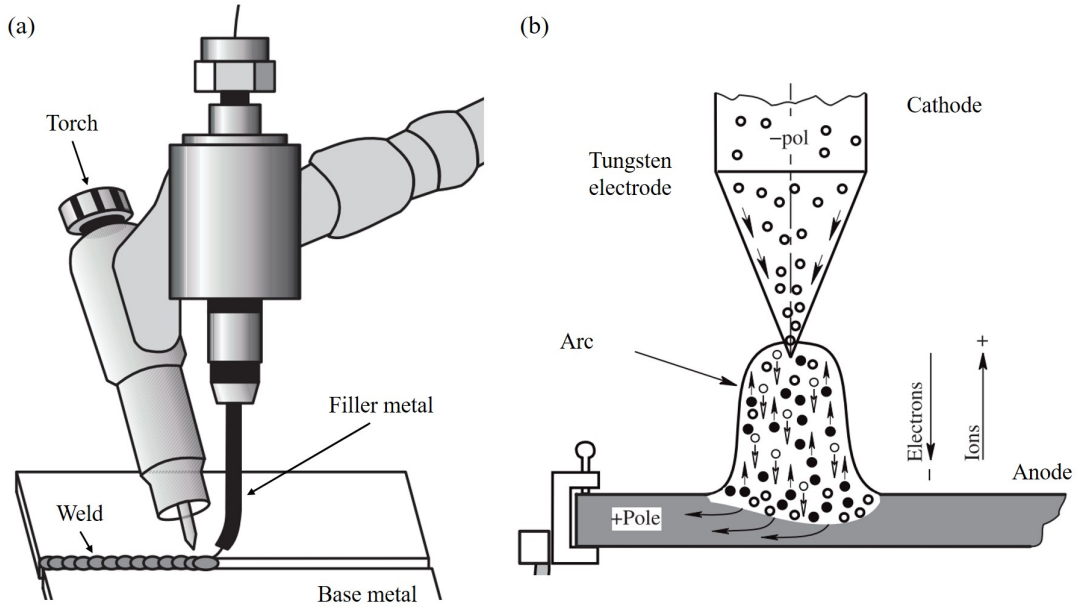

Figure 1.7: GTAW process showing (a) the displacement of the welding torch and filler metal over the base metal plate and (b) a close-up of region near the electrode tip showing the migration of electrons and ions [82].

1.3.2 Effects of welding

1.3.2.1 Microstructure of welded steels

Welding processes, and GTAW in particular, induce high thermal gradients over short periods of time in the welded material. The high temperatures reached during welding induce microstructure transformations, resulting in heterogeneous microstructures because of the heterogeneous distribution of heat. Figure 1.8 illustrates the typical heterogeneous and complex microstructure of a steel resulting from a welding process and the corresponding peaks temperatures during welding. Note that the peak temperatures indicated in the Figure 1.8 can vary by ± 100 °C depending on the steel grade. Experimental measurements or numerical simulations of the thermal fields induced by a welding allows predicting the microstructure transformations occurring in a welded material. Typically, it is theoretically possible to estimate the size of the weld pool, the nature of precipitating secondary phases, grain growth and grain refinement in the heat affected zones as a function of welding parameters. The thermodynamic stability and precipitation kinetics of the secondary phases, as presented in Section 1.2.2, can be confronted to the thermal history of a welded component to identify the phases most likely to precipitate.

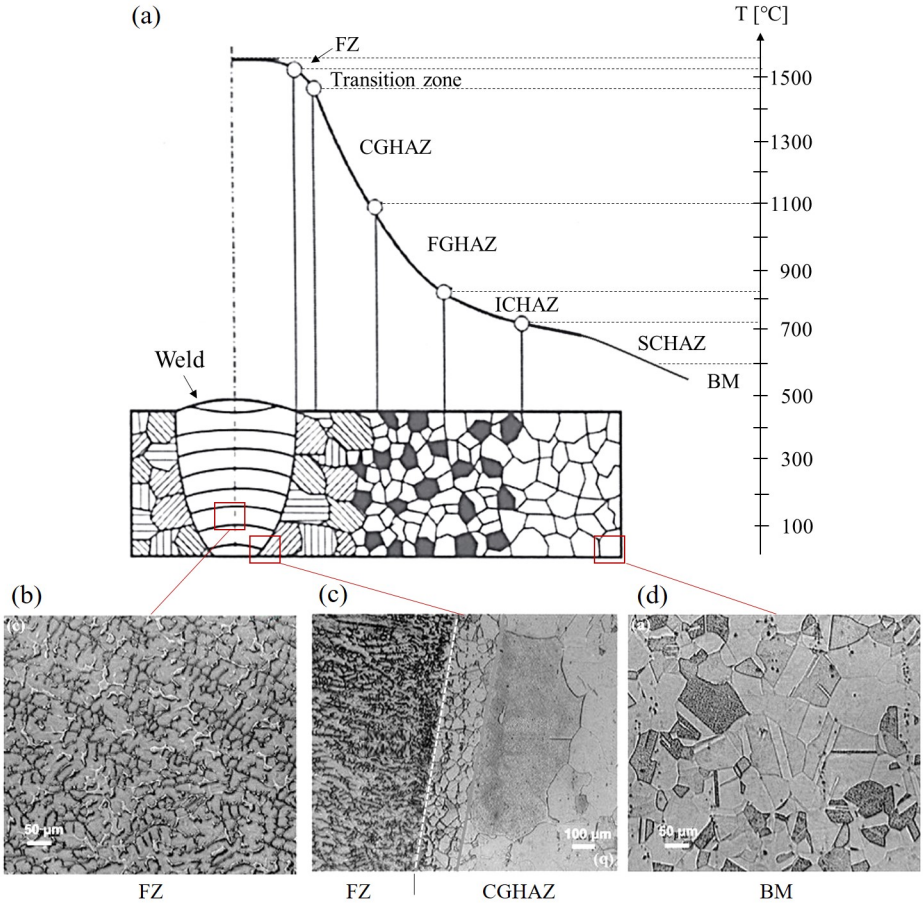

Figure 1.8: Description of microstructure after a single pass welding, showing (a) detail of zones affected by welding and corresponding peaks temperatures during welding according to Śloderbach *et al.*, Aucott and Li *et al.* [83–85] and (b), (c) and (d) micrographs of the fusion zone, coarse grain heat affected zone and base metal, respectively. Micrographs were taken in a GTA-welded 316L steel [86].

From the highest temperatures regions to the lowest, three main zones of the welded

material can be distinguished based on their microstructure: the fusion zone (FZ) or weld metal, the heat affected zone (HAZ) and the base metal (BM).

In the fusion zone, the material is exposed to temperatures higher than the melting temperature. Experimentally, it is very difficult to measure precisely the temperature peak of the weld pool. Usually, measures of temperatures at the surface of the weld pool are reported between 1800 °C [87] and 2000 °C [88] for GTAW. These temperatures can be estimated using infrared thermography. These high temperatures allow the total fusion of the metal in this region, which is quickly followed by the solidification of the metal during cooling. In this region, the resulting austenite grains are very large, formed predominantly by columnar dendritic towards the surface and equiaxed near to the transition zone [89]. A network of δ-ferrite cells distributed homogeneously in the austenite matrix and at austenite grain boundaries is generally observed in welded austenitic steels after cooling [81], as illustrated in Figure 1.8 (b). The morphology and interconnection of these ferrite cells often vary throughout the FZ, in the form of vermicular, also called skeletal, but also in the form of lacy (or lathy) structures [90, 91]. The vermicular morphology is the most commonly observed, corresponding to Figure 1.8 (b). Lacy ferrite is characterized by interlaced ferrite networks, with parallel cells in some observation plans [91]. Some lacy ferrite cells can be observed at the bottom of the FZ in Figure 1.8 (c). Precipitation of secondary phases, either carbides or intermetallics, are not often reported in the FZ of 316 type steels [81, 92]. This is due to the high cooling rate after welding which prevents the precipitation of low-precipitation kinetics phases. However, the thermal ageing of the FZ during post-welding heat treatment or during service can result in the precipitation of intermetallics such as σ, χ-phases and $M_{23}C_6$ carbide, at austenite grain boundaries or from the decomposition of the ferrite cells [81, 93]. Farneze *et al.* [93] also reported the precipitation of Mo-rich precipitates in ferrite cells in the FZ of a 317L steel after multipass GTAW process (Figure 1.9 (b)).

The heat affected zones are found below and adjacent to the fusion zone, with its size being dependent on the welding method and parameters. Heat affected zones are defined as regions of the base metal which did not melted during welding but whose properties were still affected by the heat [78, 94]. Affected zones can be divided into two main zones, from the highest peak temperatures to the lowest: the coarse grain HAZ (CGHAZ) and the rest of the heat affected zone, called HAZ in this work.

The coarse grained zone is exposed to temperatures comprised in the austenite stability range (1100 - 1400 °C), for duration which allow the growth of austenite grains, resulting in larger grains than the base metal as illustrated in Figure 1.8 (c). Temperatures higher than 1100 °C were actually reported in the literature to allow an abnormal grain growth of austenite [95], with much higher grain growth rates than at lower temperatures. In austenitic steel grades such as the 316L(N), the rest of the HAZ is usually described as one single zone, consisting in austenite grains affected by the heat by a hardening mechanism but where grain growth did not occur. In ferritic-martensitic and precipitates hardened steels, the rest of the HAZ can be divided into three additional sub-zones: the fine grain HAZ (FGHAZ), intercritical HAZ (ICHAZ) and subcritical HAZ (SCHAZ). These zones are not observed for austenitic steels, thus are not discussed further here.

The HAZs are particularly prone to precipitation of secondary phases, because of the favorable temperature range and lower cooling rate than near-surface regions. However, this is not systematic and this mostly occurs for high carbon austenitic stainless steels such as the 304H or 316H, since higher carbon content favors the precipitation of carbides [67]. Welding parameters can also strongly affect the probability of phase precipitation. Increase in both welding current and number of welding passes increase the duration of exposure to high temperatures, thus resulting in longer time in the temperature range favorable to carbides and intermetallics precipitation. Typically, Moslemi [96] observed chromium

carbides and σ-phase in the HAZ near the FZ in a multipass welded 316 steel (Figure 1.9 (a)).

Finally, metal exposed to lower temperatures (under 600 °C) is defined as the base metal, which corresponds to metal unaffected by the heat of the welding process. The resulting microstructure and mechanical properties are then the same as the as-received material, as illustrated in Figure 1.8 (d).

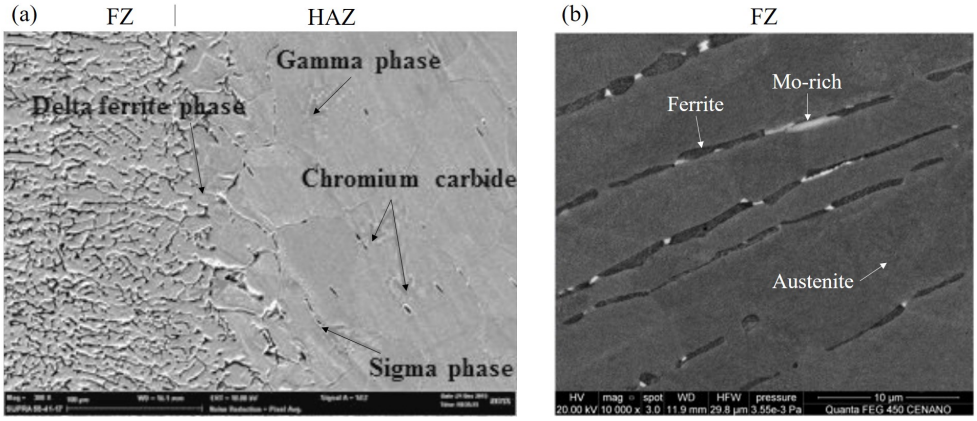

Figure 1.9: Precipitation of secondary phases induced by GTA multipass welding in austenitic stainless steels in (a) the FZ and HAZ of a 316 steel [96] and (b) the FZ of a 317L steel [93].

1.3.2.2 Welding residual stresses

Besides microstructure transformations, one of the main effect of welding on steel components is the rise of residual stresses in the regions affected by welding. Residual stresses can be beneficial or detrimental to the structure properties, depending on the stress nature, but are generally recognised as harmful to welds. Residual stress can be defined as restrained stationary stresses induced by differences in thermal expansion, strength and stiffness and introduced during thermal or mechanical treatments of the material manufacturing [97, 98]. More importantly, they remain in the material even in the absence of external loads. Residual stresses are defined as secondary stresses, contrary to primary stresses which are load-controlled [99]. It exists three types of residual stresses: macro or bulk residual stress (type I), intergranular stress (type II) related to grain-to-grain interactions and finally atomic-scale stress (type III) [99, 100].

Specifically in welded workpieces, residual stresses are caused by the exposure to high local temperature variations during the displacement of the welding torch over the material, illustrated in Figure 1.10 (a), resulting in severe temperature gradients around the weld pool [101]. At the nose of the weld pool, the high increase in temperature causes a thermal expansion of the material, which induces compressive stresses in the affected region [101] (Figure 1.10 (b) and (c)). When the metal cools down after the welding, tensile stresses appear due to thermal contractions (Figure 1.10 (b) and (d)). After welding, tensile residual stresses remain in the FZ as well as in part of the HAZ near the FZ, while the rest of the HAZ contains residual compressive stresses away from the weld (Figure 1.10 (e)) and Figure 1.11 (a)). Considering a single-pass welding on a plate, typical temperature and residual stresses profiles can be simplified as in Figure 1.10 (c) to (e), which shows the progressive increase of compressive and tensile residual stresses as the plate is cooling down. The distribution of residual stresses is heterogeneous in both longitudinal and transverse direction (Figure 1.11), with highest magnitudes found towards the middle

of the plate and weld bead. Peaks of tensile residual stresses in multipass GTAW 316 steels are generally reported to be near 400 to 500 MPa in the affected zones [102].

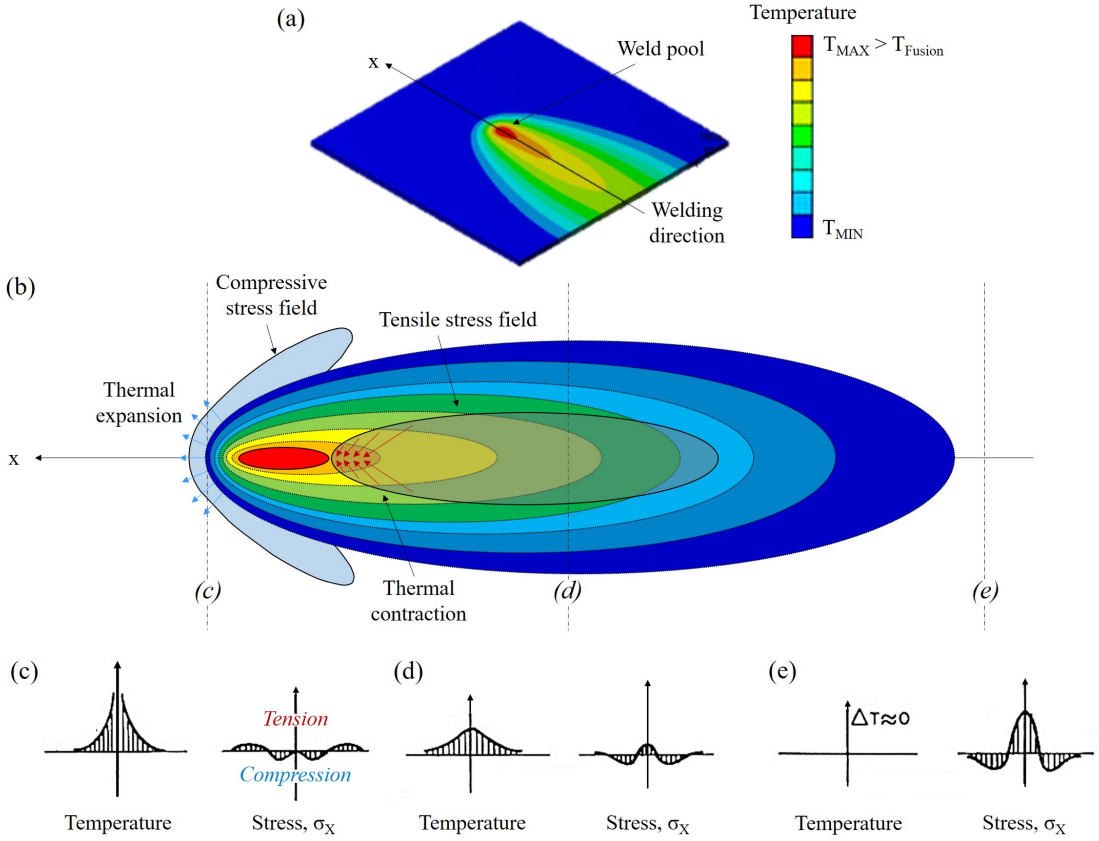

Figure 1.10: Formation of residual stresses due to the welding process with (a) simulated thermal fields during the welding torch displacement [103], (b) close-up view of the weld pool with compressive and tensile stress fields rising from the thermal expansion and contraction. Schematic surface temperature and longitudinal stresses profiles (c) ahead of the weld pool, (d) at the tail of the weld pool and (e) after welding. Figures are adapted from Selvamani *et al.* [103], Colegrove *et al.* [101] and Masubuchi *et al.* [104].

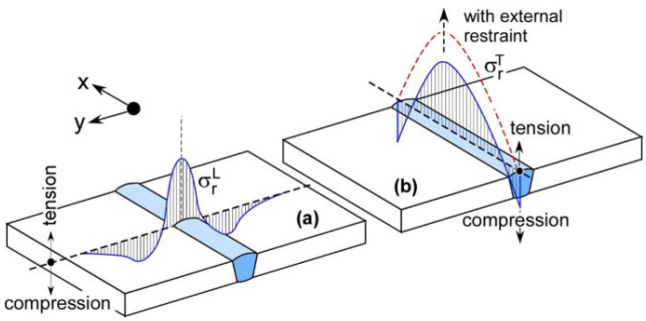

Figure 1.11: Residual stresses induced by welding in the (a) longitudinal and (b) transverse directions after the cool-down [105].

The distribution and magnitudes of welding residual stresses can be influenced by the different welding parameters, which can be tuned to reduce residual stresses and thus prevent issues associated to it. First, the clamping system, used to mechanically maintain

the steel plate during welding and hence avoid distortion, can increase the level of residual stresses because the plate is unable to deform freely (Figure 1.11 (b)) [106]. Particularly, Choobi *et al.* [107] showed that clamping a 304 steel plate prior to welding and releasing the clamps after cooling down to ambient temperature increases transverse and longitudinal residual stresses. However, if the clamps are removed immediately after welding (then called hot release), residual stresses are not affected. Elmesalamy *et al.* [102] results differ, reporting a slight increase in residual stress when no restrain was used (Figure 1.13 (c)), as compared to the restrained plate (Figure 1.13 (a)) for the multipass GTAW of a 316L.

Welding residual stresses can also be limited by lowering heat magnitudes through an adjustment of welding parameters [102]. This can be achieved by increasing the welding torch displacement velocity or lowering the power energy source [108]. However, the welding method, either single-sided (welding passes on one side of the plate) or two-sided (passes on both sides), was reported to have no significant impact of the levels of residual stresses [102] (Figure 1.13 (a) and (b)).

To lower the magnitude of residual stresses, a prior heating treatment of the plate can be carried out before welding [109]. Such process allows reducing the thermal gradient required to enable the steel fusion, thus lower the tensile and compressive stress [110]. Adedayo *et al.* [110] typically reported reduction of welding residual stresses of up to 75% thanks to a prior preheat carried out at 200 °C. Pre-heating can also reduce the risk of hot cracking and the formation of brittle martensite, induced by the rapid cooling of the welded plate [109]. However, pre-heating can also be detrimental to residual stresses [111]. Indeed, the yield strength of the steel decreases with an increase of temperature, favoring plastic strain [109]. Consequently, pre-heating method cannot be used systematically and should be carefully employed depending on the material, welding method and conditions. Specifically for the 316 grade, preheating is not recommended by the RCC-MRx [65] specifications.

Asides from the welding parameters, the choice of the filler metal can also influence residual stresses. Godin *et al.* [112] typically showed the presence of tensile residual stresses in the fusion and heat affected zones using an austenitic filler metal for the welding of a martensitic steel (Figure 1.12(a)). However, when using a martensitic filler metal, the fusion zone was found to contain high compressive residual stresses (Figure 1.12 (b)), due to a martensitic transformation occurring during the cool-down, involving a volumetric expansion and thus compressive stresses [112]. Magnitudes of residual stresses can also be reduced using low-temperature transformation (LTT) filler metal instead of regular ones [113].

One way to avoid the influence of the filler metal on the nature, distribution and magnitude of residual stresses is to operate a simple fusion line on the steel plate without filler metal, which is possible for GTAW or power beam welding processes. This also allows simplifying the microstructure of the weld. However, it is important to keep in mind that a pass of welding torch without filler metal results induces differences in stress nature, magnitude and location when compared to welding operated with filler metal [114]. As a result, Yunasz *et al.* mention that failures in welds with filler metal occur generally in the region between the base metal and HAZ, while failures in welds without filler metal rather initiate in the weld metal [114].

While stress relaxation cracking issues are often reported for thick components, Elmesalamy *et al.* [102] showed that for multipass GTAW of a 316L steel, the thickness of the plate has no significant impact on the magnitude of welding residual stresses but rather on the distribution (Figure 1.13 (a) and (d)).

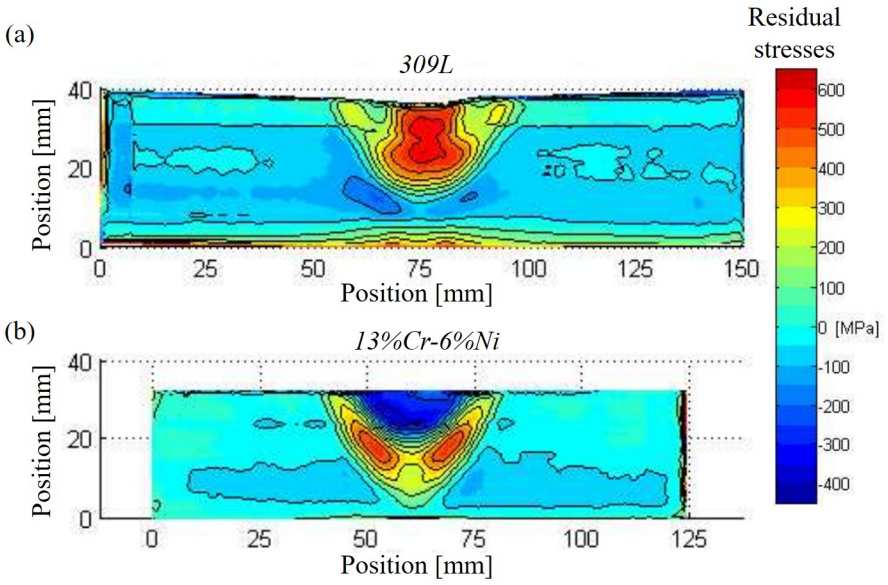

Figure 1.12: Residual stress distribution in a welded martensitic stainless steel plate measured by the contour method. Welding was carried out using a filler metal made of (a) 309L austenitic stainless steel and (b) 13%wt. Cr and 6%wt. Ni martensitic steel [112].

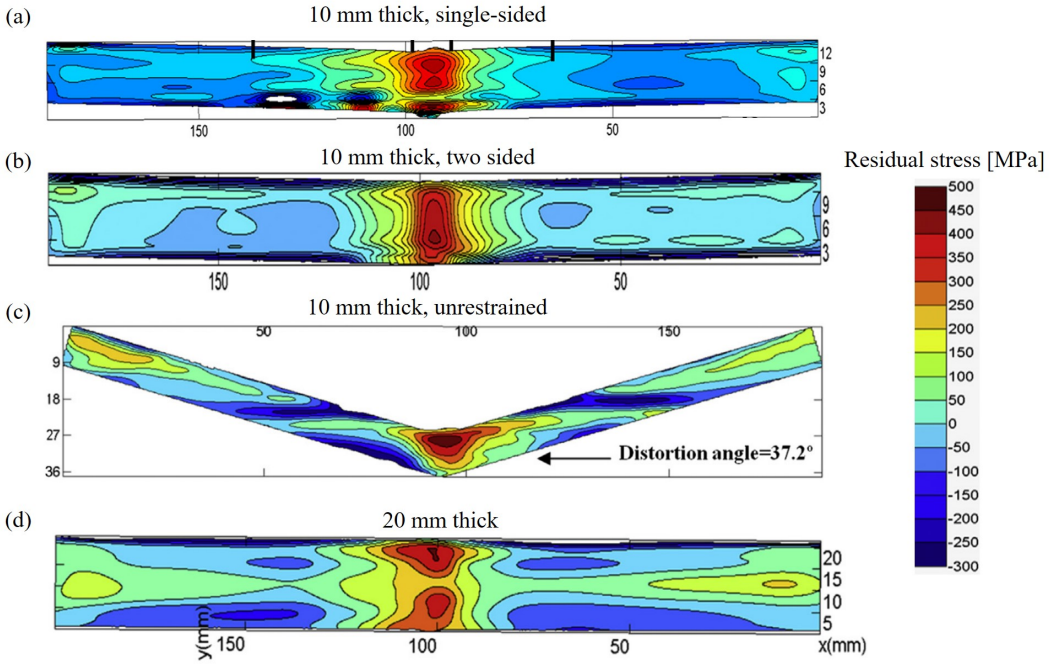

Figure 1.13: Welding residual stress distribution in a 316L steel plate after mutlipass GTAW measured by the contour method. Effect of welding strategy with (a) single-sided and (b) two-sided, (c) effect of clamping and (d) effect of thickness [102].

1.3.2.3 Effects of welding on mechanical properties

Due to the numerous microstructural transformations occurring in the regions affected by welding and the formation of residual stresses, mechanical properties of the material are directly affected.

Typically, both fatigue strength [115] and fracture toughness [101] are generally re-

ported to decrease in regions containing tensile residual stresses. Inversely, the introduction of compressive residual stresses, for instance by the shot penning method, can improve fatigue strength of stainless steels [116]. Corrosion resistance was also reported to be decreased by the presence of residual stresses [117].

The mechanical properties are also affected by microstructural transformations. Because of the coarser grains, the CGHAZ exhibits the lowest toughness [118]. This is true mainly for single-pass welding, since multi-pass welding results in a much more complex microstructure and prior CGHAZ can be affected differently during the subsequent passes. Typically, the CGHAZ can exhibit a higher hardness than the other zones for multipass welding. The other heat affected zones, with finer grains, are generally characterized by an increase in hardness [119]. Molak *et al.* [120] carried out tensile tests of microsamples machined from the FZ, HAZ and BM of a GTAW joint made of a 316L steel. They showed that the heat affected zone presented a higher yield strength (YS) and ultimate tensile strength (UTS) than the base metal, while the FZ (weld) was characterized by lower values.

Affected regions also show a decrease in creep rate at high temperature (around 600 °C) and an increase in hardness, which is related to the increase of the dislocation density introduced by the various welding passes. Auzoux *et al.* [13] typically showed that an increase in number of welding passes resulted in an important increase in Vickers hardness. They concluded on a cumulative increase in plastic strain, or hardening, by an accumulation of dislocations in the material due to the successive thermal cycles during welding. Mobile dislocations can be subjected to several interactions during their displacement, among which the solute atoms-dislocations and precipitation-dislocations interactions. The low ductility of the regions affected by welding is rather attributed to solute drag mechanism, causing intragranular hardening. This is known to be a detrimental factor for the resistance of a steel to stress relaxation cracking [45], where 316L steel grade with higher content in solute atoms was shown to be more prone to SRC. An increase in hardness may also be attributed to strain-induced intragranular precipitation, however with much less impact than dislocations interactions with solutes atoms. Besides, such effect is unlikely to occur in 316 steels [121].

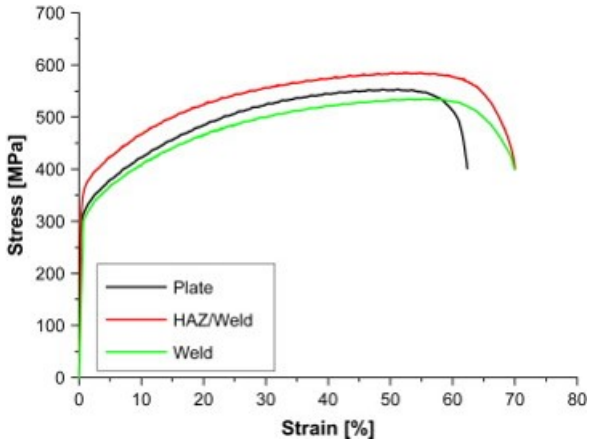

Figure 1.14: Effect of multipass GTAW on tensile properties of a 316L steel with tensile curves corresponding to each affected zone and the base metal (plate) [120].

1.3.2.4 Relaxation of residual stresses

It exists several methods to limit or relax residual stresses before and after welding, in order to prevent the degradation of the material properties and to avoid distortion during

welding. These are divided into thermal and mechanical techniques. Limitation of residual stresses by adjusting welding process parameters are not discussed here as they were presented previously in Section 1.3.2.2.

Post-weld heat treatments (PWHT) can be applied, allowing the partial relaxation of residual stresses after welding via heat treatments of several hours between 600 to 800 °C [122]. In a study on welding of the 321 stainless steel, Sadeghi *et al.* [66] reported a residual stress reduction of 35% after a PWHT of 2 h at 480 °C. Their results also suggested that an increase of the PWHT temperature did not significantly improve stress relaxation. The reduction of residual stresses can be revealed by the decrease in hardness of the HAZ and BM regions after a PWHT to some extent, as illustrated in Figure 1.15 (a) for a 316L steel [119]. Similarly to the pre-heating method, PWHT is not an ideal solution. PWHT were also found to trigger the initiation of cracks in high tensile strength materials [123], and thus should not be used for materials highly sensible to stress relaxation cracking.

Mechanical techniques for the reduction of residual stresses after welding includes two main methods, peening and vibratory stress relief [109]. Peening method consists in the impact and propagation of shock waves in the welded material, aiming for compressive residual stresses. Due to the very process, peening is limited to near-surface regions of the material and results in residual tensile stresses deeper in the components [109]. Peening method is thus less suited for large welds, as defects can initiate at several millimeters deep from the surface. Vibratory stress relief (VSR) consists in vibrating the welded component. This method is controversial as there is still a strong disagreement on whether it has an effect or not on reducing residual stresses [109]. Additionally, the process was found to induce local plastic straining where it is not desired. VSR can thus negatively affect the welded component, regarding its fatigue lifetime.

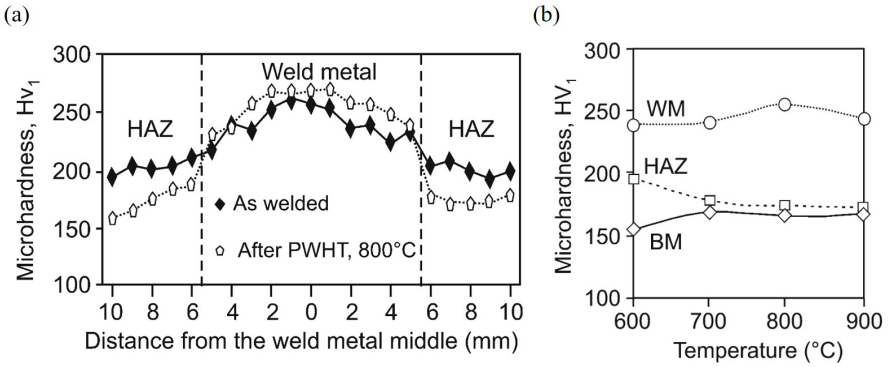

Figure 1.15: Vickers micro-hardness HV1 measurement of a 15 mm thick welded 316L steel plate. (a) Comparison of hardness between post-welding and post-weld heat treatment states. (b) Effect of annealing temperature on hardness: base metal (BM), heat affected zone (HAZ) and weld metal (WM) [119].

1.3.2.5 Measurement of residual stresses

Measurement of residual stress can be achieved through several methods, either destructive or non-destructive and are all indirectly derived from the measurement of other properties. Most common methods are shown in Figure 1.16, classified in function of spatial resolution and penetration.

The hole drilling method and contour method are destructive approaches for residual stress measurement. These methods are widely used as they can provide results quickly for different geometries and materials, not requiring complex nor costly equipment. In both cases, residual stresses are derived from the measurement of displacement while removing

successive portions of the material which spontaneously finds a new stress equilibrium. The main drawback of such methods is obviously the partial or total destruction of the sample, and the low accuracy of the measure depending on the method for displacement measure [109].

Non-destructive methods, such as X-ray, neutron or synchrotron diffraction methods, present the advantage of higher accuracy and are better suited for local analyses or high amplitude residual stresses. The measurement of strain is allowed by the measurement of crystal lattice spacing using Bragg's law, which can traduce the presence of local residual stresses knowing the elastic modulus and Poisson's ratio of the material [109]. Such methods are preferable to the destructive method when possible; however the measurement time and cost are significantly higher. Also, these methods can be sensible to material texture, grain size, and may not be suitable for highly strained material and for heterogeneous microstructures.

Other methods, such as nano-indentation and hardness measurement, are sometimes carried out to estimate the presence of residual stress. It is a simple and low cost method, however the interpretation of the results can be hazardous. For these methods, knowing precisely the microstructure of the studied material is essential, as the hardness is dependent on the microstructure of the analysed area [112]. Generally, in a homogeneous microstructure a low hardness values suggests the presence of tensile residual stresses [45]. This was observed by Simes *et al.* [124] as illustrated in Figure 1.17. Inversely, compressive residual stresses are generally associated to high hardness values. While this relationship is often observed for the melted metal and base metal regions, it is not verified for the HAZ region.

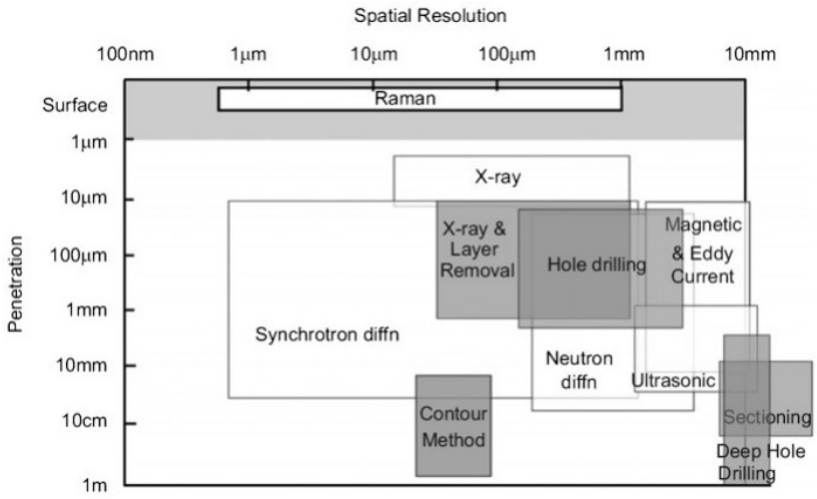

Figure 1.16: Main methods for residual stress measurement classified in function of spatial resolution and penetration [109].

1.3.3 Simulation of welding

In order to predict the material distortions, plastic straining and residual stresses resulting from the welding process, thermo-mechanical simulations can be performed using Finite Element Method (FEM) computations. Estimations of post-welding residual stresses in a welded structure and the confrontation with stress relaxation cracking thresholds for a material can allow evaluating the risk of failure for each weld zone.

Figure 1.18 shows the typical successive steps for the thermo-mechanical simulations of welding [125, 126]. More complex works also account for the microstructural transforma-

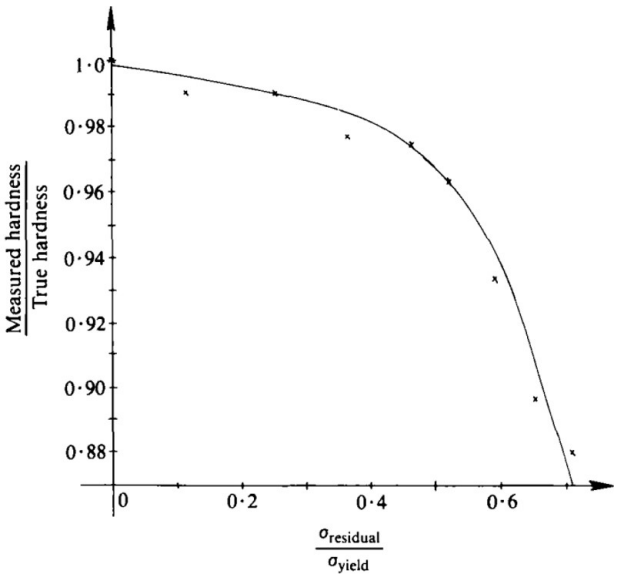

Figure 1.17: Evolution of measured hardness as a function of present residual stress in a bright drawn mild steel [124].

tions occurring in the material during welding, dictated by the thermal fields [80]. In pure thermo-mechanical simulations, computed thermal fields are used to simulate the mechanical response during the whole welding process. Thermal and mechanical considerations are discussed separately thereafter.

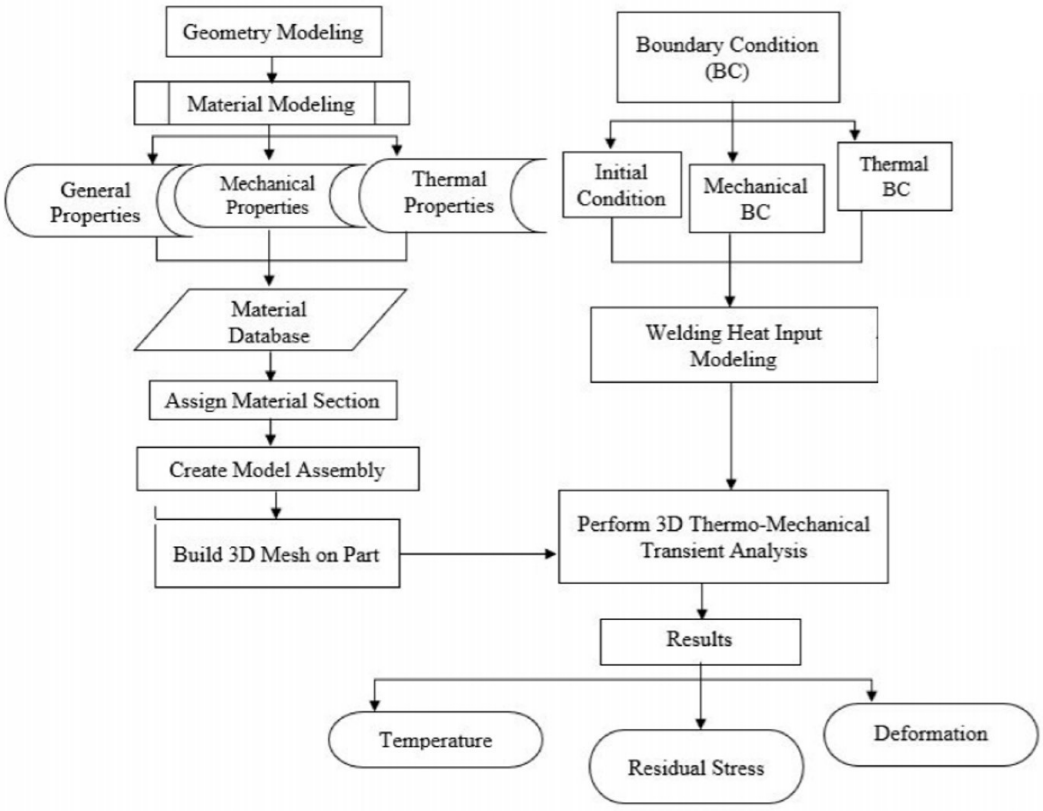

Figure 1.18: Typical Finite Element method simulation process for welding simulation accounting for thermal and mechanical considerations [126].

Thermal simulation

Thermal simulations account for conduction and convection phenomena during the displacement of the welding torch [126]. Conduction occurs throughout the material, while convection occurs between the material and the ambient air. Thermal radiation can also be considered in the thermal analysis, in order to obtain better predictions of thermal fields.

The welding arc is generally simplified as an equivalent heat source moving along the weld centreline (WCL). Many equivalent heat sources exist in the literature, such as cylindrical, semi-spherical, double-ellipsoidal and conical [127]. It is very common to consider the heat source with a double-ellipsoidal distribution [125, 126, 128], as first established by Goldak *et al.* [129] (Figure 1.19).

The displacement of the heat source near the material surface is traduced numerically by high temperature gradients at the front of the source, and smaller gradients at the rear of the melt pool depending on the convection coefficient of the studied material (Figure 1.20 (a) and (b)). These high temperature gradients make the measurement of temperatures near the weld a delicate process when placing thermocouples, leading to possible differences between experimental and simulated thermal fields [125]. Typically, temperature differences of several hundreds of °C are often reported between two close points (a few mm) near the molten metal [125, 126] (Figure 1.20 (b)).

Thermal computations of welding allow performing simulations of the mechanical response of the material, by associating the predicted thermal fields and the material properties described as a function of temperature. These are used to predict the distortion and residual stress fields resulting from the welding process. Additionally, thermal simulations allow correlating the microstructural zones affected by welding observed experimentally with ranges of temperature, as illustrated in Figure 1.20 (c). This helps understanding the areas with conditions favorable for secondary phase precipitation as discussed in Section 1.2.2, but also predicting matrix grain growth for more complex models.

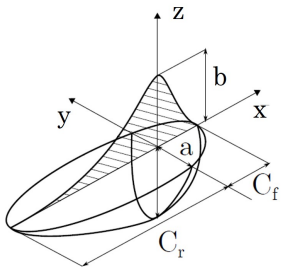

Figure 1.19: Goldak double ellipsoid geometry and parameters used to model equivalent heat source for welding thermal simulation [130].

Mechanical analysis

Mechanical simulations are then achieved using constitutive laws suited to the studied material (Figure 1.18). Numerous mechanical models have been proposed over the years, relying on the material mechanical behavior for the considered temperatures, strain rate, magnitude and nature. During welding, the steel may deform elastically, plastically and viscously.

Ideally for the 316L(N) stainless steel, the mechanical model should take into account these three deformation modes, thus an elasto-visco-plastic model. However, viscous models are more complex as they increase the number of variables (plastic strain rate for instance) and parameters to take into account, but also leads to longer simulation times.

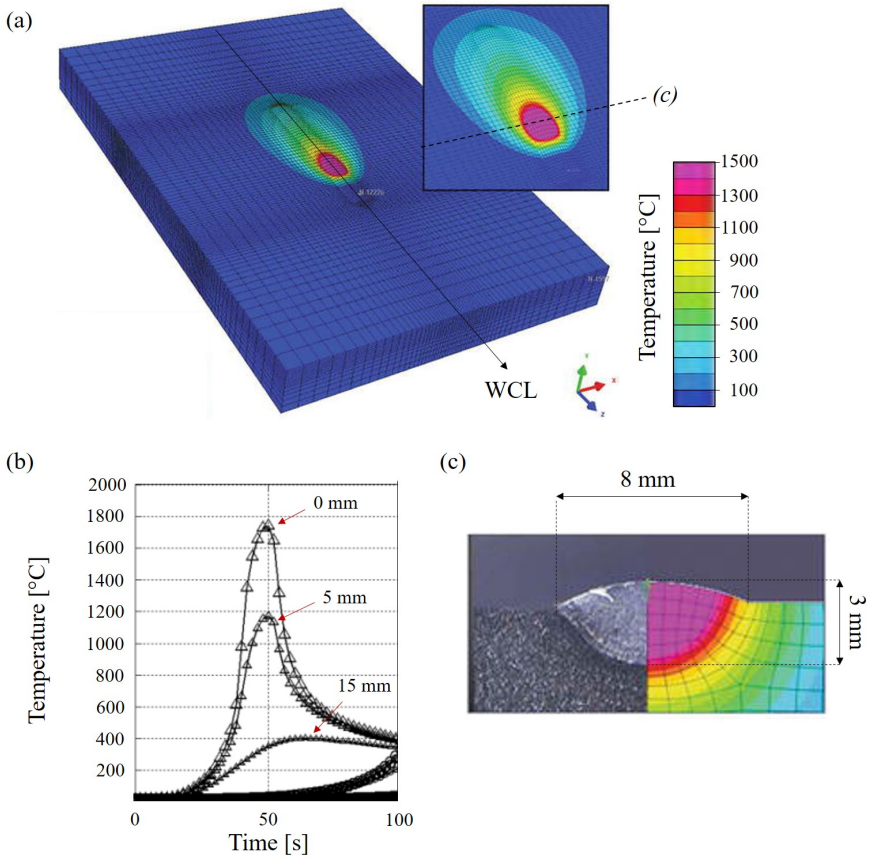

Figure 1.20: Thermal simulation of single-pass GTAW of a 316L steel plate. (a) Simulated thermal fields during the displacement of the welding torch [131], (b) evolution of temperature as a function of time for three distance from the weld center line (WCL) [132] and (c) comparison between predicted maximum temperatures in the section of the plate showed in (a) and corresponding microstructure of the weld after welding [131].

Moreover, viscoplatic data are usually not easily available. Depradeux [133] indicated that a precise prediction of welding residual stresses can be achieved simply using an elastoplastic model. Such considerations seem to be the most common compromise adopted for welding simulation in the literature [126, 128, 134–136].

The choice of an elastoplastic model should result from the understanding of the material mechanical response during welding. The welding process exposes the material to successive mechanical loading and unloading cycles induced by the thermal expansions and contractions as discussed in Section 1.3.2.2. The induced Bauschinger effect requires to take into account the kinematic hardening rather than isotropic solely, or ideally a combined model [137] such as suggested by Chaboche [138]. Indeed, Hemmesi *et al.* [131] made a comparison between isotropic, kinematic and combined hardening models for the simulation of welding of a 316L steel (Figure 1.21). Their results showed that a combined hardening model leads to computed residual stresses values closer to experimental measures than with other models. Zheng *et al.* [137] also chose a combined hardening model (Chaboche) for their mechanical simulation of welding of a 304L steel, with good agreement with experimental results (Figure 1.22) as well as theorical residual stresses as shown previously (Figure 1.11).

The estimation of residual stresses through thermo-mechanical simulations of the welding process could then help predicting the risk for stress relaxation cracking of a component, after the identification of the SRC thresholds of a material. Specifically, the identifi-

cation of SRC thresholds for each weld zone would give precise information on where the issue can be expected. This requires investigation on SRC mechanism in a heterogeneous weld microstructure, and the study of SRC microstructural influencing factors.

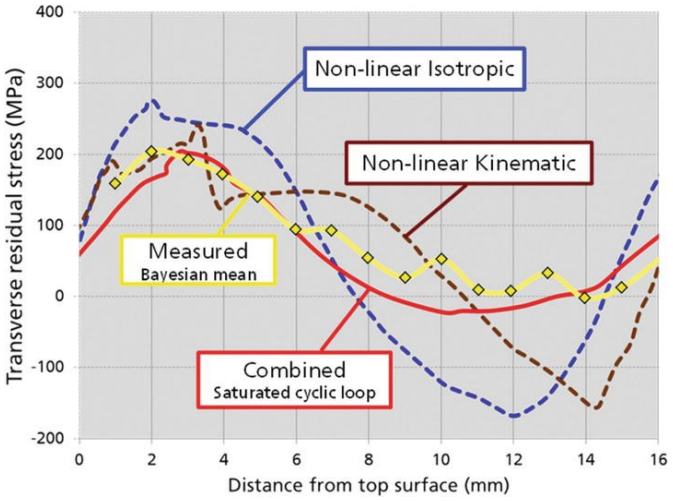

Figure 1.21: Comparison of simulated and measured transversal welding residual stresses through the thickness of a welded 316L steel plate with geometry shown in Figure 1.20 (a). Simulation of residual stresses performed with non-linear isotropic, kinematic and combined models are compared to the measurements [131].

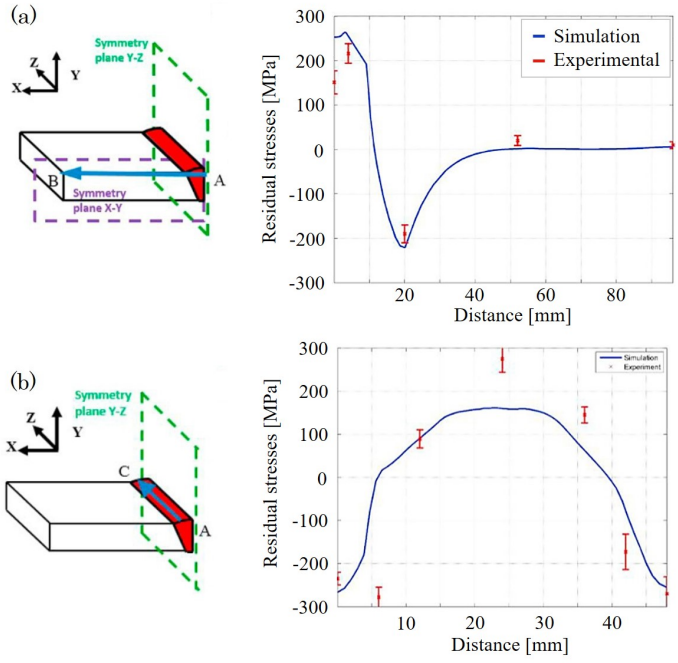

Figure 1.22: Comparison between measured and computed residual stress from welding along (a) transverse and (b) longitudinal directions using a combined isotropic and kinematic hardening model to simulate the mechanical behavior of the 304L steel [137].

1.4 Stress relaxation cracking

1.4.1 Stress relaxation cracking mechanism

SRC was described to appear primary due to the presence of residual stresses generated during the welding process presented previously, with high stress magnitudes in the HAZ, particularly in the CGHAZ [13, 18, 33, 45, 47]. During the service or a PWHT, these residual stresses cannot be sufficiently accommodated by plastic deformation due to an exhaustion of ductility of the affected zones at high temperature, eventually resulting in an intergranular cracking as described in the introduction [3, 6, 7, 12, 33, 37, 139].

SRC is usually reported to be induced by fracture either resulting from intergranular cavitation assisted by GB precipitates or from a brittle mode, commonly called low ductility intergranular fracture (LDIGF) [5, 6]. The first mode, intergranular cavitation, is the most widely adopted mechanism to explain SRC. During the use of a welded component in service, the exposure to high temperatures allows the precipitation of undesirable secondary phases at grain boundaries and in the bulk. The plastic strain, induced by the relaxation of residual stresses, is then localised at the GB precipitates (Figure 1.23 (a)) which therefore act as obstacles for both dislocation and vacancies motion [5, 7], making them favourable sites for cavity nucleation. These cavities eventually further grow, coalesce to form micro and macro-cracks, similarly to a creep cavitation mechanism [6]. The mechanism of formation of cavities is still subject to discussion, however from the knowledge of creep cavities it is commonly admitted that they result from vacancies condensation [140–143]. SRC initiated at GB precipitates is generally characterized by intergranular dimples due to the presence of the GB precipitates, as illustrated in Figure 1.23 (c).

The second mode, low ductility intergranular fracture, is rather associated to grain boundary sliding and accumulation of plastic strain at triple points [5] (Figure 1.23 (d)). In some studies related to creep cavities, it is also proposed that cavitation at GB triple points occur when GB precipitates are not present in the neighbour grains [144]. In contrast to cavitation mode, SRC initiated at GB triple points is generally characterized by smooth intergranular fractures and relatively featureless grain faces because of the absence of precipitates, as illustrated in Figure 1.23 (c).

In both modes, plastic strain induced by the relaxation of stresses is responsible for the formation of cavities at the GBs. Interestingly, Wortel [12] typically showed that plastic strains of less than 0.2% during relaxation were sufficient to cause stress relaxation damage if no PWHT was performed on welded components made of SRC-susceptible materials, such as 304H and 800H steels (Figure 1.24).

The factors inducing the transition from one mode to the other have been subject to discussion in the literature. Some authors stated that mechanisms are stress dependent, with cavitation on GB precipitates being characteristic of lower stress levels [5]. Others stated a temperature dependency, with LDIGF mode occurring at low temperatures associated to phosphorus and nitrogen GB segregation, and cavitation on GB precipitates at higher temperatures [5]. According to these authors, the LDIFG mode typically occurs between 325 and 625 °C [3, 5, 7] . It is more likely that the transition between the two modes is both temperature and stress dependent, as suggested by Lippold [5]. It is also important mentioning that cases of mixed modes of SRC were also reported [3].

1.4.2 Stress relaxation cracking factors

The main factors involved in the SRC mechanism have been investigated by many authors, testing material with very different sensitivity to the phenomenon. A list of the factors identified by these authors is proposed in the following, differentiating factors that are

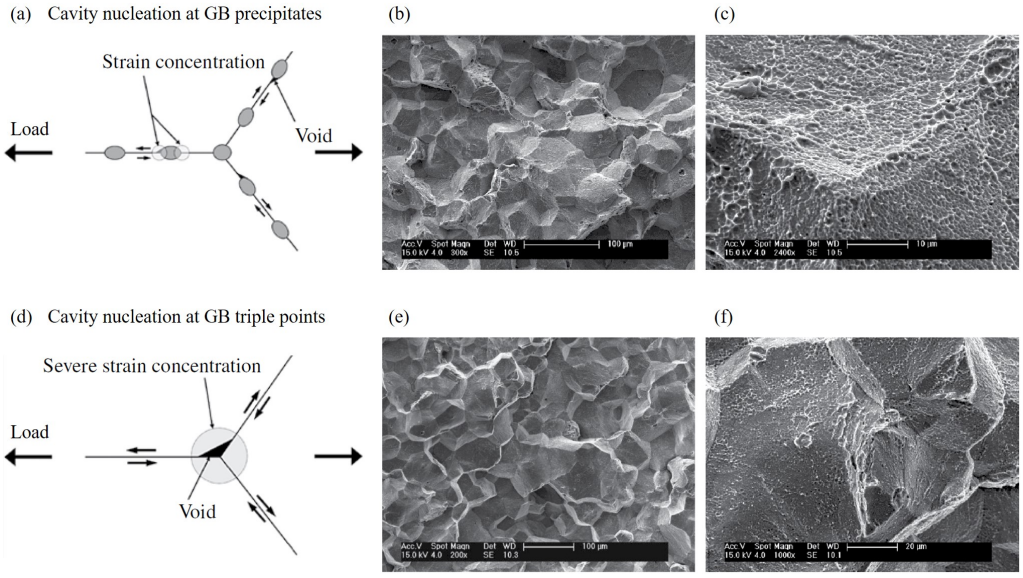

Figure 1.23: SRC mechanisms and fracture features with cavity nucleation at (a) to (c) GB precipitates and (b) to (f) GB triple point [5].

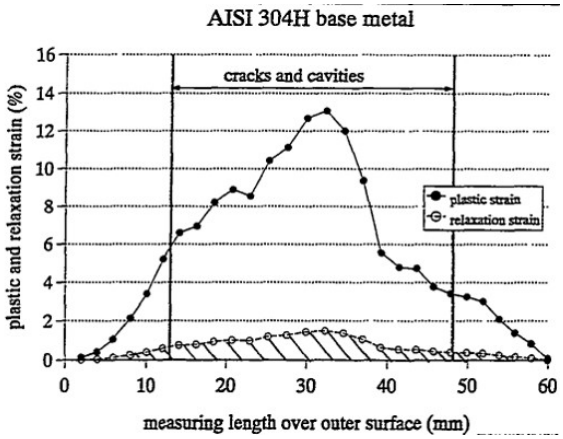

Figure 1.24: Relaxation cracks, initial and relaxed plastic strain in the BM of a 304H bending-tested at 575 °C for 300 h [12].

required for SRC to occur, and factors that influence the material resistance to SRC, but are not obligatory for triggering this phenomenon [5, 45]. More in-depth review of each of these factors is presented in dedicated sections.

- Necessary factors:
  - Residual tensile stresses induced by the welding process [5];
  - Material pre-straining or hardening due to cold-rolling, welding, mechanical solicitation or elaboration process [18, 145];
  - Reheat in critical temperature range, 500 - 775 °C, allowing stress relaxation [5];
  - Secondary phase precipitation at GBs and bulk, generally of carbides and/or intermetallic phases [5, 45, 146];
- Influencing factors:
  - Chemical composition, with higher susceptibility of high-carbon steels and stabilized steels;

- Grain size, with a damage hazard for grain diameter larger than 90 μm [24];
- Geometry and thickness of the component, with damage hazard for thickness higher than 25 mm [7, 18];
- Stress localisation typically due to welding of components of different thicknesses, or radii for pipes [18];

1.4.2.1 Stresses

The first characteristic of the relaxation cracking phenomenon is that cracks can form in the absence of external mechanical load when a susceptible material is exposed to temperatures above 500 °C. In favorable conditions, damage results from the presence of tensile residual stresses, rising from the successive thermal cycles induced by the manufacturing process, primarily welding [101]. As presented in Section 1.3, the choice of welding process and associated parameters are thus key parameters when it comes to reducing SRC risk [108]. Of course, the geometry of the welded parts and their operation conditions are very likely to aggravate the state of stress of the material and therefore to facilitate SRC, but they are not necessary for the phenomenon. During service, additional stresses can be induced by: internal pressure, difference in the coefficient of thermal expansion between the base material and weld metal, thermal stress due to temperature gradients across the components thickness and bending stresses because of the components geometry [147]. Moreover, stresses may also arise locally from phase precipitation during thermal ageing, because of lattice mismatch between the precipitates and matrix [5]. Although they can play a role, Emerson *et al.* [147] believe these other sources of stresses are negligible when compared to welding residual stresses in normal operating conditions. According to them, the peak of residual stresses from welding can reach about 480 MPa in thick-wall pipe joints. By comparison, Feng *et al.* [14] mentioned that steam pressures only induce stresses of about 20 MPa during service.

Evaluations of SRC threshold were firstly conducted in the 1950s by Curran *et al.* [17], who estimated a minimal stress of 135 MPa to cause the failure of a 347 steel at 650 °C after 62 months of industrial service.

More recently, Pommier [148] evaluated SRC threshold for a cold-rolled (22%) 316L(N) steel by correlating residual stresses estimated by FEM mechanical simulations to experimental quantification of damage. He found that residual tensile stresses higher than 740 ± 30 MPa (formed at room temperature) can induce intergranular damage in a cold-rolled 316L(N) steel after ageing time as low as 580 h carried out between 550 and 600 °C. Pommier then showed that SRC was strongly related to principal residual tensile stresses, as illustrated in Figure 1.25. However, damage measures provided by Pommier clearly show that the 740 MPa threshold is an estimation for macroscopic damage only; residual stresses magnitudes way below this limit can allow mild damage. Typically, in Figure 1.25 intergranular damage is still present in regions where principal residual stresses are lower than 500 MPa.

1.4.2.2 Work hardening

Work hardening, or pre-strain, is usually cited in the literature as a necessary factor for SRC [13, 18], even though some works rather considered it as an influencing factor [3]. Work hardening can be induced by the manufacturing process of components, as in the case of pipes bends which may require cold-bending work [3, 149, 150]. Besides from manufacturing, the welding process itself can induce hardening upon cooling, particularly in the heat-affected zones because of bulk precipitation and/or thermal expansion/contraction. Typically, Auzoux [13] distinguished three heat-affected regions of a welded 316 steel according to their relative hardness:

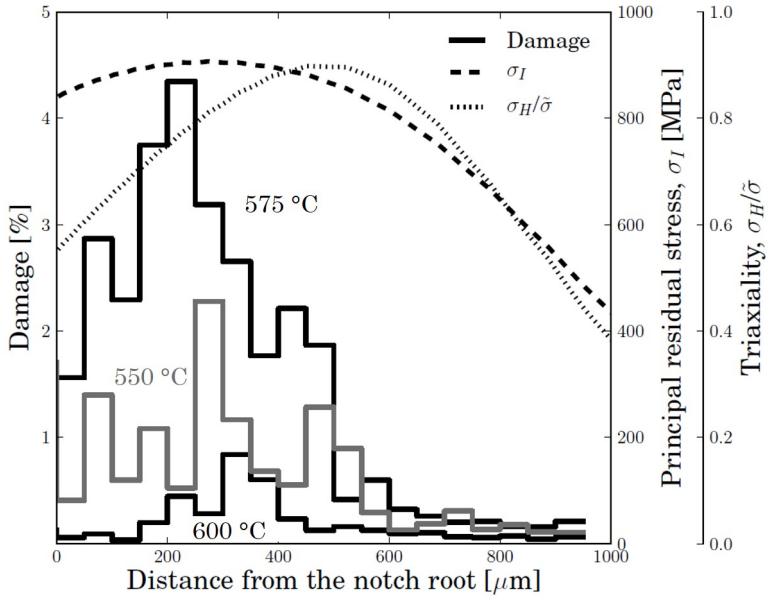

Figure 1.25: Influence of residual stress magnitude on intergranular damage in CT-like specimens used to reproduce SRC. Comparison between the computed principal residual stress and triaxiality distributions and the tomography-measured damage in a 316L(N) steel at 550 °C, 575 °C and 600 °C [45].

- Non affected material: in this region, welding had no influence because of low temperatures (inferior to 100 °C), the resulting hardness was thus similar to the as-received material.
- Affected material: this corresponds to the first region affected by welding. Temperatures between 100 and 600 °C in this region were high enough to induce hardening, with an estimated plastic strain of about 2%. Experimentally, the measured level of hardness increases as the distance to the fusion zone decreases.
- Partially restored material: in this region, hardness decreased as the distance to the FZ decreased. Temperatures in this region (650 to 1450 °C) allowed the partial restoration of the previous passes.

Heat-affected zones of weld joints and cold-worked components are more prone to SRC because of several mechanisms. Firstly, pre-work hardening of the material can increase the risk of SRC by the increase in precipitation kinetics of secondary phase favoring SRC [3, 13, 18, 151]. Indeed, cold-working generates dislocations, which represent preferential sites for precipitates nucleation [3]. Weiss *et al.* [67] typically showed that prior cold-working of 316 steels allowed quicker carbides precipitation, as illustrated in Figure 1.27. Besides, Nomura *et al.* [152] also suggested that the higher density of dislocations introduced inside the grain makes them stronger, leading to difference in strength from the GBs and thereby favoring intergranular cracking. Additionally, cold-rolling at room temperature can result in the formation of mechanical twins, susceptible to favour cavity nucleation due to stress concentration as suggested by studies related to creep cavities [141]. Finally, Auzoux [13] showed that prior cold-rolling induces a decrease of the stress relaxation rate (Figure 1.26) and a decrease in resistance to crack propagation. From the analyses of a 316H failed component, Auzoux [13] typically found that relaxation cracks appeared in the affected region of the component, where hardness values were up to 30% higher than the base metal ones (230 HV30 against 150). Note that in this case,

Auzoux [13] also observed intragranular precipitates which definitely contributed to the increase in hardness, (see Section 1.4.2.4). Additionally, multipass welding induces the accumulation of plastic strain, resulting in the hardening increasing as the welding pass number increases [13].

For Chabaud-Reytier [18], 5 to 10% of pre-strain was necessary to cause relaxation cracking in a 321 steel (Figure 1.28). In contrast, Wortel [12] reported that 2-3% of cold deformation is sufficient to make a material susceptible to SRC.

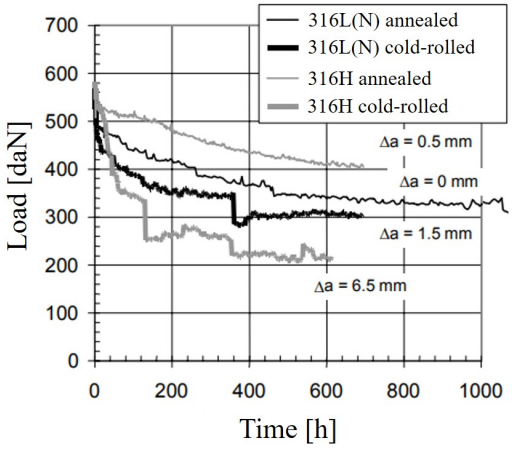

Figure 1.26: Effect of cold-rolling on stress relaxation at 600 °C of pre-notched CT specimens made of 316L(N) and 316(H) steels. Δa represents the crack propagation length after the test [13].

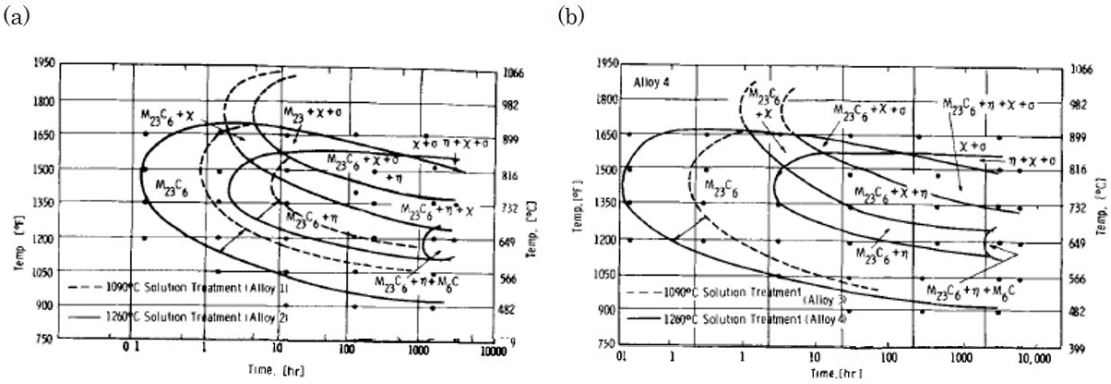

Figure 1.27: Influence of cold-rolling and prior heat treatment on phase precipitation kinetics in 316L steels (a) without and (b) with prior cold-rolling [67].

1.4.2.3 Service temperature

As discussed previously, stress relaxation cracking was most often observed for components which have been in operating at temperatures between 500 and 775 °C. Typically, stress relaxation cracking in the Phoenix nuclear power plant was observed in more than 50% of the cases in components exposed to 550 °C, but was not observed in components operating at 350 °C [18]. The service conditions, time and temperature, actually influence the kinetics of stress relaxation. Service conditions also influence secondary phase precipitation, but these are discussed in a dedicated Section 1.4.2.4.

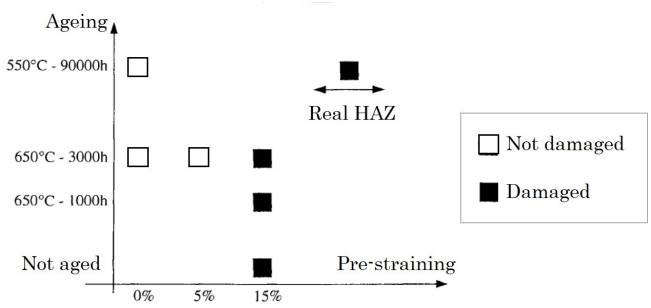

Figure 1.28: Influence of pre-straining (by cold rolling) and prior heat treatment on damage (crack formation) in a 321 steel at 600 °C [18].

It was shown in the literature [45, 145, 153] that higher service temperatures allow faster stress relaxation (Figure 1.29). In the case of 316L(N) steels, Pommier [45] observed that the temperature of 575 °C led to the highest damage, followed by 550 and 600 °C. According to Pommier, the SRC mechanism would be dependent on stress relaxation kinetics and GB degradation, which is directly linked to the chemical composition of the studied steel (particularly C and N content) and the temperature. In that sense, at 575 °C the residual stresses would exceed the GB strength quicker than at 550 and 600 °C.

One way of limiting SRC is therefore, if possible, to operate at temperatures outside of the SRC range. This obviously requires the prior identification of the most damaging temperatures depending on the material used.

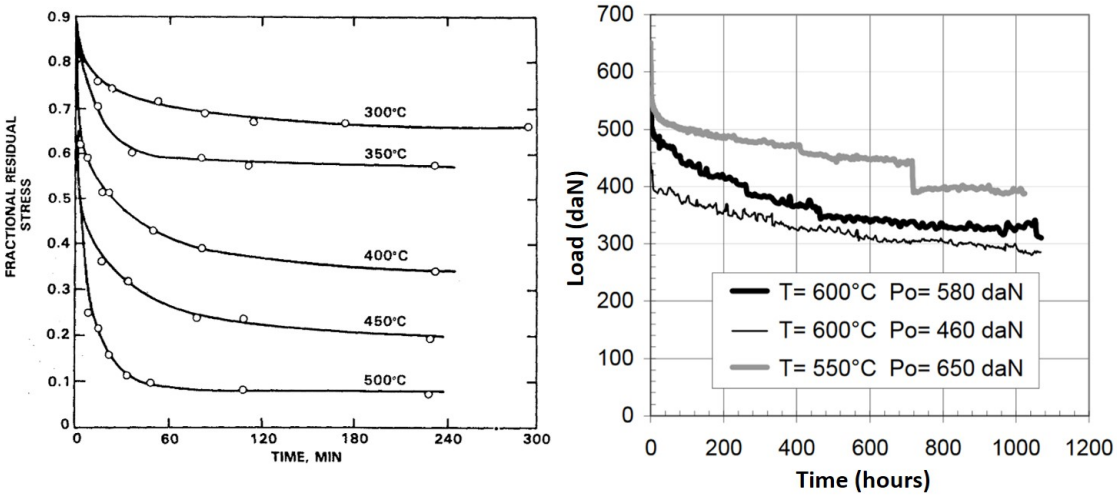

Figure 1.29: Service temperature influence on stress relaxation kinetics in (a) a low carbon steel from James [153] and (b) 316L(N) pre-notched CT specimens with a initial load of P_0 [145].

1.4.2.4 Precipitation

Grain boundary precipitates is often cited in the literature as a factor necessary for SRC [5]. Typically, Pommier [45] tested the SRC sensitivity of a cold-rolled (20%) 316L(N) steel at 550 °C and observed no damage after 1470 h. However, by applying a prior thermal treatment to the same steel at 550 °C during 1225 h which allowed phase precipitation at GBs, Pommier observed GB cavities subjecting the specimen to the same SRC test. Similar observations were made in the literature, with different weakening mechanisms depending on whether the precipitation takes place at GBs or in the bulk.

Bulk precipitation hinder dislocations motion during relaxation because of the interactions with precipitates [3], depending on the phase coherency with the matrix, size and shape [3]. Moreover, the matrix hardening can lead to plastic strain localization at GBs [3,6,36,44,46]. Wortel [22] typically reported an increase of 10% in hardness in 800H welds after 6000 h of service at 650 °C, due to bulk precipitation of carbides. However, according to Younger *et al.* [154], steels with a composition close to the 316L(N) alloy are not prone to bulk precipitation nor display strain-induced precipitation for ageing up to 1000 h at 650 °C. This effect is thus not expected to influence SRC for the studied 316L(N) steel.

Grain boundary precipitation degrades the steel ductility by lowering the ability of GB to accommodate plastic strain [33,155,156], thus restricting strain near GBs. Grain boundary precipitates act as cavity nucleation sites because of strain incompatibility with the matrix and dislocation pile-ups, which further result in stress concentration [36]. Pommier *et al.* [45] carried out TEM analyses in damaged 316L steels showing that cavitation was directly induced by the decohesion between GB precipitates and their adjacent grains, as illustrated in Figure 1.31. Additionally, Gao *et al.* [146] stated that cracks also propagate faster through a chain of carbides, thus favoring the material failure.

There is still a lot of discussion about the role and nature of the precipitating phases involved in the nucleation of cavities preceding SRC [6]. According to Swift *et al.* [157], relaxation cracking occurs when partially coherent phase precipitates in the material. When these precipitates grow in size, they no longer induce coherency strains on the matrix, and hence their impact on SRC is largely reduced [157]. Inversely, in a conference report about SRC in 347 weldment, Fen *et al.* [14] indicated that larger precipitates promote cavity nucleation. They also stated that a greater number of precipitates results in a lower capacity for the material to carry load. Because precipitates are highly related to SRC susceptibility, precipitation kinetics can also highly influence SRC [3]: if the precipitates form after the majority of the residual stresses have relaxed, the influence of precipitates is negligible.

Although residual δ-ferrite is known to be accelerate phase precipitation, there is no much information available on the role of ferrite in SRC. Lippold [5] reported that the presence of δ-ferrite in the weld deposit did not seem to influence the susceptibility of SRC of 347 type steel, without more details. It is thus expected that the residual ferrite, often present in 316 steels in low proportion, will not impact the resistance to SRC of the studied steel.

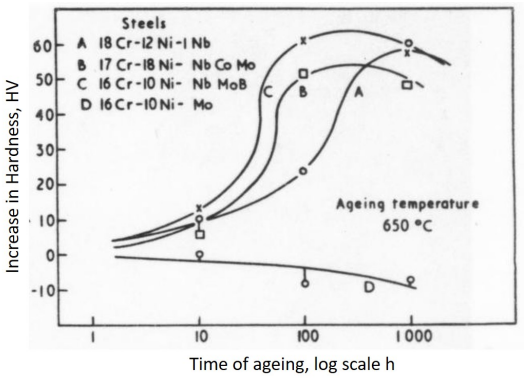

Figure 1.30: Evolution of hardness (HV30) as a function of time after ageing at 650 °C and 850 °C for four austenitic steels 5% pre-strained at room temperature [154].

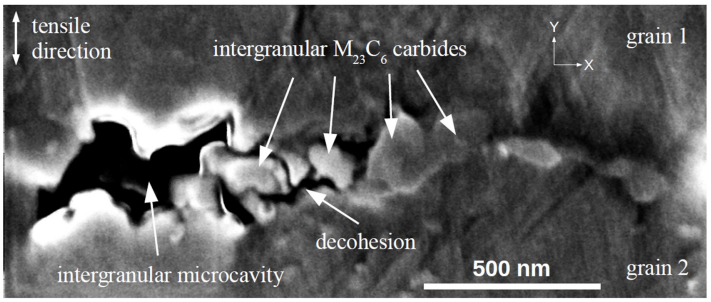

Figure 1.31: Scanning electron microscope (SEM) image of a pre-strained 316L steel specimen aged at 550 °C during 4313 h. This reveals the partial decohesion between $M_{23}C_6$ carbides and the adjacent grains [45].

1.4.2.5 Chemical composition

The influence of steel composition on SRC reported by the literature revealed a harmful effect of molybdenum, vanadium, boron [7, 33], niobium [18], carbon [45], nitrogen [45], copper [6]. These elements particularly increase the risk of carbides and nitrides precipitation ($M_{23}C_6$, TiC, AlN, V_4C_3), especially in the stabilized steels and high-carbon steels. Additionally, C and N also slow down the stress relaxation kinetics by dislocation pinning, allowing high residuals stresses for longer duration [6,18,36,45,145]. Indeed, Auzoux [145] showed that stress relaxation rate in a high carbon 316H steel was significantly lower than in the low carbon 316L steel (Figure 1.32). Similarly, the addition of nitrogen in the 316L(N) steel induced a decrease in the stress relaxation rate as compared to the 316L. The comparison of the three curves suggests that the effect of nitrogen on stress relaxation rate is greater than that of the carbon. However, the comparison of crack length showed that crack propagation was easier in 316L and 316H steels than in the 316L(N) steel. Pommier [148] specifically studied the influence of carbon, nitrogen and phosphorus content on SRC susceptibility in 316L(N) steels, concluding that steels with a nitrogen content higher than 0.06%wt and carbon content higher than 0.015%wt present a higher relative risk of SRC, when compared to other 316L(N) steels. It is important to remind though that 316L steels are still highly resistant to SRC due to their low content in C, as compared to other steels. Phosphorus was shown to have a very low impact on SRC as compared to C and N. More generally, it has been observed that elements having a detrimental effect on creep ductility also increase the susceptibility to SRC [7].

In contrast, it has been shown [5] for low-alloy steels that the introduction of calcium, sulphur-stabilizing elements (titanium, zirconium) and some rare earth elements (REM) prevented solution of sulphides during welding, delaying re-precipitation during cooling and thus further cavitation mechanism [6]. The addition of REM also helps in reducing GB segregation of impurity elements in some cases [6].

1.4.2.6 Grain size

The apparent detrimental effect of grain size on SRC is often reported in the literature [3,4,33,46,139,158,159], with observations of cracks in industrial components preferentially initiated in the coarse-grained region of the heat affected zone, adjacent to the fusion boundary (Figure 4) [15, 39]. From these different observations, it was estimated that steels with grain size larger than 130 μm present a higher risk of SRC [4, 26, 160], even though SRC was also observed in steels with grain size as small as 65 μm [4].

While it is widely admitted that coarse-grained HAZs are more prone to SRC, very few works in the literature tried to provide explanations for this sensitivity. To this day,

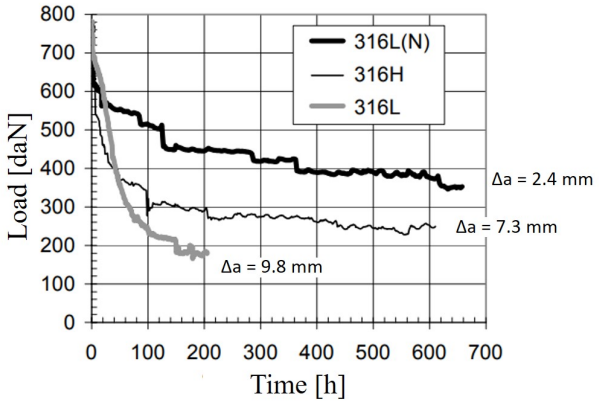

Figure 1.32: Stress relaxation tests at 600 °C for the 316H, 316L and 316L(N) steels. Specimens were pre-notched and cold-worked prior to relaxation test. Δa represents the crack propagation length after the test [13]

there is no clear understanding of this trend, particularly for austenitic steels. The most common explanations proposed by the different authors are reported in the following. It is important to keep in mind that these suggestions are mostly hypothetical, and that very few of these studies have tried to provide experimental or numerical evidence to support them.

The sensitivity of the CGHAZ was first explained by a change in the deformation behavior of the affected zone from the increase in grain size [12], which decreases the total grain boundary area and reduces area for strain accommodation but also for precipitation, increasing precipitates density at grain boundaries [8, 27, 28, 37, 161]. Nomura *et al.* [152] also found that the effect of pre-strain on SRC increased for an increase in grain size. Additionally, Auzoux [13] suggested that an increase in grain size allows reducing the number of obstacles to overcome (like triple points) in order to reach a certain crack length. Furthermore, Sung *et al.* [162] suggested that the sensitivity of coarse-grained regions was due to a much greater phosphorus segregation, thereby weakening grain boundaries. This explanation, however, is not in agreement with Pommier's results [45], who demonstrated the negligible effect of phosphorus content on the risk of SRC in 316L(N) steels.

Indacochea *et al.* [160] provided, to the author's knowledge, the only experimental investigation of the effect of grain size on SRC in a CrMoV steel. They showed by 3-point bending tests of Gleeble-simulated HAZs that an increase in grain size, while having comparable hardness, increased the risk of SRC as illustrated in Figure 1.33 (see Section 1.4.3 for details on Gleeble testing method). However, limiting the grain size was not sufficient to prevent SRC hazard, but it should be controlled in combination with hardness level. Unfortunately, the authors did not provide explanation for the higher susceptibility of larger grain miscrostructures.

1.4.2.7 Grain boundary characteristics

Lippold [5] reported that the grain boundary characteristics have a significant influence on DDC, which presents a similar mechanism to SRC. Straining at high temperature may result in GB sliding, inducing stress concentration at GB triple points thus favoring the formation of cavities (Figure 1.23). The characteristics of GBs can significantly impact this damage mechanism. Indeed, grains can grow freely during welding if no GB precipitate is present in the CGHAZ, resulting in straight GBs. However, if GB precipitates are initially present, GBs can be pinned by these precipitates during grain growth and thus GBs tend to

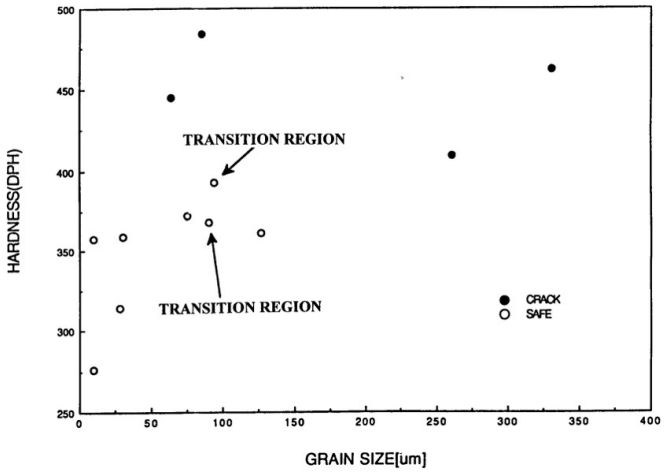

Figure 1.33: Occurrences of SRC as a function of grain size and hardness of simulated HAZs by Gleeble tests of CrMoV steels [160].

be more tortuous. GB sliding is then more difficult because of a mechanical locking effect, increasing the resistance to cracking. If GB precipitates are present after grain growth and GB sliding occurs, strain might concentrate at the precipitate-GB interfaces [5]. Because of this mechanism, long and straight GBs free of precipitates are reported to be more resistant to sliding than short tortuous ones.

Grain boundaries with an average direction perpendicular to the loading axis (or to the principal residual stresses) were also found to be more favourable to intergranular damage, due to higher tensile stresses for this configuration [45, 64, 163] (Figure 1.34). Additionally, Pommier [45] and Jin *et al.* [164] showed that GBs with misorientations between 25 and 55° are the most favorable to SRC (Figure 1.35). Besides, none of the Σ3 twin boundaries was found to be damaged, despite representing more than 50 % of the grain boundaries misorientations. These observations seem to be related to three factors: GB energy, secondary phase precipitation sites and precipitate morphology. As reported in the literature, [165–167] coherent twin boundaries Σ3 (60° for <111> rotation axis in FCC structures) have a particularly low energy compared to any other configuration. This is due to the perfect atomic fit between the two adjacent grains. In addition, GB misorientation angle particularly influences the localization of damage since $M_{23}C_6$ carbides precipitate preferentially at grain boundaries with misorientation angle from 20 to 55° [168]. In contrast, Tang [168] indicates that misorientation angles from 5 to 20°, and from 55 to 60° tend to highly delay the $M_{23}C_6$ precipitation.

Finally, Hong [163] observed higher cavitation damage during creep-fatigue tests on random boundaries ($\Sigma > 29$), where grain boundary carbides were mostly triangular shaped. Hong [163] explained this tendency by a higher interfacial energy of precipitates in this configuration than in Σ3 and Σ9 grain boundaries, where carbides present a plate morphology. Cui [64] confirmed these observations simulating stress fields near grain boundaries precipitates during mechanical loading. Cui showed that the configuration leading to higher carbide/grain boundary interface stress magnitude correspond to a semi-coherent carbide with a triangular shape. This would most probably facilitates the nucleation and growth of cavities at the tip of triangular-shaped precipitates.

1.4.2.8 Geometry of components

Industrial cases of stress relaxation cracks are mainly reported for circumferential parts such as nozzles or pipes [7, 18, 23, 33, 35, 41, 169] but also for parts with a significant

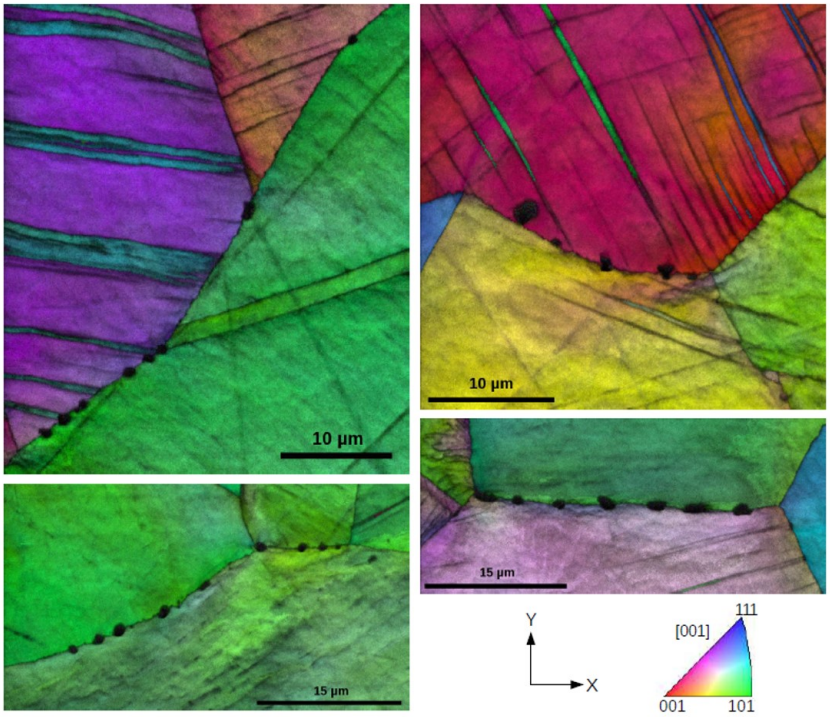

Figure 1.34: EBSD maps of damaged regions in a 316L(N) steel after a thermal ageing of 1455 h at 550 °C. The specimen was pre-aged at 550 °C for 1225 h, and pre-compressed at 50 kN in the Y direction. IPF maps show the grain orientation and cavities at some of the grain boundaries [45].

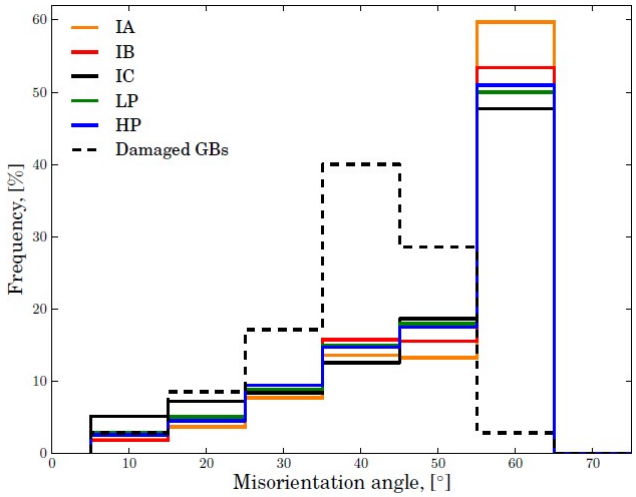

Figure 1.35: Comparison between the distributions of grain boundary misorientations measured by EBSD in five 316L(N) steels and 35 grain boundaries damaged by SRC [45].

thickness (greater than 25 mm) [7,18,24,26,28,46,170]. Curran *et al.* [17] also stated that notches or edges of welded components represent sources of stress concentration, favoring the initiation of cracks as illustrated in Figure 1.36.

To prevent SRC in service, these specific features should then be avoided when initially designing the components when it is possible.

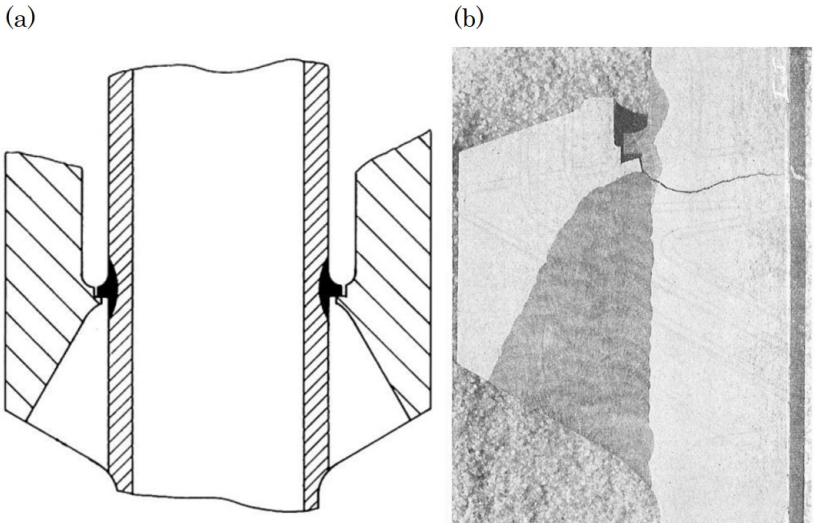

Figure 1.36: SRC of a 347 slip joint used in steam turbine generator at 565 °C after 16 months of service with (a) schematic sketch of the welded joint and (b) macrographic cross-section image of failure [17] .

1.4.2.9 Post-welding heat treatment

To relieve residual stresses induced by welding, a post-weld heat treatment, or PWHT, can be carried out (Section 1.3.2.4). It can be both beneficial and detrimental to the material, depending on the steel and the conditions of the thermal treatment conditions [154]. The process itself can induce relief cracking directly upon the treatment [5]. PWHT cracking was reported in several super alloys [171, 172] and in the HAZ of the 347 and 321 steels after 2 h of treatment at 850 and 900 °C [24]. To prevent PWHT cracking, Lippold [5] recommends reheating steels at temperatures which are not favorable to carbide precipitation, depending on the material. This would still allow partial relaxation of residual stresses while avoiding GB precipitation and thus preventing stress relaxation cracking.

When the right PWHT conditions are identified, the resistance of the steel to SRC can be improved. Wortel [173] typically indicated that post-weld heated austenitic steels can withstand more than 2% relaxation strain, against 0.2% for non-PWHT, which can prevent life-time failure in most cases. Auzoux [145] also showed that a prior heat treatment of 2 h at 700 °C carried out on cold-rolled 316L and 316L(N) steels, reduced the final crack propagation length after a stress relaxation test at 600 °C (Figure 1.37). However, the heat treatment induced a decrease of the stress relaxation rate.

1.4.3 Stress relaxation cracking testing methods

The difficulty of predicting the risk of SRC before the complete failure of welded components in service motivated numerous laboratory studies, aiming for the understanding of the SRC mechanism and the associated factors. Because of the complexity of the phenomenon and the test duration to trigger the phenomenon (up to several years), the initial testing conditions are often simplified. Since the 1950s, many methods have been developed to test the resistance of steels to SRC [3]. These different methods are summarized in Appendix A. From all of these tests, two main approaches can be distinguished (Figure 1.38).

A first approach to test SRC is to use fully welded components and expose them to thermal treatments, aiming for SRC similarly to an in-service component. These spec-

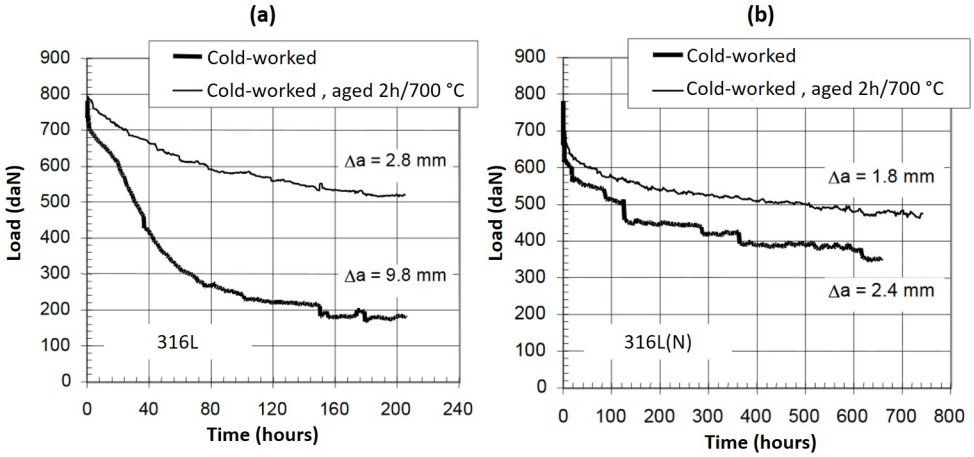

Figure 1.37: Impact of heat treatment on stress relaxation kinetics for (a) a 316L steel and (b) a 316L(N) steel. Curves show the residual stress relaxation as a function of time of pre-notched compact-tension specimens at 600 °C. Specimen were cold worked, and heat treated at 700 °C during 2 hours prior to tests. Δa is the final crack length for each case [145].

imens present the advantage of being representative of industrial cases: the heterogeneous microstructure, residual stresses and plastic strain induced by welding are preserved [174, 175]. Borland [174] developed such test by performing a multipass welding of two perpendicular pieces (Figure 1.39 (a)), a chamfered disk and a cylinder. The specimen is then put in a furnace for stress relaxation, aiming for SRC. The first difficulty for this method is the identification of damage in very large specimens. Indeed, cavities induced by stress relaxation can measure less than a micron in length, while Borland specimens typically have a region of interest of 80×20 mm^2. Besides, SRC in these specimens can only be allowed by the relaxation of welding residual stresses: since no additional residual stresses are introduced, SRC can be excepted to be triggered only for long duration treatments and thus may not be suitable for short laboratory studies. More than that, highly SRC-resistant materials such as the 316L(N) steel cannot be tested with this method, since typical welding residual stresses are lower than the SRC threshold of the steel [45]. Lundin [176] later developed in the 1990s another approach using C-ring specimens machined from welded components, and further loaded applying a constant displacement (Figure 1.39 (b)). This second approach allows restricting the high stresses regions to a lower volume, however it is not representative of an in-service stress relaxation. Similarly, Wortel [150], in the beginning of 2000s, carried out 3-point bend tests of weld joints, using a screw as a bending support (Figure 1.39 (c)). The main drawback of this test is the location of high stresses and strain during the test, which is not always in the actual weakest region of the weld and thus not representative of the in-service mechanism. This would require performing several tests varying the position of the weld relatively to the expected high-stress region. Another drawback resides in the use of a screw, which may also relax during the thermal treatment, then biasing the stress relief of the tested specimen.

In addition to these drawbacks, using multipass industrial welds often results in the variability of residual stresses and strain magnitude/distribution from a welded specimen to another, being a challenge for the repeatability of results [3, 47]. Moreover, the study of each individual driving forces, as discussed in the previous sections, is much more challenging. The measurement of residual stresses in such specimens can also be complex, thus affecting the determination of SRC thresholds.

To simplify the investigation of SRC by avoiding the use of heterogeneous microstruc-

tures and to improve the tests repeatability, some studies chose to apply mechanical and thermal treatments on the material in the as-received state, without welding. These treatments aim reproducing the microstructure and mechanical properties of a heat-affected zone, in a homogeneous manner. Considering that the CGHAZ is the most sensible region to SRC, the material is generally subjected to treatments similar to the ones attained in this zone during the welding process. Usually, the material is heated between 1100 and 1300 °C, during few minutes or a few hours [13, 18, 21, 177, 178]. This induces austenite grain growth and even GB precipitation, depending on the type of steel. Since the CGHAZ and HAZ also present much higher level of strain hardening than the other regions, the material is also priory cold-rolled [18, 45] or hot rolled between 400 and 600 °C in some studies [13], with resulting strain between 5 and 40%. These treatments allow producing a material representative of a heat affected zone, however residual stresses, which are necessary for SRC, are not present in these materials and must then be introduced artificially.

In order to introduce stresses, two methods can be considered: via a constant displacement during the heat treatment, or by introducing residual stresses priory to the heat treatment (Figure 1.38). Introducing stress by a constant applied displacement can be performed using the 3 or 4-point bending tests [22], C-ring test, Gleeble and controlled heat rate (CHRT) test.

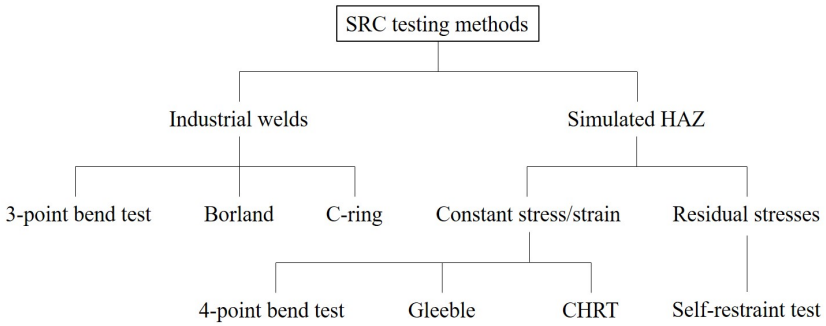

Figure 1.38: Common SRC testing methods [3].

1.4.3.1 Constant displacement tests

Saito *et al.* [180] proposed the 3 and 4-points bending test based on the test first proposed by Wortel [150], using samples with a simulated HAZ microstructure and machined a notch in the middle of the specimen to better concentrate stress (Figure 1.40 (a)). The specimen is loaded using 3 or 4 bending fixture, which is then heated in furnace with constant bend applied throughout the whole test. The advantage of using samples with a homogeneous microstructure for this test is that the result does not depend on the position of the weld relatively to the bending fixture. However, similarly to the test proposed by Wortel [150], this test has the disadvantage of being potentially influenced by the relaxation of the screws.

Another test using a constant displacement approach is the Gleeble test or controlled heat rate test (CHRT). Gleeble test is an interesting method as it allows reproducing a CGHAZ on a portion of the sample; however, the test is performed with constant applied displacement so it does not exactly correspond to a residual stress relaxation as in industrial cases. Besides, this type of test can be very expensive [3]. Typical thermal and mechanical procedures for Gleeble test are shown in Figure 1.40 (b).

Constant displacement tests present the advantages of being simple, having a good accuracy in strain measurement and good reproducibility. However, stress relaxation is

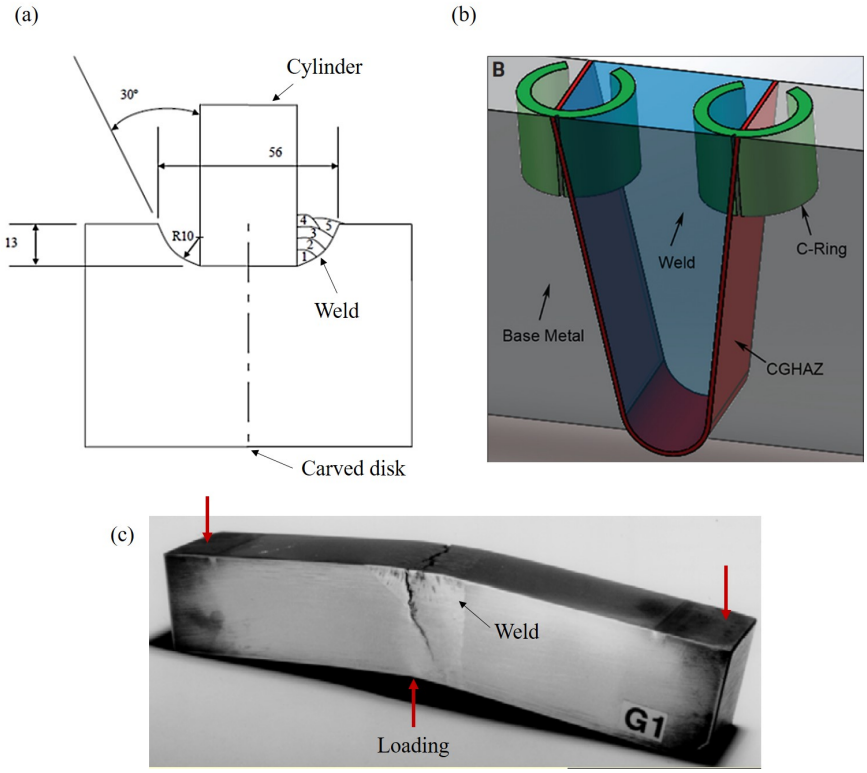

Figure 1.39: Illustration of SRC testing specimens using industrial welds, with (a) section of a Borland specimen [3], (b) C-ring specimens extracted from a weld [179] and (c) 3-points bending test of a 800 h welded joint after failure [150] .

not exactly considered as such in these tests and thus it is not exactly representative of stress relaxation of industrial cases, where usually no external load is applied on the components.

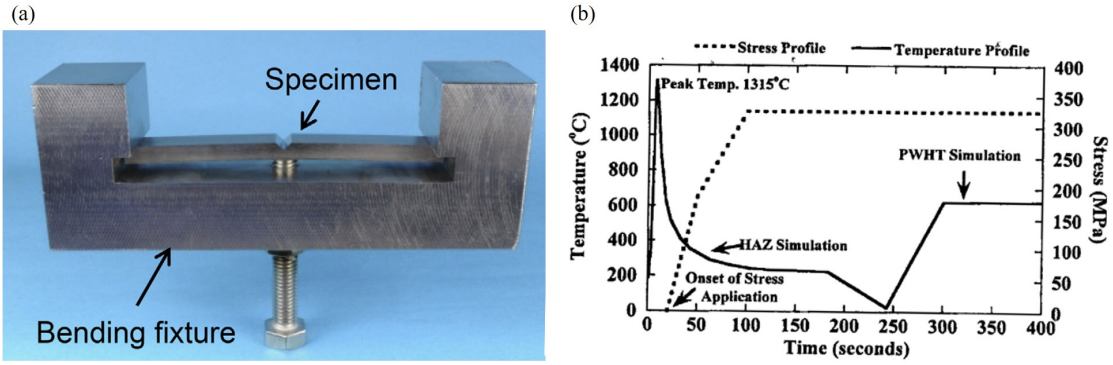

Figure 1.40: Constant displacement SRC tests using simulated HAZ, with (a) setup of a 3-point bending test with a v-notch shape specimen [180] and (b) typical Gleeble time-temperature-stress process [3].

1.4.3.2 Self-restraint tests

To address this issue, Turski *et al.* [47] proposed a self-restraint method applying a compression followed by unloading on CT like specimens, machined from ex-service 316H steam header operating at 525 °C for 60000 h. They showed that during compression be-

yond yield, localized plastic strain field forms near the notch root of the specimens. Upon unloading, residual tensile stresses rise in the same region. The samples are then heated to relax residual stresses, without any external load applied thus being representative of industrial cases. This method allows restricting the high stress region to a very small volume, facilitating the analyses and ensuring a good control of the applied conditions, unlike with specimens such as the Borland one. Aside from the applied force, the residual stress field magnitude and distribution can be controlled by adjusting the notch radius and geometry. Typically, decreasing the notch radius leads to higher residual stress values near the notch root, however the constrained area is reduced, as reported by Pommier [45]. In addition, the controlled introduction of stress and strain via compression test allows an excellent reproducibility. Moreover, since the residual stresses are introduced artificially it is possible to reach much higher magnitudes than those resulting from welding: this allows testing SRC for highly resistant steels such as the 316L(N). The main drawback of this method is the quantification of introduced stress and strain, which are generally estimated by mechanical simulations and sometimes compared to X-ray or neutron diffraction measurements. These techniques present good accuracy for residual stresses measurement but are not always available and can be costly. Pommier [45] later used the same approach proposed by Turski *et al.* but using cold-rolled 316L(N) steels instead of serviced material, aiming to reproduce HAZ properties.

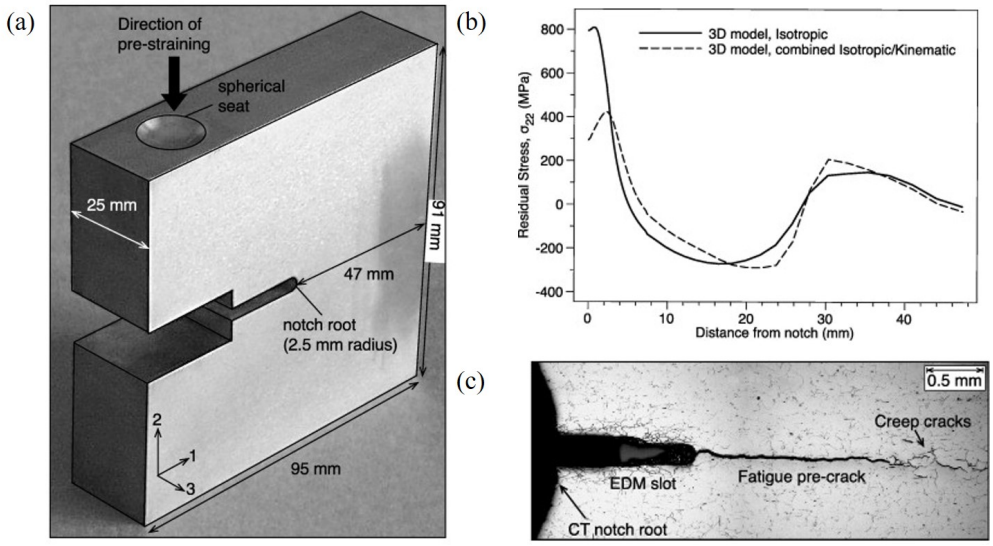

Figure 1.41: Self-restraint SRC test with (a) CT-like specimen, (b) predicted residual stresses at mid-thickness near the notch root after the unloading of the compression and (c) optical micrograph of the CT mid-thickness near the notch root showing the fatigue pre-crack and stress relaxation cracking ("creep cracks") [47].

From the review of the main approaches for testing SRC, performing self-restrain tests using specimens machined from real welds then appeared to be the most relevant combination of the two: these specimens are representative of an industrial weld having a heterogeneous microstructure but with a controlled introduction of residual stresses, thus allowing an excellent repeatability and being a relatively easy test. In this idea, recently Xiao *et al.* [181] machined CT specimens from welded 304H steel plates (Figure 1.42 (a)). However, the authors only machined specimens with the notch positioned in the FZ (Figure 1.42 (b)) and therefore did not compare the sensitivity of each region to SRC. Hence the effect of microstructural heterogeneity on the SRC was not determined.

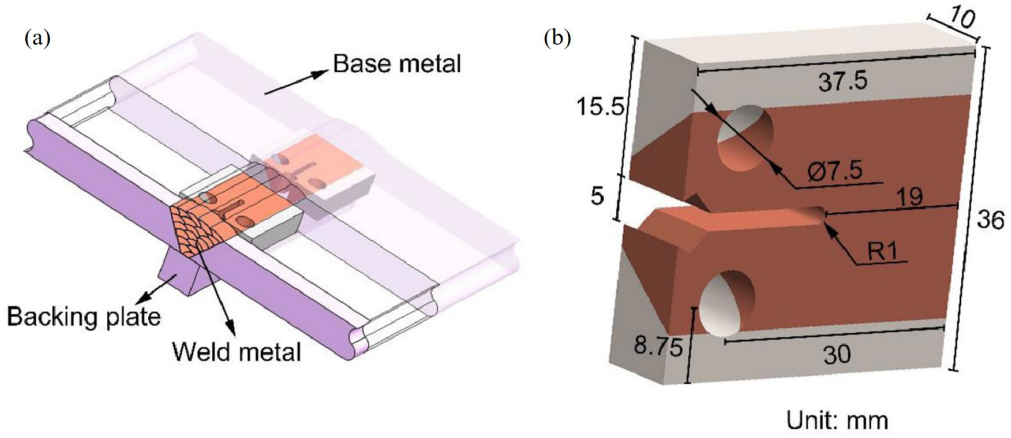

Figure 1.42: CT-like specimen with industrial welds for SRC tests with (a) position of the CT specimen in the super 304H welded plate and (b) geometry of the CT specimen with the weld in orange and base metal in grey [181].

1.4.3.3 Damage analysis

In most of the studies, the resistance of steels to SRC was evaluated by a pass/fail test, only accounting for the presence of cracks and their length. Most often, GB cavities were not considered to quantify the damage, even though cavity nucleation is known to be at the origin of cracks by stress relaxation as discussed previously. Nevertheless, Bouchard *et al.* quantified the damage accounting for the number of cavities and characterized their distribution, allowing a finer understanding of damage initiation and development [44, 182–186]. In some studies on creep damage, which can be compared in some extent to stress relaxation damage, the analysis of cavities allowed getting insight into the SRC phenomenon and therefore a finer characterization of SRC factors [64, 183, 187, 188]. It then appears that to better understand the phenomena governing the SRC especially in a heterogeneous microstructure, local initiation of damage through the cavity nucleation process should be taken into account.

1.5 Summary of literature review

The literature review showed that stress relaxation cracking is a complex intergranular damage mechanism, involving many factors introduced during the elaboration of a component and during its life in service. SRC was observed since the 1950s in weld joints after operating at high temperatures, characterized by cracks and creep-like cavities nucleated at grain boundary precipitates, mainly in the coarse grained regions of heat affected zones.

From the numerous works carried out on the phenomenon, it is widely admitted that SRC is first induced by the presence of residual stresses, plastic strain, grain boundary precipitates (mainly carbides) and the exposure to high temperatures (500-775 °C). Works carried out on the susceptibility of austenitic steels to SRC typically showed that higher levels of initial plastic strain and residual stresses, longer relaxation time all resulted in higher stress relaxation damage. Specifically for 316L(N) steels, 575 °C was identified as the relaxation temperature leading to the highest damage. These relaxation conditions will then be chosen in this work to ensure most favorable conditions for SRC.

These works also identified the main influencing factors, such as the material chemical composition, grain size and component geometry. In the particular case of 316L(N) steels, which are highly SRC-resistant, the content in nitrogen and carbon was found to be the

most influencing elements, because of their involvement in dislocation motion kinetics and thereby residual stress relaxation rate. In addition, a high carbon content can also be highly detrimental as it favor carbide precipitation. From the composition-based ranking proposed by Pommier [45], the 316L(N) steel studied in this work is expected to be prone to SRC relatively to other 316L(N) steels. Besides, the literature suggested that larger grain size is detrimental to the resistance to SRC, from the frequent observations of SRC in the CGHAZs. Since there is very little information regarding this parameter, the effect of grain size on SRC will be investigated in this work separately from other factors.

Occurrence of SRC in an industrial environment has not been reported for 316L(N) steels yet, which is consistent with the resistance of the 316L(N) steels to SRC reported in the literature. The high magnitude stress threshold (740 MPa) proposed for SRC in 316L(N) steels in laboratory conditions then require to chose severe conditions of testing for this work, especially if the steel is not pre-strained via cold-rolling. This means that the SRC tests cannot be exactly representative of the industrial welded components, where maximum stresses of 400 to 500 MPa are usually measured: the initial conditions must be exaggerated to allow the observation of SRC in the studied 316L(N) steel and most importantly, within acceptable times (a few months).

The literature review showed that many methods were developed for testing SRC since the 1950s, either using real welds or by reproducing microstructural and mechanical properties of a heat affected zone. For better repeatability and control over the SRC driving factors, tests using simulated HAZ are generally employed. The introduction of tensile residual stresses in such materials can only be achieved via self-restraint tests, such as the compression and unloading of CT-like specimens proposed by Turski [47]. The main drawback of this approach is the use of homogeneous materials, which cannot allow a full understanding of the SRC mechanism occurring in heterogeneous microstructures of welds. Recent works sought to combine the approach of real welds with self-restraint tests, but did not address the effect of a heterogeneous microstructure on SRC. As a consequence, there still remain major questions about the SRC mechanism in welds, particularly regarding the high SRC sensitivity of the coarse grained regions of heat affected zones.

Finally, the quantification of stress relaxation damage is often simplified in many SRC testing studies, with most of them only accounting for the presence of cracks while cavities are known to be at the origin of SRC. A better understanding and quantification of the phenomenon would require the characterization of both cavities and cracks after relaxation.

This work thus aims to address these issues by qualifying and quantifying the impact of a heterogeneous welding microstructure on the sensitivity of the 316L(N) stainless steel to SRC, investigating stress relaxation in welds via a Turski compression test.

Chapter 2

Experimental methodology

Contents

This chapter presents the experimental methodology adopted to investigate the effect of welding on stress relaxation cracking in the 316L(N) austenitic stainless steel. A description of the different material states tested in this work is first detailed in Section 2.1. Then, the techniques used for characterizing the microstructure and mechanical properties of each material state are presented in Section 2.2 and 2.3, respectively. The self-restraint method used to generate controlled levels of residual tensile stresses and plastic strain by compression and unloading, referred in this work as Turski compression, is presented in Section 2.4. Then, the method used to allow for the relaxation of residual stresses is detailed in Section 2.5. Finally, the techniques used to characterize the microstructure and stress relaxation damage are presented in Section 2.6.

2.1 Material states

Stress relaxation cracking in the 316L(N) steel was characterized on several material states, by applying different prior mechanical and thermal treatments on the as-received plates allowing to separate the effect of the different factors on the initiation and development of damage. Material was initially received as 450 × 90 × 15.46 mm^3 thick plates hot-rolled in the Y direction (Figure 2.2). To this end, the following material states were produced (Figure 2.1):

(i) as-received;

(ii) material with increased grain size;

(iii) cold-rolled;

(iv) single-pass welded;

(v) multi-pass welded;

(vi) cold-rolled welded.

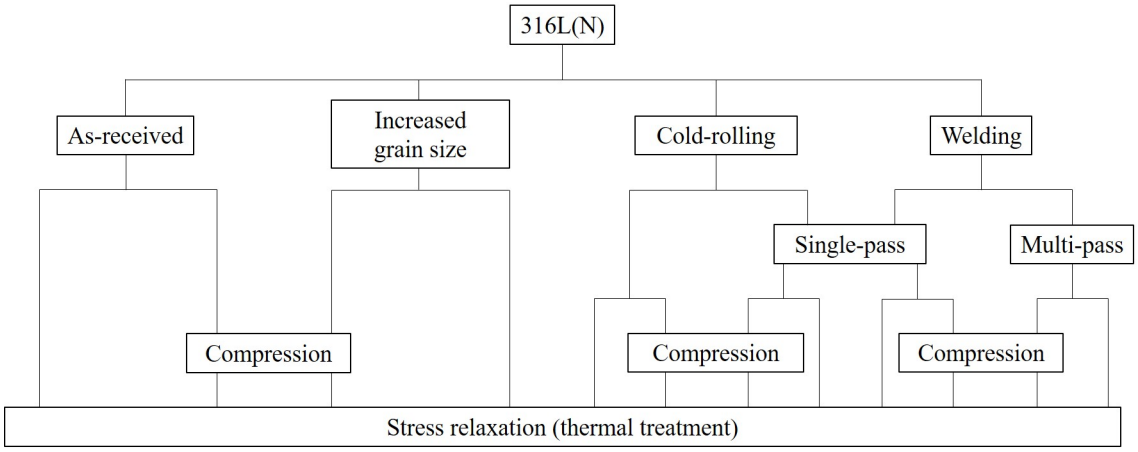

Figure 2.1: Description of prior treatments to produce different states of 316L(N) steel for further SRC.

Details about the methods for producing each material state is detailed in the following. Resulting microstructure of each state are presented further in Chapter 3.

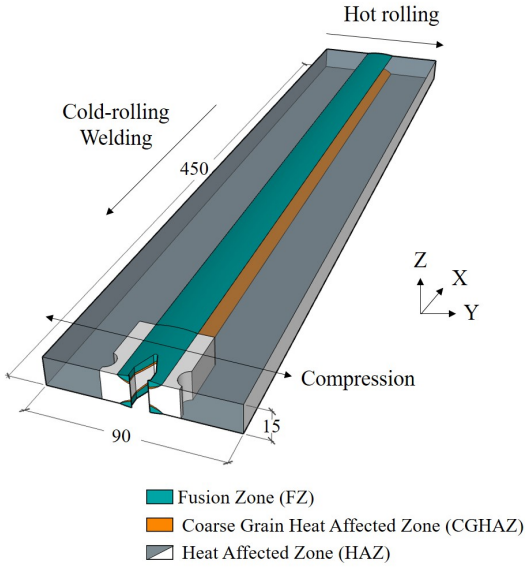

Figure 2.2: Description of prior treatments directions relative to the as-received plate.

2.1.1 As-received

The 316L(N) stainless steel in the as-received state, with an average grain size of 90 μm, was firstly tested to evaluate its SRC sensitivity without prior thermo-mechanical treatments. As-received material would thus also serve as a reference state. CT specimens were then directly machined from the as-received plates, neither presenting residual stresses, plastic strain nor precipitates.

2.1.2 Material with increased grain size

The grain size is often cited as a detrimental factor for SRC in the literature [3, 4, 33, 46, 139, 158, 159]. However, to this day there is no dedicated study characterizing the impact of grain size on SRC. For this sake, in this work the SRC sensitivity was compared between the specimens in as-received state and those with increased grain size. In CGHAZs of 316 steels, typical grain size can reach up to 400 μm in diameter [189], representing an increase of a factor 4 as compared to the as-received material. To produce such grain size, heat treatments of 1 and 2 h at 1300 °C were applied to the as-received material, subsequently followed by a water quench. These times and temperature treatments were estimated from austenite grain growth results of Kim *et al.* [190] for a similar steel.

2.1.3 Cold-rolled

SRC testing of cold-rolled material was carried out to evaluate the impact of prior straining on SRC sensitivity. Cold-rolling was carried out at room temperature by progressive thickness reduction of the as-received plate (15.46 mm thick plates) using a rolling mill in the X direction (Figure 2.2). Two successive passes were carried out, resulting in final average thickness of 11.98 mm, equivalent to a 22.5% of total reduction. This reduction rate was chosen accordingly to previous studies carried out by Pommier [45] on a similar 316L(N) steel, aiming to reproduce the hardening observed in heat affected zones [13].

2.1.4 Welded

Welded specimens constituted the major interest of the study, aiming to assess the effect of a heterogeneous microstructure on the SRC sensitivity. To evaluate the impact of a typical

welding process employed for producing industrial weld joints, a process similar to single and multi-pass welding was then applied to both as-received and cold-rolled states plates. More specifically, the plates were subjected to local fusion with subsequent solidification using Gas Tungsten Arc Welding (GTAW) equipment to simulate welding process without filler material. The whole process is detailed thereafter.

Priory to welding, the as-received plates of 316L(N) steel were clamped, in order to prevent any distortion during the welding and after that, during cooling. A system of six clamps welded to a large support, all of which were made of S235 steel, was manufactured for the purpose of this study. The whole clamping system, illustrated in Figure 2.3, was fixed to a working bench.

A WGLa15 tungsten electrode with a 3.2 mm diameter, shaped to 90° angle, was mounted in a 19.0 mm diameter nozzle. The welding torch was fixed on a motorised module, aligned with the welding axis (Figure 2.3). Two cameras were installed at the front and back of the welding torch, allowing in-situ images of the weld pool during the process. The GTAW procedure was set up using an input voltage of $U = 12$ V and current of $I = 300$ A. In this work, no filler metal was used to avoid any bias linked to its nature.

For the welding procedure, different shielding gas mixes were tested. These were either composed of 100% Ar, 70% He and 30% Ar, 95% Ar and 5% He, and finally, 100% He. The shielding gas was applied with a rate of 28 L/min. Testing parameters and resulting weld pool dimensions are detailed in Table 2.1. The corresponding macrographic images of the welds section for each condition are shown in Appendix B. After these tests, the 100% Ar shielding gas was chosen for the rest of the work, since the other options were less suitable for this work: either because the weld pool was too deep relatively to the plate thickness, or because of a poor repeatability of the pool geometry and dimensions.

During welding, the welding torch was displaced automatically along the X direction (Figure 2.2) with a 60 mm/min velocity. The arc allowed partial melting of the near-surface metal (the fusion zone) and formation of heat affected zones, as observed in industrial welding processes. For the sake of ensuring mechanical symmetric response of the CT specimen during Turski compression, as illustrated in Figure 2.9, a second fusion line was made on the other side of the plate, following the same welding procedure. In order to avoid the overlapping of heat gradients, the welded plates were cooled down between two successive welding passes. Cooling was carried out at ambient air until the measured temperature at surface of the plates was lower than 100 °C.

The recurrence of heat affected zones additionally also allowed to double the number of zones favorable to SRC. For the single-pass welded plate, both sides of the (XY) surface planes were welded only one time. For the multi-pass welded plate, each side was welded five times, turning the plate upside down between each pass. While the first pass of multi-pass welding procedure was similar to the single-pass welding, the subsequent passes were performed by re-melting solidified weld pool from the previous passes. The aim of this approach was to increase the overall impact of thermal cycles on the material, while maintaining a rather simple microstructure with only one fusion zone per side instead of a complex superposition of weld pools as it is usually the case in industrial multi-pass welds [191]. An example of a clamped plate after welding is shown in Figure 2.4.

Temperature during welding

Temperature evolution as function of time was recorded during GTAW of a plate of 316L(N) steel with dimensions of $160 \times 90 \times 15.46$ mm^3 using thermocouples (TC) welded to the surface according to scheme shown in Figure 2.5 (a). On the welding side (Figure 2.5 (a)), three TCs were positioned at 11, 13 and 15 mm from the welding centreline (WCL). Another TC was positioned at 11 mm from the WCL, symmetrically to the other ones with respect to WCL (called "intern"). On the side opposed to the welding (Figure

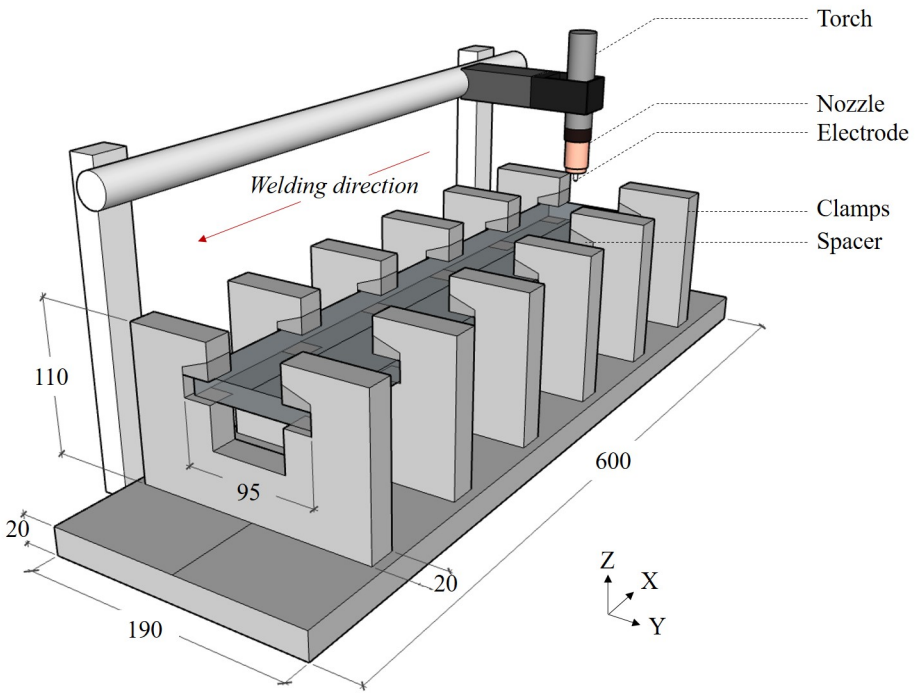

Figure 2.3: Experimental setup used for the welding of a 316L(N) steel plate restrained by a clamping system made of S235 steel. Dimensions are given in mm.

Table 2.1: Welding parameters tested for this work and resulting measured weld pool dimensions.

U [V]	**I [A]**	**Gas**	**Weld pool depth [mm]**	**Weld pool width [mm]**
12	300	100% Ar	2.8	18.2
12	300	70% He 30% Ar	4.4	19.6
12	300	95% Ar 5% H	5.6	18.5
12	300	100% He	7.3	16.2

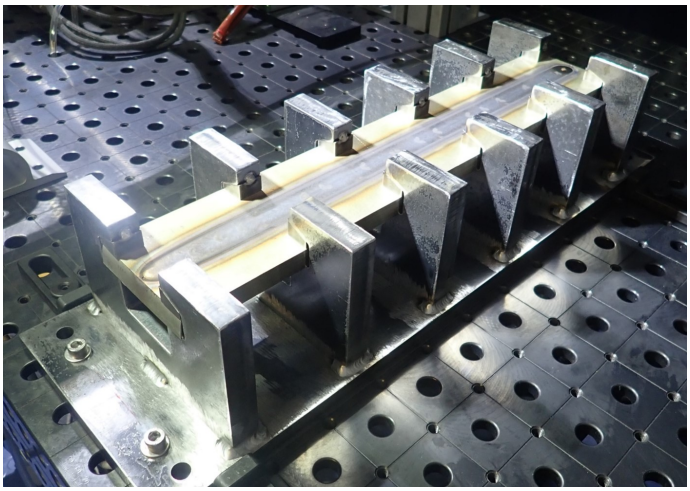

Figure 2.4: Images of the GTAW of a 316L(N) steel plate after welding.

2.5 (b)), three TCs were positioned at 0 and 13 mm from the WCL, with the third one also positioned at 13 mm symmetrically to the WCL ("intern"). Temperature evolution

with time measured on both sides are shown in Figures 2.5 (c) and (d). Results showed that temperature at 11 mm from the WCL, at about 2 mm from the side of the weld pool (Figure 3.19 (a)), reached a maximum of 1090 °C. Symmetrically to the WCL at the same distance ("intern" part), temperature was lower, with a maximum at 1000 °C. Temperature measured at distances of 13 and 15 mm from WCL reached up to 880 and 725 °C, respectively. On the side opposed to welding, temperatures at the WCL reached 812 °C. At a distance of 13 mm on the right and left side, temperatures reached 680 and 608 °C, respectively.

While these temperatures would be favorable to secondary phase precipitation (Section 1.2.2), the time of exposure to these temperatures is most probably too low (200 s at maximum) even for carbides which require a minimum of 1 h of heat treatment to precipitate in a steel of similar composition to the one studied in this work [67].

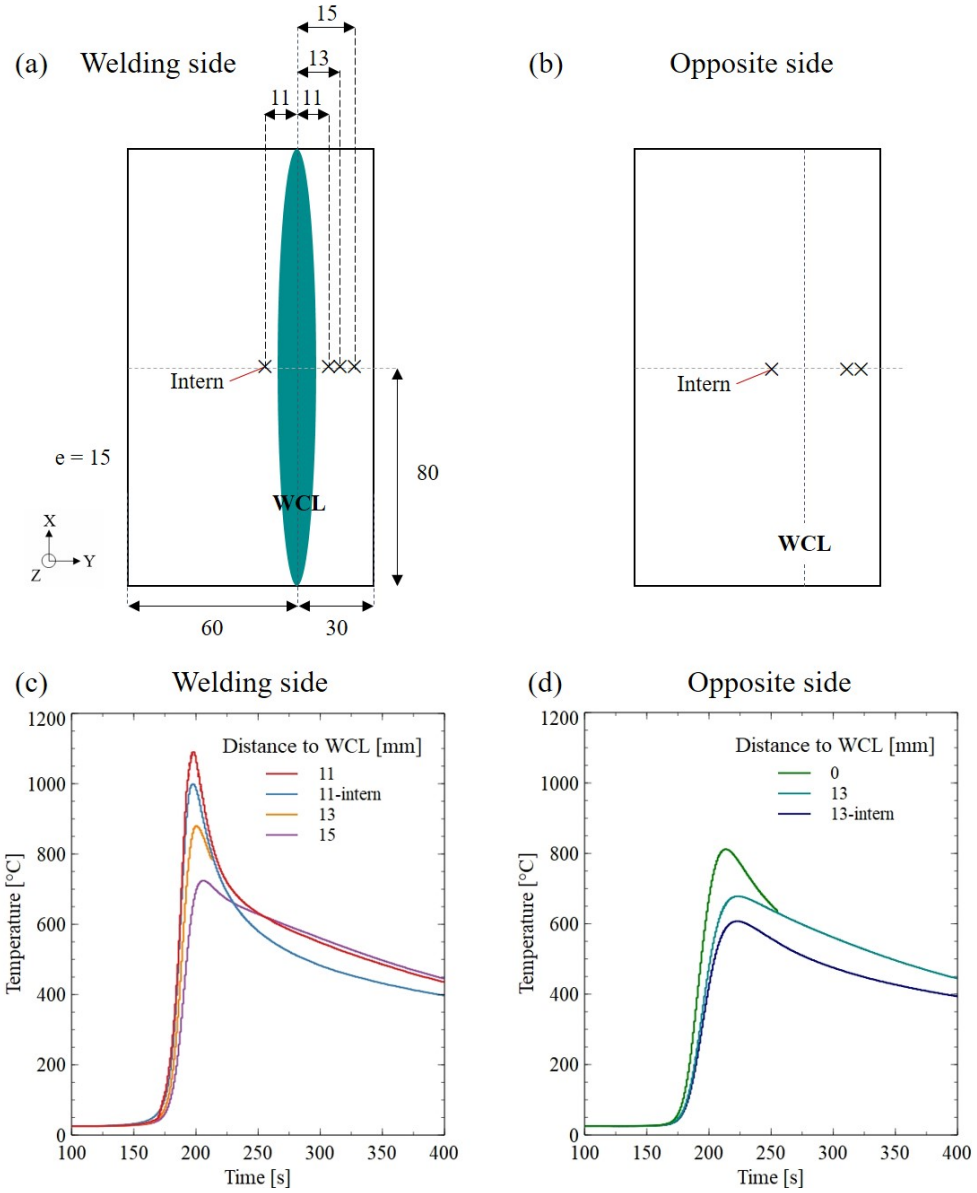

Figure 2.5: Temperature evolution during GTAW at the surface of a 316L(N) steel plate with (a, b) position of TC and (c, d) temperature as function of time.

2.2 Microstructural characterization of material states

After the production of each material state, their initial microstructure was characterized using different techniques. Microstructure was also investigated after thermal ageing to characterize its evolution without the influence of plastic strain and residual stresses, further introduced by the Turski compression. These results would then help interpreting the results of stress relaxation damage, particularly the mechanisms of damage nucleation and growth.

2.2.1 Chemical composition

Chemical composition was measured by ICP-AES (Inductively Coupled Plasma Atomic Emission Spectroscopy) for major elements. Specifically for C and S contents, they were determined by dry combustion and infrared detection, and N content by thermal conductivity and infrared detection.

2.2.2 Optical microscopy

Samples machined from the different material states were firstly polished using SiC abrasive paper of grit sizes P80 to P1200, then with diamond paste with abrasive size of 6, 3 and 1 μm and finally with a solution of colloidal silica (OPS solution). All samples from each material state were then analysed under optical microscopy to ensure the quality of polishing, get a first insight of the microstructure of each material state and to detect damage (see Section 2.6). Two optical microscopes were used to this end: a Keyence VHX-1000 using a VH-Z20R camera lens for macroscopic imaging and a Zeiss Axio Vert A1 using an Axiocam 305 color for microscopic imaging. First estimations of grain sizes were obtained using the intercept method on 800 x 682 μm^2 optical microscope images.

2.2.3 SEM/EDS/EBSD

A Zeiss Gemini Sigma 500 Scanning Electron Microscope (SEM) operating at accelerating voltage of 20 kV and using both Secondary Electrons (SE) and Backscattered Electrons (BSE) detectors was used for imaging. SE was specifically used for detecting defects, BSE for detecting inclusions and secondary phase precipitates.

Qualitative and semi-quantitative chemical composition analyses of secondary phases were carried out using an Energy-dispersive X-ray spectroscopy (EDS) Bruker XFlash6-30 under SEM.

Grain microstructure was characterized using a Bruker e-Flash camera for Electron Back Scatter Diffraction (EBSD). Grain size were determined with OIM Analysis (EDAX) and ATEX [192] softwares, setting the lowest grain size to 10 μm and using the intercept method. Grain sizes were determined both with and without considering annealing twins. EBSD analyses also allowed estimating plastic strain in the material using Grain Orientation Spread (GOS) and Kernel Average Misorientation (KAM) methods in OIM Analysis and ATEX softwares. The GOS gives the average difference between the orientation of each pixel of a given grain and the average orientation of the same grain [193]. This method is relevant to compare strain state of different grains, zones and samples. However, it is not suitable for local strain analyses and KAM criterion should be used instead. KAM calculates the misorientation between a point and its neighbors. GOS and KAM maps were computed from EBSD analyses using a 3 μm step, cleaning up of the resulting map by setting the minimum grain size to 10 μm, setting the grain tolerance angle to 7° and the minimum confidence index of 0.1. KAM map was computed setting the maximum misorientation to 7°, considering the 3^{rd} neighbour and perimeter only.

2.2.4 TEM

Nature of phases, dislocation density and structures were characterized with a Tecnai F20-ST Transmission Electron Microscope (TEM) operating at 200 kV. To produce TEM specimens, cylinders of 3 mm in diameter were machined from the material. The cylinders were then cut into several 500 μm thick disk samples. Finally, the disk samples were polished to a 100 μm thickness and electropolished, allowing the creation of a hole at the center of the samples. Areas near the edges of the hole were thin enough to allow partial transmission of electrons and thus could be analyzed under TEM.

In some specimens, the volume fraction of phases was too low to use simple TEM samples. Instead, FIB (Focused Ion Beam) preparation was performed to select specific regions of the material. This was carried out using a SEM-FIB Helios 660. First, a zone containing the region of interest was identified using SEM. Then, a carbon layer was deposited onto the region to protect it from the ion beam (Figure 2.6 (a)). The area of interest was then machined to form a lamella (Figure 2.6 (b)), which was later attached to the micro-manipulator. The lamella was then welded on the copper support for TEM analysis (Figure 2.6 (c)) and further thinned (Figure 2.6 (d)).

Both types of samples were then analyzed under TEM. Bright field imaging was used to detect inclusions, precipitates, dislocations and defects such as damage. For particularly small precipitates (less than 20 nm), high resolution TEM (HR-TEM) imaging was used. Electron diffraction was carried out on phases to determine their nature, achieved by fast Fourier transform (FFT) method in HR-TEM imaging for smallest precipitates. Chemical composition of phases was also analysed, using High-angle annular dark-field imaging (HAADF) technique, allowing for a very high resolution.

2.2.5 Hardness

The Vickers hardness of different material states was measured across the cross-sections of the plates with a 1.0 and 5.0 kgf using a Struers Duramin-A300 tester.

2.2.6 X-ray diffraction

X-ray diffraction (XRD) analyses were carried out with a Bruker D8 DISCOVER analyzer to determine the nature of phases present in the material at the initial state and after thermal exposure, using a Cu source with $K\alpha 1 = 1.5406$ Å and $K\alpha 2 = 1.54439$ Å with a ratio of 0.497. Identification of phases in the resulting diffraction patterns was carried out using CrystalDiffract software.

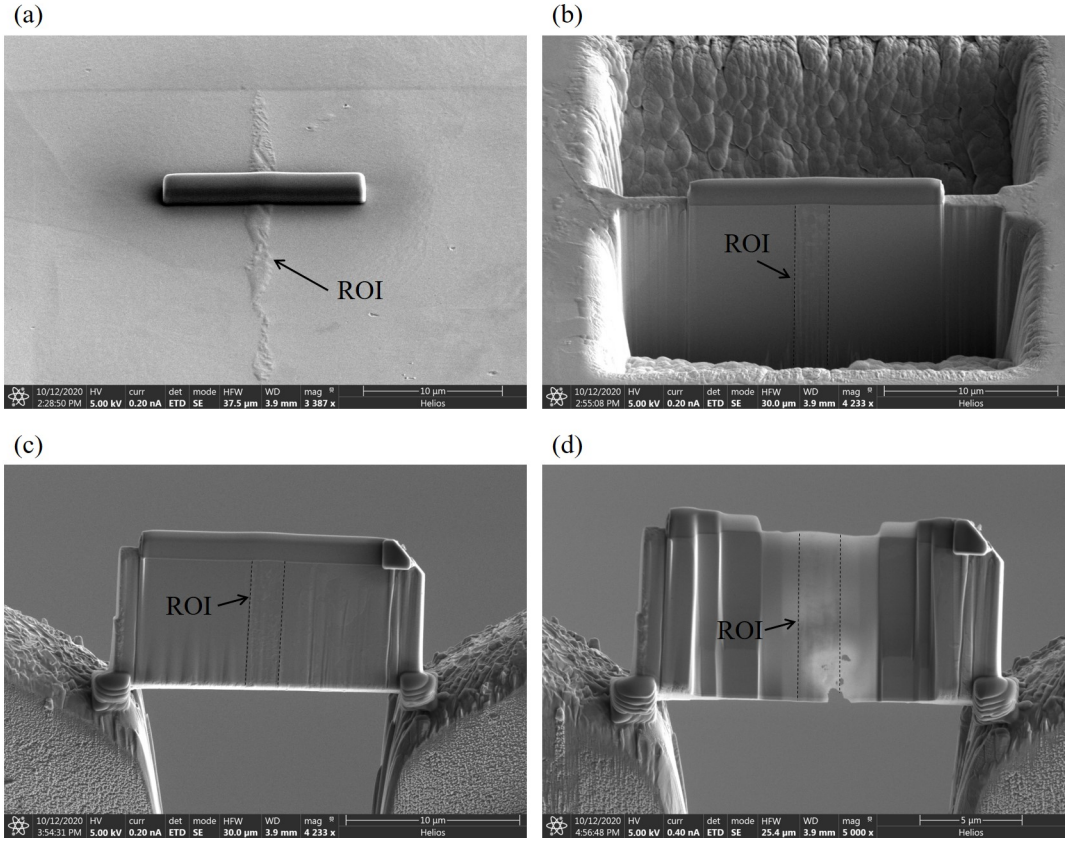

Figure 2.6: SEM images of the FIB process for the preparation of TEM lamella with (a) carbon layer deposition (b) creation of the lamella by matter extraction (c) mounting and welding of the sample to the copper sample support and (d) final lamella thickness reduction.

2.3 Mechanical characterisation of material states

In addition to microstructural properties, mechanical behavior of material states was investigated. Particularly, tensile properties of material states were characterized to determine material model parameters for each state for further FEM simulations. Specifically for the single-pass welded material, small dog-bone shaped specimens were machined in both X and Y directions from the welded plate, as illustrated in Figure 2.7. Tensile tests were carried out at room temperature for the different material states, using a 20 kN INSTRON 4507, 100 kN MTS servo-hydraulic and 10 kN capacity INSTRON machines, for specimens machined from the as-received, single-pass welded material and material with increased grain size, respectively. The strain rates in the range of $2.5\,10^{-4}\,s^{-1}$ and $5.\,10^{-4}\,s^{-1}$ were applied.

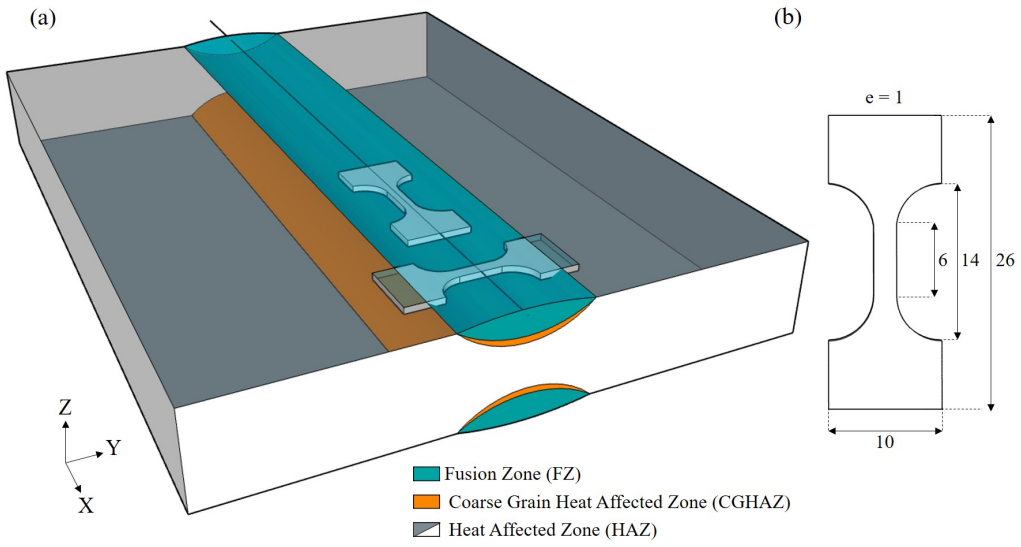

Figure 2.7: 3D scheme of tensile samples (a) location and (b) geometry machined from the single-pass welded plate (dimensions are in mm).

2.4 Generation of residual stresses by Turski compression

SRC testing of each material state was carried out using the self-restraint method by pre-compressing and unloading CT-like specimens, as first developed by Turski *et al.* [47]. This required the machining of CT specimens from each material state.

2.4.1 Geometry of CT specimens

CT specimens were machined by EDM (Electrical Discharge Machining) with a precision of ± 0.01 mm using as-received and prior-treated (increased grain size, cold-rolled, single and multi-pass welded) plates of 316L(N) steel. Location for machining of CT specimens in the welded plates is shown in Figure 2.2. Two geometries of CT were used in this work, as shown in Figure 2.8 (a) and (b). One specific geometry (Figure 2.8 (a)) was chosen for the cold-rolled specimens for comparison with results of Turski *et al.* [47] and Pommier [45] who used the same geometry. The prior hardening of the cold-rolled specimens actually allows reaching high residual stresses with a relatively low mouth displacement. However, the absence of initial pre-strain in the other material states (without cold-rolling) implied loading to higher crack mouth opening displacements during the compression to reach the same levels of residual stresses, possibly resulting in mouth crushing. As a result, the geometry used by Turski *et al.* [47] and Pommier [45] could not be used for these material states. A second geometry, shown in Figure 2.8 (b), had to be designed for the as-received, pre-aged (grain growth) single-pass welded, cold-rolled welded and multi-pass welded specimens. Thickness and notch radius of CT samples used for each material state are detailed in Table 2.2.

After cold-rolling, CT specimens with two different thicknesses as well as two notch radii were machined (Table 2.2) to induce different residual stresses magnitudes and distributions during the compression. For the as-received, material with increased grain size, welded and cold-rolled welded states, a single notch radius of 0.75 mm was used. It is worth noting that the thickness of the welded plates was not even due to the presence of the weld pool creating a slight bulge on the surface (illustrated in Figure 2.8 (b)). As a result, thickness of CT specimens machined from the welded was not even either. This resulted in higher thickness at the weld centreline and lower thickness at the edges of the

CT specimens.

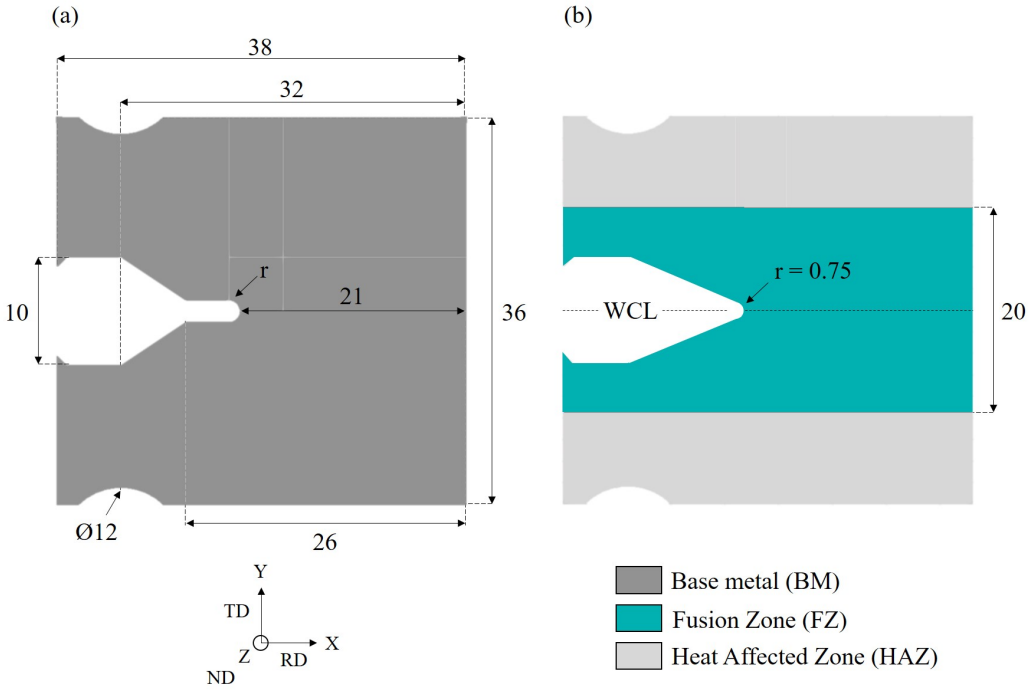

Figure 2.8: Geometry of CT specimens used for Turski compression: (a) for cold-rolled state with r ϵ $\{0.75, 1\}$ and (b) for as-received, material with increased grain size and welded states. Thicknesses are detailed in Table 2.2. RD, TD and ND correspond to rolling, transverse and normal directions to cold-rolling, respectively. Dimensions are in mm.

2.4.2 Turski compression procedure

After machining the CT specimens from the different material states, Turski compression was applied to each specimen to generate controlled levels of residual stresses and plastic strain. The compression tests were carried out with an MTS hydraulic machine with a 250 kN load capacity monitored with the MTS 793 software. CT specimens were maintained between two metallic pieces presenting a round edge with the radius of the CT top and bottom spherical seat, as illustrated in Figure 2.9. In order to measure the deformation of the specimens during the test, a calibrated MTS clip extensometer (ref. 632.02F-21 ID-10452811E) was placed into the crack mouth opening of the CT samples as illustrated in Figure 2.9. Crack mouth opening displacement (CMOD) evolution as a function of time, force and machine displacement could then be measured.

FEM simulations of the Turski compression tests were priory carried out to determine the loading conditions required to reach residual stress sufficient to trigger SRC for each state of the 316L(N) steel, accordingly to thresholds levels reported in the literature [45]. For these simulations, the mechanical behavior of each state was obtained by mechanical testing and from the different results reported in the literature. These are presented further in Chapter 4.

Turski compression of cold-rolled specimens was controlled by force, to be compared to results of Pommier [45], who followed the same method for SRC testing of a 316L(N) of similar composition to the one studied in this work. The specimens made of cold-rolled material were then compressed to a maximum force, $F = 25$ kN, with a 0.5 kN/s loading rate (Table 2.2). Then, the specimens were completely unloaded. Typical displacement

response of cold-rolled specimens with CMOD measure during compression is shown in Figure 2.10 (a). As shown by Pommier [45], the Turski compression of pre-hardened material allows reaching high levels of residual stresses with low CMODs. For these conditions, the evolution of both CMOD and force with time is almost linear and hence allowed good control of displacement.

The same procedure was firstly applied to the CT specimens made of welded materials; however the same level of precision was not always obtained. As it will be discussed in Chapter 4, it is necessary to reach much higher CMODs to obtain the same levels of residual stresses in non-hardened specimens in comparison to the cold-rolled ones. As it is illustrated in Figure 2.10 (b), the Turski compression of a welded specimen controlled by force is more complex than in the case of cold-rolled specimens because of the too rapid increase of CMOD after about 0.5 mm of displacement. For this sake, Turski compression of non-hardened material states were then carried out using a displacement control with a 0.005 mm/s rate, allowing better monitoring the displacement evolution. Instead of a controlled force, different magnitudes of maximum CMOD were imposed. Typical displacement response of welded specimens during such compression is shown in Figure 2.10 (c). This approach allowed obtaining more linear CMOD evolution with time, closer to the one observed for cold-rolled specimens.

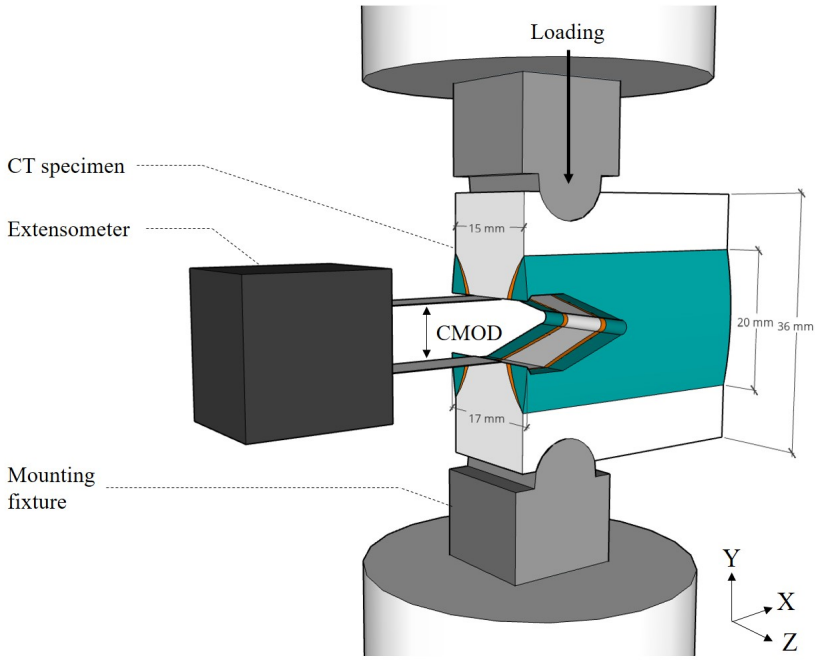

Figure 2.9: Scheme of Turski compression experimental set-up with welded CT specimen. Dimensions are in mm.

Table 2.2: Geometry of CT specimens (see Figure 2.8) and testing conditions for different states of 316L(N) steel.

	Geometry			Compression		Relaxation	
Material state	e [mm]	e at weld [mm]	r [mm]	F [kN]	CMOD [mm]	T [°C]	t [s]
As-received	15.5	-	0.75	28	1.73	575	580
						575	1470
				30	2.34	575	1470
Increased grain size	14.6	-	0.75	24	2.34	575	1470
				27	5.62	575	1470
Cold-rolled	11.9	-	0.75	25	0.34	575	580
		-	1	25	0.37	575	580
		-	0.75	25	0.34	575	1470
		-	1	25	0.37	575	1470
		-	1	25	0.37	600	580
Single-pass welded	15.4	16.5	0.75	41	6.09	575	580
				34	1.73	575	1470
				41	6.41	575	1470
				34	1.22	575	1470
				34	1.39	575	1470
				34	1.85	575	1470
Multi-pass welded	16.0	21.0	0.75	41	1.82	575	580
				41	1.82	575	1470
				41	1.56	575	1470
Cold-rolled welded	12.1	13.9	0.75	30	2.49	575	1470

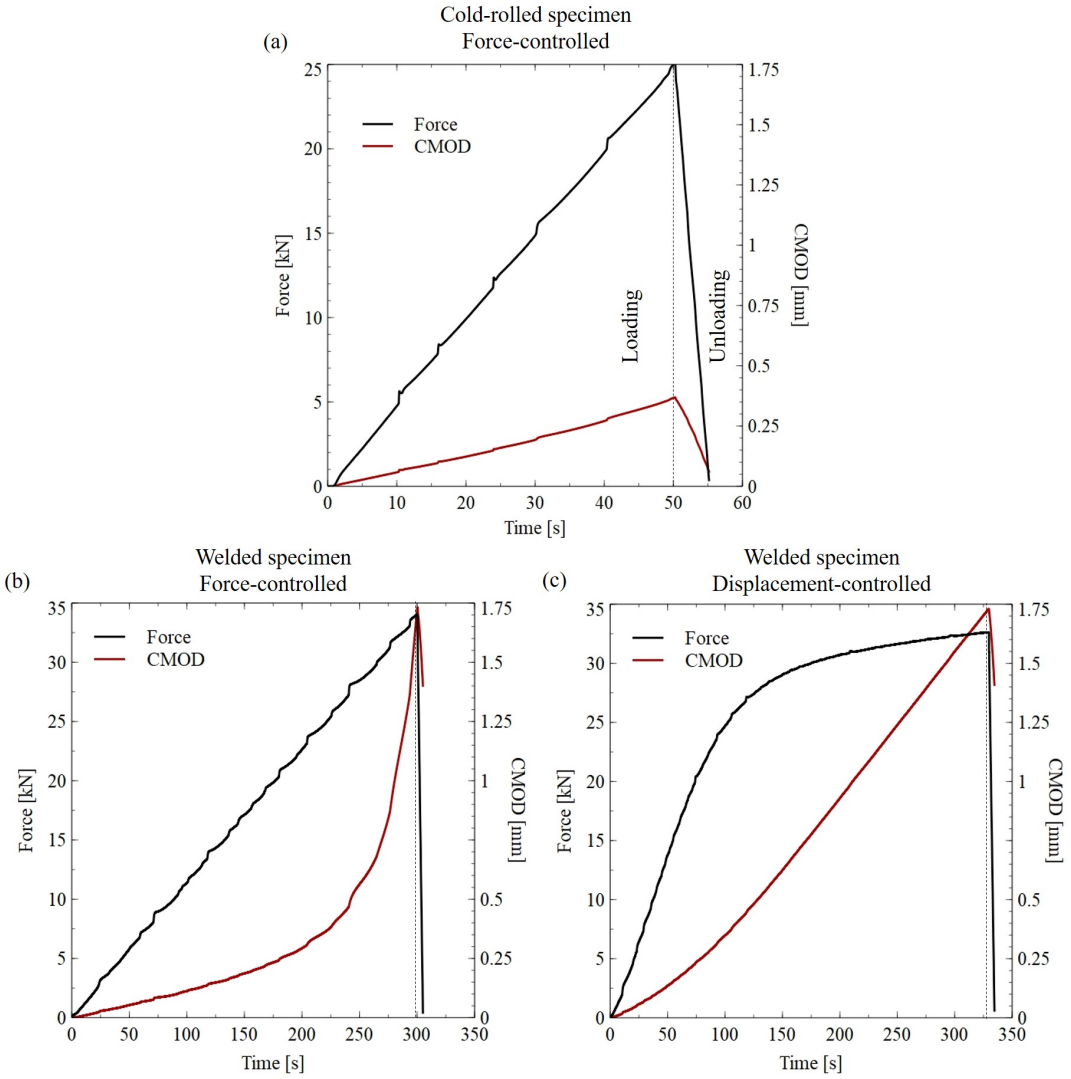

Figure 2.10: Turski compression testing with force and CMOD (both in absolute values) as a function of time in the case of the (a) force control of a cold-rolled specimens, (b) force control of a welded specimen and (c) displacement control of a welded specimen.

2.5 Heat treatment for stress relaxation

After the Turski compression, CT specimens were heat treated in ambient air at 575 and 600 °C for 580 and 1470 h using a PLF Ceradel furnace to relax the residual stresses. In addition, samples of each material state were also subjected to the same thermal treatments without prior Turski compression, in order to characterize the microstructure evolution without the influence of residual stresses and plastic strain. Temperature was monitored during the whole treatment using a LR8410-20 Hioki station and K-type thermocouples welded to the surface of surface of control samples made of 316L(N) steel. After the heat treatment, specimens were removed from the furnace and cooled down to ambient air. Relaxation testing conditions for each material state are detailed in Table 2.2.

2.6 Characterization of relaxation damage

After the heat treatment allowing stress relaxation, specimens were analyzed to detect damage, characterize and quantify it but also to characterize associated microstructural

features. For damage characterization, specimens were cut by EDM in sections relative to two different planes as illustrated in Figure 2.11 (a), allowing different kind of observations:

(i) specimens were first cut in the (XY) plane at mid-thickness, transverse to the notch axis (Figure 2.11 (a)-(1)). In this region, the distribution of residual stresses and plastic strain predicted by FEM simulations was heterogeneous, allowing correlations between damage, stress and strain levels. In the specific case of welded specimens, this plane also corresponds to sections containing only one of the weld zones, thus with one type of homogeneous microstructure. At mid-thickness of the specimens, this corresponds to the HAZ;

(ii) the other half of the CT specimen made from welded materials (single and multi-pass) was cut in the (YZ) plane near the notch root (Figure 2.11 (a)-(2)). The sample was further polished using SiC abrasive paper of grain size P80 removing the section illustrated in Figure 2.11 (a)-(3). This allowed reaching the plane of the notch root, illustrated in Figure 2.11 (a)-(4). The remaining section was further polished with SiC abrasive paper of grit size P1200. In average, the final (YZ) plane of observation was located at about 40 μm from the notch root after polishing. This allowed investigating the damage over the heterogeneous microstructure near the notch, in the plane containing the highest levels of residual stresses and plastic strain according to the numerical simulations (see Chapter 4), thus highest probability of stress relaxation damage.

Observations were carried out using different microscopy techniques, requiring the samples to be further polished with diamond paste with abrasive size of 6, 3 and 1 μm and finally with a solution of colloidal silica (OPS solution). These were used to characterize the microstructure and quantify damage induced by stress relaxation in the specimens, i.e. cavities and cracks.

2.6.1 Optical microscopy

For a large scale detection of damaged regions in each specimens, optical microscopy analyses were first carried out on the entire surface of sections using microscopes previously described in Section 2.2.2. These represented areas of 36 $\times$ 38 mm^2 in the (XY) plane and 9 $\times$ 36 mm^2 in the (YZ) plane. Microscopic imaging allowed identification of objects as small 1 μm.

2.6.2 SEM/EDS/EBSD

After the identification of highest damaged region of each specimen by optical microscopy, further observations of these damaged zones were carried out using an SEM for more precise imaging and damage quantification, using detectors described previously in Section 2.2.3. SEM imaging allowed observation of objects as small as 30 nm. Observations in the (XY) plane were carried out in the region of 2 $\times$ 2 mm^2 close to the notch root (Figure 2.11 (a)). Observations in the (YZ) plane were carried out in a region of 1 $\times$ 8 mm^2 at the notch root. Specifically for damage quantification by image analysis (Section 2.6.4), this represented about 37 SEM images at a $\times$171 magnification for one section.

2.6.3 TEM

TEM observations were also carried out to identify the nature of secondary phases precipitates associated with stress relaxation cavities and the dislocations structures in damaged regions. To this end, TEM samples were machined from CT specimens after relaxation as

illustrated in Figure 2.11 (b). To do so, cylinders of 3 mm in diameter were machined by EDM with their center positioned at a 1 mm distance from the notch root. This allowed positioning the areas of interest (in the center of the samples) as close as possible to the highest residual stresses region (i.e. notch root), without compromising the elaboration process of the samples. Then, the cylinders were cut into TEM samples following the same procedure as described in Section 2.2.4. Specifically to carry out analyses in the CGHAZ, disk samples were cut at depths between 2.7 and 3.8 mm from the surface.

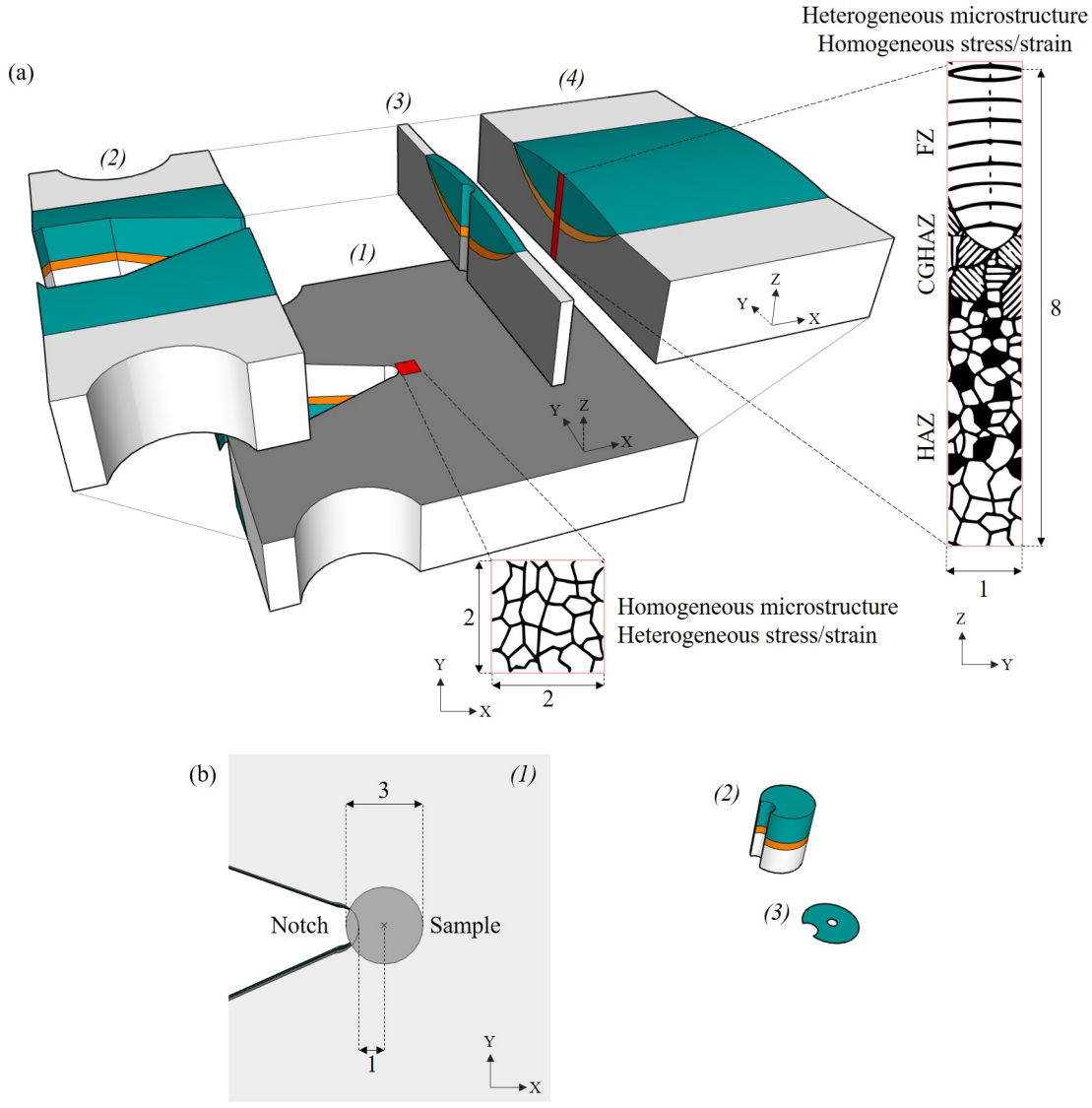

Figure 2.11: Sample preparation for damage analysis after stress relaxation of CT specimens: (a) for SEM observations *(1)* cutting in the (XY) plane at mid-thickness of CT sample allowing observation of damage in a homogeneous microstructure, *(2)* cutting near the notch in the (YZ) plane and *(3)* polishing through the notch to reach *(4)* the high residual stress plane, allowing observation of damage in a heterogeneous microstructure; (b) for TEM (1) machining near the notch, *(2)* extraction of the sample and (3) realisation of thin foil. Dimensions are in mm.

2.6.4 Image analysis for damage quantification

In order to characterize the effect of a weld microstructure on the SRC with the highest accuracy, the quantification of damage considering both cavities and cracks has been carried out on CT specimens after Turski compression, relaxation and cutting steps described previously.

Because some of the cross-sections of damaged specimens contained thousands of cavities, manual counting could not be considered for damage quantification. Consequently, two image analysis tools were developed for damage quantification in addition to manual counting: machine learning and contour detection. These were priory compared using practical examples to determine the most suited for the rest of the study.

2.6.4.1 Machine learning object recognition

In order to detect cavities in SEM images, a machine learning object recognition tool was developed using the Python library *ImageAI* [194]. This required the creation of an image database of damaged regions and manual initial identification of defects using *Labelimg* annotation tool under Python. The main difficulty for the recognition of damage in SEM images was the variation in size, shape of cavities and cracks, but also the observation conditions. Typically, the tool was developed specifically to be able to recognize cavities in SE and BSE images, but also at high ($>\times$13 K) and low ($<\times$170) magnifications to be more versatile.

It thus was necessary to establish a database representative of the observed cases. The model was then trained to recognize single and coalesced cavities, surface defects due to polishing and inclusions such as MnS and TiN, which also appeared in dark contrast in BSE images. This allowed avoiding misinterpretations, improving the statistics. The algorithm was trained over 158 different SEM images containing over 3360 objects identified manually (mainly cavities), gathered from the stress relaxation cracking analyses presented later in Chapter 5. Two examples of cavity detection by the trained model are shown in Figure 2.12. Figure 2.12 (a) shows isolated cavities at grain boundaries and Figure 2.12 (b) shows dispersed cavities, as well as coalesced cavities and cracks at a lower magnification. Despite the cavities size and shape being very different in both cases, the model was able to identify isolated and coalesced cavities/cracks. However, as illustrated in Figure 2.12 (c) the model sometimes confused single cavities and coalesced cavities, due to the variation in shape. This type of issue could be simply resolved with an automatic sorting by size. Besides, it was also possible to sort identified objects based on their identification confidence index, as shown in Figure 2.12 (c).

2.6.4.2 Contour detection method

A contour detection tool was also developed to identify cavities in SEM images using a gray scale conversion. This relies on the fact that cavities in SEM images appear in black contrast whether in SE or BSE imaging. For more relevant results, large defects such as inclusions and polishing surface defects were manually removed from the images prior to image processing.

The input images containing cavities (Figure 2.13 (a)) were first transformed respecting a binary threshold (Figure 2.13 (b)) and slightly blurred to smoothen the objects edges. Edges of objects from the gray scale image were detected, the open gaps between objects edges were then closed (Figure 2.13 (c)) so that the resulted closed contours could be identified distinctively. From these contours, the position, length and width of the cavities could be determined (Figure 2.13 (d)). A similar example is given for a low magnification image of damage in Figure 2.14. For this work, detected objects with measured length

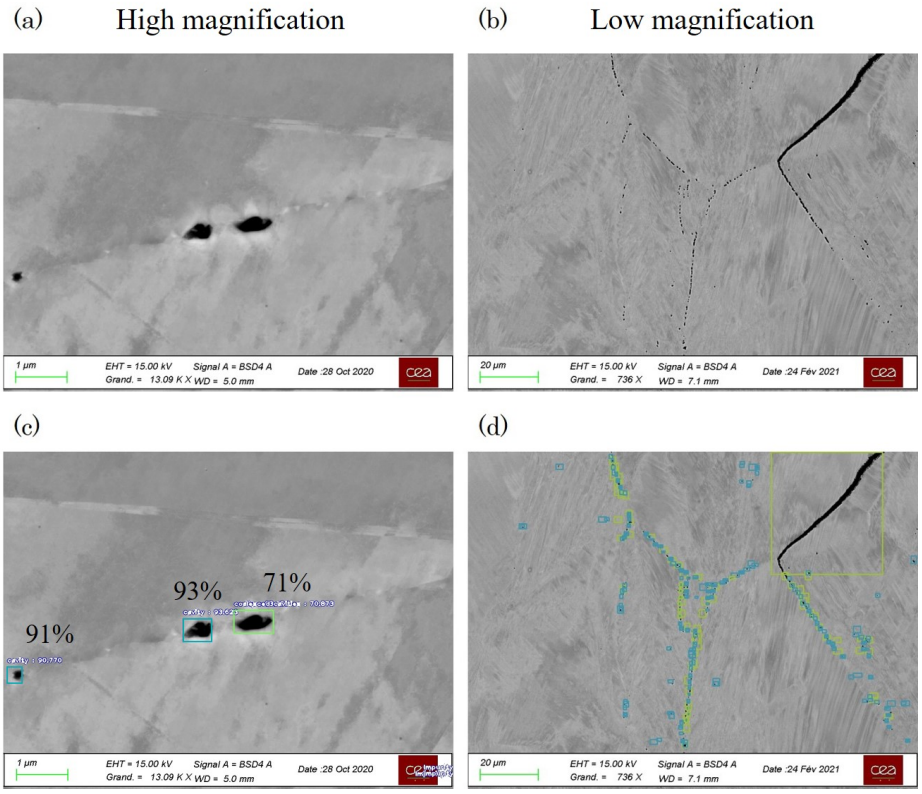

Figure 2.12: Example of machine learning cavity recognition in SEM images with (a) and (b) the images used for recognition, (c) and (d) the resulting images after cavities identification. Blue squares correspond to identified single cavities and green ones to coalesced cavities/cracks. Confidence indexes resulting from the detection of image (a) are shown in (c).

lower than 50 nm or higher than 5 μm were excluded, since cavities and coalesced cavities typically present lengths within this range (discussed in Chapter 5).

As illustrated in Figure 2.14 (d), the detection of cracks with the contour detection method is often difficult because SEM images contain only a part of the cracks. As a result, the contour of the crack could not be considered as a closed contour (Figure 2.14 (c)) and thus it was not taken into account for the counting of damage. However, cracks were significantly larger and less numerous than cavities thus they could be easily counted manually in addition to the automatic count of cavities.

2.6.4.3 Comparison of the methods

The main advantage of the machine learning method is the automatic recognition of damage only, which is based on a trained artificial intelligence, meaning the model most often does not account for other defects in the image such as inclusions or polishing defects. The model is thus based on the recognition of an actual physical object, rather than grey shades. Also, the model is capable of distinguishing cavities from coalesced cavities, while the contour detection method does not consider cavities longer than the maximum length indicated by the user. The main issue which can occur with the machine learning method is the multiple count of the same cavity. This issue can be limited by filtering the cavity by their position, but it could only work to a certain extent: cavities in low magnification SE images are usually very close to each others, thus the sorting by position sometimes resulted in erasing cavities which were actually present. As a result, the machine learning

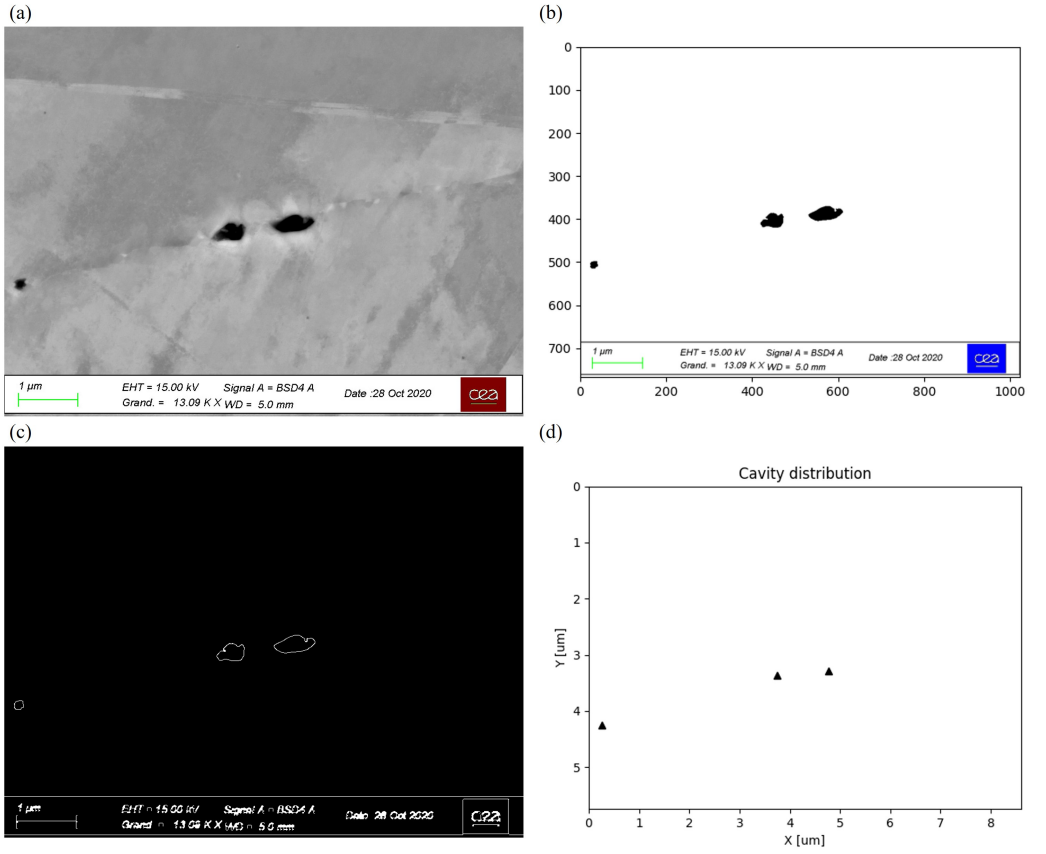

Figure 2.13: Example of contour detection method in a high magnification SEM image with (a) the input image, (b) the gray scale image, (c) the detection of contour for each object and (d) distribution of cavities.

method presented a lower precision for large scale images. Unfortunately, due to the size of the zones analysed during this study, SEM analysis for damage quantification mostly consisted in large scale images. The machine learning method also requires training a model, which is highly time consuming and requires a numerous different images containing damage, at various scales and damage levels. On the contrary, the contour detection method can be used without prior images database.

Images analysis tests were conducted using the two methods to be compared with manual counting for a low magnification SEM image, which was the most precise approach for damage quantification. An example is shown in Figure 2.15. In most of the cases, the contour detection method appeared to be more precise than the machine learning method both in terms of cavities distribution and cavity number, with results closer to the ones obtained manually. The image processing of a SEM image at a $\times 171$ magnification such as shown in Figure 2.15 takes about 10 min for a manual count against only 7 s for the machine learning method and less than 3 s for the contour detection method. The machine learning method could be interesting to use in the case of material with several kind of defects and particularly for high magnification images; for this work however, the contour detection method was found to be the most suited for damage quantification and was thus used in the rest of the study.

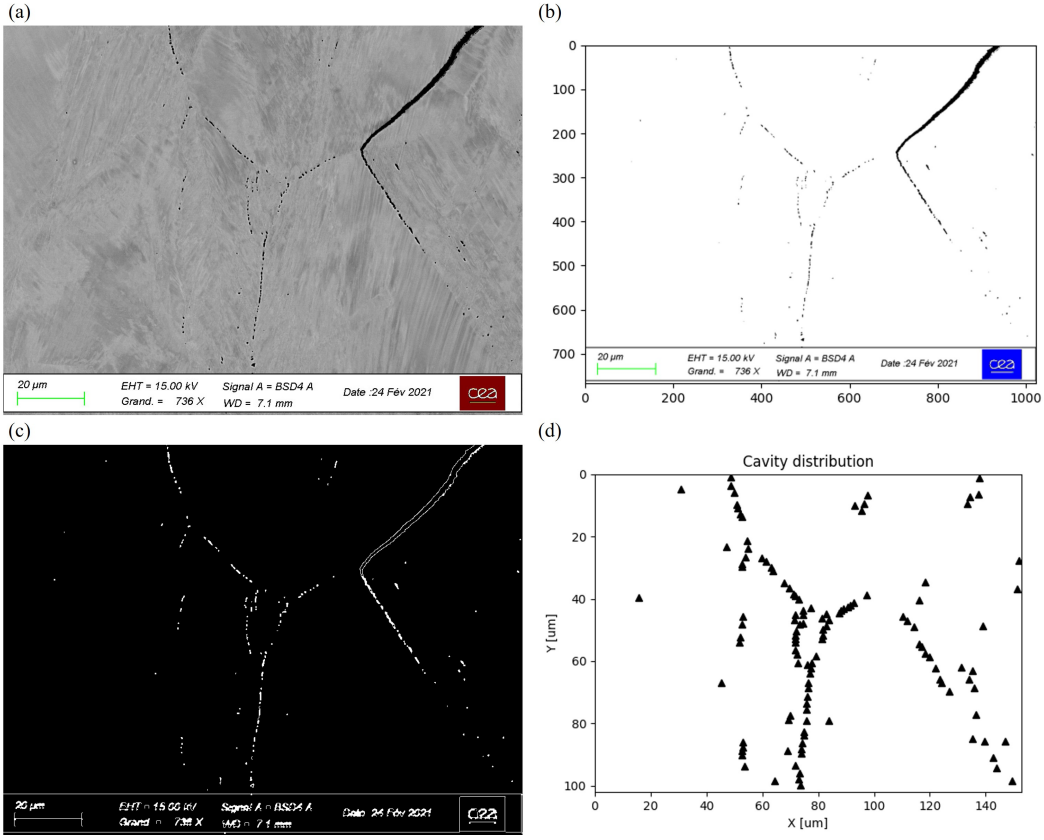

Figure 2.14: Example of contour detection method in a low magnification SEM image with (a) the input image, (b) the gray scale image, (c) the detection of contour for each object and (d) distribution of cavities.

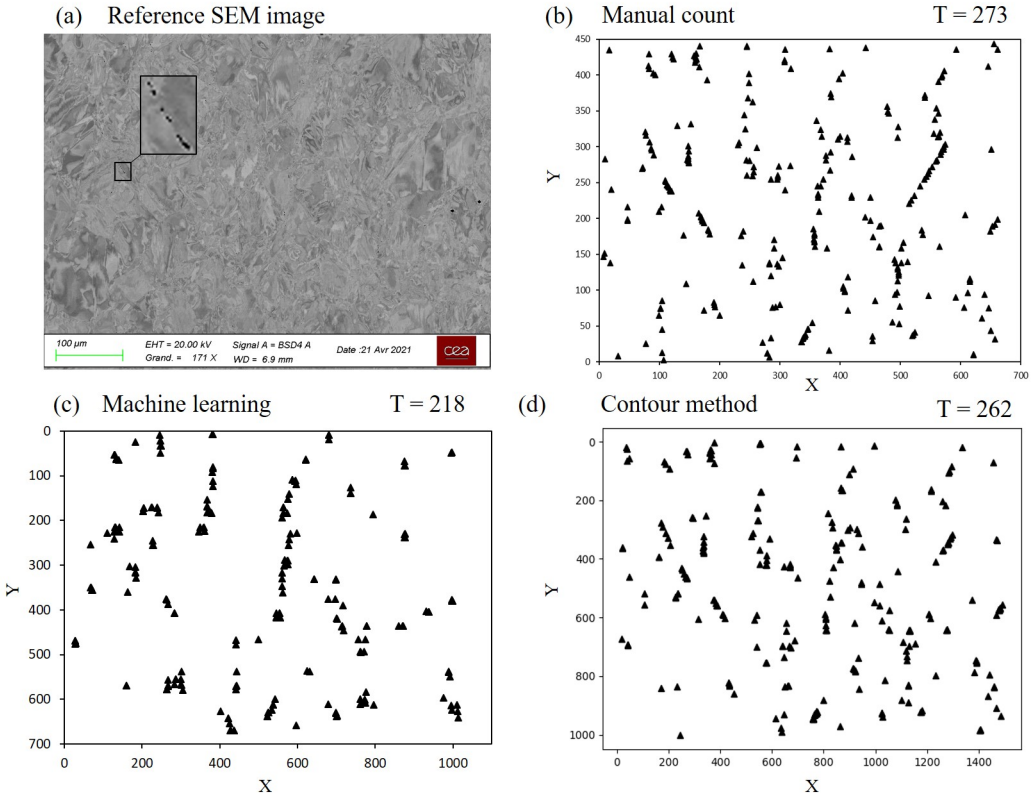

Figure 2.15: Comparison of cavity distribution and count in a (a) SEM image of a damage specimen, using (b) the manual count, (c) machine learning detection and (d) the contour method. T corresponds to the total number of cavities detected.

2.7 Summary of methods

A graphical summary of the method for SRC sensitivity testing in this work is proposed in Figure 2.16. While most SRC testing methods either chose to study the phenomenon in welded specimens or in non-welded specimens but with controlled addition of residual stresses, it was chosen here to combine both approaches. To investigate the effect of a heterogeneous weld microstructure on SRC in a 316L(N) using the Turski compression, CT specimens were machined from the plates of different material states: as-received, material with increased grain size, cold-rolled, single and multi-pass welded plates. These CT specimens were subjected to Turski compression, which unloading resulted in the generation of tensile residual stresses. Specimens were then put in furnace for stress relaxation, aiming for SRC. Several characterization techniques were used to both investigate the microstructure and stress relaxation damage. Mainly, optical microscopes, scanning and transmission electron microscopes, EBSD and EDS detectors. Damage observed in SEM images was quantified using image analysis tools, allowing the counting of defects and their spatial distribution.

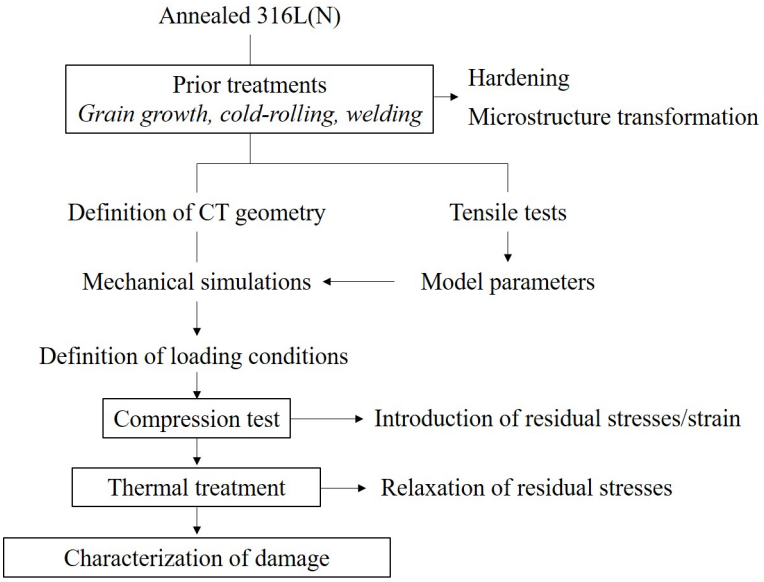

Figure 2.16: Description of the method for the SRC test on CT specimens.

Chapter 3

Microstructure of material states

Contents

3.1 Introduction

The literature review on SRC proposed in Chapter 1 allowed the identification of the main SRC factors: residual stresses (due to welding and component geometry), plastic strain, reheat, secondary phase precipitates and grain size. To characterize the effect of these SRC factors, six different states were produced from the studied 316L(N) steel: as-received, cold-rolled, single and multi-pass welded, cold-rolled single-pass welded states and finally material with increased grain size. The aim of each material state for this study and the method for producing them is detailed in Section 2.1.

The microstructure of each of these states was characterized in terms of grain size, inclusions and plastic strain priory to further Turski compression and relaxation treatment. Strain hardening was evaluated using hardness measurements and strain analysis using EBSD data. In addition, all these states were subjected to thermal treatments to characterise the precipitation of secondary phases, identifying their nature and precipitation kinetics, which play a major role in stress relaxation damage mechanism. The as-received state was more particularly studied as it served as a reference state. The other states were then subjected to similar treatments to study, for instance, the effect of strain hardening and welding on precipitation. The results obtained for each material state would then help predicting their relative risk to SRC and further facilitate the understanding of stress relaxation damage analysed in Chapter 5.

3.2 Presentation of the 316L(N) steel

The chemical composition of the studied 316L(N) austenitic stainless steel, referenced as K46-T9 in CEA database, is given in Table 3.1. Method of composition measurement is detailed in Section 2.2.1. The steel was supplied by ArcelorMittal after standard casting and hot-rolling processes, parallel to Y direction (while the cold-rolling process presented further (Section 3.4) was applied in the X direction). Austenitization for 35 minutes at 1100 °C followed by water quenching were finally applied to produce the microstructure corresponding to the "as-received" state.

Table 3.1: Chemical composition [%wt.] of the studied 316L(N) steel measured by elementary analyser for C, S and N and by ICP-AES for the other elements.

Fe	Cr	C	Ni	Mo	Mn	N	Al	P	Co	Cu
Bal.	16.9	0.024	11.9	2.42	1.74	0.073	0.010	0.029	0.041	0.15

To get the first insight of temperature effect on 316L(N) steel, thermodynamic computations for the temperature range of interest for the present work, between 300 and 1000 °C, were performed using the Thermo-Calc software and the TCFE9 database. Diamond and graphite phases were excluded from calculations since they cannot form in the steels. The chemical composition of the 316L(N) measured in this work was used for simulations, accounting for all elements identified in Table 3.1. From these results, several secondary phases could be expected to form during a thermal treatment: the tetragonal σ phase can be expected to form between 373 to 836 °C; Laves phase η (C14) from 300 to 776 °C; HCP ε phase from 442 to 855 °C; $M_{23}C_6$ phase from 300 to 904 °C; M_3P phase from 300 to 742 °C; and finally AlN phase from 300 to 900 °C (Figure 3.1 (a)).

Since carbides are known to be one of the driving forces for SRC in austenitic stainless steels and particularly the 316L(N) steel [13, 45], additional simulations were then carried out, accounting for the carbide phases other than the $M_{23}C_6$ susceptible to precipitate in the considered temperature range. Indeed, it possible that thermal exposure leads to a

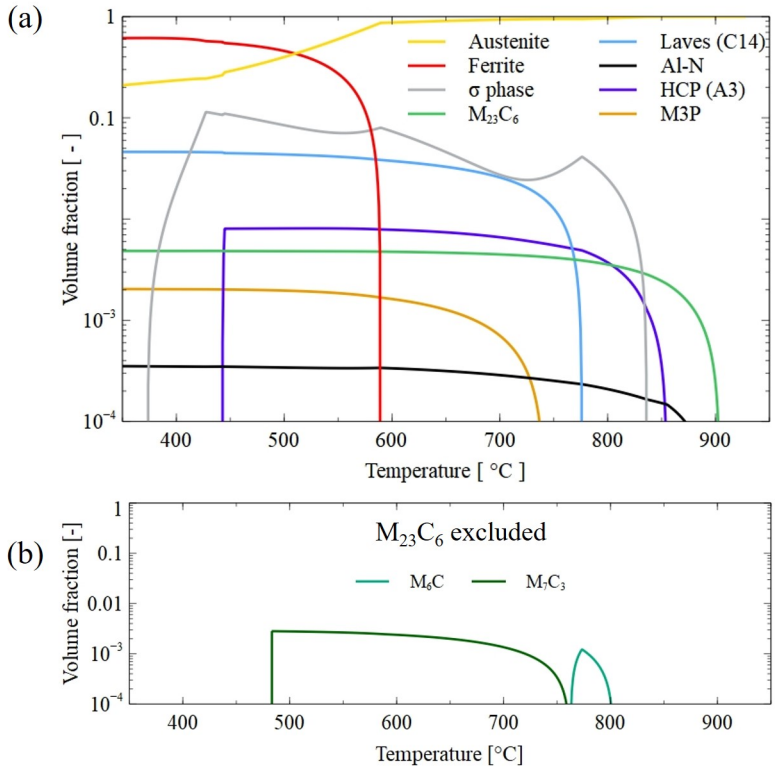

Figure 3.1: Computed phase volume fraction in the studied 316L(N) steel between 350 and 950 °C with (a) diamond and graphite phases excluded and (b) volume fraction of M_7C_3 and M_6C phases excluding additionally the $M_{23}C_6$ phase.

metastable equilibrium and hence allows the formation of other phases [195]. Computations were thus performed excluding the $M_{23}C_6$ phase. Results showed that the domain of stability of the phases previously discussed (other than carbides) remained unaffected by these new conditions. However, simulations predicted the stability of the M_7C_3 phase from 483 to 762 °C and M_6C phase from 762 to 803 °C (Figure 3.1 (b)). Similarly, by excluding the σ phase from the system, simulations predicted the stability of the χ phase between 734 and 754 °C. These results are in agreement with typical stable phases found in the literature for 316L(N) steels [63, 76].

Computed chemical compositions of the stable phases are given in Table 3.2. These were all computed at 650 °C or indicated if otherwise, depending on their stability domain. The chemical composition of residual δ-ferrite was calculated at 1400 °C, considered as the casting temperature for the 316L(N) steel.

Table 3.2: Chemical compositions [%wt.] of stable phases in the 316L(N) steel computed at 650 °C (or indicated if otherwise) using Thermo-Calc software and TCFE9 database.

Phase	Fe	Cr	C	Ni	Mo	Mn	N	Al
Austenite	69.17	15.13	0	12.91	0.52	1.84	0	0
δ-ferrite (1400 °C)	66.36	18.95	0	9.27	3.44	1.58	0	0
σ	52.31	38.86	0	3.63	3.72	1.46	0	0
χ (800 °C)	54.02	23.38	0	3.57	19.03	0	0	0
Laves η (C14)	36.29	16.84	0	0.47	46.26	0	0	0
HCP ε	0.18	80.64	0	0	7.54	0.47	11.06	0
$M_{23}C_6$	7.1	67.87	5.17	0.31	18.61	0	0	0
M_3P	30.68	46.91	0	4.24	2.01	0.19	0	0
AlN	0	0	0	0	0	0	34.17	65.83
M_7C_3	1.59	87.6	8.93	0	1.68	0.21	0	0
M_6C (800 °C)	26.54	11.69	2.64	0	58.95	0	0	0

3.3 As-received

The microstructure of the as-received state observed by optical microscopy is shown in Figures 3.2 (a) and (b). IQ (Image Quality) and ferrite phase maps obtained from EBSD data are shown in Figures 3.2 (c) and (d). Residual δ-ferrite was observed in the form of islands or bands oriented in the hot rolling direction, with higher fraction towards the plate mid-thickness. This is probably due to a lower cooling rate at mid-thickness than at the surface. X-ray diffraction (XRD) analysis showed no diffraction peak of ferrite (Figure 3.9) suggesting a low ferrite fraction, less than 1% wt.

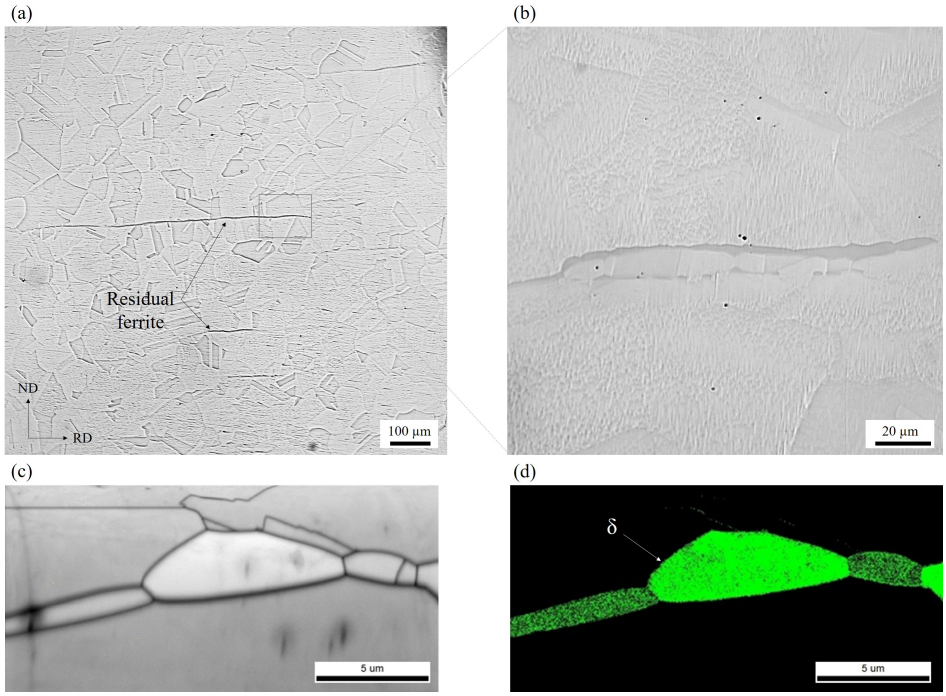

Figure 3.2: Microstructure of the as-received 316L(N) steel, revealing (a) austenite matrix and (b) residual δ-ferrite bands. Identification of ferrite phase by EBSD with (c) index quality and (d) phase maps acquired with by EBSD analyses, with 30 nm step size. RD and ND stand for hot rolling and normal directions, respectively.

EDS measures of the δ-ferrite revealed higher Cr and Mo content than that in the austenitic matrix (Table 3.3). This was expected as these elements are known to be ferrite stabilizers, while Ni and Mn contents, which are austenite stabilizers, were found to be lower in δ-ferrite than in the matrix.

Table 3.3: Chemical composition [%wt.] of austenite and δ-ferrite measured by EDS in as-received state.

Phase	Fe	Cr	Ni	Mo	Mn
Austenite	68.45	16.8	11.8	1.4	1.5
Ferrite	63.90	25.05	5.73	3.85	1.47

The microstructure observed by EBSD is shown in Figure 3.3. According to the Inverse Pole Figure (IPF) and GB maps with IQ, typical annealed microstructure was observed with equiaxed grains and no texture. As suggested by the boundaries map corresponding to CSL $\Sigma 3$ boundaries (Figure 3.3 (b)), many annealing twins were present in the as-received state. The IPF map where the twins boundaries were excluded is shown in

Figure 3.3 (c). The distributions of grain size with and without twins are shown in Figure 3.3 (c). According to ASTM, twin boundaries must be ignored for grain size measurement, meaning either side of a twin boundary is considered to belong to the same grain [196]. The grain size was then measured by not accounting for twin boundaries, with an average of 90 μm obtained by the intercept method (Section 2.2).

SEM and TEM analyses also revealed the presence of several inclusions in the as-received state. Large Al_2O_3 oxides with an average size of 4 μm were observed in some of the austenite grains, as illustrated in Figure 3.4 (a). In addition, round and elongated penny-shaped MnS inclusions were found, mostly at the ferrite-austenite interfaces, as shown in Figure 3.4 (b). Numerous small square-shaped TiN nitrides with an average size of 70 nm were observed in the austenite grains. These appeared to be mostly located on dislocation lines, as shown in Figure 3.4 (c). Asides from inclusions, neither bulk nor GB precipitates were observed in the as-received state, as illustrated in Figure 3.4 (d). Low dislocation density corresponding to well annealed microstructure could be observed using TEM.

Hardness measurements carried out in the as-received stated gave an average value of 155 HV1, in agreement with hardness usually measured for 316L steels [197]. GOS and KAM maps obtained from EBSD data (Figure 3.3 (e) and (f)) also suggested very low or no strain in the as-received state.

Effect of thermal exposure

Phase precipitation in a welded component can occur at two moments of its lifetime. First, phase precipitation can occur during the welding process, which induces high temperatures peaks for short duration (less than a minute). Typically, it was shown in Section 2.1.4 that temperatures outside of the weld pool can go from room temperature to temperatures higher than 1100 °C. Theoretically, all phases identified in Figure 3.1 are stable in this temperature range and are thus prone to form, if the kinetics allow it. Secondly, phase precipitation can occur during the service of the component. The 316L(N) steel was typically aimed to be used in 4^{th} generation of nuclear reactors with exposure to temperatures between 500 and 600 °C, but for much longer times (several decades).

Consequently, to simulate microstructure evolution due to exposure to temperature, samples of as-received state were thermally aged at 550, 575, 650 and 800 °C for duration varying from 1 to several thousands of hours. Multiple conditions of these ageing treatments (both in terms of temperature and time) were intentionally chosen to cover all scenarios of microstructure evolution of the studied 316L(N) steel. This would also allow distinguishing the effect of time/temperature and that of post-welding or post-compression residual stress/strain on precipitation and damage. Since the effect of thermal ageing on austenite and ferrite are very different, they will be discussed separately.

Precipitation in austenite

After thermal ageing for 24 h at 550 °C, SEM analyses did not reveal any precipitate in the material. Besides, XRD analysis of the aged specimen showed diffraction peaks corresponding to the austenite phase, one attributed to the ferrite and another to the TiN inclusions (Figure 3.5). None of the measured peaks was coincident with any of the expected precipitating phases identified previously (Figure 3.1), in agreement with SEM analyses.

No additional phase was observed to form in the samples thermally aged at 575 °C for 580 h (Figure 3.6 (a)). After 1470 h of heat treatment at this temperature, precipitates with size in the range between 50 and 400 nm were observed at austenite grain boundaries (Figure 3.6 (b)). EDS analyses carried out on these precipitates revealed Cr and Mo

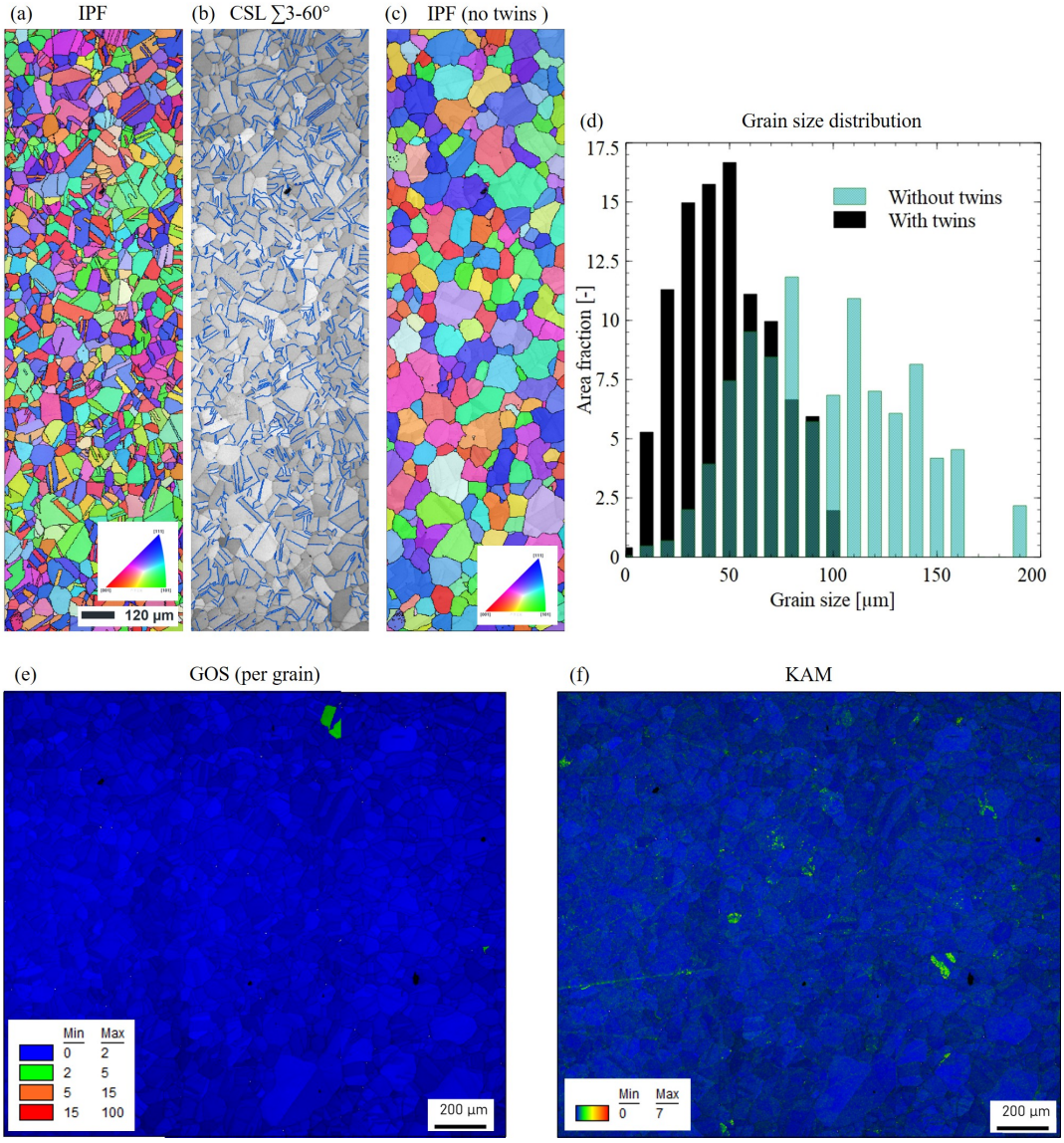

Figure 3.3: Grain structure of the as-received state of studied 316L(N) steel analysed using EBSD: (a) IPF map, (b) boundary map for Σ3 GBs, (c) IPF map excluding twins and (d) grain size distribution computed from maps (a) and (c) by intercept method. (e) GOS and (f) KAM map of the analyzed region.

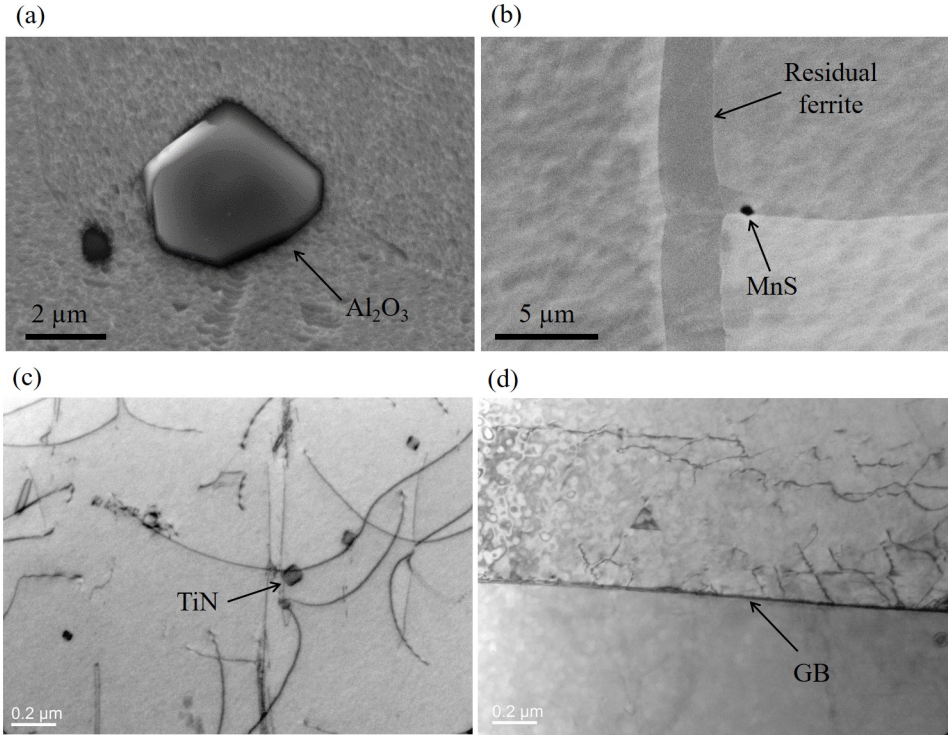

Figure 3.4: Images of (a) an Al_2O_3 inclusion in an austenite grain, (b) MnS inclusion at a ferrite/austenite boundary, (c) TiN inclusions at dislocation lines and (d) an austenite grain boundary free of precipitates.

contents almost twice higher than those in the austenitic matrix. Even though SEM-EDS analyses are not particularly suited for measuring the carbon content, high percentage of carbon was also measured in these precipitates as compared to that in the austenitic matrix. From these measurements, the literature data [63,67] and results on phase stability simulations (Table 3.2), these precipitates were assumed to be chromium carbides $Cr_{23}C_6$.

Carbides were often observed close to smaller Mo-rich intermetallics, measuring between 20 and 150 nm, with an average size of 58 nm (Figure 3.6 (b)). These precipitates could favor carbide nucleation, as it was mentioned by Rhouma *et al.* [63] for a 316L steel. Even though thermodynamic simulations suggested that these precipitates could either be σ or Laves η phase (Table 3.2), these phases are usually observed to form at higher temperature (> 600 °C) and for longer ageing time than carbides, according to the literature [67]. Likewise, the χ phase was not considered as it was numerically predicted to be stable only near 800 °C. Instead, it was admitted that the observed Mo-rich phase belongs to the stacking faulted Frank Kasper phase group, as stated by Rhouma *et al.* [63] from similar observations. It is probable that the precipitation of Mo-rich intermetallics at austenite GBs was favoured by GB segregation of Mo. Indeed, austenite GB enrichment by Mo was observed using EDS analysis in TEM for some heat treatment conditions (Figure 3.7).

At 650 °C, thermal ageing treatments of 1, 8, 24 and 168 h were performed. At this temperature, precipitation at austenite grain boundaries was only detected after 168 h of thermal ageing (Figure 3.6 (d)). The precipitates were similar to those observed at 575 °C, with high content of Cr and Mo. Further analysis with electron diffraction in TEM (Figure 3.8) and XRD analysis (Figure 3.9) allowed identifying these precipitates as $Cr_{23}C_6$ phase, confirming the assumptions made previously. TEM analyses showed that these $Cr_{23}C_6$ precipitates had a lattice parameter of 10.65 Å, in agreement with literature data [68, 70]. $Cr_{23}C_6$ carbides were observed to have either triangular, platelet-like or

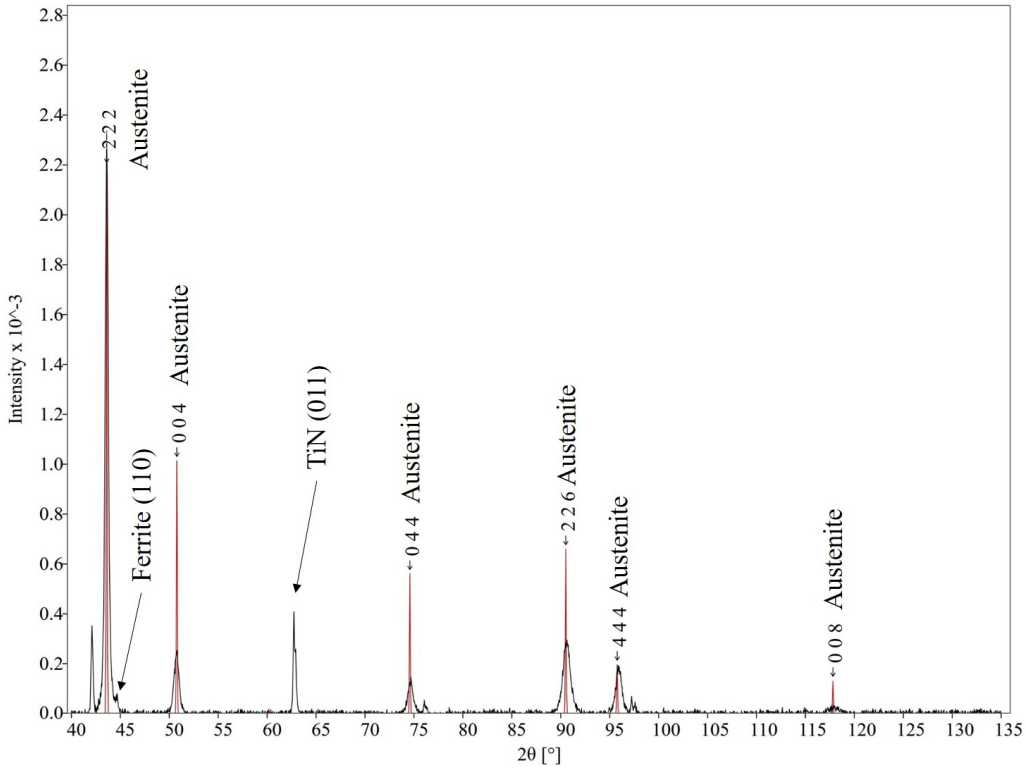

Figure 3.5: XRD analysis of 316L(N) steel aged at 550 °C for 24 h.

hexagonal morphology which most probably depend on GB misorientation angle [163]. The chemical composition of the $Cr_{23}C_6$ precipitates was measured by EDS in TEM (Table 3.4), revealing high Cr and C contents. One can note that measured chemical composition of the $Cr_{23}C_6$ precipitates did not respect the stoichiometry of the phase, probably due to the uncertainty of the measure for carbon detection but also due to the influence of the surrounding matrix. It is worth noting that smaller bright-contrast objects with a round to globular morphology and an average size of 50 nm were observed in TEM images (Figure 3.8). These voids could correspond to the removal of the small Mo-rich precipitates due to the electro-polishing process of sample preparation for TEM. Indeed, these small defects were not observed at GBs of the as-received state (Figure 3.4). These defects are to be distinguished from stress relaxation cavities discussed further (Chapter 5).

After ageing of 1 h at 800 °C, two types of large precipitates both presenting high Cr and Mo contents, were observed at austenite grain boundaries (Figure 3.6 (e) and (f)). One presented a slightly brighter BSE contrast (captioned "phase 1") than the other (captioned "phase 2"), due to differences in Cr and Mo content. These precipitates could probably be of the σ and/or χ phases, as both present high content in Cr and Mo and were predicted to be stable at temperatures close to 800 °C. According to the literature for a 316L steel [67], only the $M_{23}C_6$ and χ phases can be expected after 1 h of ageing at 800 °C. The σ phase is rather expected after 10 h of ageing at 800 °C. Besides, the χ phase was identified in the studied material for other ageing conditions, as presented later in Figure 5.17. Thermodynamic simulations also indicated that Laves η phase can be theoretically stable at temperatures close to 800 °C (Figure 3.1), but it has Cr content close to that of the matrix. Bright precipitates could also be identified as the R phase, often reported in the literature [63], which was also identified from the decomposition of the residual ferrite of the studied steel as presented later (Figure 3.11). The χ and R phases thus appeared to be the two most probable phases, but no actual crystallographic

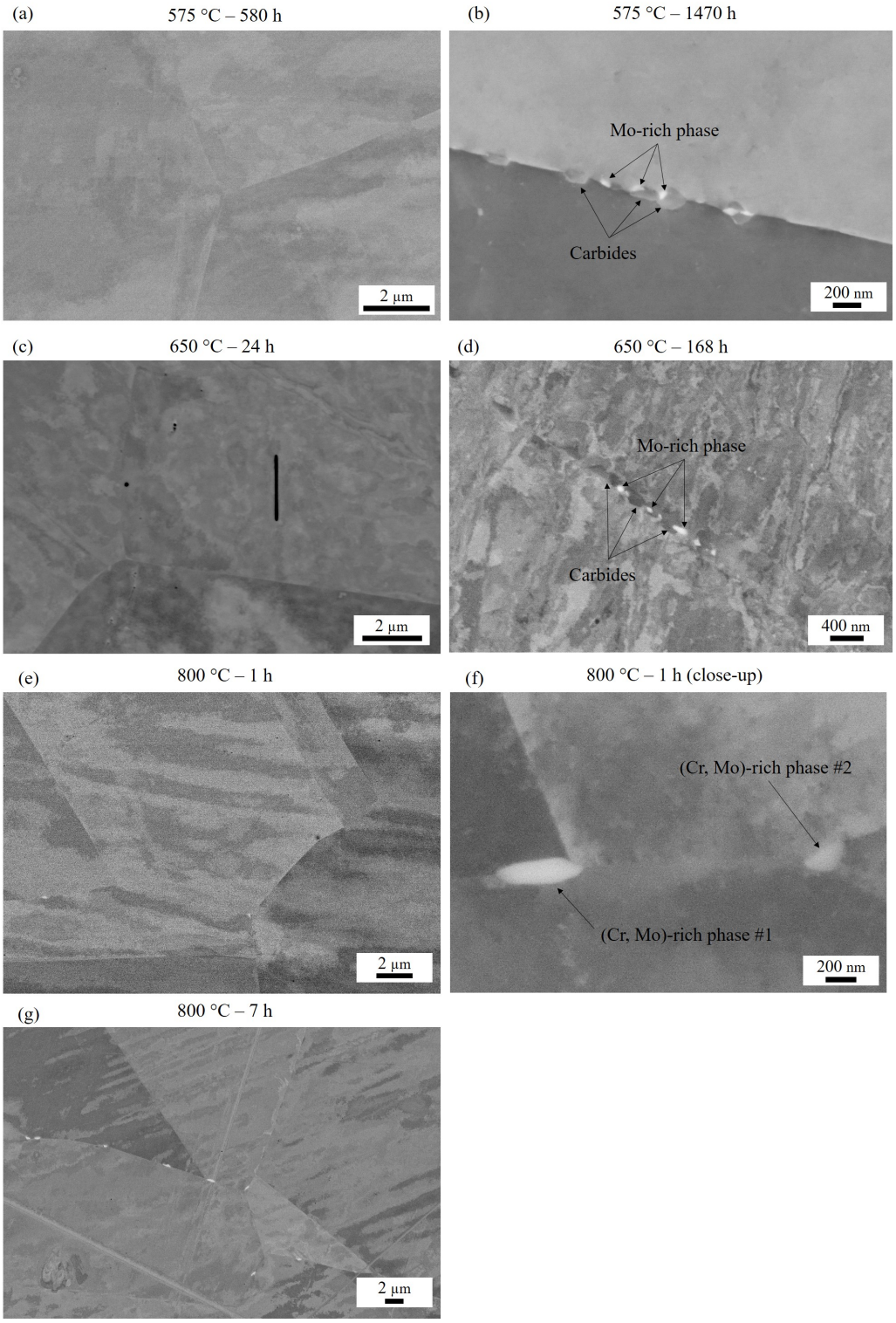

Figure 3.6: SEM-BSE images of precipitates at austenite grain boundaries after (a) 580 h and (b) 1470 h at 575 °C, (c) 24 and (d) 168 h at 650 °C, (e) and (f) 1 h and (g) 7 h at 800 °C.

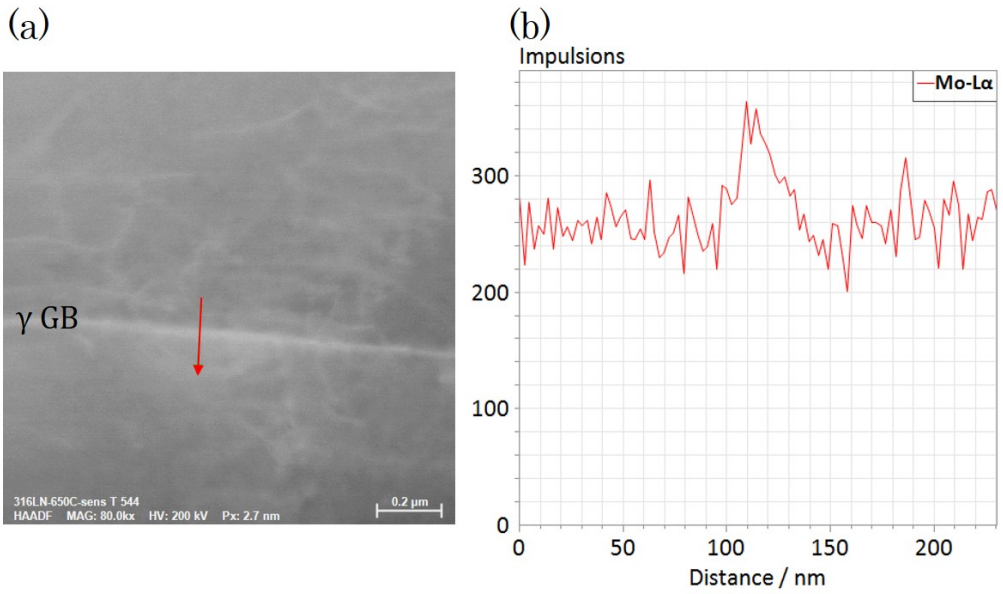

Figure 3.7: Local Mo enrichment at austenite (γ) grain boundary after thermal ageing of 24 h at 650 °C with (a) scanning TEM-HAADF (High-Angle Annular Dark- Field) image and (b) corresponding element profile along the red line, indicating Mo maximum at GB area.

Table 3.4: Average chemical composition (from 3 measures) of the $Cr_{23}C_6$ precipitates identified in the 316L(N) steel after thermal heat treatment of the samples in as-received state at 650 °C for 168 h. Elements content was measured using EDS in TEM.

Element	Fe	Cr	C	Ni	Mo
[%wt]	20.09	47.55	24.13	3.34	4.89
[%at]	24.48	54.46	6.43	4.28	10.36

analysis could confirm this statement. After ageing of 7 h at 800 °C, the same phases as after 1 h were observed but in higher number per grain boundary (Figure 3.6 (g)).

It is worth noting that no precipitate was observed in the bulk of austenite grains for any of the ageing conditions.

Ferrite decomposition

Ferrite in the studied steel was present in the form of residual δ-ferrite dispersed in the austenite matrix (Figure 3.2), but ferrite can also form in the fusion zone during the welding [198], as it will be presented further (Section 3.5). Transformation of ferrite as function of time and temperature was thus investigated.

After 24 h of ageing at 550 °C, the δ-ferrite bands did not show any difference with the as-received state (Figure 3.10 (a)). At 575 °C after 580 h, δ-ferrite was observed to be partially decomposed into several precipitates: small Mo-rich precipitates in the ferrite grains, C/Cr-rich larger precipitates in the ferrite grains as well and finally a very thin Mo-rich layer at the ferrite-austenite interface (Figure 3.10 (b)). This layer is believed to be at the origin of Mo-rich precipitates observed for longer ageing times. From the TEM-diffraction analyses carried out in a sample aged at 650 °C for 24 h (presented further), the observed Mo-rich precipitates were assumed to be of the χ and R phase, C/Cr-rich precipitates to be $M_{23}C_6$ carbides. After 1470 h at 575 °C, the ferrite bands were much more decomposed, showing higher fraction of the same phases with distinct

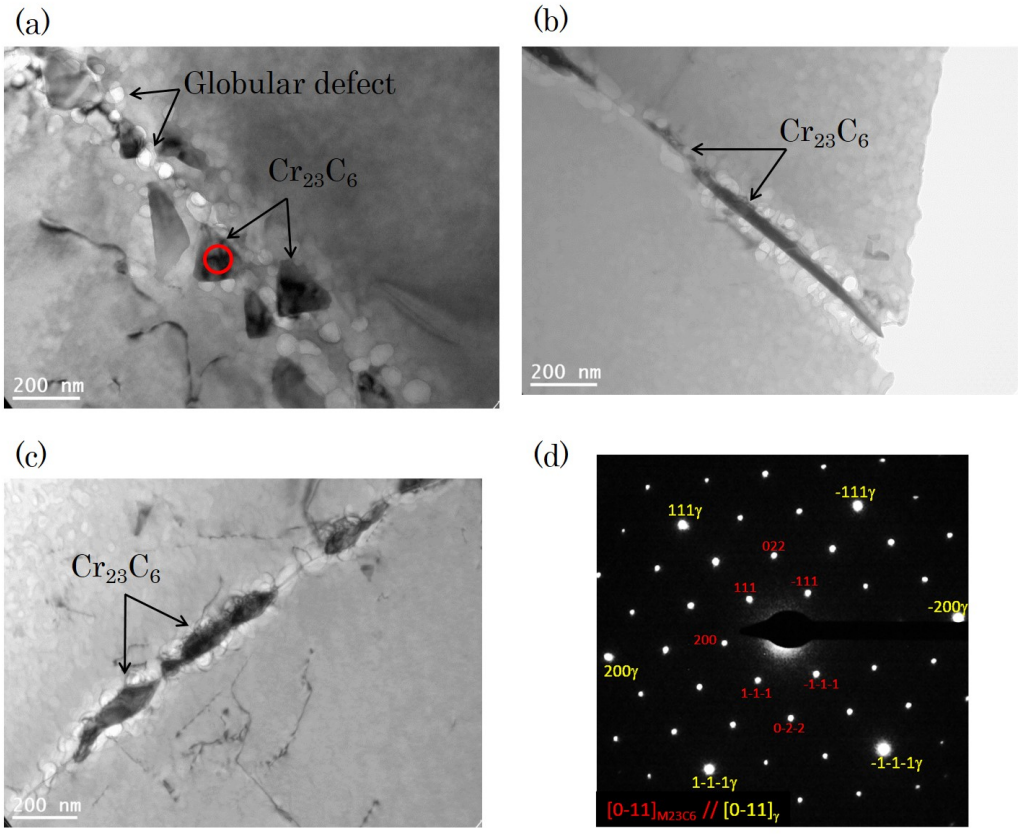

Figure 3.8: Analysis of $Cr_{23}C_6$ precipitates at austenite GBs after thermal ageing at 650 °C for 168 h with (a), (b) and (c) TEM bright-field images showing triangular, platelet and quasi-hexagonal morphology respectively, (d) selected area electron diffraction pattern of the precipitate indicated in (a) by red circle, revealing the $Cr_{23}C_6$ phase (red coordinates) and austenite matrix (yellow coordinates).

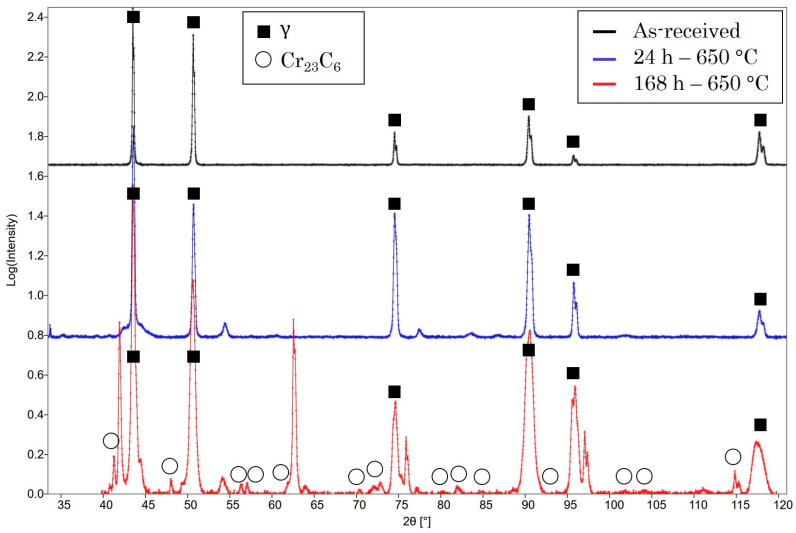

Figure 3.9: XRD analysis of 316L(N) steel in the as-received state and in as-received state aged at 650 °C for 24 and 168 h.

Mo-rich precipitates at the austenite-ferrite interface (Figure 3.10 (c)).

At 650 °C after 1 h of ageing, only small Mo-rich precipitates were observed in the ferrite grains and thin layer at the austenite-ferrite interface (Figure 3.10 (d)). After 24 h, large C/Cr-rich precipitates were observed (Figure 3.10 (e)) additionally to the Mo-rich precipitates. After 168 h at 650 °C, C/Cr-rich precipitates appeared to be progressively replaced by larger precipitates with brighter contrast as observed using BSE detector in SEM. EDS analyses showed higher content in Fe, lower in Cr, similar in Mo as compared to carbides but more importantly, the absence of C. From the computed chemical compositions of predicted stable phase (Figure 3.2), such precipitate could correspond to the σ phase. Indeed, σ phase is often described in the literature to form after carbides precipitation in decomposing δ-ferrite of 316L(N) steels [63, 67]. Besides, σ phase was identified after the partial decomposition of vermicular ferrite in welded material as discussed further (Figure 5.28).

A detailed analysis of the nature of phases resulting from the ferrite decomposition was performed using TEM for a sample aged at 650 °C during 24 h. This condition was chosen as it corresponded to a sufficiently advanced state of the decomposition of the ferrite grains, presenting most of the phases observed in the other ageing conditions. Because of the low fraction of ferrite in the as-received state ($< 1\%$vol.), machining of TEM sample had to be performed via Focus Ion Beam (FIB) technique, as described in Section 2.2.4. Scanning TEM-HAADF analysis of the partially decomposed δ-ferrite region revealed a complex microstructure (Figure 3.11) composed of the ferrite phase, one phase rich in Cr and C, one phase rich in Ni and one (or more) phase rich in Mo. Electron diffraction of these precipitates allowed the identification of the phases, shown in Figure 3.12. The ferrite was identified with a lattice parameter of $a = 2.87$ Å. Cr and C rich phase was identified as $Cr_{23}C_6$ carbide, with a lattice parameter of $a = 10.66$ Å, similarly to GB precipitates discussed previously. Small Mo-rich precipitates were identified as BCC χ phase, with a lattice parameter of $a = 8.92$ Å, and as an hexagonal R phase with lattice parameters of $a = 10.90$ Å and $c = 19.34$ Å. Finally, the Ni-rich phase was identified as regenerated austenite, γ_R, with a lattice parameter of $a = 3.60$ Å, similarly to the austenitic matrix. Chemical composition and crystalline structure of these phases are summarized in Table 3.5. It should be noted that while χ and R phases are different in terms of crystalline structure, their chemical compositions made it difficult to distinguish them from EDS analysis only. For this reason, small Mo-rich precipitates in ferrite will named as such the rest of this work, similarly to precipitates observed at austenite GBs.

After 1 h of ageing at 800 °C, most of ferrite grains were partially transformed into several Mo-rich phases, one Cr/C rich phase, one Cr/Mo rich phase and a Ni rich phase (Figure 3.10 (g)). From the identifications made previously in the sample aged at 650 °C for 24 h, Mo-rich phases were assumed to be χ and/or R phases, and the Cr/C rich phase to be $Cr_{23}C_6$ carbide. The Ni-rich phase was assumed to correspond to regenerated austenite γ_R. Finally, the Cr and Mo rich phase could correspond to the σ-phase, as discussed previously for ageing at lower temperature. It is worth noting that the distribution and apparent volume fraction of each of these phases in the ferrite grains was not equal in the whole sample: this is illustrated in Figures 3.10 (g), (h) and (i) where BSE contrast reveal very different microstructures between the three ferrite grains.

The nature of the different phases in residual ferrite observed after ageing is in agreement with results of Rhouma *et al.* [63] for decomposed residual ferrite in a 316L(N) steel. However, time to precipitation was different. Indeed, Rhouma *et al.* [63] observed χ, σ and R phases after 10 000 h of ageing at 650 °C, whereas in this work they were observed after only 24 h at 650 °C, and after 168 h for the σ phase. This difference could come from a difference in the composition of the residual ferrite (not disclosed by Rhouma *et al.* [63]), but also from the austenitization process: Rhouma *et al.* carried out two treatment of

Table 3.5: Composition in %at. of phases identified from the partial ferrite decomposition after ageing of the as-received state of the studied 316L(N) steel at 650 °C for 24 h, measured by TEM-EDS. Crystalline structure and corresponding lattice parameters of each phase are also indicated.

Phase	Cr	C	Ni	Mo		Structure	a [Å]	c [Å]
δ-ferrite	24.6	5.5	2.7	1.5		BCC	2.87	-
$Cr_{23}C_6$	58.1	20.9	1.6	3.9		FCC	10.66	-
R	25.9	6.4	3.3	20.7		Hexagonal	10.9	19.34
χ	28.8	8	2.4	20.3		BCC	8.92	-
Austenite	17.1	6.9	10.8	1.2		FCC	3.6	-

1 h at 1070 °C, while in this work the steel was treated at 1100 °C for 35 min. Still, the significant differences in precipitation kinetics are surprising.

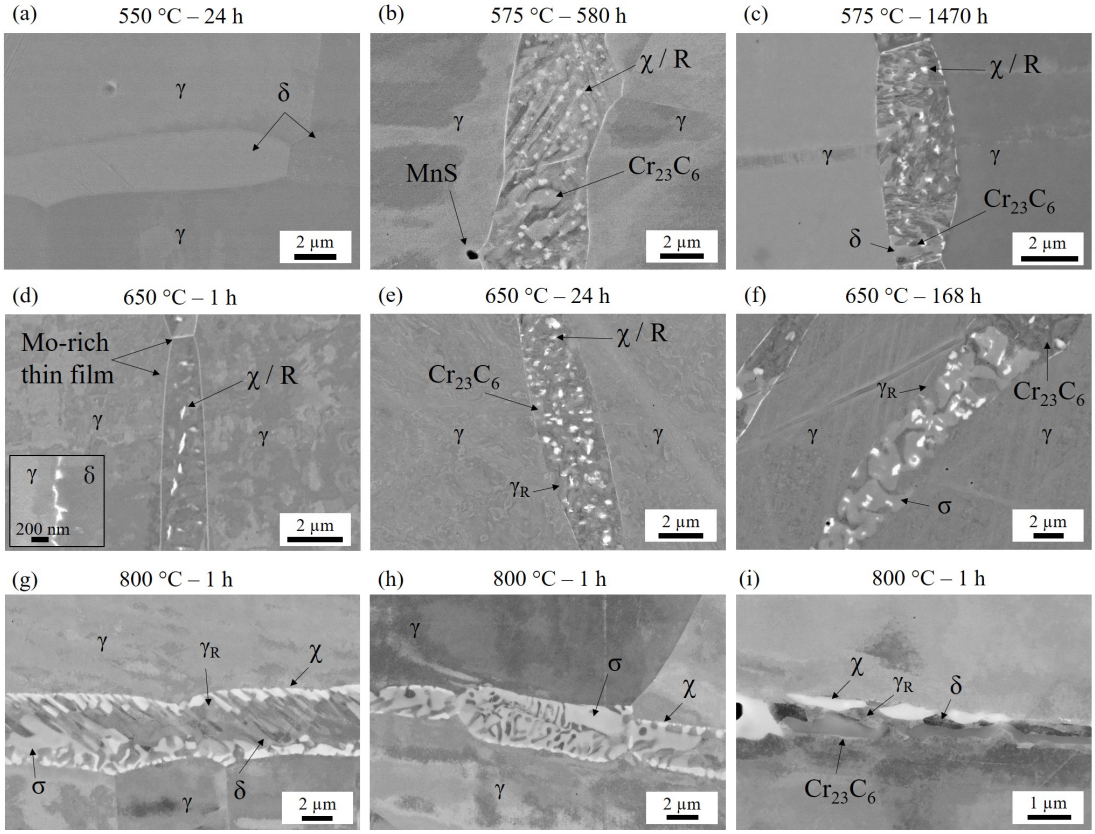

Figure 3.10: Microstructure of residual δ-ferrite grains after ageing for (a) 24 h at 550 °C, (b) 580 and (c) 1470 h at 575 °C, (d) 1 and (e) 20 and (f) 168 h at 650 °C and (g) to (i) 1 h at 800 °C (SEM-BSE).

The effect of thermal exposure on precipitation at austenite GBs as well as inside ferrite regions is summarised in time temperature precipitation diagram shown in Figure 3.13 (a). It is worth noting that $Cr_{23}C_6$ precipitation was significantly slower, as compared to the results found in the literature [67]. This could be due to the particularly low content in carbon of the studied 316L(N) steel. For ferrite, almost all conditions used for thermal ageing led to its decomposition (Figure 3.13 (b)).

Time to precipitation of secondary phase identified for the as-received material can already give some insight about the risk of stress relaxation damage. Indeed, it was shown

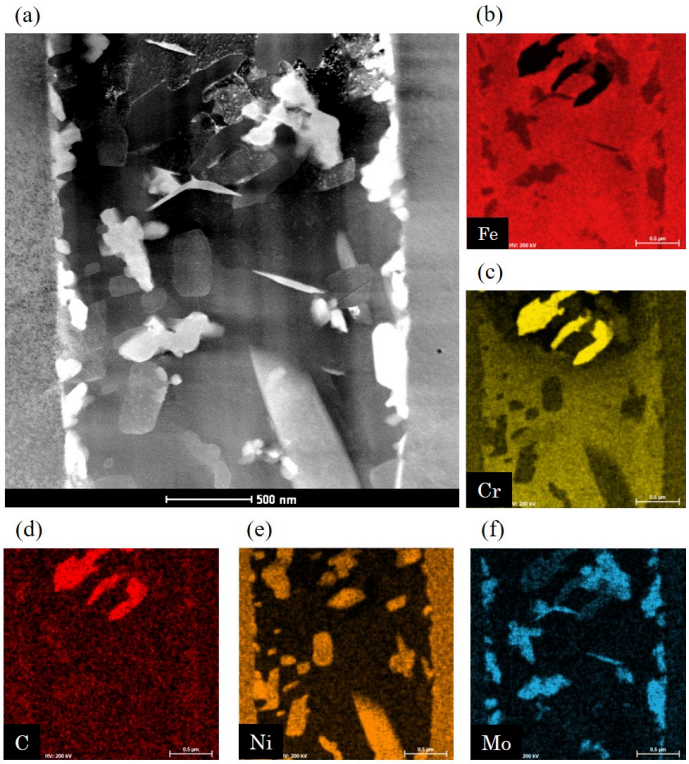

Figure 3.11: Element analysis of partially decomposed ferrite using TEM after ageing of as-received state of the studied 316L(N) steel for 24 h at 650 °C: (a) STEM-HAADF image and EDS maps of (b) Fe, (c) Cr, (d) C, (e) Ni and (f) Mo.

in the literature [45] that SRC occurs first by the nucleation of cavities on GB precipitates. As a result, SRC is limited by the time to precipitation of these phases. In the studied case, this means cavity nucleation upon stress relaxation in an as-received state can nucleate on austenite GBs only after 1470 h of ageing at 575 °C, 168 h at 650 °C and after 1 h (or earlier) at 800 °C (Figure 3.13 (a)). In ferrite regions, cavities can be expected earlier: after 580 h at 575 °C, 1 h at 650 °C and 1 h (or earlier) at 800 °C (Figure 3.13 (b)).

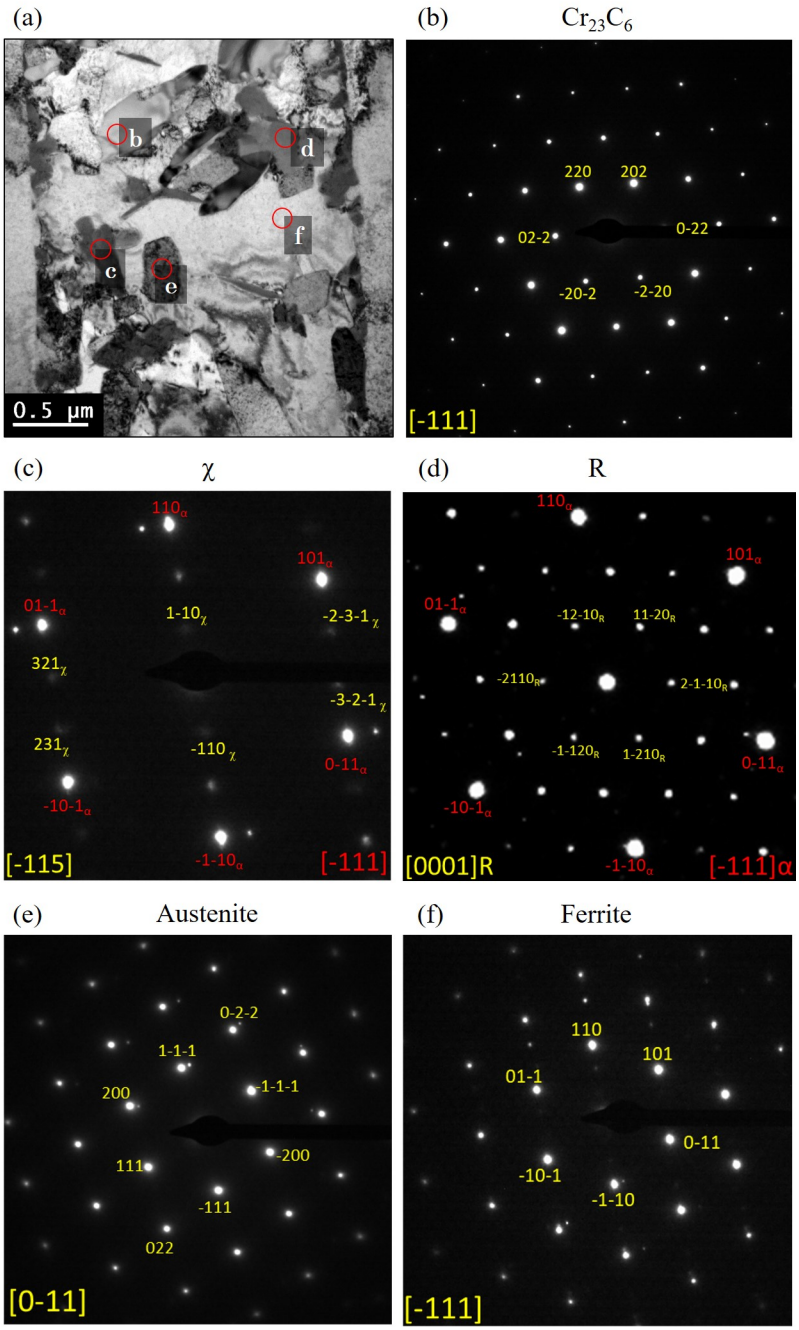

Figure 3.12: Identification of phases issued from residual ferrite decomposition after ageing at 650 °C for 24 h with (a) TEM bright field of a ferrite grain and diffraction patterns of (b) diffraction pattern of $Cr_{23}C_6$, (c) χ phase, (d) R phase, (e) regenerated austenite γ_R and (f) ferrite.

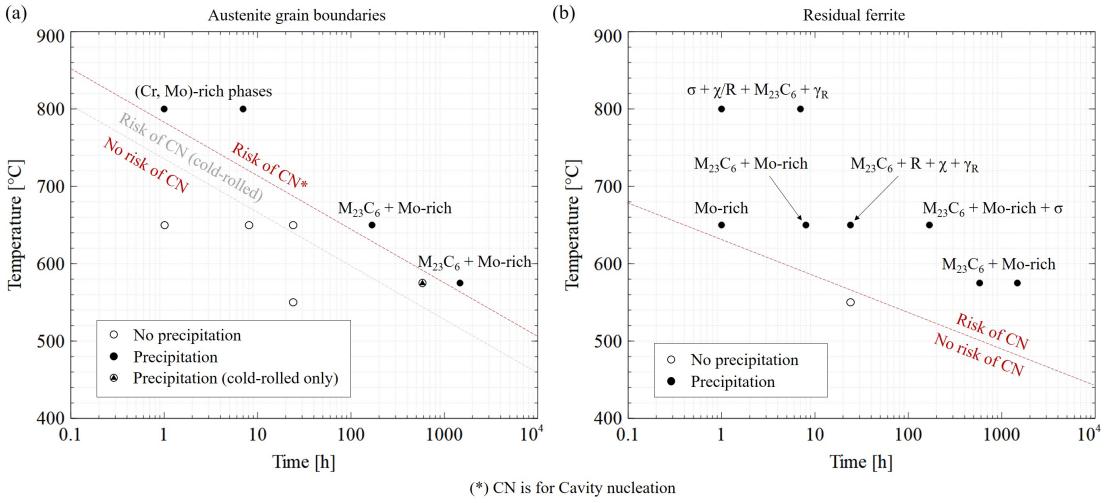

Figure 3.13: Time temperature precipitation diagram for the as-received and cold-rolled states of the studied 316L(N) steel with expected risk of cavity nucleation upon by stress relaxation: (a) at austenite grain boundaries and (b) in the residual ferrite.

3.4 Cold-rolled

Cold-rolled material was produced to evaluate the influence of pre-straining on stress relaxation cracking comparing the results with damage in the as-received material. Additionally, this approach would allow to directly compare the results with SRC analyses carried out by Pommier [45], who used CT-like specimens made of a 20±2% cold-rolled 316L(N) steel of very similar composition to the one studied in this work. In addition, the effect of prior strain on the microstructure, such as time to precipitation, could be investigated here.

The as-received 316L(N) steel was cold-rolled at room temperature, using successive passes to reach a 22.5% reduction in thickness, corresponding to a final thickness of 11.9 mm. After the cold-rolling, the microstructure analysis revealed, in some of the grains, features resembling mechanical twins (Figure 3.14) which were not observed in as-received state. Twin traces with similar aspects were observed by Astafurova *et al.* [199] after cold-rolling of austenitic steels. Although mechanical twins are not so common in 316L(N) steels, they can be observed after high straining at low temperatures, as shown by Pommier in a 20% cold-rolled steel of very similar composition to the one studied in this work [45].

The presence of these mechanical twins was confirmed by EBSD analyses, showing thin bands (around 1 μm thick) in some of the grains (Figure 3.15 (b)). These were revealed by boundary map of $\Sigma 3$ GBs, showing boundaries with a 60° misorientation with respect to the grain (Figure 3.15 (c)). Additionally, local lattice rotations were observed in some of the grains as illustrated in Figure 3.15 (b), due to the high straining. Such internal misorientation were mostly observed near GBs and could traduce an accumulation of dislocations in this region. The profile in Figure 3.15 (d) typically show disorientation angles up to 7° from one point to another within the grain.

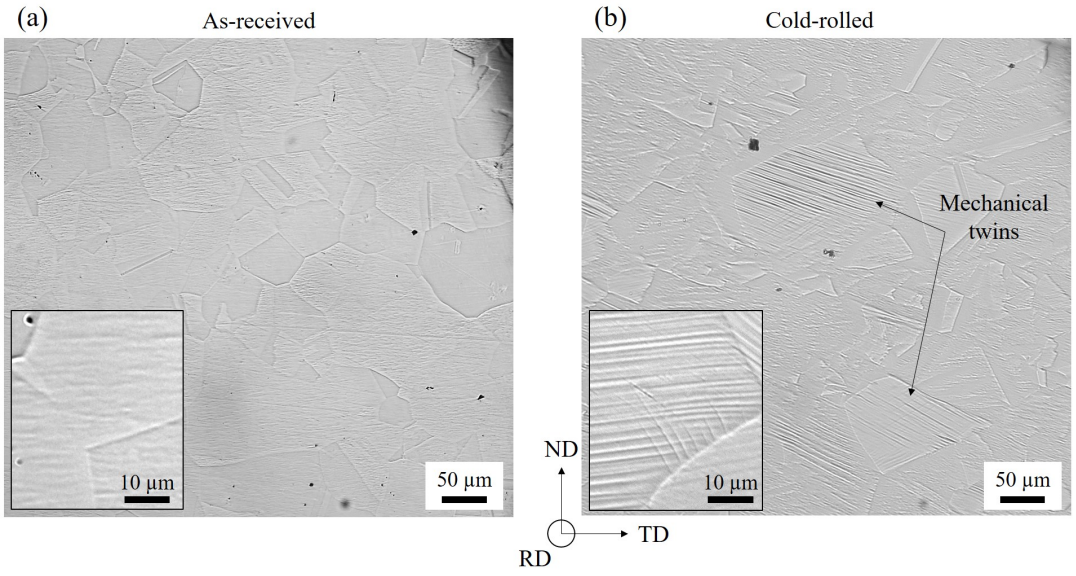

Figure 3.14: Microstructure observation using optical microscopy for (a) as-received and (b) cold-rolled states of studied 316L(N) steel. Mechanical twins resulting from cold-rolling can be observed. TD, ND and RD stand for transverse, normal and (cold) rolling directions, respectively.

Similarly to samples made of as-received state, those of cold-rolled state were exposed to temperature ageing at 575 °C for 580 and 1470 h to induce microstructure modifications which might be further observed after welding and relaxation. Because composition of

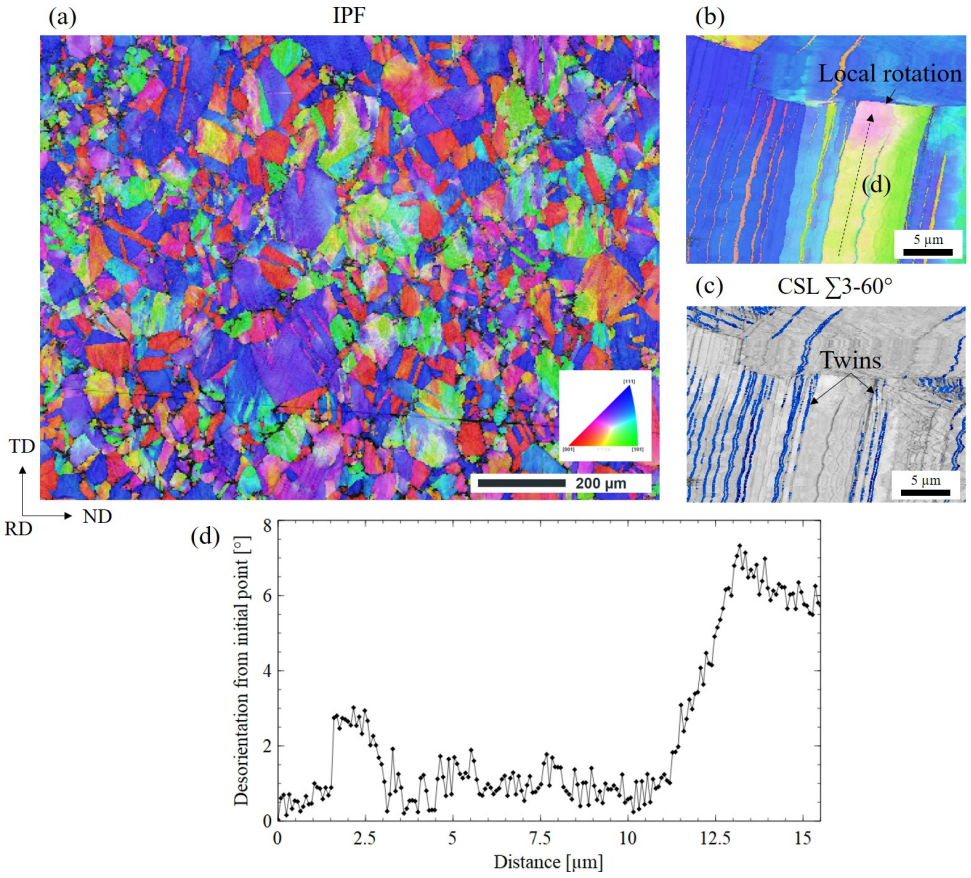

Figure 3.15: Grain structure of the cold-rolled state analysed using EBSD : (a) IPF map (b) local IPF map showing mechanical twins and local crystal rotation in grains, (c) boundary map for Σ3 GBs and (d) disorientation angle from initial point along the profile shown in (b).

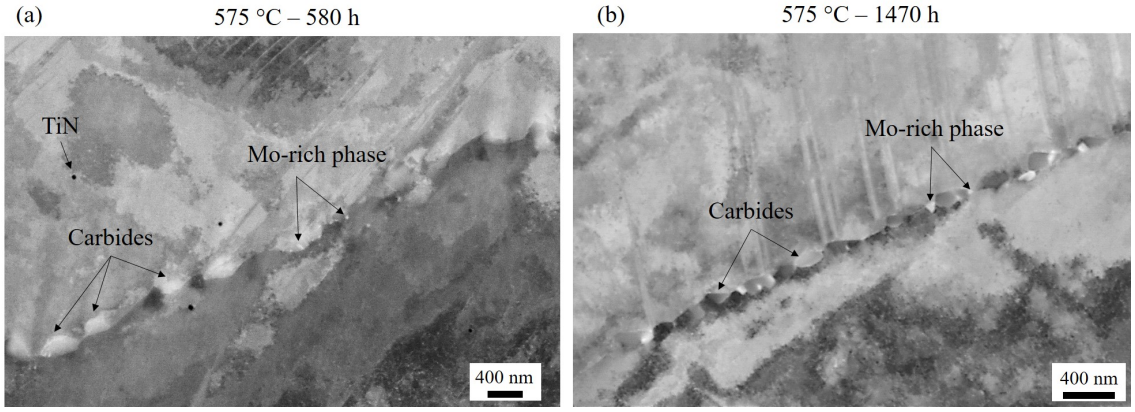

Figure 3.16: SEM-BSE images of precipitates at austenite grain boundaries in the cold-rolled material after ageing at 575 °C for (a) 580 h and (b) 1470 h.

the cold-rolled material was the same as of as-received material, the stable phases were assumed to be the same as identified earlier. Cold-rolled material was thus only aged at the temperature and duration used further for relaxation.

In samples made of cold-rolled state, SEM analyses revealed the presence of GB precipitates as early as 580 h of ageing (Figure 3.16 (a)), assumed to be carbides due to their high content in Cr, C and Mo. Additionally, Mo-rich precipitates were again observed near carbides. After 1470 h, the same precipitates were observed (Figure 3.16 (b)) at austenite grain boundaries, with slightly larger and more numerous Mo-rich precipitates. This is in agreement with results reported by Weiss *et al.* [67], who reported a quicker carbide precipitation in a cold-rolled 316L steel as compared to the annealed state. The authors explained this effect by an increase in nucleation sites (dislocations and faults) and by an increased diffusion rate in the matrix due to the high dislocation density.

To evaluate strain hardening induced by cold-rolling, hardness was measured across the thickness of the cold-rolled plate. An average hardness of 294 HV1 was measured, corresponding to a significant increase as compared to the average 155 HV1 obtained for the as-received state. The hardness profile suggested straining was mostly homogeneous across the thickness Z, with slightly higher values towards the plate surface as shown in Figure 3.17. The lowest point, near Z = 2 mm, is believed to be a measurement error. Variations of hardness throughout the thickness were not taken into account since damage analyses of CT-like specimens machined from cold-rolled material and further used for SRC testing were performed at mid-thickness only.

Similarly to the as-received material, GOS and KAM maps were computed from EBSD analysis of the cold-rolled material (Figure 3.18). In contrast with the as-received material, many grains of the cold-rolled material showed significant GOS and KAM values, suggesting the presence of high dislocation densities in agreement with hardness measurements. It is worth noting that the apparent strain was not homogeneous throughout the microstructure, with some highly strained grains and some grains with no apparent strain as illustrated with the GOS distribution in Figure 3.18 (b). This is probably due to differences of grain orientations relatively to the straining (cold-rolling) direction, which can be more or less favorable to plastic strain.

The characterization of the cold-rolled state showed that the initial hardening of the material was higher than in the as-received state, as intended. This is expected to induce higher susceptibility to stress relaxation cracking, as reported by the literature [18]. Additionally, the prior straining of the material induces the nucleation of mechanical twins and the formation of local rotation within grains, which can both lead to higher local stresses

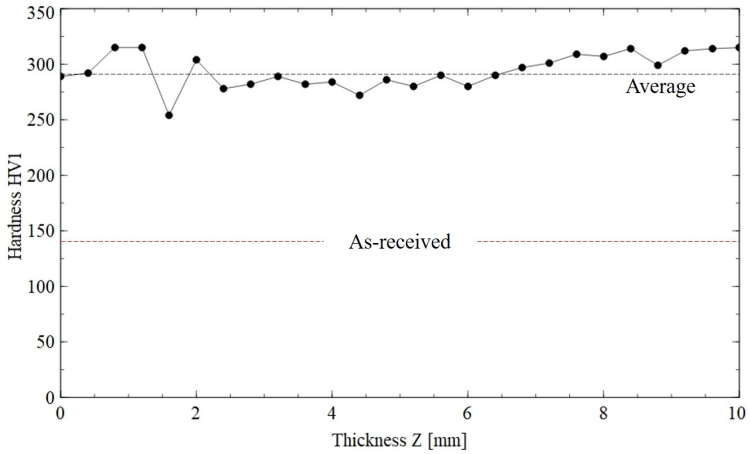

Figure 3.17: HV1 hardness profile of the cold-rolled plate across the thickness (Z) compared to the average hardness measured for as-received state.

and thus favor cavity nucleation. Besides, time to precipitation in cold-rolled state was lower than in the as-received state for the same ageing conditions, meaning that cavity nucleation can be expected earlier. Overall, the pre-straining of the material is expected to be detrimental to the material resistance to SRC.

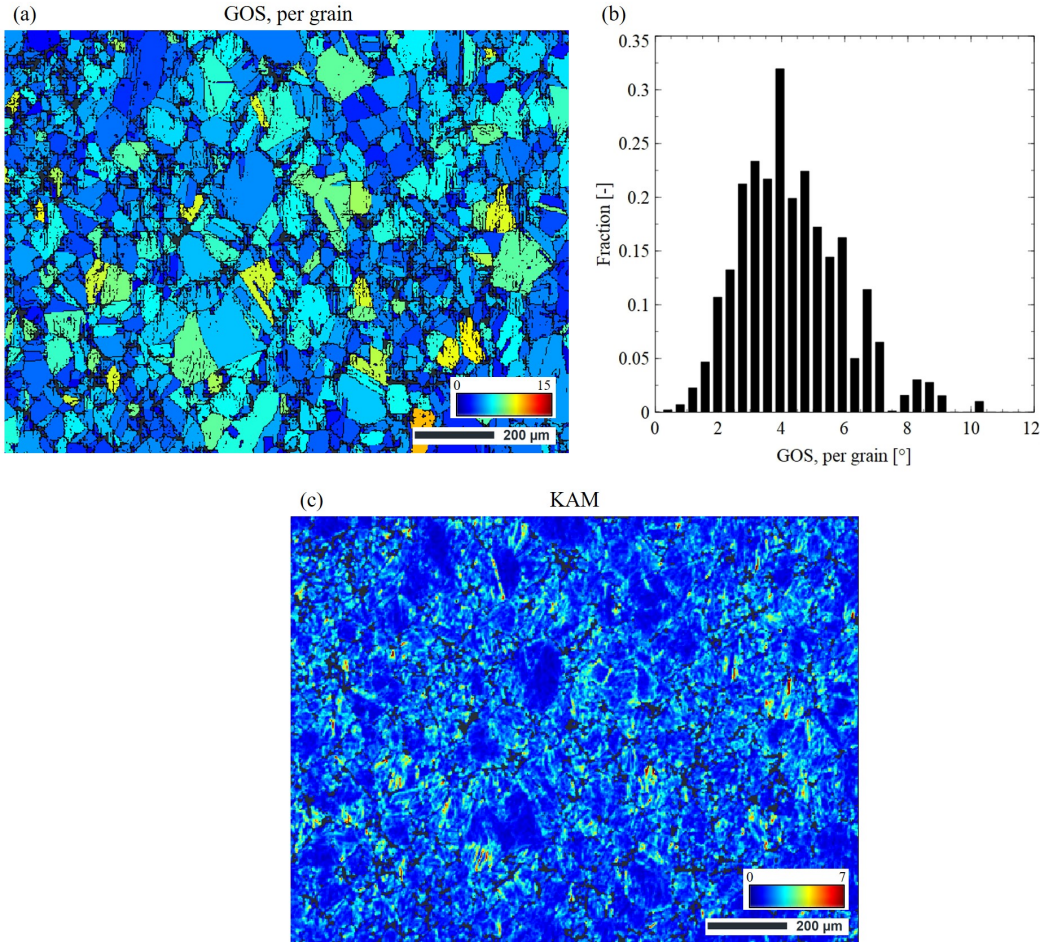

Figure 3.18: Strain state of the cold-rolled material with (a) GOS per grain map, (b) distribution of GOS per grain and (c) KAM map of the region shown in Figure 3.15.

3.5 Single-pass weld

Welded materials, either single or multi-pass, constituted the most important states of this study. These allowed obtaining heterogeneous microstructure representative of industrial weld components and thus would allow investigating the effect of a heterogeneous microstructure on SRC. A first welded state, single-pass welded, was produced as the simplest case for welded material.

Different welding conditions were tested in this work (Table 2.2). Micrographs of cross-sections of the welded plates and dimensions of the weld pools for each condition are shown in Appendix B. As discussed in Section 2.1, welding using 100% Ar gas was chosen for the rest of the study. Microstructure characterizations were thus only focused on this welding condition. Optical micrograph obtained in the cross-section of the welded sample and SEM images of the main weld regions are shown in Figure 3.19. EBSD analyses (Figure 3.20) allowed characterizing the microstructure and estimating the strain state after welding. Based on these observations, three distinct zones could be distinguished according to the grain morphology and size:

(i) The fusion zone (FZ), where temperature during welding was higher than the steel melting temperature (T > 1400 °C). In this region, the austenitic grain morphology varied from columnar at the bottom of the FZ to mostly equiaxed near the surface of the plate (Figure 3.20 (c)). Grains were much larger than the ones observed in as-received state, with an average size of 310 μm (not accounting for twin boundaries). The largest grains were the columnar ones at the bottom of FZ, with an average size of 400 μm while equiaxed grains at the top of the FZ presented an average size of 160 μm. The high temperatures also allowed the formation of vermicular ferrite at the austenite grain boundaries and within austenite grains, with both vermicular (Figure 3.19 (d)) and lacy (Figure 3.19 (e)) structures. Such ferrite cells structures are commonly observed in weld microstructure of austenitic stainless steels [198].

(ii) The Coarse Grain Heat Affected Zone (CGHAZ) was observed just below the FZ, forming a semi-circular band along the bottom of the FZ, being 1 mm thick at maximum at the welding centreline (Figure 3.20 (c)). In this zone, temperatures during welding were high enough (between 1000 and 1400 °C) to induce austenite grain growth without melting [200]. Austenite grains in this region measured an average of 330 μm, with a few intergranular vermicular ferrite cells observed near the FZ/CGHAZ boundary. Residual ferrite islands in this region were mostly decomposed into several secondary phases rich in Cr and Mo.

(iii) Finally, the Heat Affected Zone (HAZ) was observed below the CGHAZ (Figure 3.20 (c)). This region was exposed to lower temperatures than the CGHAZ during welding, between 600 and 1100 °C, which does not allow grain growth for the short welding process duration (less than a minute). Therefore, the microstructure in HAZ was very similar to the one observed for the as-received material.

Additional characterisations were carried out using SEM, EBSD and EDS to characterize local GB features for each of the weld zones, revealing differences in GB properties between the three regions. Figure 3.21 (a) shows GB misorientation angles comprised between 25 and 55°, which are most susceptible to SRC as discussed later in Section 6.2. The number and total length of GBs was lower in the CGHAZ because of the higher average grain size than that of the HAZ. Besides, the absence of vermicular ferrite in the CGHAZ, which was observed in the FZ, also resulted in lower total length (Figure 3.21 (b)) and lower fraction of boundaries with misorientation angle comprised between 25 and 55° (Figure 3.21 (c)) as compared to the other two zones.

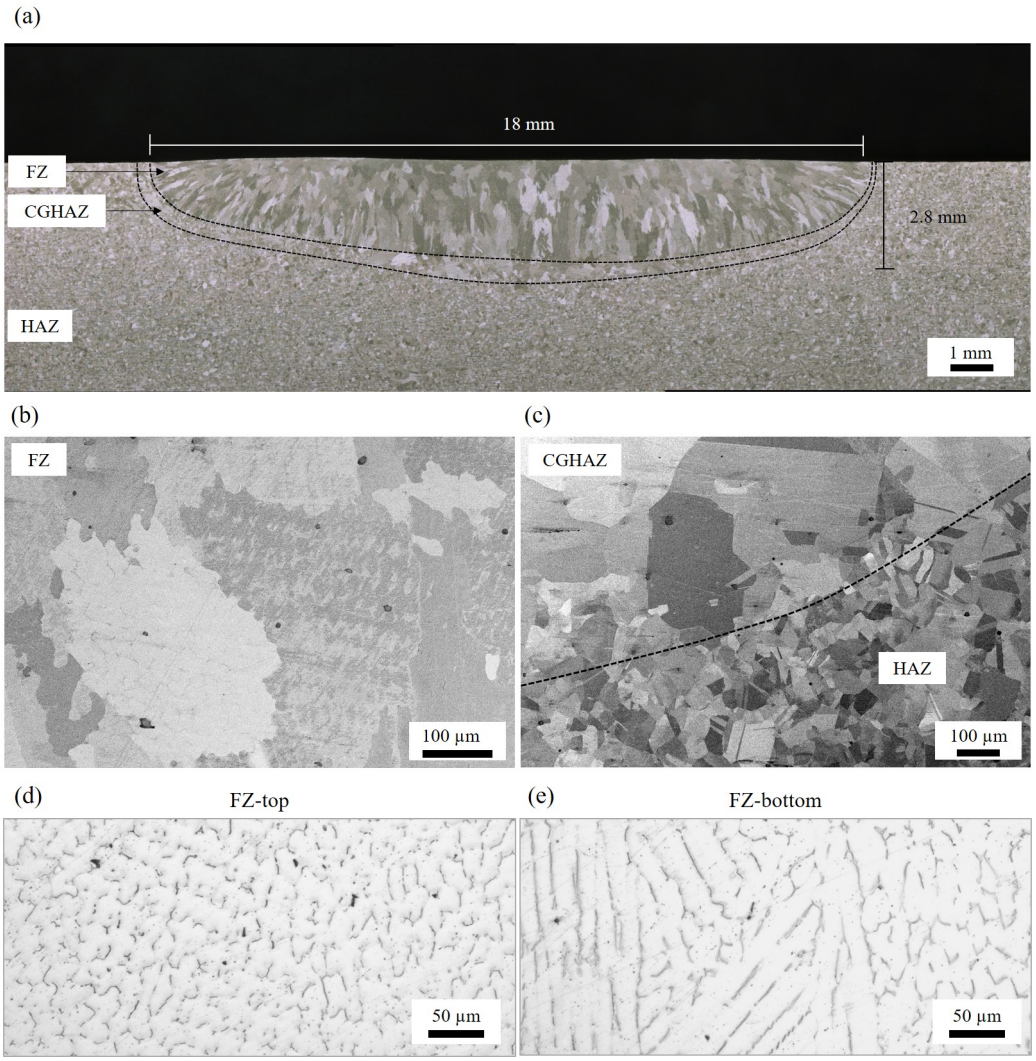

Figure 3.19: Microstructure of a single-pass welded state with (a) optical observation of etched weld pool (FZ), CGHAZ and HAZ, (b) and (c) SEM images showing the FZ, CGHAZ and HAZ and (d) and (e) ferrite cells at the top and bottom of the FZ, respectively

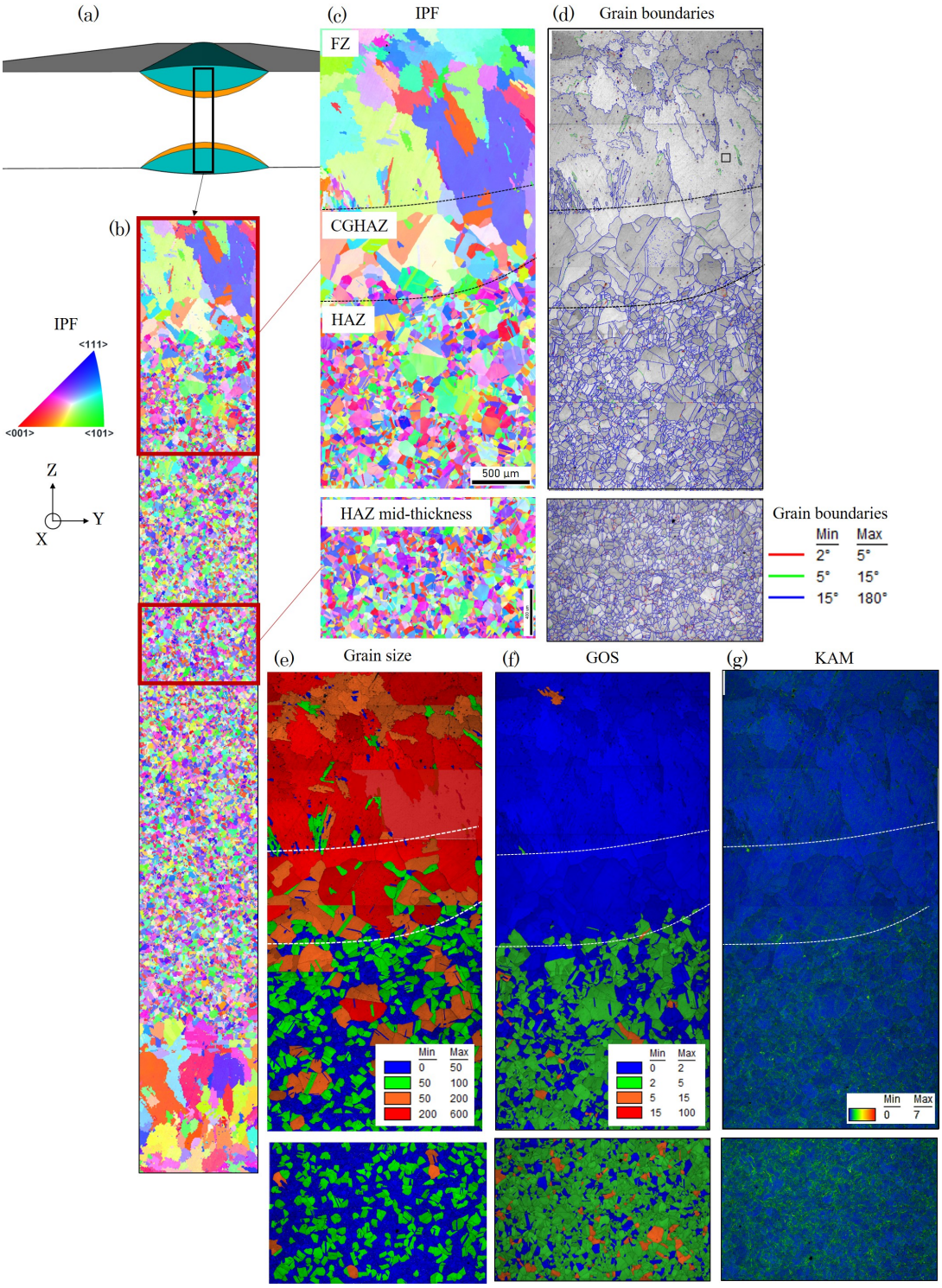

Figure 3.20: Microstructure of studied 316L(N) steel after welding: (a) schematized view of the welded plate zone analysed by EBSD, (b) IPF of the whole cross section, (c) Close-up IPF, (d) IQ and GB maps, (e) grain size map, (f) GOS map and (g) KAM map of the FZ, the CGHAZ, the HAZ and mid-thickness HAZ. Analysis was performed with acquisition step of 3 μm.

These analyses did not reveal any austenite GB carbide in any of the weld zones, which is consistent with common observations for low carbons steels [78] and particularly with results found by Weiss *et al.* [67] for a 316L(N) steel with a similar chemical composition. According to the microstructure characterisation after thermal exposure of as-received state (Section 3.3), carbide precipitation at austenitic GBs requires a minimum exposure time at high temperature (168 h at 650 °C), which is not allowed by the welding process. However, a few precipitates were observed at some austenite/ferrite interfaces (Figures 3.22 (a) and (b)). They were only observed within a distance from 3.0 to 8.2 mm relative to the weld pool, corresponding exclusively to the HAZ. EDS maps shown in Figure 3.22 (c) revealed that these precipitates had a higher Mo content than both ferrite and austenite phases, while the Fe content was lower. According to computed compositions of secondary phases discussed previously (Table 3.2), these precipitates could correspond either to the Laves η or R phases. These precipitates presented mostly a globular/diamond morphology (Figure 3.22 (a)) with a mean size of 315 nm, and more rarely a more elongated morphology (Figure 3.22 (b)).

Regarding the risk of SRC, stress relaxation cavity could be expected to nucleate earlier at the austenite/residual ferrite interfaces in the HAZ because of the GB precipitates.

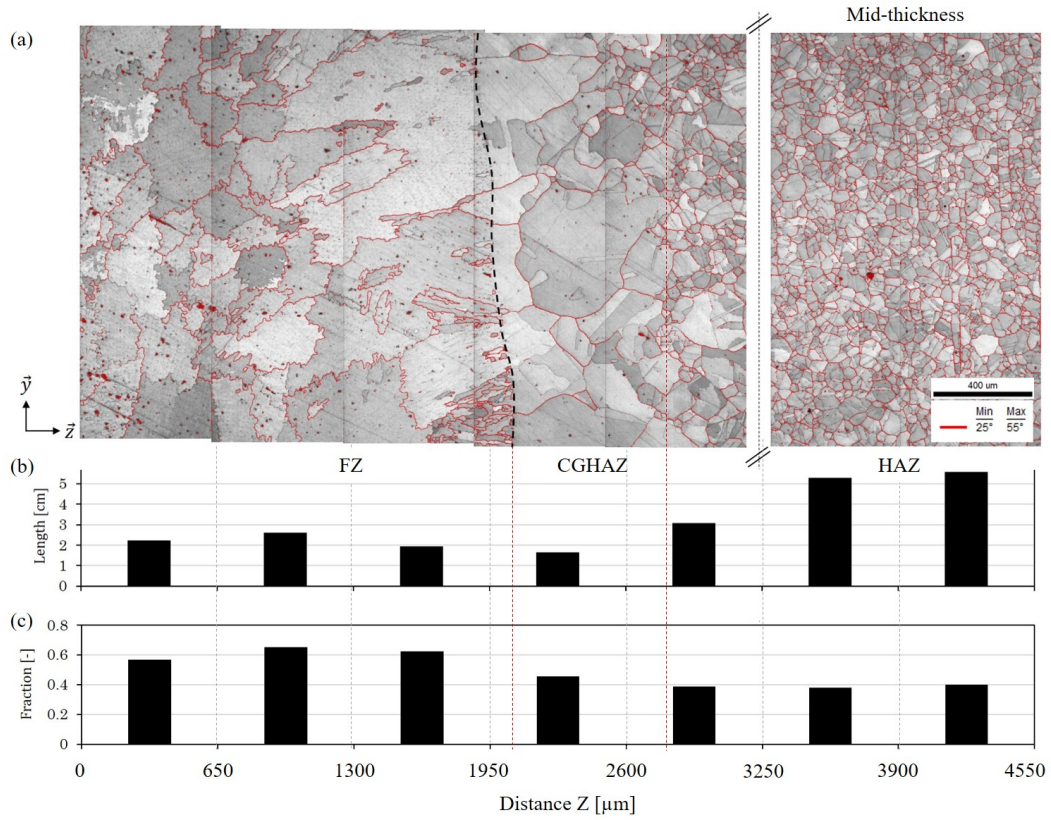

Figure 3.21: Austenite GB misorientation angle and length across the microstructure in single-pass welded state of 316L(N) steel: (a) GBs (in red) with misorientation angle between 25 and 55° over the quality index map. (b) Total GB length fraction and (c) GB fraction with misorientation angle between 25 and 55°.

3.5.1 Strain state

The strain state of each weld zone was evaluated using HV1 and HV5 hardness measurements but also from EBSD data. Hardness maps are shown in Figure 3.23 and a hardness

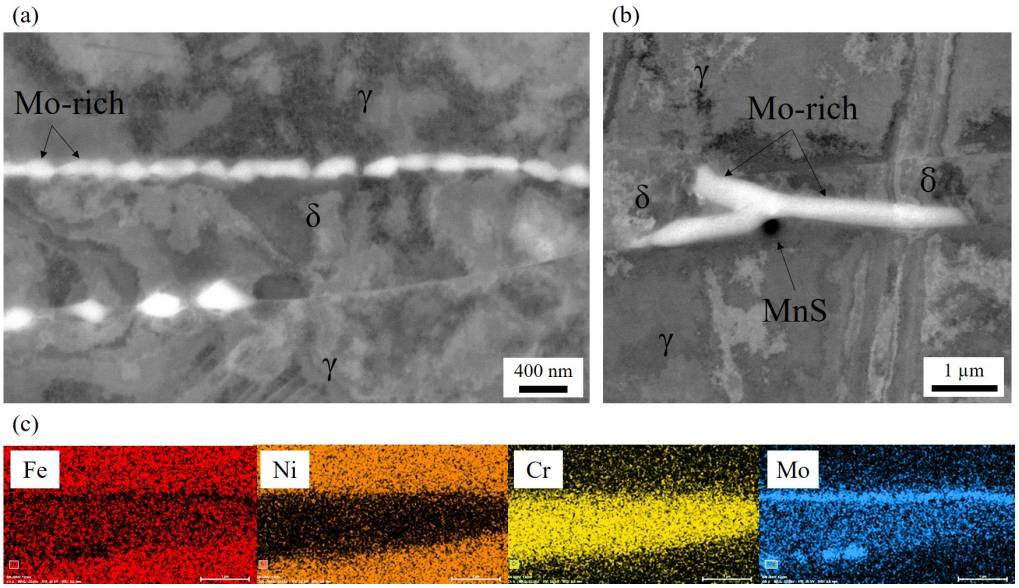

Figure 3.22: Residual δ-ferrite bands with Mo-rich precipitates (bright contrast) observed in HAZ at the austenite/ferrite interface with a (a) diamond and (b) elongated morphologies and (c) EDS maps of major elements in (a): Fe, Ni, Cr and Mo.

profile crossing the three weld zones is shown in Figure 3.31. Hardness values in the FZ, between 137 and 163 HV1 (Figure 3.31), were comparable to that of the as-received material (155 HV1). Moreover, in this zone no significant strain was observed, as suggested by the GOS and KAM maps shown in Figures 3.20 (f) and (g), respectively.

In the CGHAZ, GOS and KAM maps (Figures 3.20 (f) and (g)) showed very similar values to those obtained for the as-received state and the FZ, suggesting the absence of plastic strain. This is also consistent with low hardness values obtained in this zone, between 140 and 150 HV1. A decrease of hardness is commonly observed in the CGHAZs [201] and might be induced by the grain growth, in relation to the Hall-Petch effect, and/or the presence of tensile residual stresses, as it was suggested by Pommier [45].

In the HAZ, GOS and KAM maps of the HAZ suggested higher strains in comparison to the other two zones and the as-received state, especially towards the plate mid-thickness ((Figure 3.20 (f) and (g)). This is consistent with the hardness increase measured in the cross-section of the welded plate, with the highest value, close to 180 HV1, found at distance of 4 to 5 mm from the FZ, near the plate mid-thickness (Figure 3.31). Such a result is in agreement with the data reported by Auzoux *et al.* [13], who observed hardening due to welding in regions up to 15 mm away from the FZ, with highest values at 4 mm from the FZ. Both GOS maps and hardness profile of the welded plate section were not perfectly symmetrical with respect to the mid-thickness plan (XY). This was most certainly due to a partial recovery induced by the second welding pass. From these observations, it was concluded that the specimens in single-pass welded state further used for SRC tests did not contain any region perfectly equivalent to the as-received state (i.e. annealed). Instead, all of the plate was considered to be affected by the welding heat.

From these strain analyses, cavity nucleation could be expected to be more favorable in the HAZ due to higher hardening than the two other regions. Besides, cavity nucleation in the HAZ of the single-pass welded material could be expected to be more favorable than in the as-received material, but less favorable than the higher strained cold-rolled material.

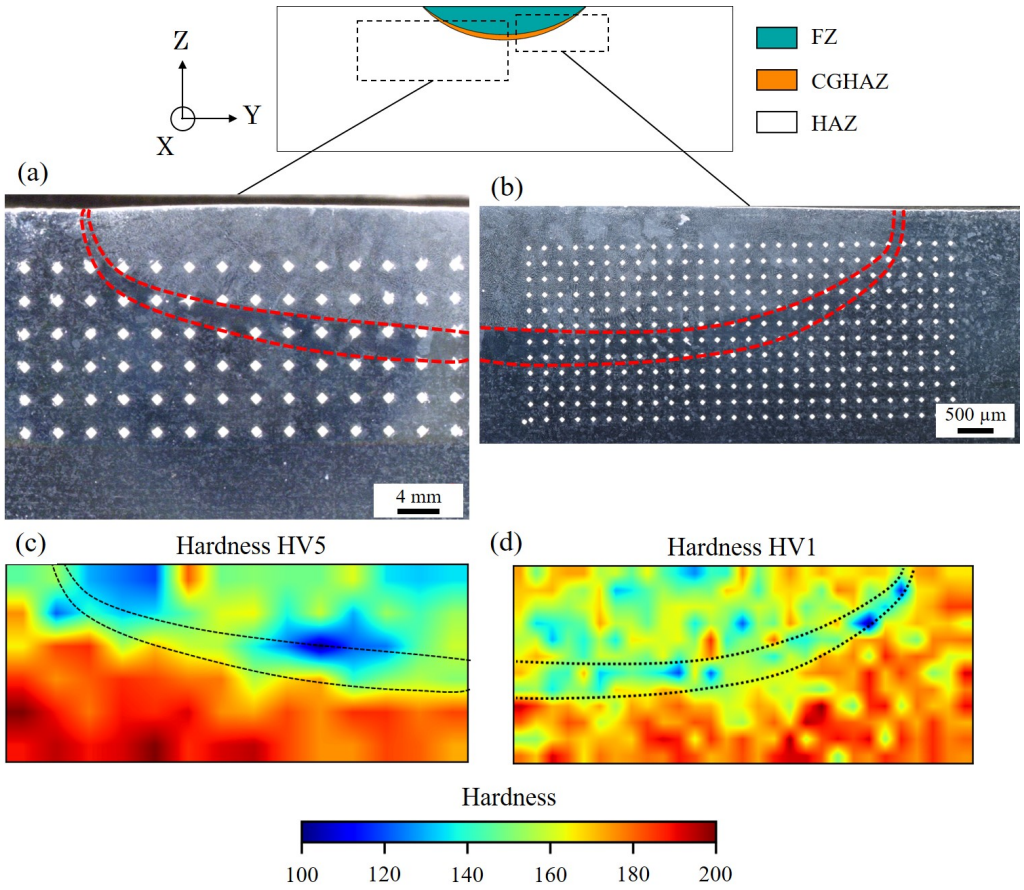

Figure 3.23: Hardness in a cross-section of the plate in a single-pass welded state with (a) and (b) locations of hardness measurements, (c) and (d) bilinear interpolation maps of HV5 and HV1 hardness, respectively.

3.5.2 Effect of thermal exposure

To simulate microstructure evolution induced by further relaxation treatment, specimens in single-pass welded state were aged at 575 °C for 580 and 1470 h. Because composition of the single-pass welded material was the same as of the as-received material, the stable phases were assumed to be the same as identified earlier. Single-pass welded material was thus only aged at the temperature and duration used further for relaxation, also to be compared to the as-received and cold rolled materials.

After 580 h, ferrite grains, both in the form of vermicular ferrite in the FZ or residual ferrite in the CGHAZ/HAZ, showed a complex microstructure composed of multiple phases as suggested by the BSE contrast under SEM (Figure 3.25 (a) and (g)). Element analysis performed by EDS under SEM was carried out on those partially decomposed ferrite grains (Figure 3.24), revealing similar results to the residual ferrite in the aged as-received material: Mo-rich film at austenite/ferrite interface, small Mo-rich precipitates (named "2" in Figure 3.24 (a)), large Mo-rich and slightly Cr enriched precipitates (named "4"), Mo/Cr/C rich but Fe-poor precipitates (named "5"), Ni-rich precipitates (named "6") and finally Ti/N rich inclusions. By comparing chemical composition of the phases identified in the residual ferrite of the as-received material aged at 650 °C for 24 h and those measured here, hypothesis on the nature of these phases could be made: small Mo-rich precipitates would correspond to χ and/or R phases, Mo/Cr/C rich would correspond to chromium carbides $Cr_{23}C_6$ and Ni-rich precipitates to regenerated austenite γ_R. The last phase, rich in Cr and in Mo to a lesser extent, could correspond to the σ-phase, as discussed for previous material states. Note that the presence of σ-phase is commonly observed in partially decomposed vermicular ferrite in welded 316L(N) steel [202].

Asides from the vermicular ferrite, no precipitate was observed at the austenite grain boundaries in the FZ nor in the CGHAZ. However, a few precipitates rich in Cr/C/Mo, assumed to be chromium carbides, were observed at the austenite grain boundaries exclusively in the HAZ with an average size of 230 nm and were accompanied by smaller Mo-rich precipitates (Figure 3.25 (e)). After 1470 h of ageing, some Mo-rich precipitates were observed at austenite GBs in the FZ (Figure 3.25 (b)), but chromium carbides were still absent. In the vermicular ferrite of the FZ, the same phases as after 580 h were observed. However, the fraction of ferrite appeared to be lower than after 580 h. In the CGHAZ, carbides were observed at the austenite GBs (Figure 3.25 (d)). In the HAZ, a much higher number of carbides was observed at austenite GBs after ageing for 1480 h (Figure 3.25 (f)) as compared to the 580 h treatment, with an average size of 220 nm.

The carbide precipitation was observed to be faster in the HAZ than in the CGHAZ and the as-received state, in which no precipitation was observed after 580 h at 575 °C. This is most probably due to the higher strain state of the HAZ, accelerating precipitation [67].

From the results of thermal ageing of the single-pass welded material, additional insight on SRC susceptibility of each zone can be discussed: firstly, the earlier precipitation of carbides in the HAZ makes it more prone to SRC than the CGHAZ. Secondly, similarly to the residual ferrite in the as-received material, cavity nucleation in the FZ can be expected to occur first in vermicular ferrite grains. Besides, the absence of carbides on austenite GBs in the FZ even after 1470 h at 575 °C make these sites very unfavorable to SRC.

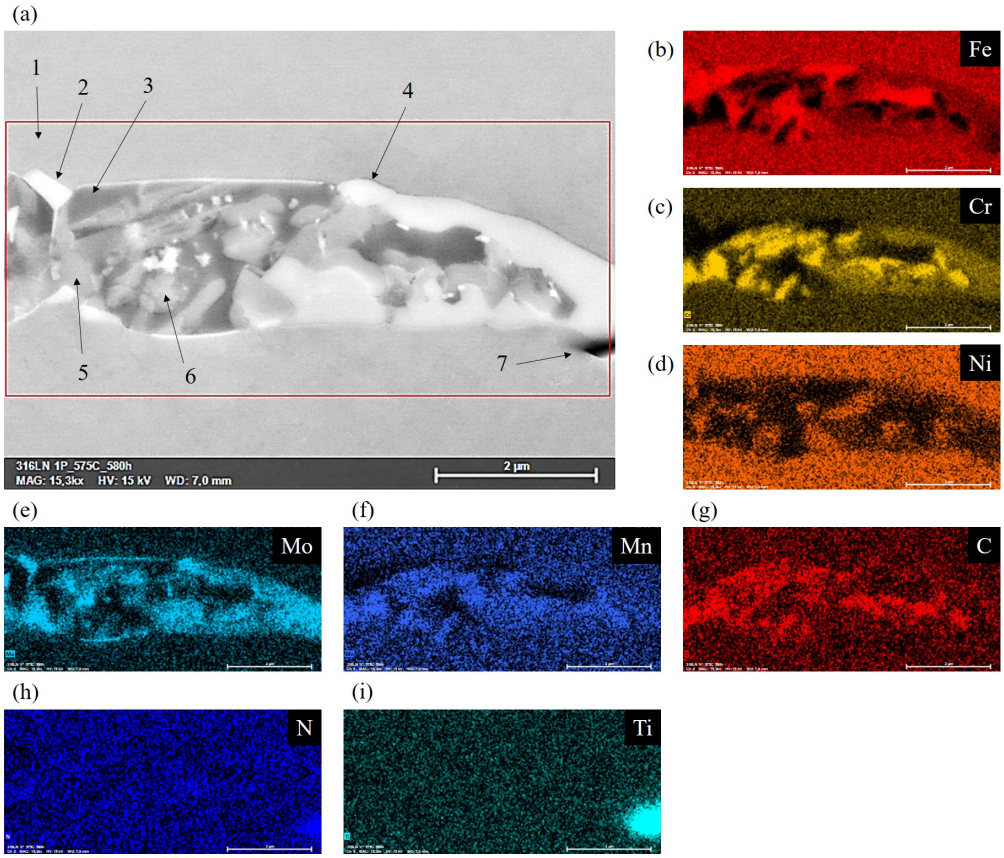

Figure 3.24: Microstructure of residual ferrite in a single-pass welded state aged at 575 °C for 580 h, showing the (a) BSE image of the ferrite grain and EDS maps of (b) Fe, (c) Cr, (d) Ni, (e) Mo, (f) Mn, (g) C, (h) N and (i) Ti (SEM-BSE and EDS).

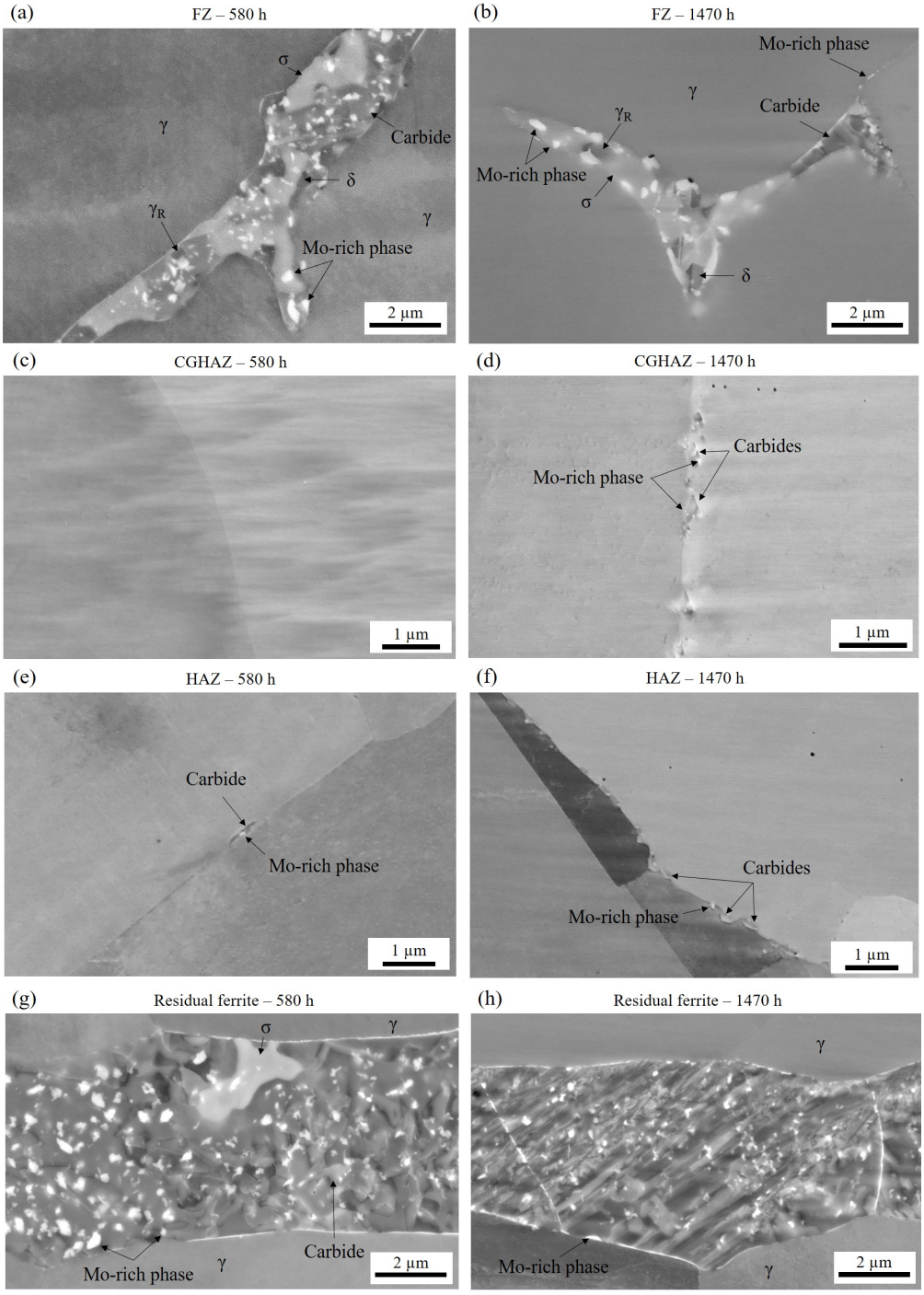

Figure 3.25: Microstructure of a single-pass welded state aged at 575 °C for 580 and 1470 h, showing the (a) and (b) microstructure evolution of the vermicular ferrite in the fusion zone (FZ), (c) and (d) carbide precipitation at the austenite GBs in the HAZ and (e) and (f) decomposition of the residual ferrite in HAZ (SEM-BSE).

3.6 Multi-pass weld

Real industrial weld joints require multi-pass welding of the material, with sometimes more than 20 successive passes. Therefore, to produce material closer to industrial weldments, multi-pass welding state was achieved performing multiple passes on each face of the 316L(N) steel plate in as-received state. It was chosen to operate only five successive passes on each face, as these allowed reaching comparable hardening to that of the HAZs of industrial multipass welds [13]. Typically, hardness in HAZs of industrial welds reaches up to a 30% increase from the base metal (as-received state). As it will be presented further, the five welding passes chosen for this work allowed a hardness increase of 27% from the as-received state, while single-pass welding only allowed an increase of 17% at maximum. Besides, it is important noting that industrial welds are achieved by the successive deposition of molten metal on top of the previous solidified passes, thus the first weld passes are not significantly affected by welding heat of the last passes. In this work, the choice of not using filler metal allowed to apply successive welding heat cycles on the same regions.

The geometry of the resulting multi-pass weld was observed using optical microscopy, shown in Figure 3.26. The main difference with the single-pass welded state was the shape of the weld pool, which formed a bulge in the outer surface of the plate due to the successive accumulation of molten metal at the welding centreline. The formation of this bulge also led to a global distortion of affected zones, visible by the distribution of residual ferrite bands under the weld pool (small lines in bright contrast in Figure 3.26 (a)). These appeared to be aligned along a curve rather than the usual horizontal line as on the sides of the weld pool.

The microstructure of the FZ appeared to be more complex than in the single-pass welded state due to the overlapping microstructure resulting from the successive welding passes. Transition regions between the multiple weld pools were observed by the presence of curved regions with bright contrast in the weld pool (Figure 3.26 (a)) enlarged in Figures 3.26 (b) and (c). The microstructure of the transition region between weld pools of two different passes illustrated in Figure 3.26 (c) revealed variations in morphology and size of the vermicular ferrite formed during welding. Similarly to the single-pass welded state, no GB precipitates were observed after multi-pass welding.

EBSD analyses carried out for the multi-pass welded state showed a microstructure very similar to the one observed in the single pass welded specimen, also constituted of the FZ, CGHAZ and HAZ (Figures 3.27 (a) and (b)).

3.6.1 Strain state

EBSD data together with hardness measurements were used to evaluate strain state of each weld zone. Hardness in the HAZ was higher in the multi-pass state than in the single-pass one, with a maximum value of 205 against 186 HV1, respectively (Figure 3.31). Hardness in the FZ and CGHAZ was quite similar, even though CGHAZ hardness was slightly higher than that in single-pass state in one of the two sides of plate (around d = 13 mm in the profile). The GOS map revealed significant differences (Figure 3.27 (c)) as compared to that obtained for the single-pass welded state, with GOS values between 0.5 and 4° in both CGHAZ and FZ. In addition, it appeared that the CGHAZ was composed of several regions, with a peak of GOS in the middle of the zone (Figure 3.27 (c) and Figure 3.27 (d)). This is most certainly the consequence of the overlapping welding microstructures from different welding passes, which were not exactly performed at the same position or height at each pass and resulted in heterogeneity within the zones themselves.

Hardness of the multi-pass welded state after ageing at 575 °C for 1470 h was also measured (Figure 3.28). It showed a decrease in the center of the HAZ, between 10 and

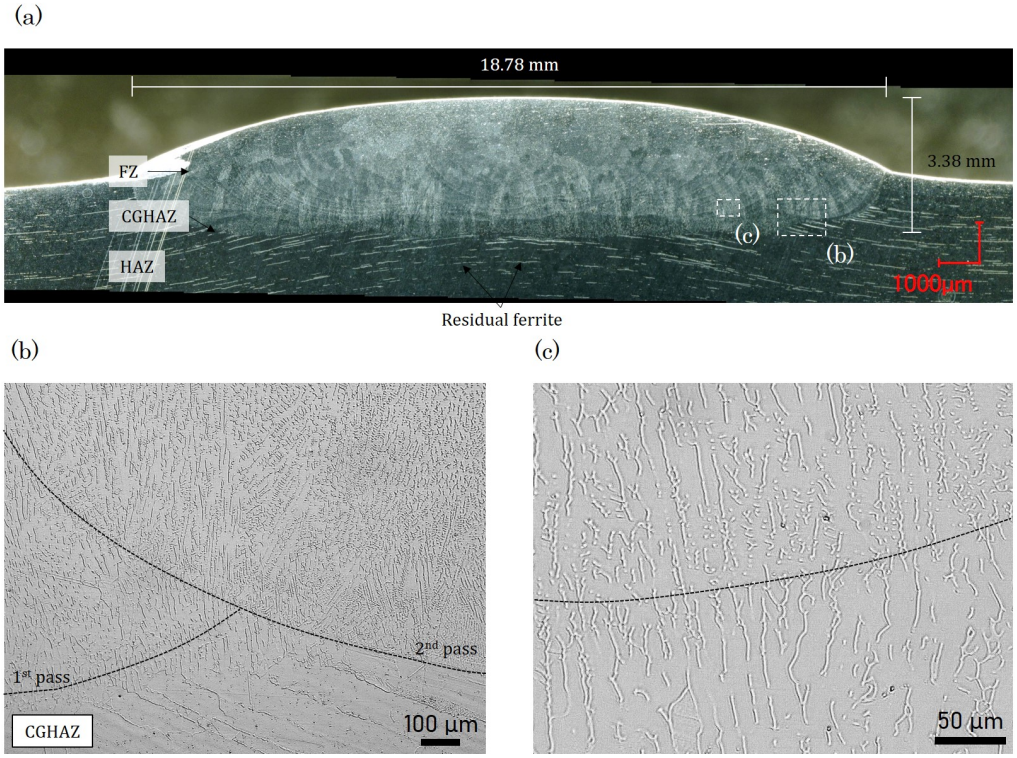

Figure 3.26: Geometry of the weld with different zones as observed by optical microscope of the multi-pass welded sheet, with: (a) overview of the whole weld pool; (b) the intersection of two weld pools from two different welding passes delimited by black dashed lines; (c) enlarged view of discontinuities of the vermicular/skeletal ferrite between two welding passes. Locations of images (b) and (c) are indicated in image (a).

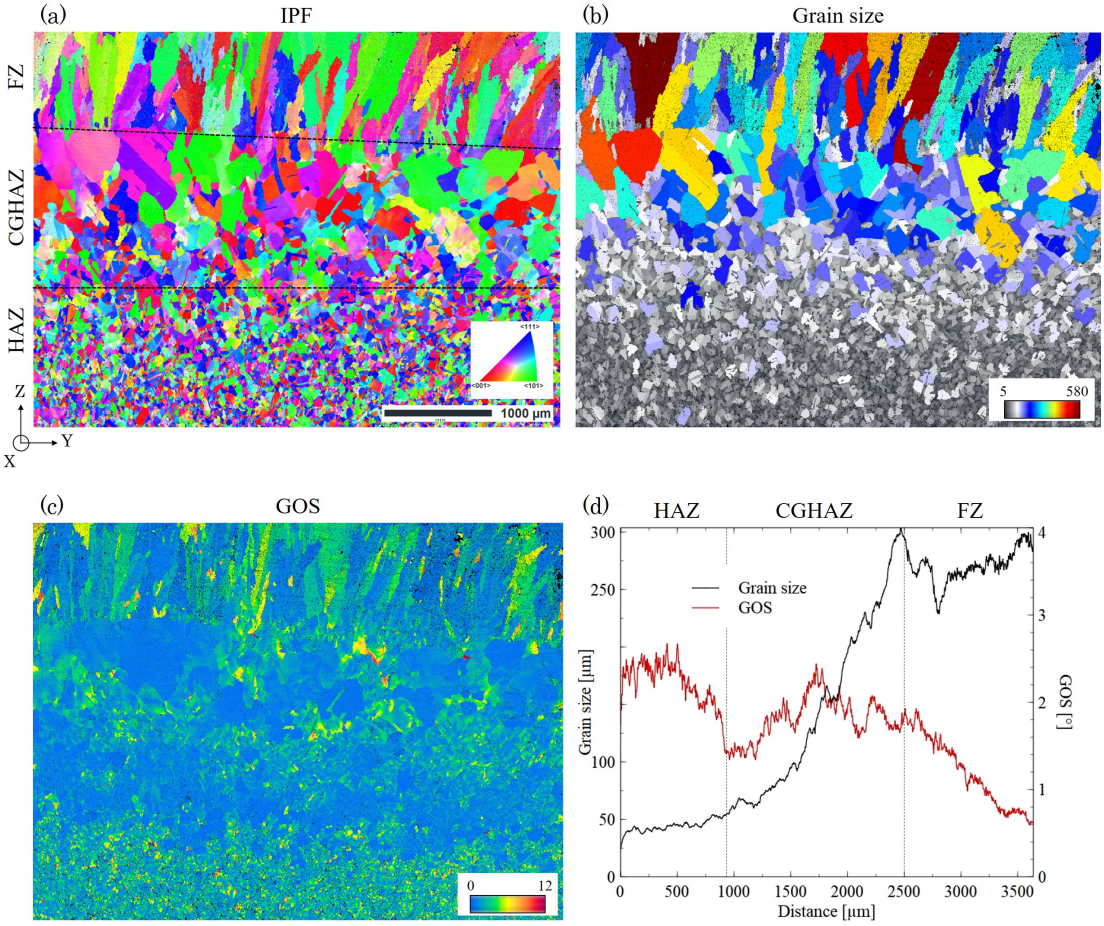

Figure 3.27: EBSD analysis of welding microstructure in multi-pass welded state: (a) IPF in X direction, (b) grain size (μm) map, (c) GOS map and (d) profiles of grain size and GOS integrated along the Z axis. Analysis was performed with acquisition step of 3 μm.

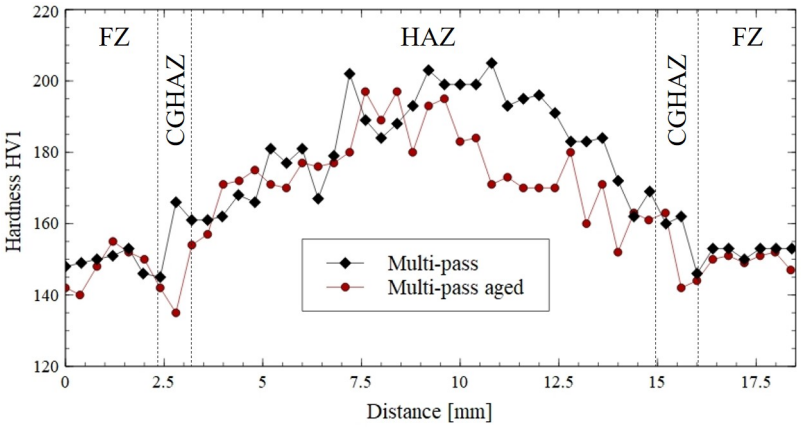

Figure 3.28: Hardness HV1 profiles measured in a plate cross-section in as multi-pass welded plate (black) and after 1470 h at 575 °C thermal ageing (red).

13 mm from the plate surface, suggesting the partial recovery in the HAZ.

Because of the higher hardening in the HAZ of the multi-pass welded material than in both the as-received and the single-pass welded materials, the HAZ of the multi-pass welding would be expected to be more prone to SRC. Also, the heterogeneous distribution of strain observed in the CGHAZ could induce a heterogeneous distribution of damage and eventually particularly weak regions. Similarly, the FZ can be expected to behave differently to that of the single-pass welded material because of the overlapping welding passes.

3.6.2 Effect of thermal exposure

To investigate the effect of temperature on microstructure of the multi-pass welded state, a specimen was aged at 575 °C for 1470 h. The resulting microstructure observed in the FZ was similar to the one obtained after ageing under similar conditions of that of the single-pass welded state, and the residual ferrite of the as-received state. From the BSE contrast in SEM and by comparison with other aged states, these phases were presumed to be chromium carbides, regenerated austenite γ_R, σ-phase and Mo-rich phase precipitates (χ/R phases), resulting from the partial ferrite decomposition (Figure 3.29 (a)). In both CGHAZ and HAZ, carbide precipitates and Mo-rich phase precipitates were observed at the austenite grain boundaries (Figure 3.29 (b)), but their density did not appear to be higher than in the single-pass welded state aged in the same conditions.

Thermal ageing of multi-pass welded material showed no notable differences with single-pass welding material. As a result, no difference in the cavity nucleation location is expected.

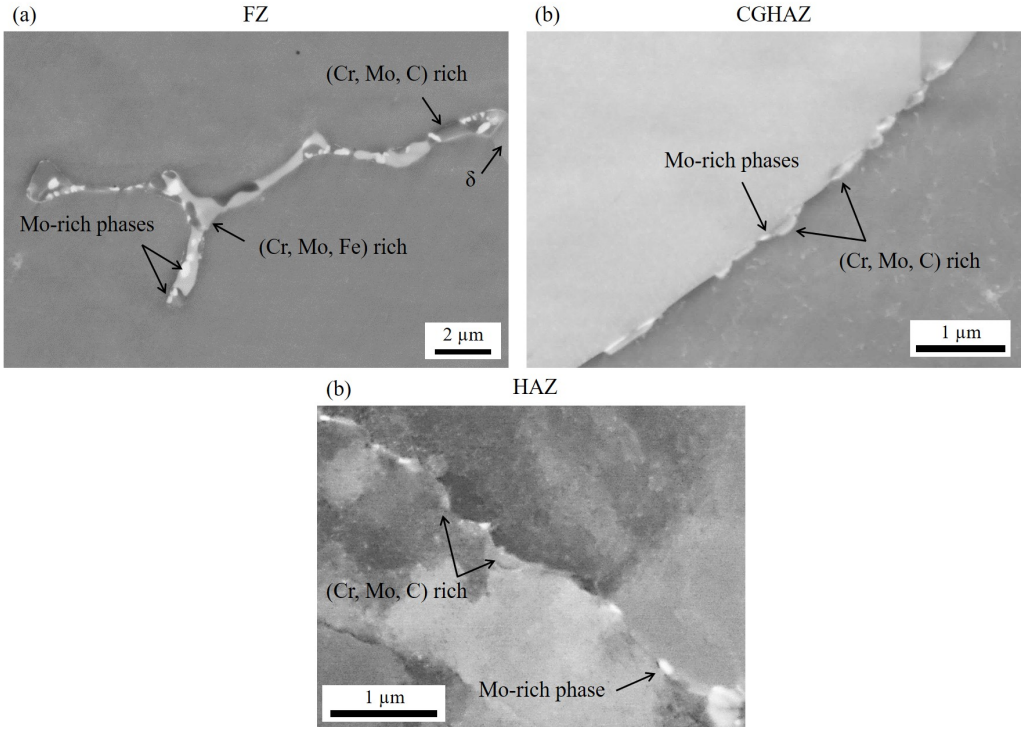

Figure 3.29: Microstructure of multi-pass welded state aged at 575 °C for 1470 h, with (a) the partial vermicular ferrite decomposition in the fusion zone (FZ), (b) precipitates at the austenite GB in the CGHAZ and (b) in the HAZ (SEM-BSE).

3.7 Cold-rolled single-pass welded

Single-pass welding was applied on a priory cold-rolled plate to introduce additional strain in a weld microstructure (Section 2.1). While this was originally carried out to introduce additional plastic strain in both the CGHAZ and HAZ, hardness measurement presented further actually showed that the process led to a very homogeneous straining throughout the weld zones. This would allow studying the susceptibility of each zone to SRC without the influence of hardening usually observed in the HAZ.

The geometry of resulting weld pool was observed using optical microscope and is shown in Figure 3.30. The shape of resulting weld pool was close to that observed in the single-pass welded plate, with a slightly larger and deeper welding pool indicating only minor effect of prior cold-rolling on the weld geometry.

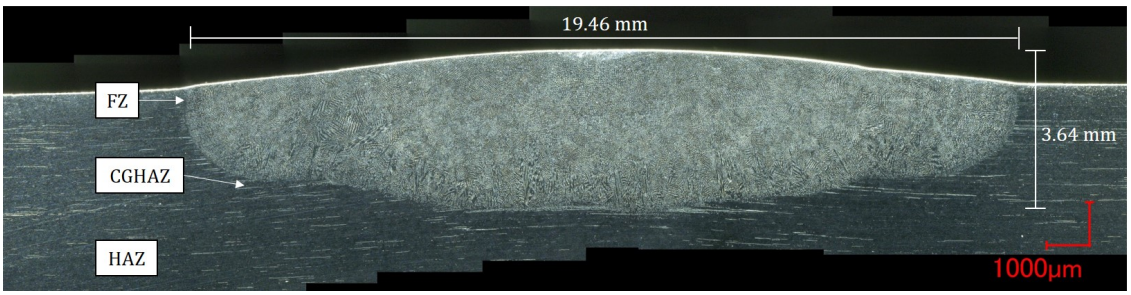

Figure 3.30: Geometry of the weld with different zones as observed by optical microscope of the cold-rolled and subsequently single-pass welded state.

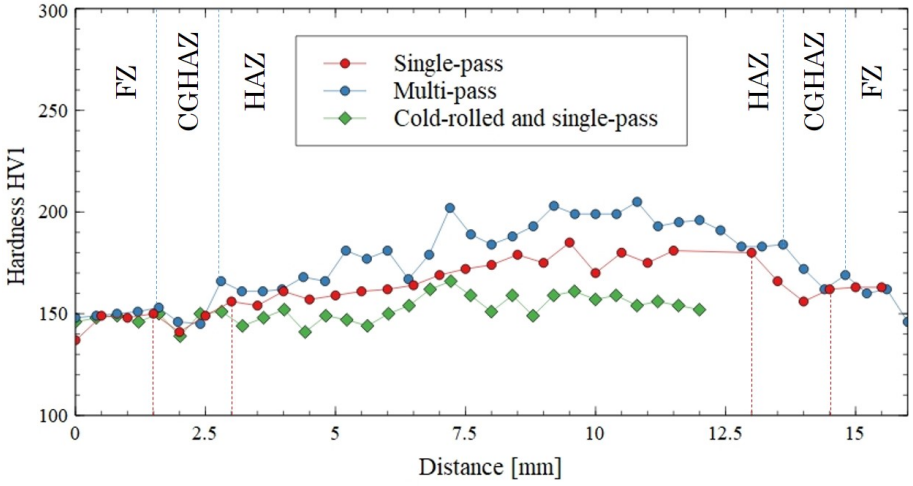

Figure 3.31: Hardness HV1 profiles across the thickness of welded plates, for single-pass welded plate (red), multi-pass welded plate (blue) and cold-rolled and single-pass welded plate (green).

3.7.1 Strain state

Hardness profile of the cold-rolled single-pass welded state obtained across plate thickness showed that despite an important initial straining due to cold-rolling as compared to as-received state, the hardness of the cold-rolled single-pass welded state was lower than that measured for both single-pass and multi-pass welded states (Figure 3.31). It seems thus that increased strain hardening induced by cold-rolling was partially recovered by thermal exposure during the welding process. According to Auzoux [13], recovery annealing of prior work-hardening in a 316L(N) steel occurs mostly between 650 and 1400 °C (liquidus temperature). Due to the cold-rolling process, the plate thickness is lower (12 mm) than that of the plates in single-pass and multi-pass welded states (both about 15 mm thick). Consequently, temperatures reached at mid-thickness during welding were expected to be higher, allowing even more important recovery. Indeed, FEM simulations of welding were performed using Cast3M software [203] 'test case' of TIG welding, using the experimental welding parameters described in Section 2.1.4 and real dimensions of the 316L(N) steel plates. Resulting estimations of thermal fields showed that the decrease of plate thickness from 15.45 to 12 mm led to an increase up to 45% of the peak temperature at the side of the plate opposed to welding (Appendix B.2).

Finally, the hardness measurements carried out for cold-rolled single-pass welded state showed that prior cold rolling allowed the homogenisation of strain state throughout the whole weld for FZ, CGHAZ and HAZ (Figure 3.31). This is particularly interesting regarding SRC tests: if differences in damage between the three zones in this material state are observed, it could only be due to the microstructure. As a result, it is expected that the FZ and the CGHAZ will be more prone to SRC, because of larger grains than in the HAZ.

3.8 With increased grain size

Grain size is often described in the literature as an influencing factor for SRC, increasing the susceptibility of a material to damage (Section 1.4). In order to evaluate the influence of this factor only, material with grain size larger than the as-received state was produced.

In order to a material with higher grain size than the as-received state, the steel in as-received state was submitted to heat treatment at 1300 °C for 1 and 2 h. The resulting

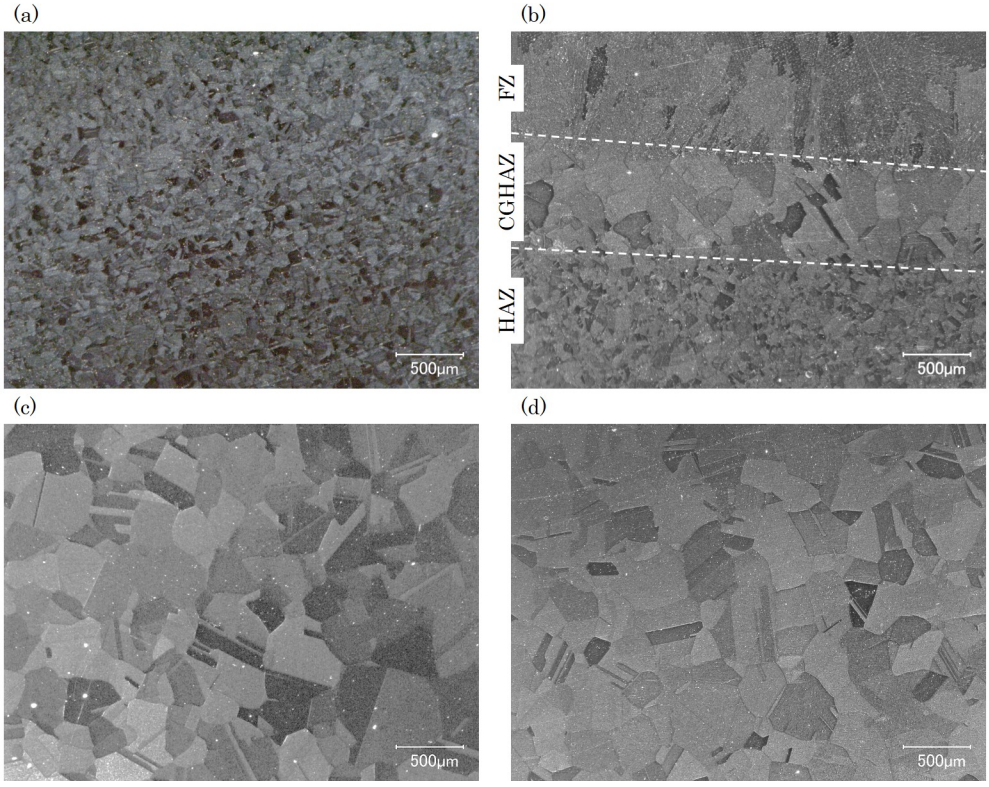

Figure 3.32: Images of the (a) as-received material, (b) single pass weld, (c) as-received after 1 h and (d) 2 h at 1300 °C.

microstructure was compared to that in as-received state and to CGHAZ of single-pass welded state (Figure 3.32). The increase of heat treatment duration from 1 to 2 h at this temperature did not appear to significantly increase the grain size. An average grain size of 270 (when the twins are considered to form grains) and 470 μm (when the twins are considered to be inside the grains) was obtained for both cases (Figure 3.33 (c) and (d)). These represented higher grain sizes than those measured in both as-received state (90 μm) and CGHAZ of a single-pass welded state (200 μm).

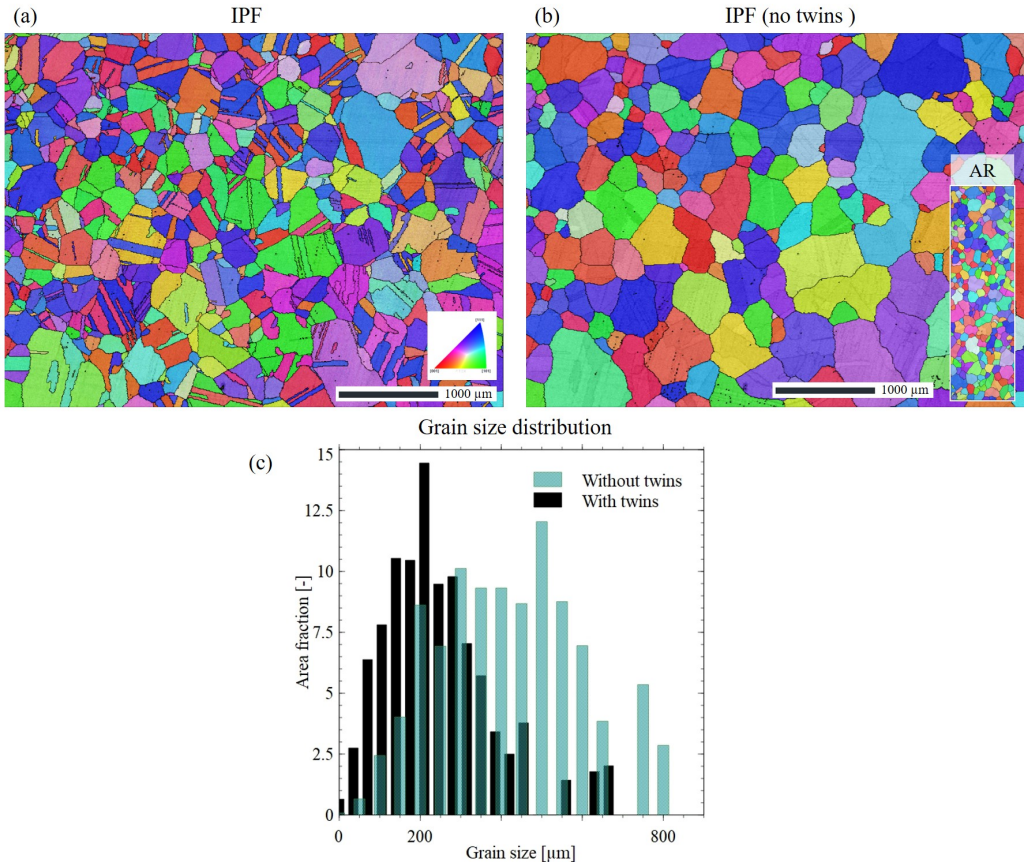

Figure 3.33: EBSD analysis of a sample heat treated at 1300 °C for 2 h, with (a) IPF-IQ with twins, (b) IPF-IQ simulated without annealing twins and as-received (AR) IPF map to scale of the as-received sample for comparison (c) grain size distribution maps for both maps.

3.9 Summary and conclusions

Different microstructural states of the studied 316L(N) steel were produced to get insight into the micromechanisms of the SRC phenomenon. Every state accounted for different parameters known to have a significant effect on SRC, namely, grain size and morphology, hardening and secondary phase precipitates.

Characterization of the material states prior to thermal ageing revealed the following properties:

- As-received state showed a well-annealed austenitic microstructure consisting of equiaxed grains of size of 90 μm and no crystal texture with a low fraction of residual ferrite and few inclusions.
- Cold-rolled state showed a strained microstructure, with mechanical twins, local rotation of grains.
- Single-pass welded state presented a typical heterogeneous welding microstructure composed of three main regions: the fusion zone (FZ), the coarse grain heat affected zone (CGHAZ) and the heat affected zone (HAZ). Because of the low plate thickness (about 15 mm), all the material was considered to be affected by the heat from welding, leading to higher hardening than that in as-received state throughout the plate thickness, as suggested by hardness measures and EBSD analysis (with GOS and KAM methods).
- Multi-pass welded state presented the same three weld zones but with hardening heterogeneity being revealed within both FZ and CGHAZ, resulting from the successive welding passes. A higher overall hardening was observed in the HAZ as compared to the HAZ of the single-pass welded material.
- Cold-rolled welded plate showed the same three weld zones but revealed a homogeneous level of hardening over the zones.

To better understand the precipitation nature and kinetics in the different material states without the effect of pre-strain from Turski compression, the different states were heat treated at different conditions. Subsequent microstructure characterisation revealed precipitates at the austenite grain boundaries and within residual ferrite:

- In the as-received material after ageing, but also in the CGHAZ and HAZ of aged welded specimens, $Cr_{23}C_6$ carbides often close to Mo-rich intermetallics were observed at austenite grain boundaries. While the precipitation of carbides was expected from thermodynamic computations, the $Cr_{23}C_6$ were found to precipitate slower than reported in the literature [67]. This could lead to a higher resistance to SRC of the studied 316L(N) steel to other 316L(N) steels studied in the literature, because residual stresses could relax faster than the time required for secondary phases precipitation at grain boundaries. Indeed, it was shown in the literature that during a relaxation test applying a constant strain, most of stresses (70%) relaxed before 500 h of ageing at 575 °C in a 316L(N) steel similar in composition to the one studied [45].
- Prior cold-rolling was found to accelerate GB precipitation, in agreement with the literature [67].
- In both vermicular and residual ferrite regions, the partial ferrite decomposition into a complex distribution of $Cr_{23}C_6$, χ, R phases and regenerated austenite was

observed after thermal ageing. $Cr_{23}C_6$ precipitated faster in the ferrite, after a few hours at 650 °C in the as-received state, than at the austenite grain boundaries (168 h at 650 °C), due to the higher content in chromium and molybdenum and faster diffusion in the ferrite.

Based on these analyses, hypotheses on susceptibility to SRC of each material state could be made:

- Cold-rolled state is excepted to be more prone to SRC than the as-received state because of the higher hardening but also faster precipitation of carbides.
- The material with increased grain size is also expected to be more prone to SRC than the as-received material, according to industrial observations [3,4,33,46,139,158,159].
- Similarly, heat affected zones (HAZ and CGHAZ) of welded materials (single and multi-pass welded) are expected to be more prone to SRC than as-received material, both because of a higher grain size (in the CGHAZ) and higher hardening (in the HAZ) than that in the fusion zone.

Chapter 4

Generation of residual stresses and strains

Contents

The previous chapter provided characterisation results of the microstructures of each material state and consequently identification of the ones that might be most prone to stress relaxation cracking. The mechanical tensile properties associated to the different microstructures had then to be characterized for further elasto-plastic mechanical FEM simulations.

Pre-straining by compression and unloading (Turski compression) was applied to the different material states to generate residual stresses and induce plastic strain using CT-like specimens, prior to the thermal relaxation. The residual stresses resulting from the Turski compression had to be sufficiently high to trigger SRC, thus, numerical simulations using finite-element method (FEM) were used to design the CT-like specimen geometry and to chose the compression conditions. The results of FEM were further used to evaluate SRC thresholds for each microstructure after stress relaxation, by confronting the measured damage to the computed stress and strain.

4.1 Tensile properties of material states

To adjust the mechanical behaviour law parameters required for FEM simulations, tensile tests were performed at room temperature following the procedure described in Section 2.3. Tensile curves for as-received, single-pass welded materials and material with increased grain size are shown in Figure 4.1. The average yield, $R_P0.2$, and maximum, R_m, strength are detailed in Table 4.1.

Standard tensile specimens made of the as-received material were machined in two directions: hot rolling direction (Y-axis) and transverse direction (X-axis). Results showed very similar properties for both directions (Figure 4.1 (a) and Table 4.1), suggesting an isotropic behavior in the (XY) plane. The tensile curve obtained for the material with increased grain size (Figure 4.1 (a)) showed a significant decrease in both R_m and $R_P0.2$ as compared to the as-received state, due to the higher grain size, which is consistent with the Hall-Petch relationship. For the single-pass welded material, 1 mm thick tensile specimens were machined across the welded plate thickness, transversely (Figure 4.1 (a)), and parallel (Figure 4.1 (b)), to the welding direction. A total of 30 tests were carried out, with 8 specimens machined from the FZ, 4 from the CGHAZ and 18 from the HAZ. The difference in number of specimen for each weld zone is due to the difference in thickness of each weld zone in the welded plate. Slightly higher values for both $R_P0.2$ and R_m were measured for the three weld zones of the single-pass welded specimens machined in the parallel direction (X-axis) as compared to the transversal one (Y-axis) (Table 4.1), suggesting a slight higher strength in the X direction.

The yield strength, $R_P0.2$, measured for the HAZ was higher than the one obtained for the as-received material, and than in the other two weld zones (CGHAZ and FZ), confirming the strain hardening induced by the heat of the welding process (Section 3.5.1). As expected, the maximum strength value, R_m, measured for the HAZ was only slightly higher than the one obtained for the as-received material, since no significant microstructure transformation was observed in the HAZ. On the contrary, the larger grain size in the FZ, as compared to that in as-received material, induced a decrease of both $R_P0.2$ and R_m. In general, the mechanical behavior of the CGHAZ appeared to be in between that of the FZ and HAZ. It is worth noting that the mechanical behavior of this zone was difficult to interpret, since the CGHAZ thickness (between 0.55 and 1 mm) was about (or even lower) that of the tensile specimen thickness. Thus, it is possible that several of the CGHAZ specimens contained also a part of the FZ or the HAZ, thereby affecting the measured values of $R_P0.2$ and R_m. In the CGHAZ, while the measured R_m was slightly lower than the one obtained for the as-received material, the average $R_P0.2$ was about 10 MPa higher. This is not a significant difference, given that the standard deviation of $R_P0.2$ measured for the CGHAZ was about 15 MPa. The significant difference in grain size between the CGHAZ and the material with increased grain size, 330 against 470 μm, respectively, is most probably responsible of the difference in $R_P0.2$ and R_m values measured here.

Table 4.1: Yield, $R_P0.2$, and maximum tensile, R_m, strength in MPa of the as-received state (AR), material state with increased grain size (MIGS) and different weld zones of the single-pass welded material. Averaged values are presented for each welding zone, considering tensile test performed in both Y (transverse to welding) and X (parallel to welding) directions. Directions are detailed in Figure 2.2.

Material	AR		MIGS		FZ		CGHAZ		HAZ	
Property	$R_P0.2$	R_m	$R_P0.2$	R_m	$R_P0.2$	R_m	$R_P0.2$	R_m	$R_P0.2$	R_m
X direction	301	593	-	-	295	545	319	588	362	624
Y direction	301	591	208	518	285	544	300	576	346	606
Average	301	592	-	-	290	544	310	582	354	615

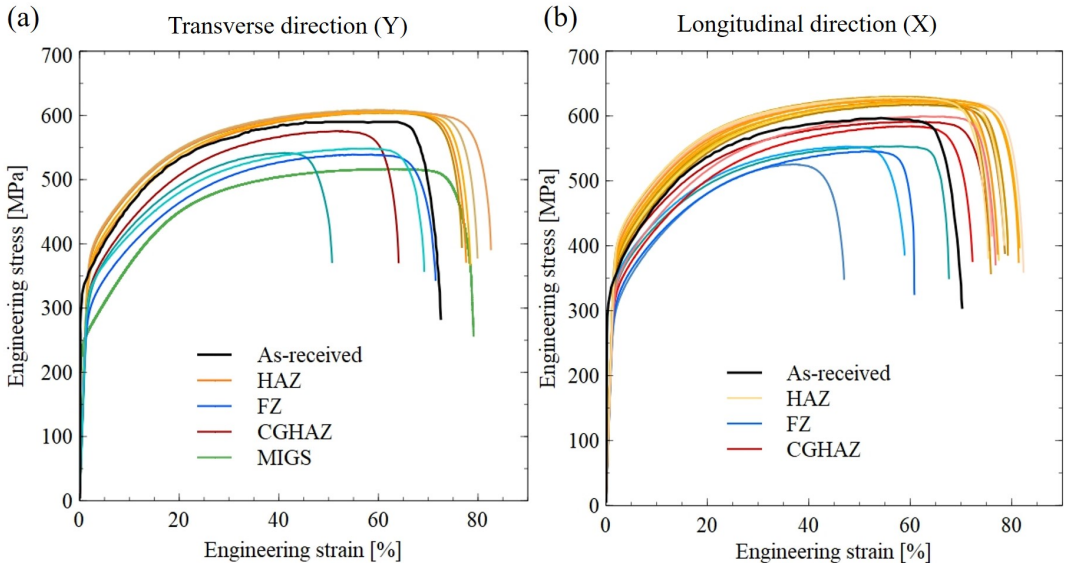

Figure 4.1: Tensile curves for as-received state, material state with increased grain size (MIGS), single-pass welded material (mini specimens) with the FZ, CGHAZ and the HAZ, in which tensile test specimens were machined in the (a) Y (transverse to welding) and (b) X (parallel to welding) directions.

4.2 Mechanical simulations

Mechanical simulations using finite element method were performed to predict residual stresses generated in the notch root of the CT-like specimens after the Turski compression, ensuring the necessary conditions to trigger SRC by compression. The FEM computations were performed with Cast3M software [203], by considering 3D symmetry. Only a quarter of the CT-specimen was represented.

4.2.1 Model and parameters

The simulations were carried out under continuum mechanics hypothesis, and thus did not take into account local heterogeneities due to the microstructure: namely, grain orientation and morphology, grain boundaries, secondary phase precipitates. The mechanical behavior of the 316L(N) steel at room temperature was described by the constitutive equations proposed by Chaboche [204], accounting for both isotropic and kinematic hardening. The elastic behavior was described by Hook's law. In the elasto-plastic framework, the plasticity criterion follows the equation (4.1). Equations (4.2) and (4.3), (4.4) describe kinematic hardening, while equation (4.5) describe the isotropic hardening.

$$J_2(\bar{\bar{\sigma}} - \bar{\bar{X}}) = R(p) \tag{4.1}$$

$$\bar{\bar{X}} = \bar{\bar{X}}_1 + \bar{\bar{X}}_2 \tag{4.2}$$

$$d\bar{\bar{X}}_i = C_i.(\frac{2}{3}.A_i.\phi(p).d\bar{\bar{\varepsilon}}_p - \bar{\bar{X}}_i.dp) \tag{4.3}$$

$$\phi(p) = 1 + (\psi - 1).e^{-\Omega.p} \tag{4.4}$$

$$dR = b.(R_M - R).dp, \; with \; R(0) = R_0 \tag{4.5}$$

Table 4.2: Chaboche model parameters used in this work to simulate the compression tests of the different states of 316L(N) steel.

Parameter	As-received	FZ
E [MPa]	200.10^3	200.10^3
ν [-]	0.3	0.3
A_1 [MPa]	70	70
C_1 [-]	100	200
A_2 [MPa]	200	200
C_2 [-]	2	2
ψ [-]	1.25	1.25
Ω [-]	2	2
R_0 [MPa]	230	230
R_M [MPa]	830	950
b [-]	3	2.05

J_2 denotes for the second principal invariant of the stress deviatoric tensor, $\bar{\bar{\sigma}}$ the stress tensor, $\bar{\bar{X}}$ the kinematic stress tensor, $\bar{\bar{\varepsilon}}_p$ the plastic strain tensor and p the cumulated plastic strain. A_i, C_i, ψ, Ω, b, R_M and R_0 are material-dependent parameters. Table 4.2.1 details the values of parameters adjusted from experimental data, and the Young's modulus, E, and Poisson's ratio, ν, for each material state and weld zone. Kinematic hardening parameters were fitted using experimental tension-compression curves for a 316L(N) of very similar composition to the one studied, taken from Pommier [45] and shown in Figure 4.2. The other model parameters were adjusted using experimental tensile curves obtained for each type of material state.

Comparisons of experimental and simulated curves for both as-received (Figure 4.2 (a)) and cold-rolled (Figure 4.2 (b)) states show that they are in good agreement. Cold-rolled state was simulated by imposing an initial accumulated plastic strain of 22% prior to compression, representative of the cold-rolling process.

As the similar microstructure was observed in both as-received state and HAZ of single and multi-pass welded state, the same material parameters was considered for both. However, as shown by the tensile tests the hardening in the HAZs was different than the as-received state (Figure 4.1). The work hardening induced by welding heat was then accounted for by imposing an initial cumulated plastic strain of 4% in the HAZ for the single-pass weld material, value chosen to fit the experimental tensile curve of the zone (Figure 4.2 (c)). Because of time and cost limitations, tensile testing of multi-pass welding material was not performed. Consequently, the initial cumulated plastic strain of the HAZ in the multi-pass welding material was estimated from the empirical relationship between hardness increase and cumulated plastic strain known for the cold-rolled material and that of the HAZ of the single-pass welded material (Chapter 3). Indeed, the cold-rolled material showed a increase in hardness of 90% as compared to the as-received material, and was correlated to a cumulated plastic strain of 22%. HAZ of the single-pass welded material presented a hardness increase of 5%, equivalent to a cumulated plastic strain of 4%. A linear fit of this tendency suggested a cumulated plastic strain of 5.3% for a hardness increase of 17%, corresponding to the average hardness increase of the HAZ in the multi-pass welding material. While this approach is disputable, it was proven to lead to relevant results for simulations as presented further (Figure 4.10).

CGHAZ was not accounted for in the numerical simulations due to its small thickness (less than 1 mm) and consequently the uncertainty concerning its mechanical properties, as previously discussed in Section 4.1. Comparison of experimental and simulated tensile curves of the as-received, single-pass welded material (FZ, CGHAZ and HAZ) and material

with increased grain size is shown in Figure 4.2 (c). Behavior of material with increased grain size was simulated using parameters used for the as-received state, with the exception of R_0 which was adjusted to 180 MPa to fit tensile curves. True strain ε was computed from engineering strain e using the formula $\varepsilon = ln(1 + e)$ with ln being the natural logarithm. True stress σ was computed from engineering stress s using the formula $\sigma = s(1 + e)$

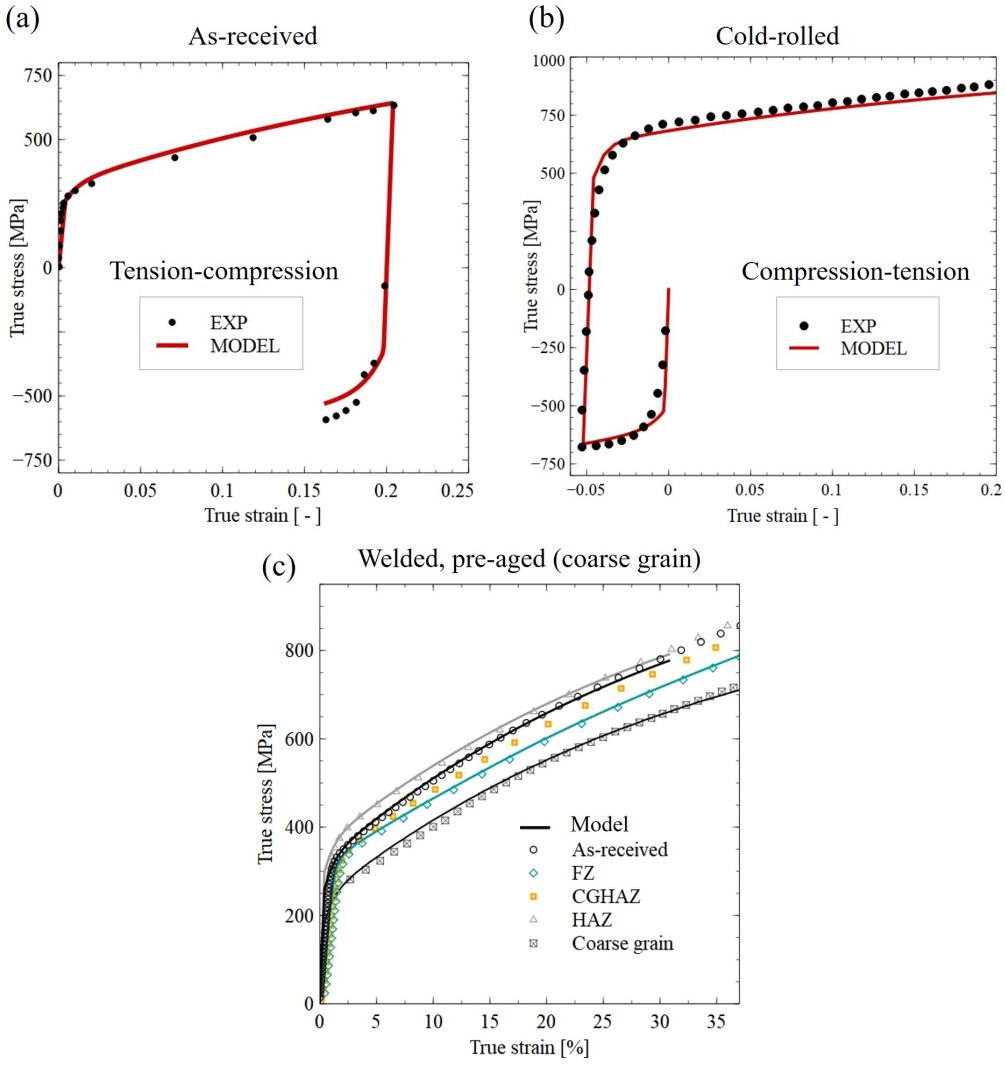

Figure 4.2: Tension-compression and compression-tension tests experimental and simulated curves for a 316L(N) steel in the (a) as-received, (b) cold-rolled and (c) single-pass welded material and material with increase grain size. Experimental data of (a) and (b) was gathered from Pommier [45]. Data in (c) was obtained in this work.

4.2.2 Design of the CT-like specimen geometry

Several CT-sample geometries were tested numerically, varying the notch radius, but also the crack mouth geometry, as illustrated in Figure 4.3 (a). Due to the symmetry of the problem, only a quarter of the CT-specimen was considered for the FEM simulations. The "notch 1" geometry was used for CT specimens made of cold-rolled material for comparison with literature results [45, 47]. Two additional notch geometries were tested for the CT made of the other material states, notches "2" and "3". These were designed to avoid notch crushing during high compression loads. Indeed, cold-rolled specimens were hardened prior to compression, as a consequence the displacement necessary to reach high levels of

residual stress was much lower than for CT made of as-received, single-pass, multi-pass welded material. Notch "3" was designed to withstand the highest risk of mouth crushing but with a mouth design relatively different from the original notch "1", while notch "2" was designed as an intermediate of the two latter. The three notch designs were then compared using the same material parameters and compression conditions. Simulations results showed very similar trend and values of residual stresses. As an example, prediction of residual stresses at mid-thickness after compression at 26 kN of CT made of cold-rolled material are shown in Figure 4.3. These showed maxima of 754, 756 and 757 MPa for notch geometry 1, 2 and 3, respectively.

Since the difference between the three notch geometries was negligible, it was chosen to use the design allowing the highest safety of all three, thus the notch "3". Asides from cold-rolled material, this design was kept for all CT made of other materials.

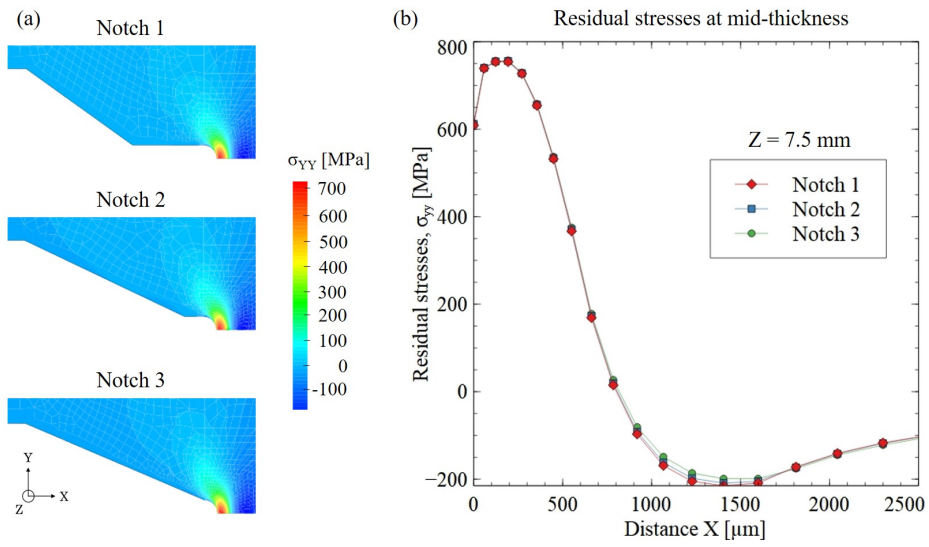

Figure 4.3: Comparison of computed residual stresses for different CT notch geometries: (a) fields and (b) σ_{YY} profile at mid-thickness of CT-like samples after the compression loading and unloading of a 26 kN load, considering material parameters identified for the cold-rolled material as an example, and geometries with thickness e = 15 mm and notch radius r = 0.75 mm.

4.2.3 Mesh and sensitivity analysis

A 3D mesh of a quarter of the CT specimen with notch "3" geometry for FEM simulation was made using cubic finite-elements, with bigger elements (size of 1.00 mm) being located in areas where low strain was expected and smaller ones near the notch root, as shown in Figure 4.4. The size of elements near the notch root was determined by gradually increasing the number of finite elements in this region, where the mesh was the most sensitive to the element size. Figure 4.5 compares residual stresses computed at mid-thickness near the notch root using element sizes ranging from 1613 to 10 μm. An element size of 17 μm allowed achieving a difference in the residual stress peak lower than 1% in comparison to the finest tested mesh size (10 μm), while allowing much quicker computation time. This mesh size was thus kept for all simulations.

In the case of CT made of single and multi-pass welded materials, the shape and dimensions of the mesh for the fusion zones were determined from experimental macroscopic images of single (Figure 3.19 (a)) and multi-pass (Figure 3.26 (a)) welded plates. CGHAZ was not included in the mesh due to its size, as previously discussed in Section 4.2.1.

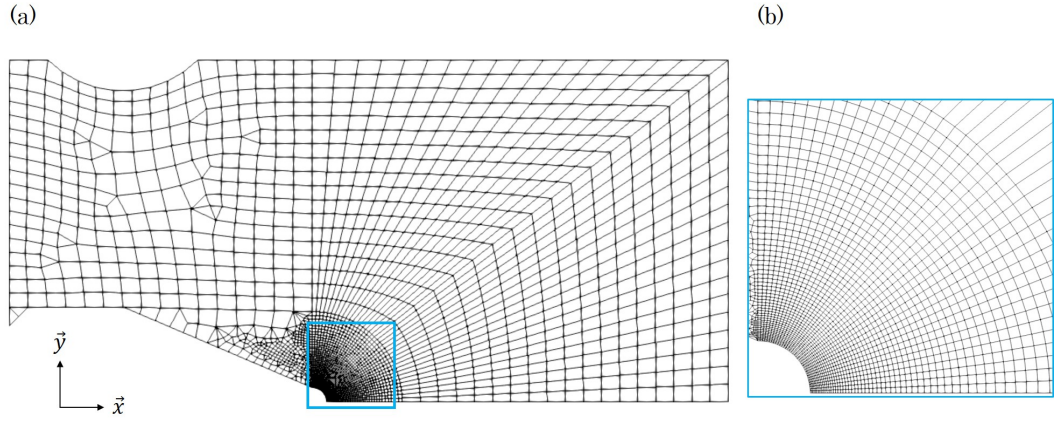

Figure 4.4: Section of the 3D mesh constructed with the CAST3M software, and accounting for a quarter of CT-like specimen used for FEM simulations with (a) the whole section and (b) a close-up near the notch root.

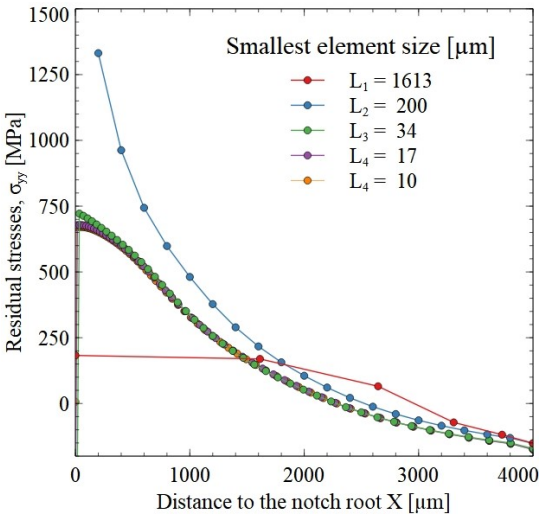

Figure 4.5: Comparison of computed residual stress σ_{YY} profile at mid-thickness from the notch root, considering parameters adjusted for the as-received material, using different mesh density for the CT-like specimen.

Figure 4.6 (a) and (b) show the quarter 3D meshes for the single and multi-pass welded states, respectively.

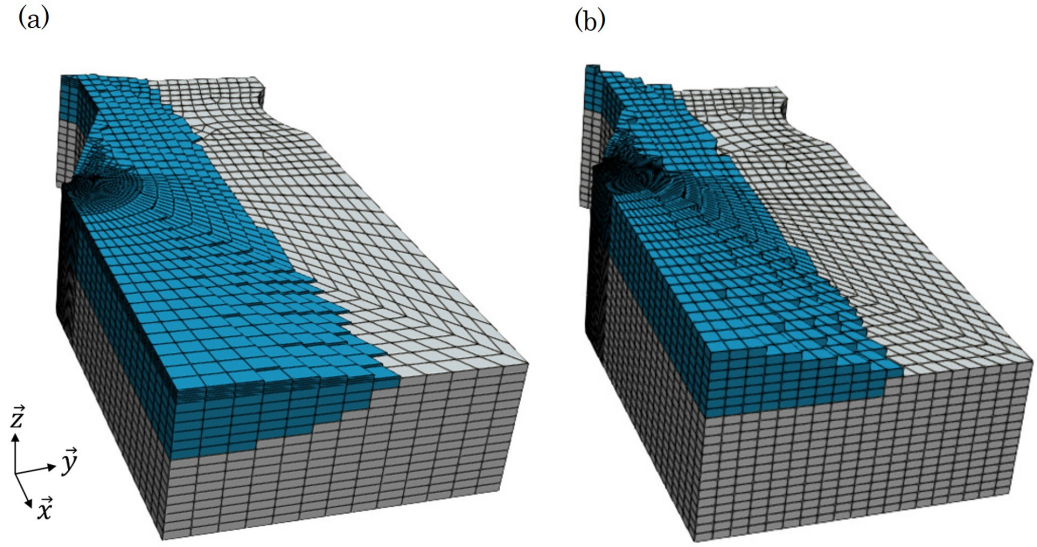

Figure 4.6: 3D mesh of a quarter of the CT-like specimen of (a) single-pass welded state and (b) multi-pass welded state, used for FEM computation. FZ is displayed in blue and HAZ in grey.

4.2.4 Influence of prior residual stresses

Residual stresses are one of the main driving forces required for SRC in metallic components, hence they must be carefully considered for the characterization of the mechanical behavior of welded plates. Even though the hardening induced by welding was taken into account in the FEM simulations by imposing representative plastic strains as initial boundary conditions, the influence of prior residual stresses was not accounted for.

To determine the effect of prior residual stresses on the mechanical response of a CT specimen made of single-pass welded material, simulations of Turski compression were also carried out imposing residual stresses prior to loading. Experimental measurements or numerical simulations of GTAW found in the literature typically indicate complex distributions of residual stresses within metallic plates [131,137,205]. Besides, GTA multi-pass welding was performed at the CEA Saclay on the studied 316L(N) steel in the form of Borland specimens (see details of the specimen in Section 1.4.3) with a 19-15 steel as filler metal for another study, with a total of 18 welding passes. Post-welding residual stresses of these specimens were measured by contour and incremental deep hole drilling (iDHD) methods, showing a maximum of 436 MPa. Hence, in the case of the steel plates studied here, welded with a much lower number of passes (5 at maximum), were expected to have post-welding residual stresses lower than 436 MPa. X-ray diffraction method was also used in this work to estimate residual stresses in a single-pass welded plate, but the obtained results were not relevant enough to be considered. Measured magnitudes and distribution of residual stresses were too far off from what is commonly found in the literature. This could be due to the source used, or to the chosen diffraction peak used for measurement. Typically, it was shown in the literature that using Mn-Kβ X-rays significantly improves the accuracy of stress measurements for austenitic stainless steels [206]. Unfortunately, this source was not available in the equipment used for this work so this could not be tested. The value of 436 MPa was then kept as the maximum post-welding residual stress magnitude possible in the welded materials studied in this work.

To simulate the compressive loads experienced by the affected zones of the weld during welding process, leading to both hardening and tensile residual stresses, a prior compression at lower load was then applied numerically to a CT specimen as described in Figure 4.7 ("double load 1^{st} cycle"). The load was chosen aiming for maximum residual stresses of about 435 MPa, corresponding to the extreme case of multi-pass welding passes of a 316L(N) steel. As shown by the resulting residual stresses profiles in Figures 4.8 (a) and (b), this first loading ("Double load 1^{st} cycle") allowed reaching tensile residual stresses of about 435 MPa up to a distance of 0.5 mm from the notch, which then quickly decreased. This prior loading also allowed the hardening of the specimen, up to 8% of cumulated plastic strain at the notch root. After unloading, the CT specimen was compressed a second time with the higher load, shown in Figure 4.7 ("Double load 2^{nd} cycle"). This second load allowed reaching residual stresses of 578 MPa at maximum, and plastic strain of 18% (Figure 4.8). This second load was compared to the normal single load procedure (Figure 4.7), compressed to the same final load. After unloading, the single load allowed reaching residual stresses of 568 MPa and plastic strain of 17%.

As suggested by the results, the slight increase in maximum stress (less than 2%) at the notch root is most probably due to the higher initial hardening induced by the first loading cycle of the double loading procedure. These results finally showed that differences between the two cases were negligible. This suggested that post-compression residual stresses magnitude and distribution in CT-like specimens depended very little on the prior welding residual stresses. It was then decided to not take into account welding residual stresses for simulations of CT specimens made of welded material (either single or multi-pass). Besides, theses results also showed that if damage resulting from stress relaxation is different between the weld zones (FZ, CGHAZ and HAZ), this would either be due to a difference in initial hardening or to differences of microstructure.

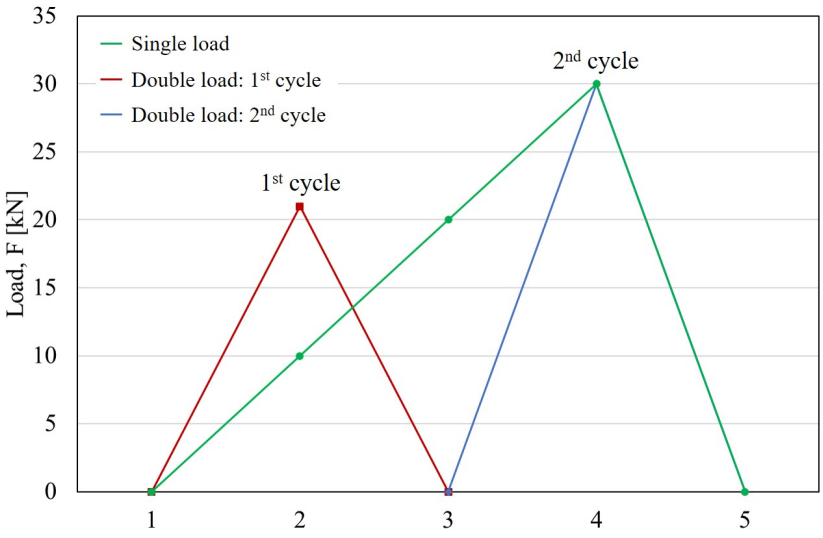

Figure 4.7: Method for comparison of single load (normal procedure) to the double load allowing the introduction of initial hardening and residual stresses simulating that of welding.

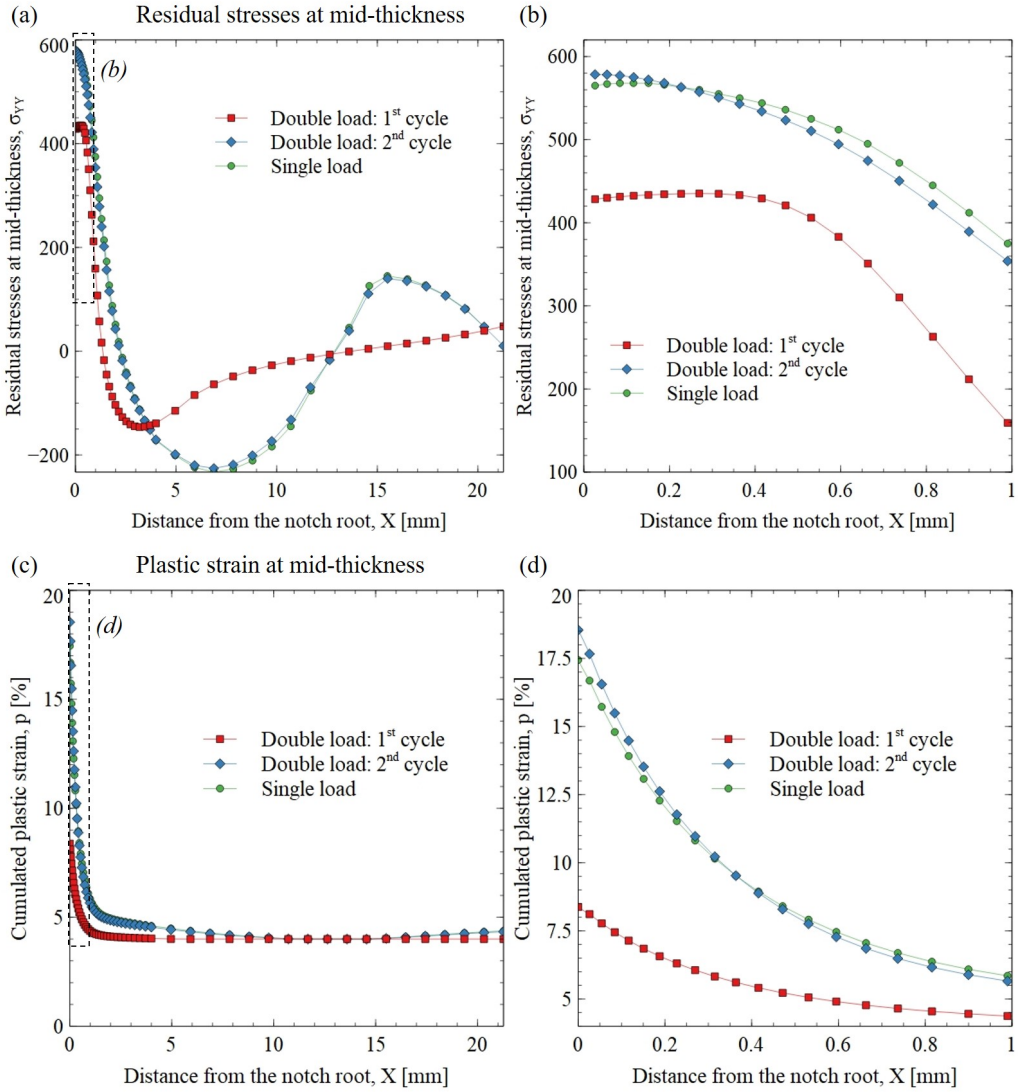

Figure 4.8: Comparison of computed (a) and (b) σ_{YY} residual stresses, (c) and (d) cumulated plastic strain profiles as a function of the distance from the notch root and at half-thickness of a CT-like specimen made of single-pass welded material, after the unloading of the compression, considering welding residual stresses (double load) or not (single load).

4.3 Turski compression

In this work, a compression loading and unloading, named Turski compression, was performed using CT-like specimens aiming to generate sufficient residual stresses to induce SRC during subsequent thermal treatment. This method was first introduced by Turski *et al.* [47] and used more recently by Pommier [45] and Xiao *et al.* [181]. For the non-welded states, the compression was the only step allowing generating residual stresses. After the welding, residual stresses were already present as a result of the welding process. Nevertheless, no industrial case of SRC in welded 316L(N) steels has been reported yet, which is most probably due to an elevated SRC threshold level (740± 40 MPa [45]) much higher in comparison to the GTAW residual stresses commonly measured for 316 steels (about 400 MPa [131, 137]), even for multi-pass welding processes as stated in previous Section 4.2.4 (about 436 MPa). For this reason, the prior Turski compression of welded specimens was carried out to generate sufficient residual stresses. In order to observe and characterize

SRC in the studied steel, and better understand the physical mechanisms associated to the phenomenon, numerous pre-loading conditions were applied, as summarized in Table 4.3.

Compression tests were performed at room temperature (Chapter 2), being controlled by imposed force in the case of cold-rolled material, or CMOD (Crack Mouth Opening Displacement), for all other specimens.

Experimental and simulated Force-CMOD curves obtained for the as-received material and material with increased grain size (MIGS) are shown in Figures 4.9 (a) and (b), respectively. Three CT specimens made of as-received state were compressed to CMODs of 1.73 mm and one specimen to 2.34 mm. It is worth noting a maximum difference of 2% was observed between the maximum forces of the three specimens compressed to a CMOD of 1.73 mm. Simulated curves for CT specimens made of as-received material were in good agreement with the ones obtained experimentally. A maximum difference of 4 and 5% was obtained between predicted and experimental forces for a CMOD of 1.73 and 2.34 mm, respectively. The CT specimens machined from material with increased grain size were compressed to CMODs of 2.34 and 5.62 mm. For these specimens, slight differences between numerical predictions and experimental results were observed, especially during the plastic strain hardening. A maximum difference of 6 and 9% was obtained between predicted and experimental forces for a CMOD of 2.34 and 5.62 mm, respectively.

CT specimens made of cold-rolled material were compressed to a maximum force of 25 kN. Results obtained for this material state, using CT-like specimen thickness of 11.90 and 10.00 mm, are shown in Figure 4.9 (c) and (d), respectively. Two notch radii were analysed. One notch radius was chosen to be able to compare directly the specimens of the present study to those of Pommier [148]. For both thicknesses, the lower notch radius specimen resulted in lower CMODs, even though the residual CMODs were very close for both investigated cases at the end of the unloading. Besides, the final CMOD was larger for a lower thickness. The multiple compression performed on different CT-like specimens with the thickness of 11.90 mm showed a good results repeatability. Comparison between experimental and simulated curved showed good overall agreement, for both thicknesses and radii, with a maximum difference of 9% in CMOD between them.

Experimental and simulated Force-CMOD curves for the specimens made of single-pass welded material compressed to CMODs of 1.22, 1.39, 1.73, 1.85, 6.09 and 6.41 mm, are shown in Figure 4.10 (a) and (b). For the single-pass welded state a higher scatter in the mechanical behavior than specimens made of cold-rolled was observed, most probably due to differences in dimensions and position of the weld pools within the CT samples as well as weld microstructure itself. Even though some simplifying assumptions were made for the numerical simulation of these specimens, such as not considering the CGHAZ in the mesh, comparison between experimental and simulated curves showed a good agreement for lower CMODs (Figure 4.10 (a)), with a maximum force difference of 5% between them. For compression tests imposing higher CMODs, the difference between experimental and computed curves were slightly higher than for lower CMODs, with a maximum force difference of 7% (Figure 4.10 (b)).

The mechanical responses of CT specimens made of the cold-rolled single-pass welded and the multi-pass welded states are shown in Figure 4.10 (c) and (d), respectively. Similarly to the single-pass welded state, simulated response of the multi-pass welded state showed a good agreement with experimental data, with 5% of difference of the maximum force. Simulation for cold-rolled single-pass welded state was not performed in this work due to a lack of data for the mechanical properties of this state.

4.3.1 Estimation of residual stresses and strains

To ensure that the SRC threshold stresses were reached after the compression of the different material states, predictions of residual stresses and plastic strains have been

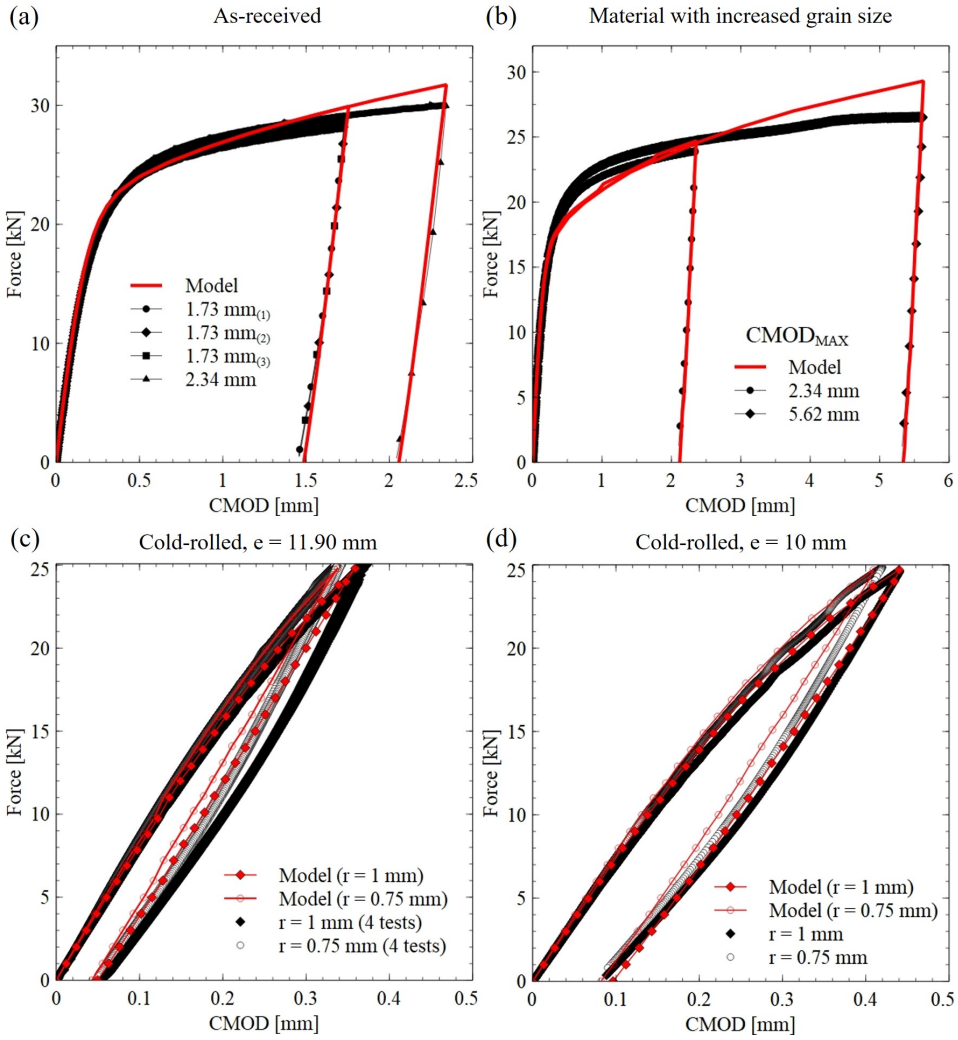

Figure 4.9: Experimental and simulated curves of force as a function of CMOD for CT specimens made of (a) as-received material (b) material with increased grain size, (c) cold-rolled material with e = 11.90 mm and (c) cold-rolled material with e = 10 mm.

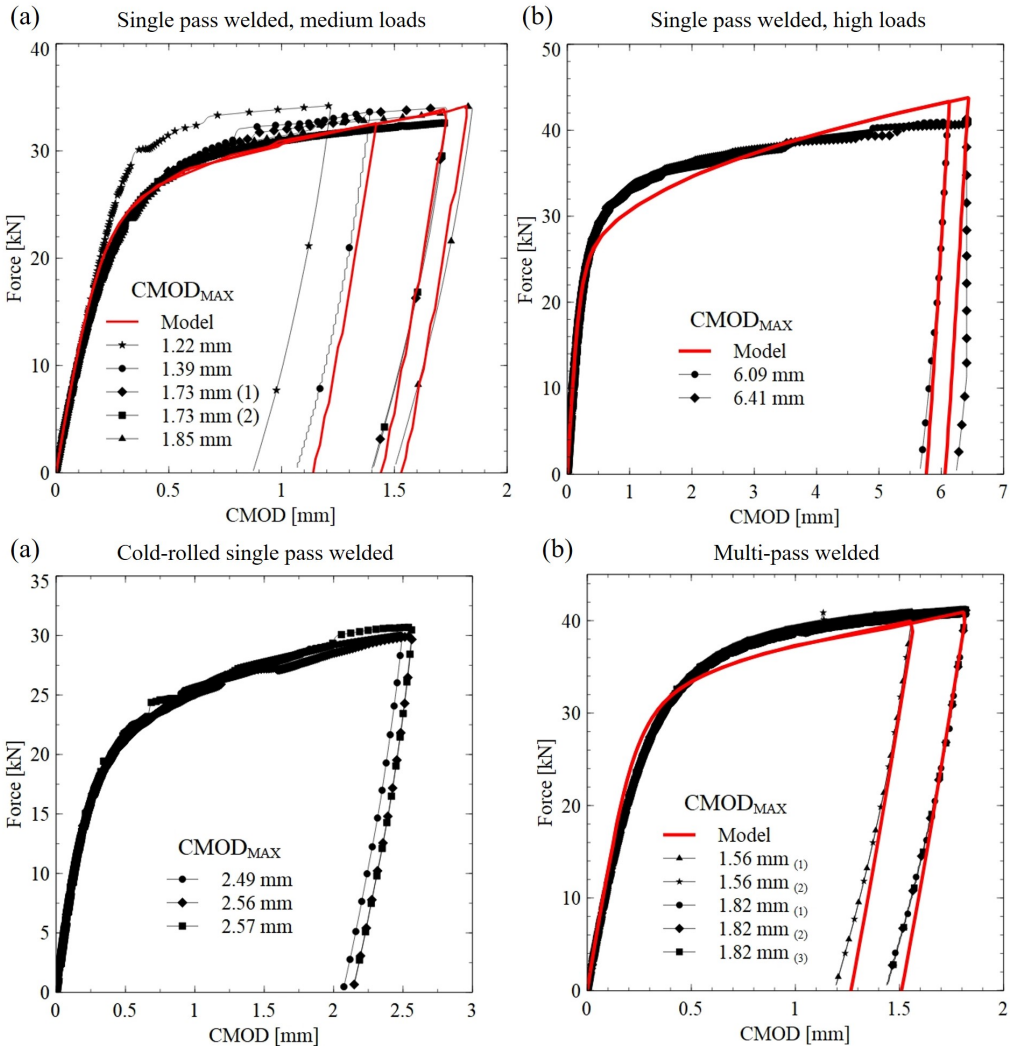

Figure 4.10: Experimental and simulated curves of force as a function of CMOD for single-pass welded state at (a) medium and (b) high loads, (c) cold-rolled and single pass welded, and (d) multi-pass welded states.

calculated simulating the compression test. Similarly to single-pass welded plate, residual stresses in compressed CT specimens were measured by X-ray diffraction method using a copper source. However, the same issues were encountered, and resulting data could not be used. Specifically for the compressed CT, it is possible that the compression induced a slight texture of the material near the notch (highest strain region) and thereby biased the results. Besides, the huge stresses and strain gradients formed at the notch after the Turski compression (up to 700 MPa within 1 mm) made measurement very difficult. Because of that, quantification of residual stresses and strain in the compressed CT specimens for this work were exclusively estimated by FEM simulations.

The macroscopic experimental and simulated responses for each material state during Turski compression tests were shown to be in good agreement in previous section, which gave confidence in the prediction of residual stresses and strain fields via these simulations. A typical simulated residual stress field at mid-thickness of an unloaded compressed specimen is shown in Figure 4.12. After unloading, the highest levels of residual stresses and plastic strain were very localized near the notch root (Figure 4.12 (a)). Because of these high stresses and strains, this region was considered to be the most favorable to stress relaxation damage and thus constituted the region of interest for damage analyses, as it will be shown in Chapter 5. Cutting numerically the CT specimen at the notch root in the (YZ) plan allowed investigating the evolution of residual stresses across the thickness (Figure 4.12 (b)). In the case of CT specimens made of welded materials, this corresponded to an evolution across the different weld zones. As plotted in Figure 4.12 (c), residual stresses at the surface of CT-like specimens were lower than at mid-thickness (Z/2), meaning that the top surface of the FZ was submitted to lower residual stresses than the HAZ. However, the region between Z = 2.5 and 4.5 mm, containing all the three weld zones, presented very similar levels of residual stresses. This specific region would thus allow investigating the effect only of the heterogeneous microstructure on SRC. This represents a strong advantage over other types of weld samples used in other SRC testing methods, such as the Borland specimen (Section 1.4.3), where the residual stress fields are not equivalent throughout the different weld zones.

Simulated residual stresses, σ_{YY}, and cumulated plastic strain, p, computed at mid-thickness for non-welded and welded states are shown in Figures 4.13 and 4.14, respectively. Estimated maximums of σ_{YY} and p after Turski compression for all material states are summarized in Table 4.3. Because the different material states did not have the same levels of initial plastic strain prior to Turski compression, cumulated plastic strain curves plotted in Figures 4.13 and 4.14 also account for prior strain related to hardening due to cold-rolling or welding to be more relevant.

Numerical predictions for the as-received state and material with increased grain size showed that these material states, compressed to the same CMOD of 2.34 mm, had relatively different values of residual stresses but similar cumulated plastic strain (Table 4.3). Turski compression of the specimen made of as-received material allowed reaching higher residual stresses for similar plastic to the material with increased grain size. Such differences should mainly be related to difference in grain size between both material states. Closer residual stresses magnitudes between the two states were achieved compressing a specimen in as-received state to 1.73 mm and material with increased grain size specimen to 5.62 mm.

Computed residual stresses and plastic strain curves for the cold-rolled state are shown in Figure 4.13 (c). Because of cold-rolling, cumulated plastic strain after compression was high over the entire specimen. Near the notch root, plastic strain magnitudes were comparable to the ones obtained for the as-received state. Prior cold-rolling allowed reaching much higher levels of residual stresses by Turski compression for lower CMODs. Distribution and magnitudes of residual stresses were very similar to results found in the literature

for similar steels [45, 47].

In order to verify that the considerations of the heterogeneous welding microstructure were relevant, simulations of Turski compression performed with two different sets of model parameters were computed and compared with experimental compression curve of a CT made of single-pass welded material. In that sense, while using the same CT specimen geometry and compression conditions, one Turski compression was performed using model parameters of the as-received state and a second one using parameters of the single-pass welded state. The comparison of the three curves is shown in Figure 4.11. This revealed that the simulated compression curve using model parameters of the single-pass welded state was closer to the experimental one that that using as-received parameters. These results showed that accounting for the heterogeneous welding microstructure allowed a better prediction of the mechanical response and was thus relevant for the study.

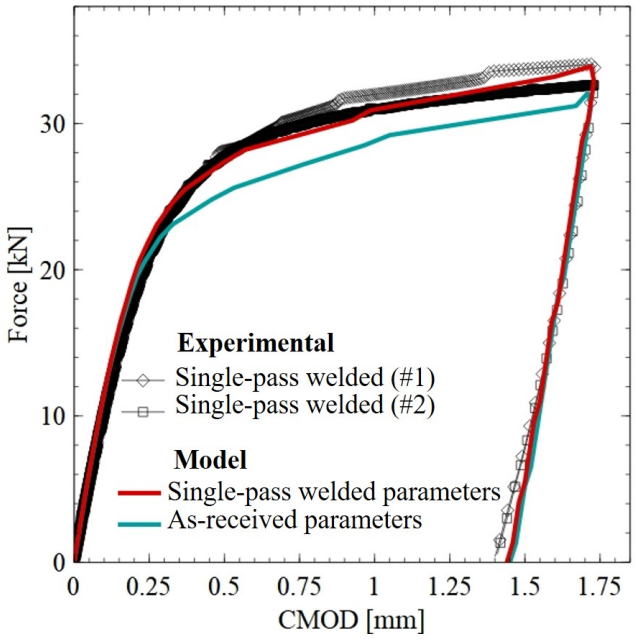

Figure 4.11: Comparison of experimental compression curve of a single-pass welded specimen compressed to a CMOD of 1.73 mm and simulations using single-pass welded (red) and as-received (blue) model parameters. Plotted force and CMOD are in absolute values.

Residual stresses and cumulated plastic strain profiles were then computed for the single and multi-pass welded states using parameters identified for the FZ and HAZ, as discussed in Section 4.2.1. Results for both material states are shown in Figures 4.14 (a) and (b).

Specimens made of single-pass welded material compressed to CMODs of 6.09 and 6.41 mm aimed to generate residual stresses with magnitudes comparable to the ones obtained for the cold-rolled state. However, much higher cumulated plastic strain was observed, as shown in Figure 4.14 (a), due to the initial material state compared to the cold-rolled material. The specimens in single-pass welded state compressed to CMODs of 1.39, 1.73 and 1.85 mm aimed to generate residual stresses with magnitudes comparable to the ones obtained for the as-received state and that with increased grain size, but also to the multi-pass welded state compressed to CMODs of 1.56 and 1.82 mm shown in Figure 4.14 (b). The response of the specimen in single-pass welded state compressed to a CMOD of 1.22 mm was not simulated because the experimental force-CMOD curve was found to be too different from other specimens.

From the predictions of residual stresses and plastic strain for each specimen of each

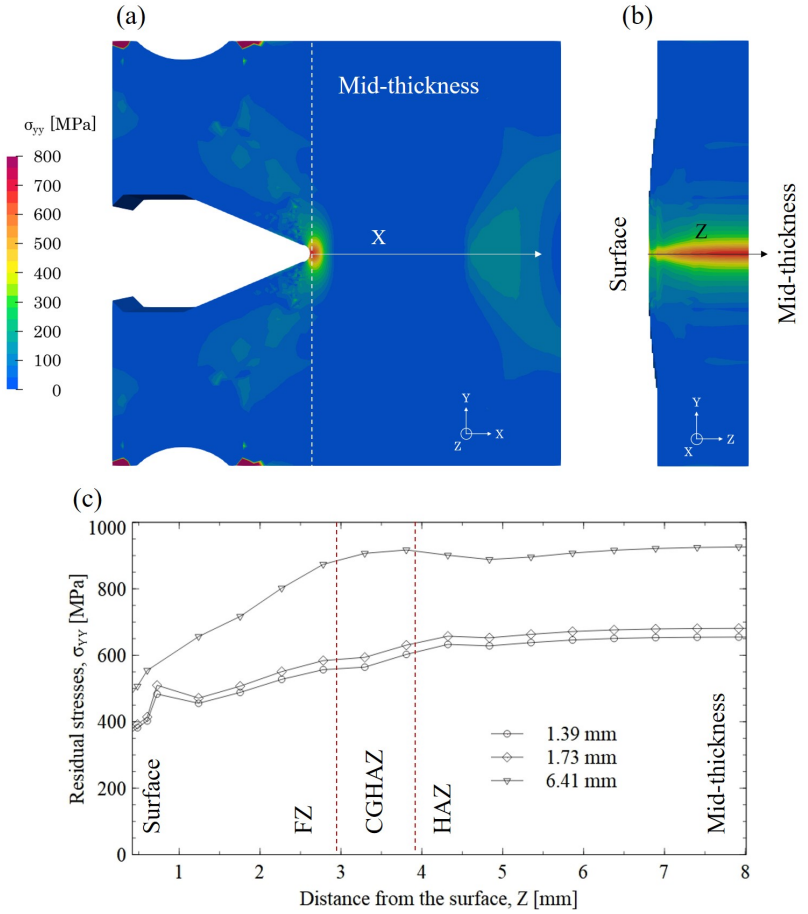

Figure 4.12: Computed residual stresses fields for single-pass welded state, with σ_{YY} stress fields at (a) mid-thickness and (b) at the notch of a CT-like specimen compressed at a CMOD of 1.73 mm. (c) shows the evolution of σ_{YY} at the notch across the thickness (i.e. across the weld zones) for three CMODs: 1.39, 1.73 and 6.41 mm.

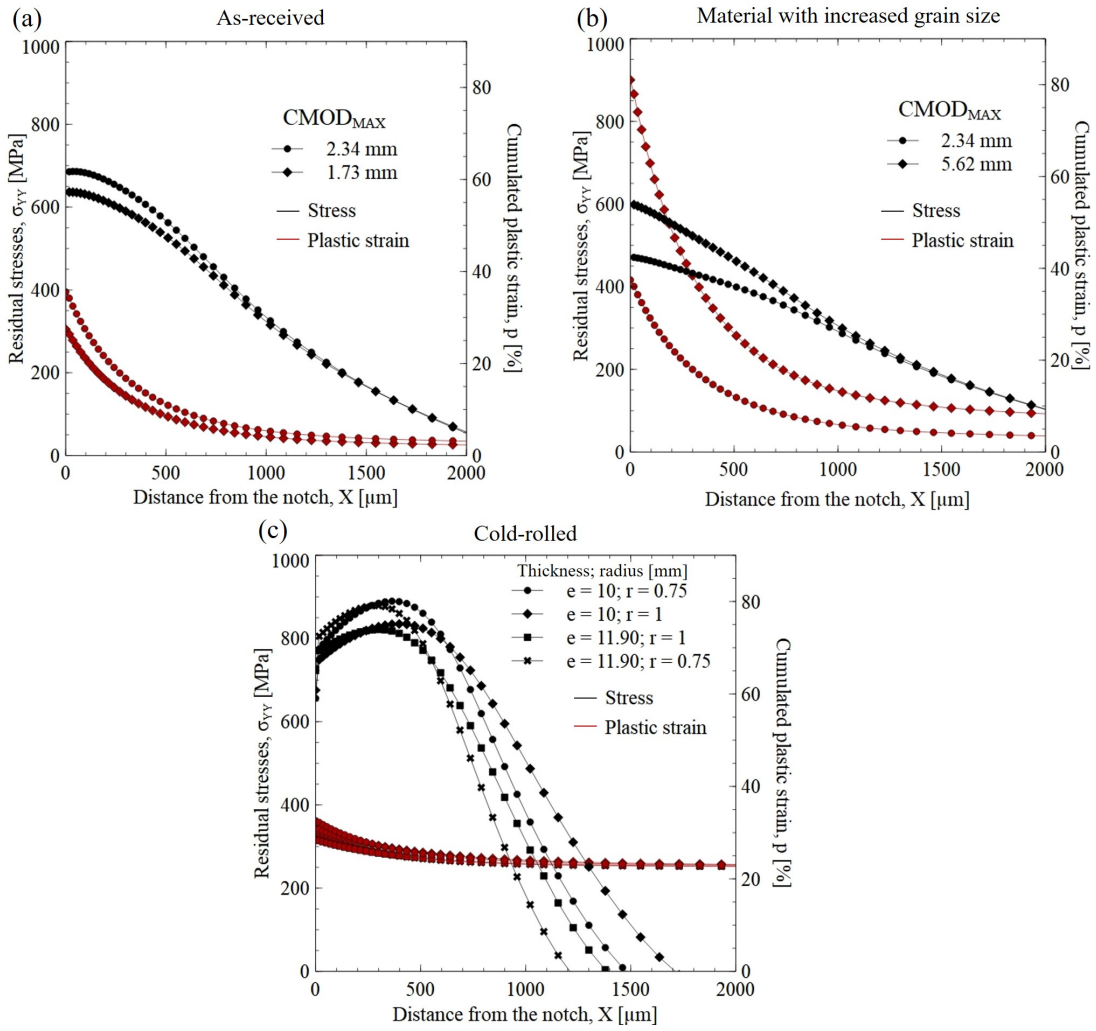

Figure 4.13: Computed residual stress, σ_{YY}, and cumulated plastic strain, p, at mid-thickness after compression unloading for (a) as-received state, (b) material with increased grain size and (c) cold-rolled state.

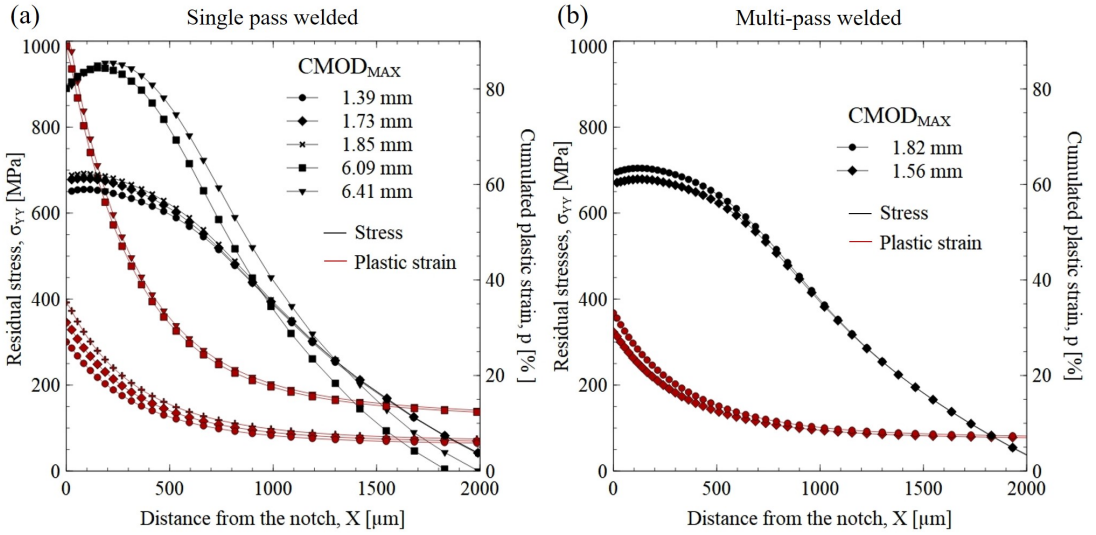

Figure 4.14: Computed residual stress, σ_{YY}, and cumulated plastic strain, p, at mid-thickness after compression unloading for (a) single-pass and (b) multi-pass welded states.

Table 4.3: Experimental and simulated maximum values obtained for all material states after compression loading ($CMOD$ and F) and unloading (σ [MPa] and p), along with the maximum experimental/simulation difference Δ and samples thickness e (measured at weld for welded states). "AR" stands for as-received material, "MIGS" for material with increased grain size, "CR" for cold-rolled, "1W" for single-pass welding, "5W" for multi-pass welding and "CR-1W" for cold-rolled single-pass welded.

State	$CMOD$ [mm]	F [kN]	σ [MPa]	p [%]	$\Delta_{sim-exp}$ [%]	e [mm]
AR	1.73	28	636	27	4	15.5
	2.34	30	686	36	5	15.5
MIGS	2.34	24	471	37	6	14.6
	5.62	27	599	81	9	14.6
CR	0.37	25	822	28	9	11.9
	0.34	25	879	30	7	11.9
	0.44	25	835	31	4	10.0
	0.42	25	890	33	7	10.0
1W	1.22	34	-	-	-	16.5
	1.39	34	655	27	5	16.5
	1.73	34	681	31	4	16.5
	1.85	34	692	35	3	16.5
	6.09	41	938	89	6	16.5
	6.41	41	949	93	7	16.5
5W	1.56	41	679	29	5	21.0
	1.82	41	704	33	4	21.0
CR-1W	2.49	30	-	-	-	13.9

material state shown in Table 4.3, it is possible stating on the expected stress relaxation damage following the heat treatment. In all of the compressed specimens, predictions of plastic strain suggested levels higher than the threshold of 10% estimated by Chabaud [18]. However, some specimens presented lower residual stresses values than the SRC threshold of 740 ± 40 MPa suggested by Pommier [45]. Compressed specimens with lower residual stresses than the stress threshold were then expected to develop at most mild damage, in the form of grain boundary cavities, or at lowest no damage at all, while specimens with residual stresses higher than the threshold were expected to develop cracks. Typically, stress relaxation cracks could be expected in all CT specimens made of cold-rolled state and in the CT specimens made of single-pass welded state compressed to CMODs higher than 6 mm. In all the other specimens presenting residual stresses relatively lower than the threshold, cavities could be expected at most.

4.4 Summary and conclusions

In this Chapter, a compression loading followed by unloading, named Turski compression, was applied to CT-like specimens machined from each investigated material states to generate controlled levels of tensile residual stresses and plastic strain.

Each material state was exposed to various compression loads, aiming for different levels of SRC-driving forces, i.e. residual stress and strains, consequently aiming for different levels of damage after relaxation. To estimate residual stresses and strain fields after the unloading, 3D FEM simulations of the Turski compression were carried out. The Chaboche elasto-plastic model was used, with parameters accounting for each type of microstructure. Kinematic parameters of the model were determined from tension-compression and compression-tension tests of the as-received and cold-rolled states. In

order to identify the material parameters related to the isotropic hardening, tensile tests of the as-received, material with increased grain size and single-pass welded states were carried out. The tensile behavior of the different weld zones was assessed using 1 mm thick dog-bone shaped samples. Specifically for the single and multi-pass welded materials, a heterogeneous mesh was made accordingly to the macrographic observations of welded plate sections, accounting for the shape of the welds and the different properties of the weld zones.

The mechanical study of the different material states led to several conclusions:

- In agreement with hardness measurements presented in Chapter 3, strain hardening was revealed in the HAZs of both single and multi-pass welded materials as compared to the FZ and CGHAZ but also to the as-received state.
- The macroscopic Force-CMOD experimental response of each material state to the Turski compression was compared to simulation results, showing overall good agreements. This suggested that simulations were trustworthy to estimate residual stresses and strain fields generated by the compression.
- In CT specimens made of single and multi-pass welded materials, the residual stresses generated by welding were completely changed by the Turski compression and were shown to have negligible influence on the post-compression residual stresses. Welding residual stresses of welded states were thus no accounted for the rest of the study.
- The residual stress level gradient through the sample thickness computed by simulation was estimated to be rather low so that the different weld zones could be considered to be subjected to similar residual stress levels.
- Simulations revealed that it was not possible to achieve similar levels of both residual stresses and plastic strain at the same time between the different material states. As a consequence, comparison of mechanical state following the compression could only be made either by the final CMOD, the maximum residual stress or maximum cumulated plastic strain level, but not all of them simultaneously.
- From the comparison with the SRC stress and plastic strain thresholds found in the literature, simulation results showed that some of the compressed specimens for each state could be expected to develop stress relaxation cracks, others only cavities or no damage at all.

Chapter 5

Stress relaxation cracking tests and damage analysis

Contents

To investigate the sensitivity of the studied 316L(N) steel within acceptable time, SRC tests were conducted by compressing and unloading (Turski compression) CT-like specimens for each material state, generating controlled levels of stresses and plastic strain, as detailed in Chapter 4. Following the Turski compression, specimens were heat treated in a furnace for 580 and 1470 h at 575 and 600 °C to relax residual stresses. Specimens were further cut by EDM (electrical discharge machining). Subsequently, damage was characterized according to the procedure detailed in Chapter 2.

The present Chapter first describes the analysis of stress relaxation damage in non-welded specimens, which includes the as-received and cold-rolled states. Damage type, location and damage levels are presented as a function of stress and strain magnitudes, stress relaxation time and temperature. Similarly, damage analyses for welded states are further presented, with details of SRC in each weld zone and comparisons between the zones. The effect of a heterogeneous microstructure on SRC is then presented. Finally, results of SRC tests of material with increased grain size are described.

5.1 As-received state

To characterize the impact of welding on SRC, the damage observed in welded states had to be compared to that in non-welded states. In this context, the CT specimens machined from material without prior welding were first studied. Particularly, SRC tests were initially carried out on CT specimens made from as-received state of the 316L(N) steel. These were compressed to CMODs of 1.73 and 2.34 mm at room temperature, heat-treated at 575 °C for 580 and 1470 h, then analyzed.

5.1.1 Damage analysis

Optical analyses of a CT specimen compressed to a CMOD of 1.73 mm and further aged at 575 °C for 1470 h were carried out at half-thickness (Z = 7.75 mm) in the (XY) plane (Figure 5.1 (a)), following the process detailed in Section 2.6. These did not reveal any damage at a macroscopic scale, as shown in Figure 5.1 (b). Further SEM investigations revealed mild damage near the notch root in the form of grain boundary cavities similar to creep cavities (Figure 5.1 (c) and (d)), which were not observed prior to the heat treatment. These presented sizes ranging from a few tenths of nm to a few microns and often located at GBs perpendicular to the compression axis (Y axis). A total of 41 cavities was observed, with five GBs containing more than one cavity, and a maximum of 8 cavities on a single GB. Damaged GBs had an average of 1.7 cavities per GB.

The distribution of these cavities near the notch root was analyzed for the CT specimens compressed to CMODs of 1.73 and 2.34 mm and subsequently aged at 575 °C for 1470 h. Damage distributions were then correlated to the predicted accumulated plastic strain (Figure 5.2) and residual stresses σ_{YY} fields (Figure 5.3) estimated from simulations of the Turski compression previously presented (Figure 4.14). The number of cavities was also investigated along the X axis in Figure 5.6 (a). The highest number of cavities was found close to the notch root (X = 0 μm), which then abruptly decreased for distances from the notch higher than 200 μm. This appeared to follow the distribution of residual stresses and accumulated plastic strain shown in Figure 5.6 (a). Particularly, damage distribution seemed to be related to the sharp decrease of plastic strain near the notch. For the present case, simulation results suggested that the furthest cavity from the notch root nucleated for residual stresses of about 310 MPa and cumulated plastic strain of 5%. The precise determination of cavity nucleation stress and strain thresholds is a very challenging task since observations are carried out on one section of the CT specimen and thus other cavities might be present further away from the notch if analyses were performed in another section of the same specimen. Instead, it was rather estimated that a more significant number of cavities appeared for residual principal stresses higher than 590 MPa and cumulated plastic strain higher than 13%. The absence of cracks in the specimen is in agreement with the maximum predicted residual stresses, lower than the SRC threshold of 740 MPa suggested by Pommier [45] for a cold-rolled 316L(N) steel of similar composition. However, as compared to Pommier's results, the distribution of damage observed here is slightly different: as shown in the literature review (Figure 1.25), Pommier observed the maximum of damage at a distance of 200 μm from the notch root. This is due to the distribution of residual stresses, which in the case of Pommier presented a maximum near 200 μm from the notch root. Besides, Pommier carried out SRC tests using priory cold-rolled CT specimens, thus the distribution of initial plastic strain was also very different.

In the specimen compressed to a CMOD of 2.34 mm, a total of 85 cavities was observed at mid-thickness of CT specimen, more than the double of that observed after Turski compression to a CMOD of 1.73 mm. Twenty GBs contained more than one cavity, four times higher than that found for the CMOD of 1.73 mm. In average, damaged

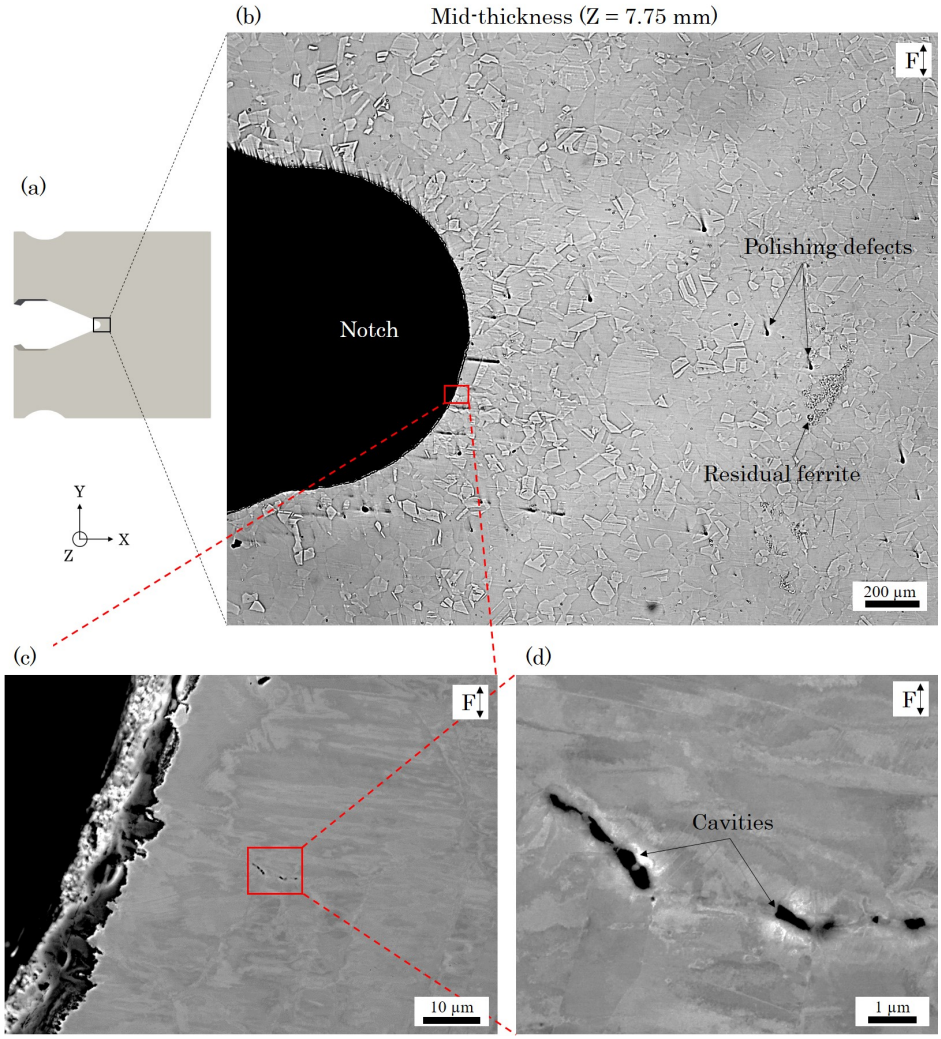

Figure 5.1: Damage analysis at mid-thickness (Z = 7.75 mm) in the (XY)-plane of a CT specimen made from as-received state compressed to a CMOD of 1.73 mm and aged at 575 °C for 1470 h. (a) Location of the analysis and (b) optical image of the notch, (c) and (d) SEM-BSE images of grain boundary cavities.

GBs presented a total of 1.9 cavities, also higher than that for the CMOD of 1.73 mm. These results showed that the increase in Turski compression load induced a higher total number of cavities, but also an increase in damage level per GB. Spatial distribution of cavities compared to predicted post-Turski compression cumulated plastic strain and residual stresses σ_{YY} fields are shown in Figure 5.4 and 5.5, respectively. The number of cavities was also projected along the X axis, shown in Figure 5.6 (b). Results of distribution are very similar to the specimen compressed to a CMOD of 1.73 mm, with again a maximum of cavities near the notch root, and an abrupt decrease after a distance of X = 200 μm. Surprisingly, the higher Turski compression did not allow cavities nucleating further away from the notch. Instead, damage level increased locally.

Comparison of spatial distribution of cavities and residual stress-strain fields for both specimens showed again that cavities appeared to be preferentially located in the highest strained regions, instead of highest stresses regions. Surprisingly, the closest point to the notch root, being at X = Y = 0 μm, appeared in both specimens to be depleted in cavities while this corresponded to the highest stress and strain. Similar observations can be made from Pommier's results [45], where macroscopic damage seemed to be distributed

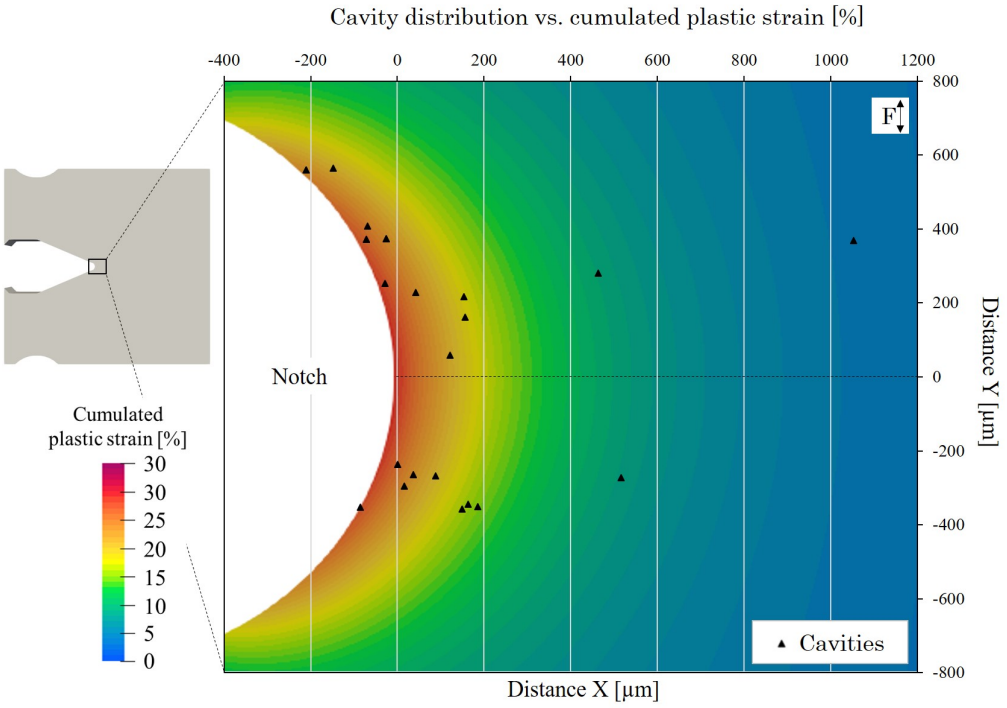

Figure 5.2: Comparison between post-Turski compression cumulated plastic p strain and post-ageing (575 °C for 1470 h) spatial cavity distribution at the notch at half-thickness in the (XY) plane of CT specimen of as-received state compressed to a CMOD of 1.73 mm.

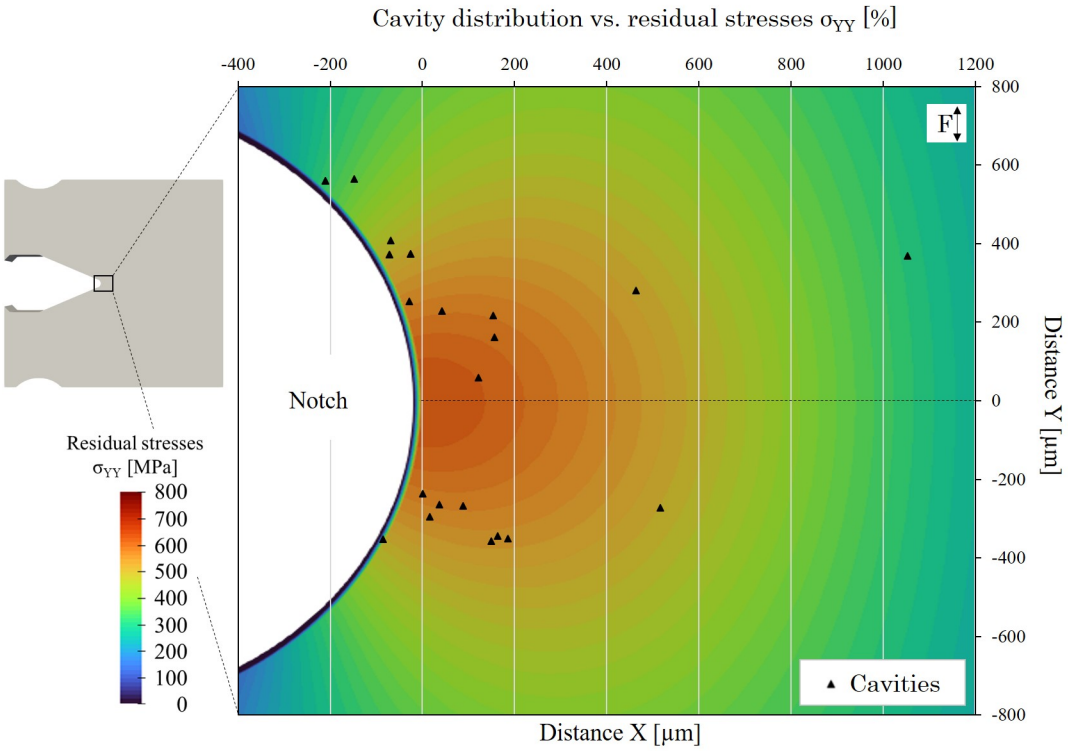

Figure 5.3: Comparison between post-Tuski compression residual stresses σ_{YY} and post-ageing (575 °C for 1470 h) spatial cavity distribution at the notch at half-thickness in the (XY) plane of CT specimen of as-received state compressed to a CMOD of 1.73 mm.

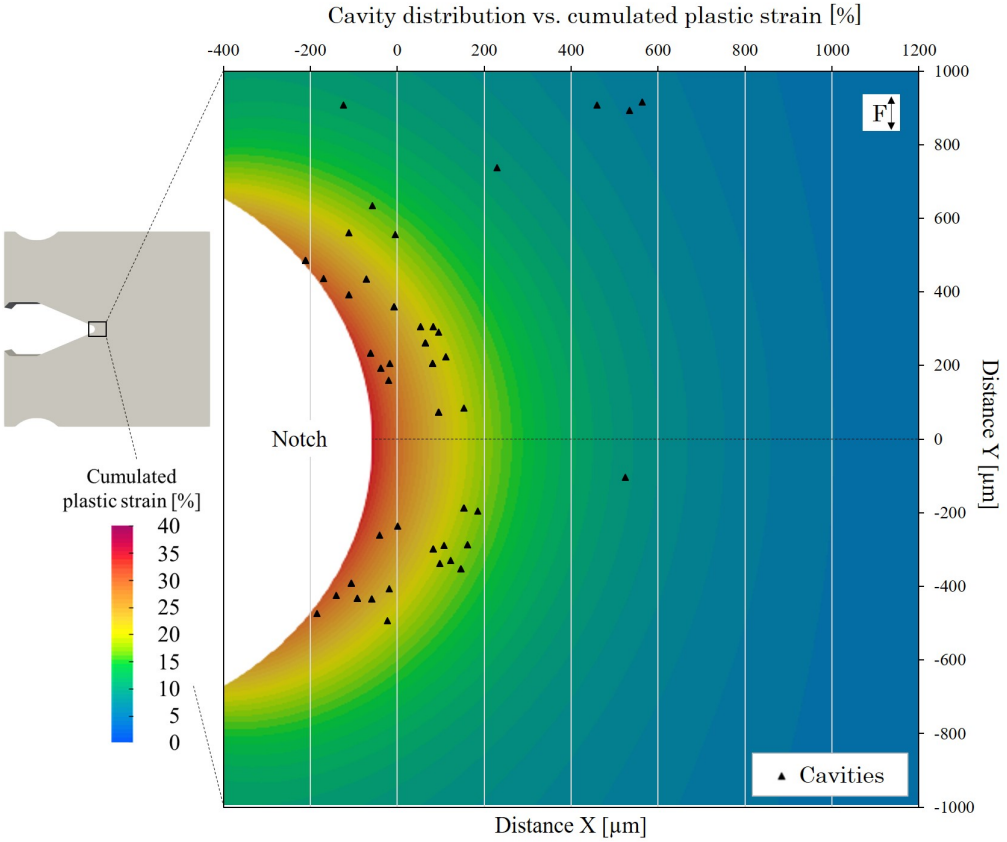

Figure 5.4: Comparison between post-Turski compression cumulated plastic strain p and post-ageing (575 °C for 1470 h) spatial cavity distribution at the notch at half-thickness in the (XY) plane of CT specimen of as-received state compressed to a CMOD of 2.34 mm.

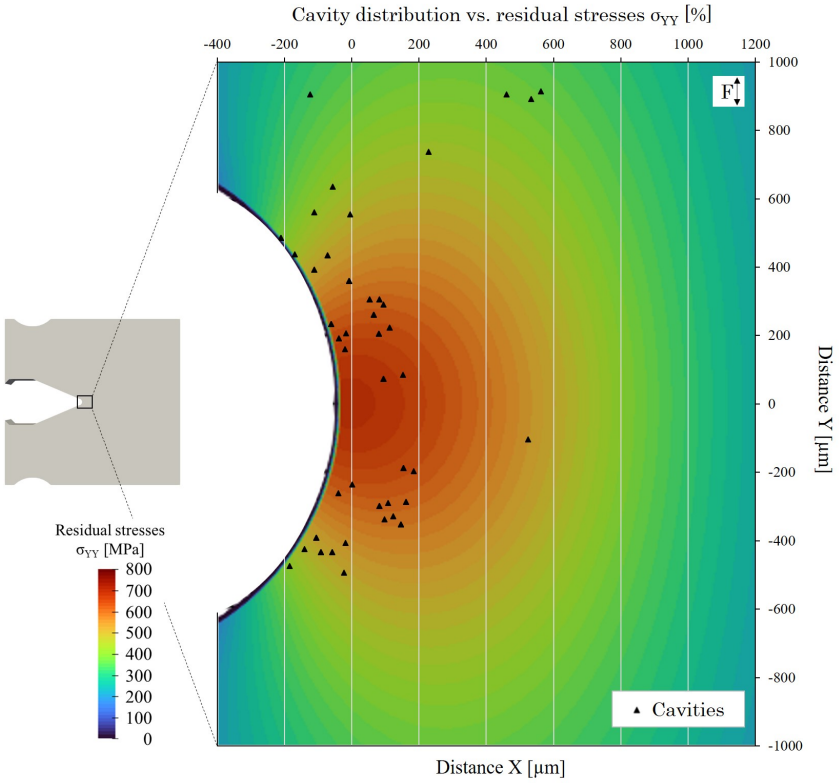

Figure 5.5: Comparison between post-Turski compression residual stresses and post-ageing (575 °C for 1470 h) spatial cavity distribution at the notch at half-thickness in the (XY) plane of as-received CT specimen compressed to a CMOD of 2.34 mm.

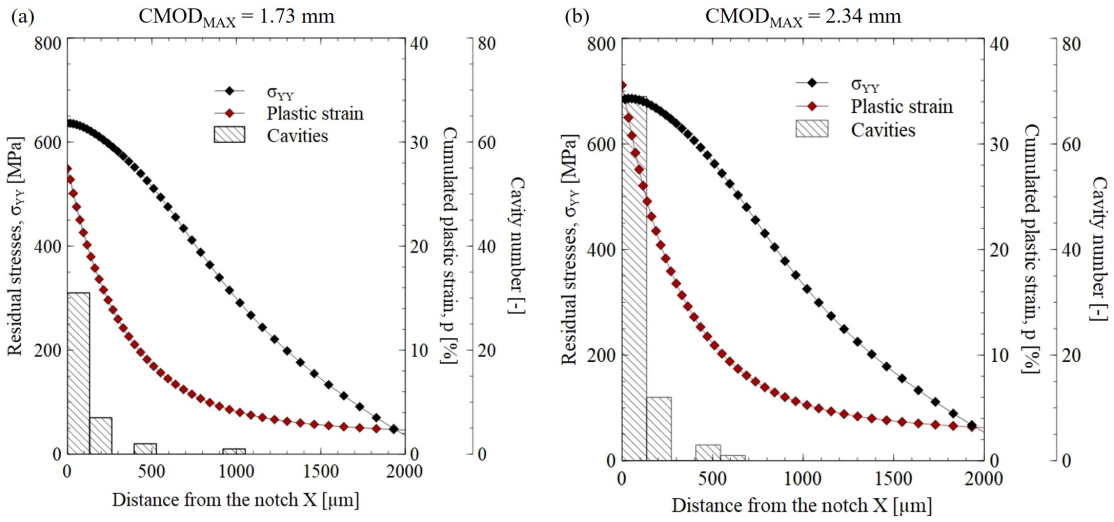

Figure 5.6: Comparison between post-Turski compression residual principal stresses σ_{YY} and post-ageing (575 °C for 1470 h) cavity distribution at half-thickness in the (XY) plane of CT specimen of as-received state compressed to a CMOD of (a) 1.73 and (b) 2.34 mm.

around the highest residual stresses point. It is important keeping in mind that mechanical simulations were carried out using continuum mechanics hypotheses, thus cannot account for local heterogeneities due to the microstructure. It is thus possible that the Turski compression induces local features at a microscopic scale which could not be revealed with simulations used here.

The investigation of damage in these two specimens first showed that it is possible to observe damage induced by stress relaxation in the studied 316L(N) steel. Secondly, these first results showed that the levels of stresses typically measured in industrial multi-pass welds (about 450 MPa) would not be sufficient to induce severe relaxation damage (cracks) in a weld joint made of 316L(N) steel. Besides, these results showed that it was possible to trigger SRC in laboratory conditions in a material in an as-received state without prior cold-rolling, pre-ageing or welding. This is a new result as compared to methods commonly used in the literature to test SRC (Section 1.4.3) and could lead to the development of new approaches for evaluating the susceptibility of different alloys to SRC, requiring less processing steps and ensuring better results repeatability. In addition, results also showed that while the damage was influenced by residual stresses, in agreement with results of the literature, plastic strain appeared to play a more important role. As a result, high residual stresses were not sufficient to induce stress relaxation damage in regions where plastic strain was too low. This is also a significant result since residual stresses are most often cited in the literature as the main driving factor for SRC [45]. Plastic strains are very important to consider in an industrial context as well: even though plastic strain resulting from the welding process may not be sufficiently high to induce SRC, especially in SRC resistant steels, additional plastic strain can be induced by operating errors. For instance, Picker and Fraser [207] observed several stress relaxation cracks in reheater and superheater (evaporator components) initiated at regions where severe deformation was present, due to heavy grinding before rectification welding. For these reasons, control of welding process quality is also primordial when looking to prevent SRC.

5.1.2 Damage nucleation sites

Further SEM investigations were carried out on damaged CT specimens made of as-received state of 316L(N) steel to identify microstructure features involved in cavity nucleation and growth. Figure 5.7 (a) suggests that the cavities nucleation occurred at the interface between precipitates and austenite, mostly at grain boundaries, in agreement with observations made by Pommier [45]. The interface between matrix and precipitates most certainly presented favorable sites for cavity nucleation due to its high energy, but also due to stress concentration at precipitates tips during relaxation as demonstrated numerically by Cui [208] for creep cavitation. These precipitates were assumed to be mainly chromium carbides, according to TEM analyses carried out in thermally aged as-received state presented earlier (Figure 3.8). In addition, chromium carbides were identified in damaged CT specimens made of cold-rolled state presented further in Section 5.2. Cavities were found either to be single (Figure 5.7 (a)), coalesced (Figure 5.7 (b)) or multiple at the same GB (Figure 5.7 (c)).

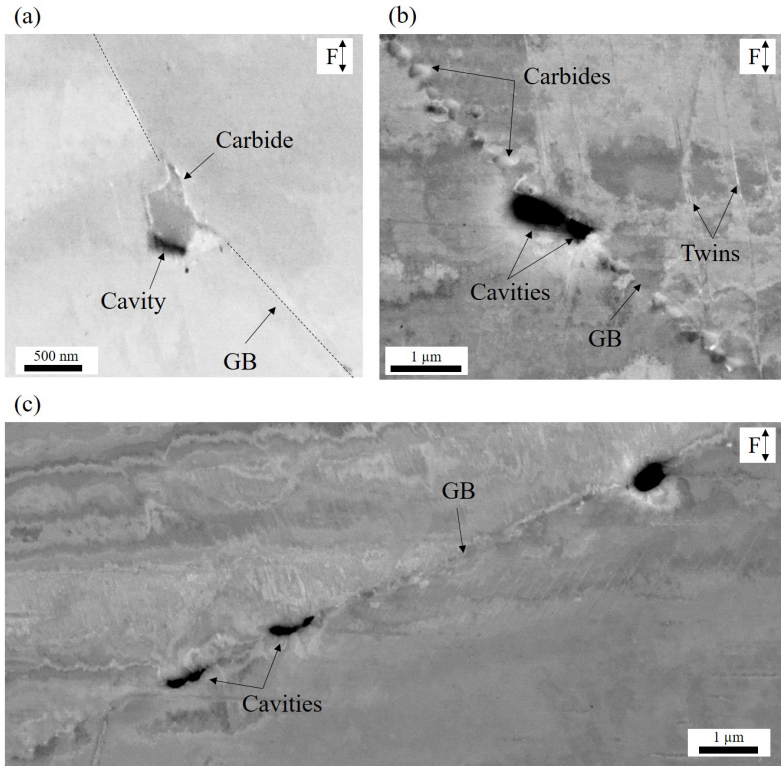

Figure 5.7: SEM images taken near the notch root at half-thickness in the plate (XY)-plane and showing stress relaxation intergranular damage of a CT specimen made of as-received state, compressed to a CMOD of 1.73 mm and aged at 575 °C for 1470 h. (a) SE image of a single cavity, (b) BSE image of coalesced cavities and (c) multiple cavities. F indicates the direction of the Turski compression load.

5.2 Cold-rolled state

Cold-rolling was applied to the 316L(N) steel in order to reproduce the hardening observed in the HAZs of welds, considered in literature as the weld zone most prone to the SRC phenomenon. Similar approach was used for SRC testing by Turski *et al.* [47], Chabaud [18] and more recently by Pommier [45], for different grades of austenitic stainless steel. The "IB" steel in the latter study had a composition and microstructure similar to the material of the present study. One objective of the following analyses was to verify that the sensitivity to SRC is similar for notch root radii of 1 mm. In comparison to the as-received state, this also allowed studying the effect of plastic strain in the whole specimen as a first SRC driving factor. CT specimens machined from cold-rolled plate were tested at both 575 and 600 °C, for 580 and 1470 h. A specimen aged at 600 °C for 580 h is first presented for illustration purpose as it presented the highest damage of all cold-rolled specimens.

5.2.1 Damage analysis

Optical analyses of a CT specimen made of cold-rolled state compressed to 25 kN[1] (CMOD = 0.37 mm) and aged at 600 °C for 580 h were carried out at half-thickness in the (XY) plane (Figure 5.8 (a)). Optical analyses of the specimen did not reveal any damage at a macroscopic scale, as shown in Figure 5.8 (b). Further SEM investigations of

[1]For CT specimens machined from cold-rolled plate, Turski compression was carried out aiming a maximum force instead of a CMOD as for other states. See section 4.3 for additional information.

this region revealed mild damage in the form of grain boundary cavities similar to creep cavities at the notch root, as shown in Figure 5.8 (c) and (d). Similarly to CT sample made of as-received state, stress relaxation damage was quantified in CT sample made of cold-rolled state counting cavities near the notch root.

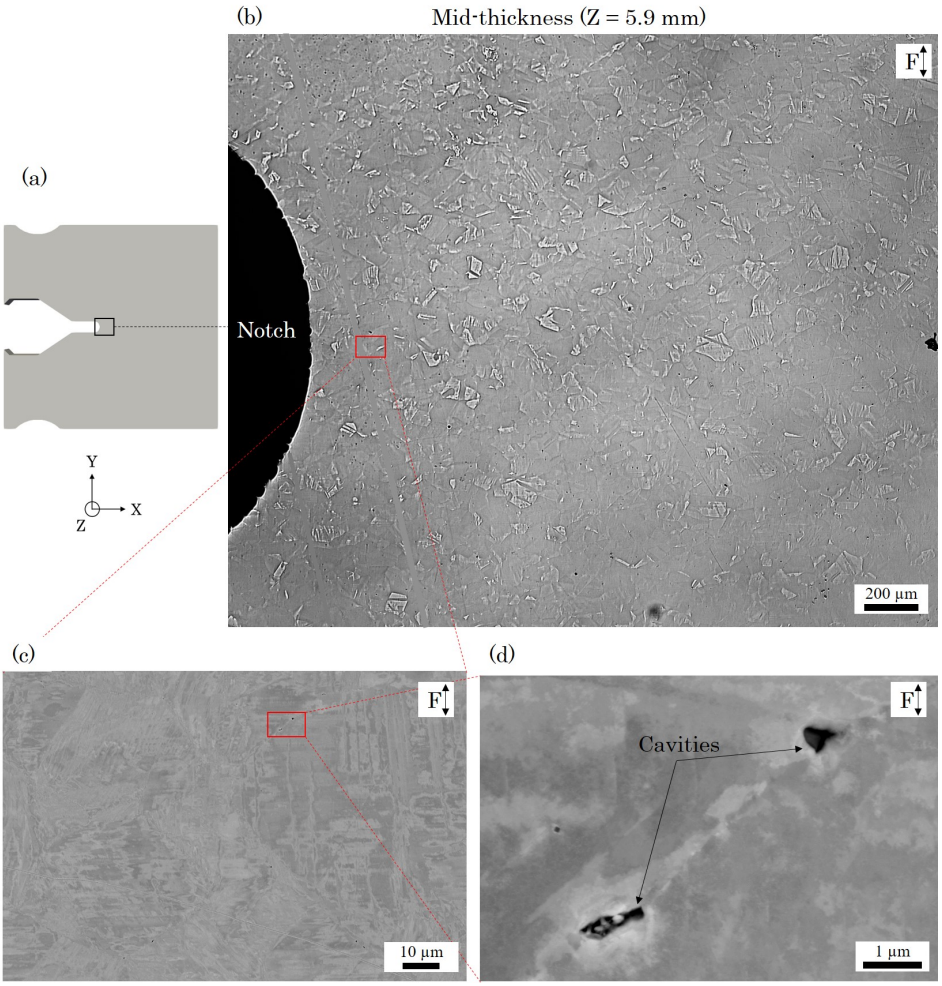

Figure 5.8: Damage analysis at mid-thickness in the (XY)-plane of a CT specimen made of cold-rolled state compressed to 25 kN (CMOD = 0.37 mm) and aged at 600 °C for 580 h: (a) analysis area, (b) optical image of the region close to the notch, (c) and (d) SEM-BSE images of grain boundary cavities.

In specimens aged at 575 °C for 580 h, the observed damage near the notch root was very low, with about 10 cavities spread over a 2 × 2 mm^2 region and located on the sides or tips of grain boundary carbides, as shown in Figure 5.10 (a) and (c). The detected cavities measured from 50 to 200 nm in length and a few nm wide. For this ageing condition, the difference of notch radius did not appear to induce significant effect on the number, distribution or size of cavities (Figure 5.9 (a)). As shown in Figure 4.14 (c), an increase in the notch radius from 0.75 to 1 mm actually led to an increase in maximum tensile residual stresses, but also to smaller area where the high residual stresses were confined. Because of this, the overall number of cavities could be expected to be similar for both notch radii, with higher maximum damage for the smallest radius.

In specimens aged at the same temperature for longer time (1470 h), the number of cavities increased (Figure 5.9 (a)), but also their size, as shown in Figure 5.9 (b). Finally, the nature of damage also changed by increasing the relaxation time: after 1470 h, some of the cavities were coalesced (Figure 5.10 (b)) and more than one cavity per GB was

observed for the smallest notch radius of CT specimen (Figure 5.10 (d)). The higher cavity number per GB for the smaller notch radius represents a higher risk for the development of cracks, due to higher probability of coalescence. These analyses showed that longer relaxation time, higher initial residual stresses and plastic strain favored the initiation of SRC damage.

In the specimen aged at 600 °C for 580 h, the highest level of damage for the cold-rolled state was observed, with a total of 51 cavities counted in the 2 × 2 mm^2 region near the notch root. This represents an increase by a factor 5 as compared to the same notch radius of CT specimen aged at 575 °C for 580 h. Additionally, a higher number of GBs presented multiple cavities (Figure 5.10 (e)), showing that the temperature of 600 °C was significantly more damaging than 575 °C. This could be explained by the higher temperature allowing a faster diffusion for the elements like C and Cr which form the carbides [209], thus increasing precipitation kinetics, as well as faster vacancy diffusion along GBs favoring cavity nucleation [141]. It is worth noting, however, that such results do not agree the observations reported by Pommier [45] for a 316L(N) steel of similar composition, where he observed higher damage after ageing at 575 °C than after ageing at 600 °C.

Interestingly, for all cases, cavities were mainly observed at GBs oriented between 70 and 90° (almost perpendicular) to the Turski compression axis (Figure 5.9 (c)) in agreement with results of Pommier [45] for a similar steel and similar relaxation conditions. This is also in agreement with what is often observed for creep damage [141], since the principal tensile stresses magnitude is higher for GBs perpendicular to the loading axis. These observations suggested that cavitation by grain boundary sliding (GBSL) cited in the literature for creep cavitation [210] was not the predominant SRC mechanism here, since it would be easier for grain boundaries forming an angle close to 45° with the loading direction, wherein the shear stress is maximal. Moreover, cavity nucleation by GBSL can occur without precipitates while all cavities observed in this study were exclusively located on precipitates. Instead, cavity nucleation by vacancy accumulation and dislocation pile-ups [211] might be suggested as a mechanism to explain the observed damage. The maximum principal residual stress (oriented in the Y direction) then seems to play a role in the nucleation of cavities from precipitates.

5.2.2 Damage comparison with post Turski compression simulations

Since the specimen heat treated at 600 °C presented the highest number of cavities, it was chosen for comparison with results of simulations of post-Turski compression mechanical state. The comparison between observed cavities distribution, computed residual stresses and cumulated plastic strain is shown in Figure 5.11. Cavities were observed up to a distance of 2000 μm from the notch root, with a maximum concentration at X = 330 μm. This distance was coincident with the maximum principal residual stress, σ_{YY}, suggesting that it governed the distribution of cavities. However, some isolated cavities were also observed for distances higher than X = 500 μm, while the estimated principal residual stress σ_{YY} quickly decreased. On one hand, the presence of cavities beyond X = 500 μm could be eventually assisted by the presence of the principal residual stress σ_{XX} in this region, despite its lower value. On the other hand, the continuous high level of plastic strain ($> 22\%$) could still favour the presence of cavities despite the low residual stresses levels, similarly to observations made for the as-received state. This last hypothesis seems more likely, since cavity nucleation was extremely limited as soon as the plastic strain levels dropped for the as-received state.

The study of the cold-rolled state confirmed thus the importance of plastic strain in the SRC mechanism, with low levels of residual stresses associated to high plastic strain being sufficient for the apparition of damage, at least for cavity nucleation. Besides, results

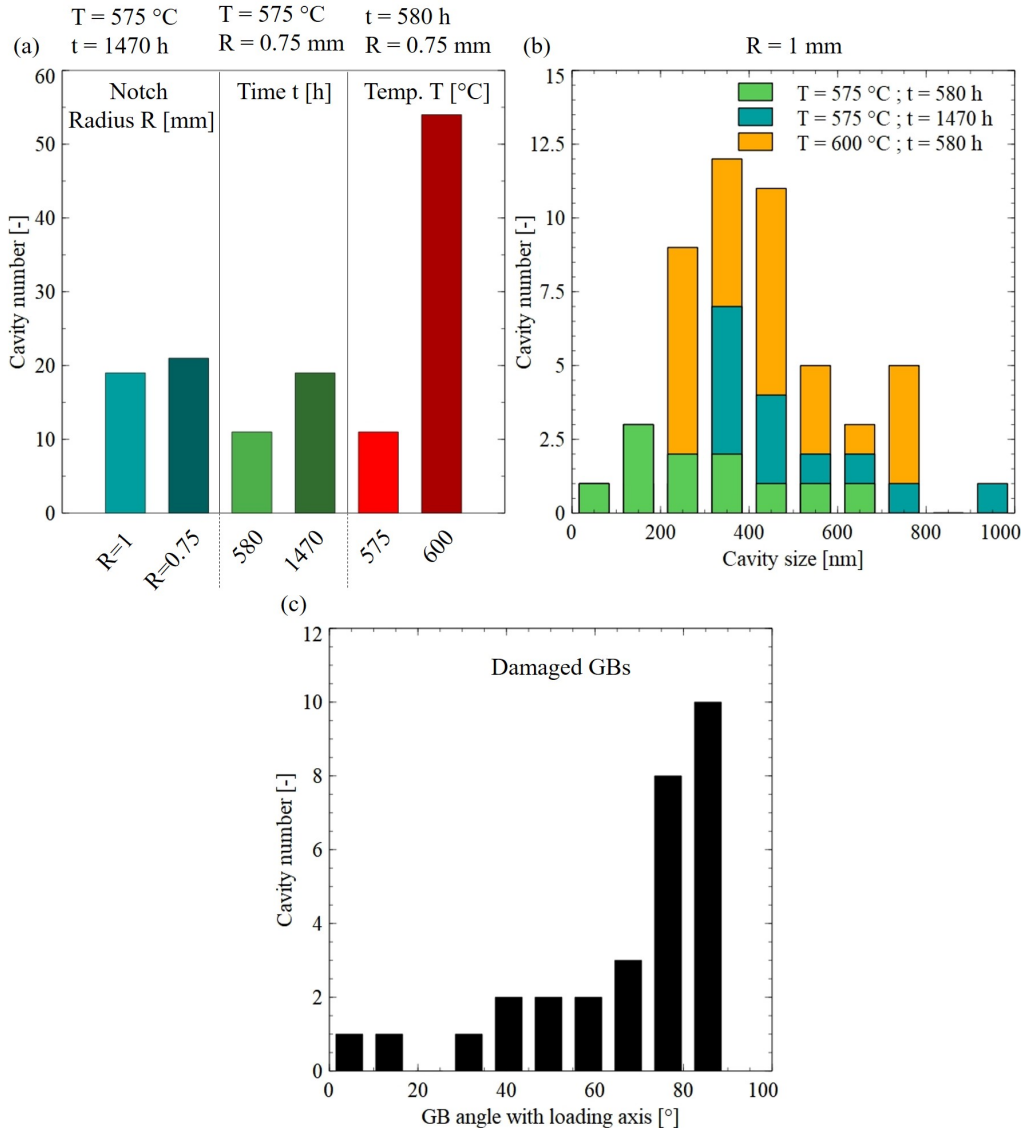

Figure 5.9: Influence of (a) notch radius, relaxation time, temperature on cavity number, (b) relaxation time, temperature on cavity size distribution, and (c) GB angle formed with the loading axis on cavity number in CT specimens made of cold-rolled material.

showed that in the presence of a homogeneous high-level plastic strain field, it is rather the residual stresses that dictate the distribution of damage.

As compared with results of Pommier [45] for a cold-rolled 316L(N) steel of similar composition, damage distribution and its correlation with residual stresses were very similar to those observed by Pommier [45]. However, the quantification of damage could not be properly compared for several reasons. First, the more obvious, it is due to the difference in the method used for damage quantification. To quantify damage, Pommier machined tensile specimens from the notch of the damaged CT specimens [45]. He incrementally deformed these specimens up to 20±3% true strain in-situ in synchrotron while performing 3D X-ray tomography top open up existing cavities and cracks, allowing the detection of damage contained in the volume of the specimen. Here, damage was directly quantified after the relaxation of stresses without additional steps and was hence much less severe. Besides, damage was analyzed only on 2D sections. As a result, damage level could be expected to be lower. In addition, difference in damage levels could also be due to difference in Turski compression magnitude: Pommier [45] predicted residual stresses

higher than 940 MPa and plastic strain higher than 29±2% in the CT specimen he used for SRC testing, while stresses of 822 MPa and strain of 28% were predicted in this work for an equivalent CT geometry.

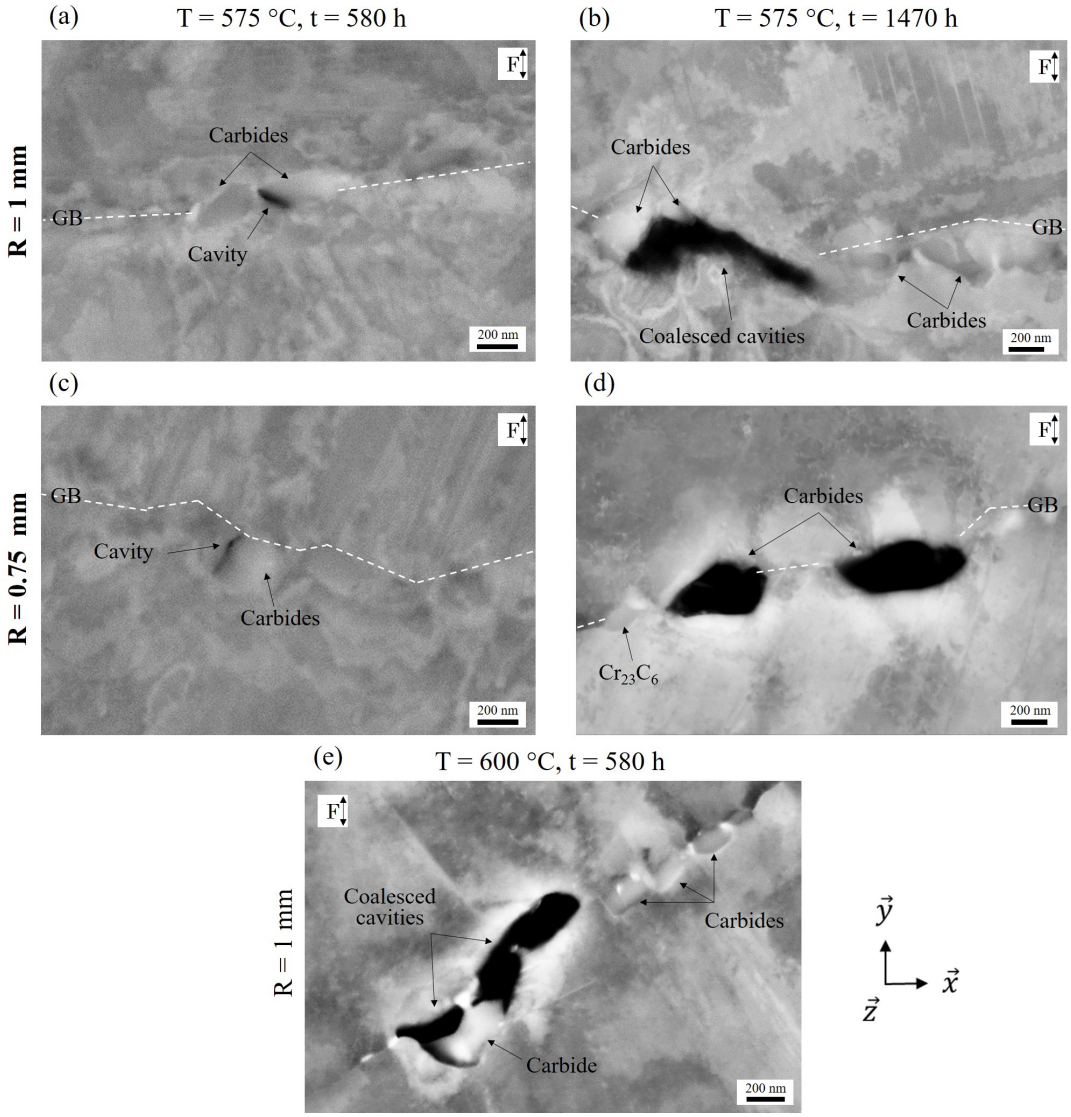

Figure 5.10: Damage formed due stress relaxation at the notch root of CT specimens of cold-rolled state compressed at 25 kN for notch radii of 0.75 (CMOD = 0.34 mm) and 1 mm (CMOD = 0.37 mm), relaxation times of 580 and 1470 h at (a) to (d) 575 °C and (e) 600 °C.

5.2.3 Damage nucleation sites

Damage was observed to be in the form of GB cavities located on different types of site, but always related to GB precipitates with similar morphology and size to the ones observed in the as-received state. Qualitative EDS analysis in SEM showed these precipitates had higher Cr/Mo but lower Fe content than the matrix. Cavities were found at the tip of these precipitates (Figure 5.12 (a)), at the interface between two precipitates (Figure 5.12 (b)), at the austenite/precipitate interface (Figure 5.12 (c)), in precipitate clusters (Figure 5.12 (d)), at a GB triple points (Figure 5.12 (e)) and less often at the austenite/precipitate interfaces in the bulk (Figure 5.12 (f)).

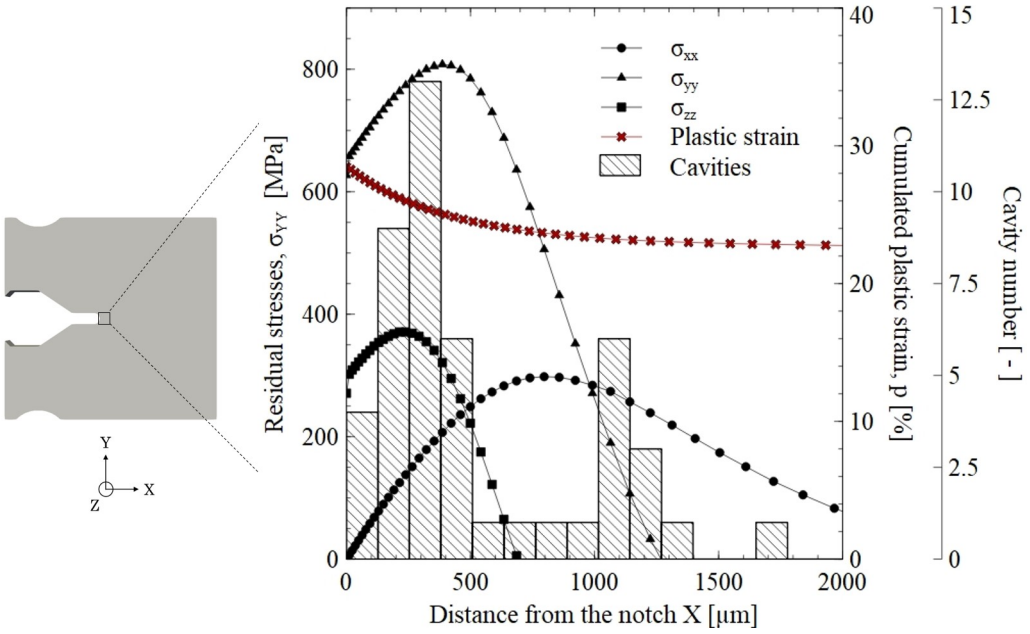

Figure 5.11: Comparison between computed post-Turski compression residual stresses, cumulated plastic strain and cavity distribution near the notch root at half-thickness in the (XY) plane of a CT specimen of cold-rolled state, compressed at 25 kN (CMOD = 0.37 mm) and aged at 600 °C for 580 h.

This is different from SRC observations made of the as-received state after SRC, where no cavity was observed in the bulk. Here, cavity nucleation sites in the bulk represented up to a maximum of 20% of the identified cavities. The particularly high plastic strain levels appeared to have favored the formation of cavity on bulk precipitates which could nucleate on dislocations within the grains. TiN, MnS and Al_2O_3 inclusions, already observed in the as-received state, did not appear to have a particular effect on SRC since very few cavities were observed on these sites. Their intragranular location and morphology was most probably not favourable to cavity nucleation. Finally, a few cavities (generally less than 5%) were observed in former residual ferrite regions, as illustrated in Figure 5.13.

EDS analysis of the GB precipitates shown in Figure 5.14 (a) revealed high content of Cr/Mo/Mn, and C to a lesser extent, but a depletion in Fe/Ni relatively to the matrix. Close to these precipitates, other smaller precipitates were often observed appearing with a brighter BSE contrast under SEM (Figure 5.14 (b)), with higher content in Mo but lower content in Cr than the larger precipitates. This is similar to the phases observed in the thermally aged as-received state (Section 3.3). Although many cavities were located on large precipitates, the precipitate size did not seem to have an impact on cavity nucleation as some cavities were also observed on small precipitates. Besides, the morphology of precipitates, with round or sharp edges, did not appear to be a critical factor for cavity nucleation either, since cavities were observed on both edge types. This can be surprising since FE simulations of creep for a 316L(N) steel carried out by Cui [208] suggested that maximal normal stresses at the interfaces of round edge precipitates are lower than those at sharp edge precipitates. It is worth mentioning that the characterization of precipitates morphology can be very difficult in a post-mortem analysis, as the presence of cavities prevent proper identification of the precipitates edges. Besides, the metallographic preparation can also deteriorate the precipitates morphology.

TEM analyses of damaged specimens were carried out to identify the nature of the large and small GB precipitates. Thin foils were extracted from two CT specimens made of cold-rolled material compressed to 25 kN (CMOD = 0.34 mm); one aged at 575 °C for 1470 h

and the other at 600 °C for 580 h, following the procedure described in Section 2.6. TEM bright field observations revealed several large globular defects at the austenite GBs near precipitates which were assumed to be cavities induced by stress relaxation, as illustrated in Figure 5.15. Although these objects were observed on several GBs, the identification of the origin of such a defect using TEM can be difficult, since the artefacts (induced for example by sample preparation) as previously observed for non-compressed aged specimens

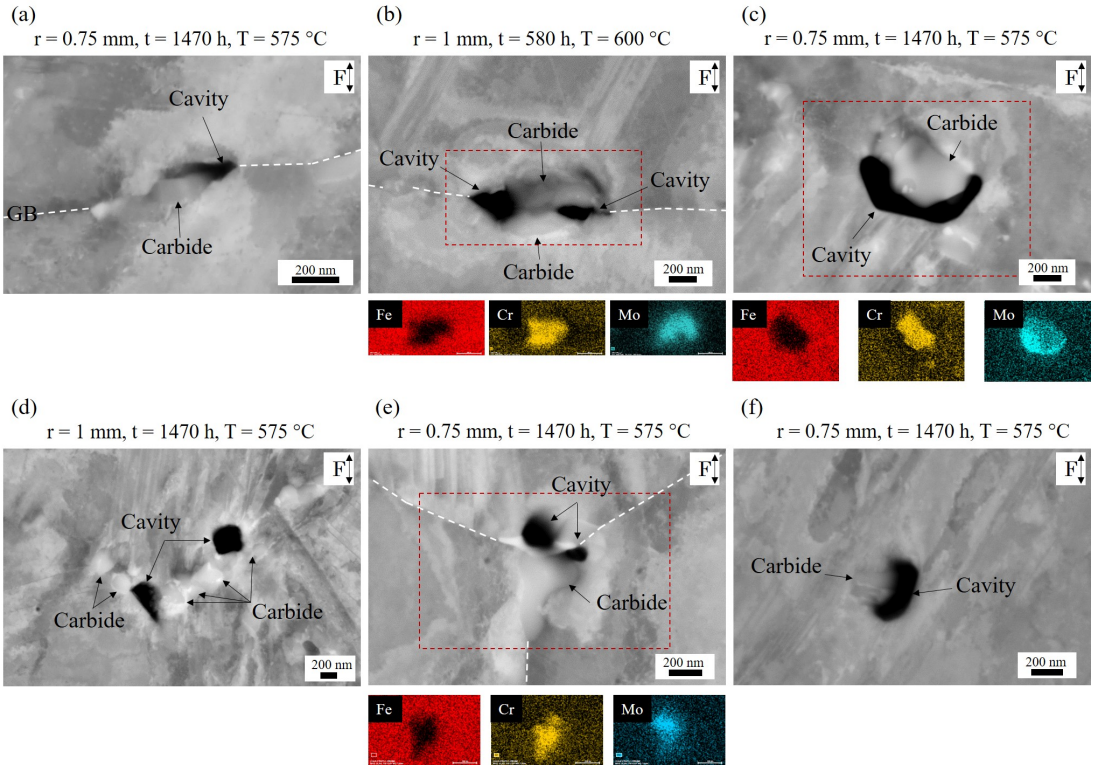

Figure 5.12: Cavity nucleation sites in CT specimens made of cold-rolled state: (a) at a carbide tip, (b) between two carbides, (c) at the carbide/austenite interface, (d) in a carbide cluster, (e) at a GB triple point, (f) in the bulk on a carbide. EDS maps carried out at precipitates/cavities interfaces are also presented, showing distribution of Fe, Cr and Mo.

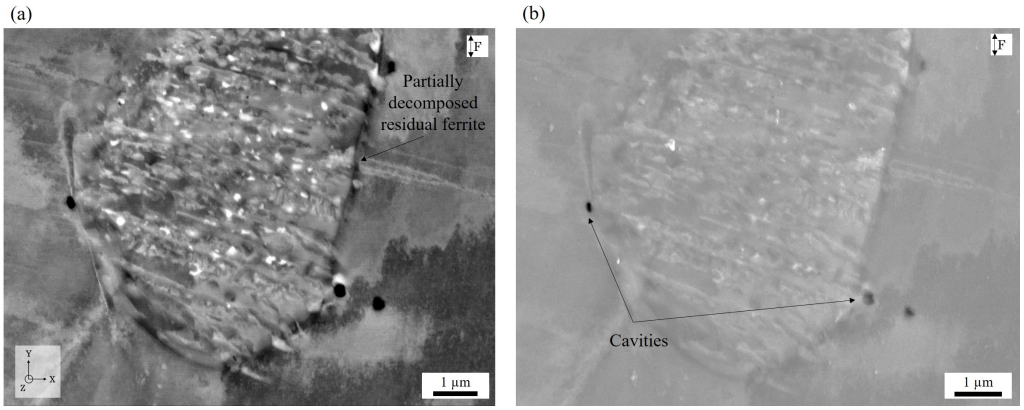

Figure 5.13: Cavities at the interface between the austenite matrix and partially decomposed ferrite, observed with (a) BSE and (b) SE detectors near the notch root of a CT specimen made of cold-rolled state compressed to 25 kN (CMOD = 0.34 mm) and aged at 575 °C for 1470 h.

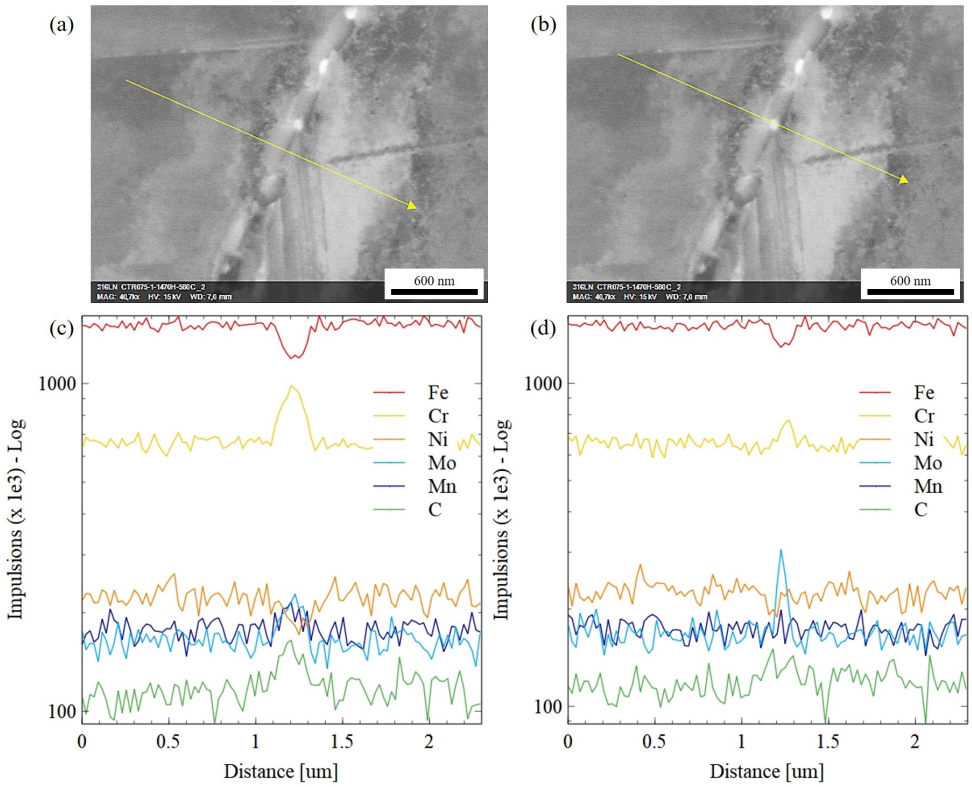

Figure 5.14: SEM-EDS profiles of the two types of GB precipitates observed in a CT specimen of cold-rolled state with r = 0.75 mm , after Turski compression and ageing at 575 °C for 1470 h, with (a) (Cr, Mo, C)-rich and (b) Mo-rich precipitates.

(Figure 3.8) could be mistaken for stress relaxation cavities. Moreover, although these were stress relaxation cavities, their size and morphology may have been modified during the electropolishing process applied to prepare the TEM thin foils. Therefore, the smaller round cavities observed in Figure 5.15 were not considered as cavity damage; however, the larger ones were considered to be associated to stress relaxation damage since they were not present in the thermally aged material (without Turski compression). These larger cavities were observed to have lenticular and globular morphologies and an average length of 100 nm and width of 70 nm. They were very similar to the creep cavities identified under TEM by Fleck *et al.* [212] and Luecke *et al.* [213].

TEM analyses also revealed the presence of mechanical twins near cavities (Figure 5.15 (a) and (c)). These twins often formed a triple point with adjacent GB and sometimes with precipitates. Although the cavities were not systematically related to the mechanical twins, the literature data [141] reported that mechanical twin/GB triple points can considerably favor GB precipitation and cavity nucleation by inducing important stress concentration points [214].

Due to the small size of the Mo-rich precipitates, their nature was investigated using HRTEM (High-Resolution TEM). FFT (Fast Fourier Transformation) patterns for different phases observed at damaged grain boundaries are shown in Figure 5.16 (a). The largest GB precipitates rich in Cr/Mo/C were found to be $Cr_{23}C_6$ precipitates as shown with the pattern in Figure 5.16 (f). This is in agreement with analyses carried out in thermally aged specimens discussed in Section 3.3. The smaller intermetallic precipitates accompanying the chromium carbides might be of two different natures (Figure 5.16 (d) and (e)):

(i) the BCC-structured χ phase (Figure 5.16 (b) and (d)). The lattice parameter was

measured to be 8.92 Å, in agreement with results reported by Plaut *et al.* [71].

(ii) the τ phase (Figure 5.16 (b) and (e)). Such phase has been only reported once in the literature by Redjaimia *et al.* [215], observed in the δ-ferrite of a duplex steel after ageing at temperatures between 500 and 650 °C. Here, the τ phase was identified as an orthorhombic-structure with lattice parameters a = 4.05 Å, b = 4.84 Å and c = 2.86 Å. Very few information is available for this phase most probably because of its size, with only a few tens of nm in length and less than 20 nm wide in average. These precipitates were very often found to be localised on $Cr_{23}C_6$ precipitates.

HRTEM analyses also revealed some cavities as small as 10 nm in radius at the tip of τ precipitates for both ageing conditions (Figure 5.17 (b) and (c)), suggesting these could act as preferential nucleation sites for cavities. Indeed, these precipitates could represent additional stress concentration points at the tips or edges of carbides, thus favoring cavity nucleation. Chemical composition of all identified phases was measured by EDS under TEM, with results given in Table 5.1.

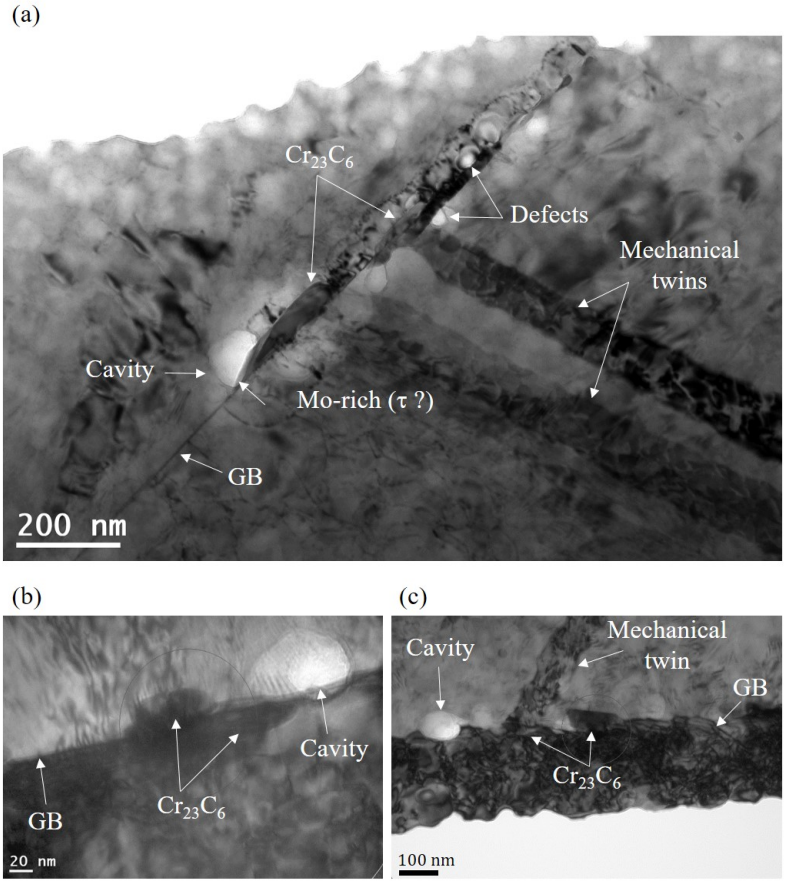

Figure 5.15: TEM bright field images of damaged austenite grain boundaries, showing $Cr_{23}C_6$ and Mo-rich precipitates (probably τ phase) and cavities in near-notch region of CT specimens of cold-rolled state compressed at F = 25 kN and aged at (a) 600 °C for 580 h, (b) and (c) at 575 °C for 1470 h.

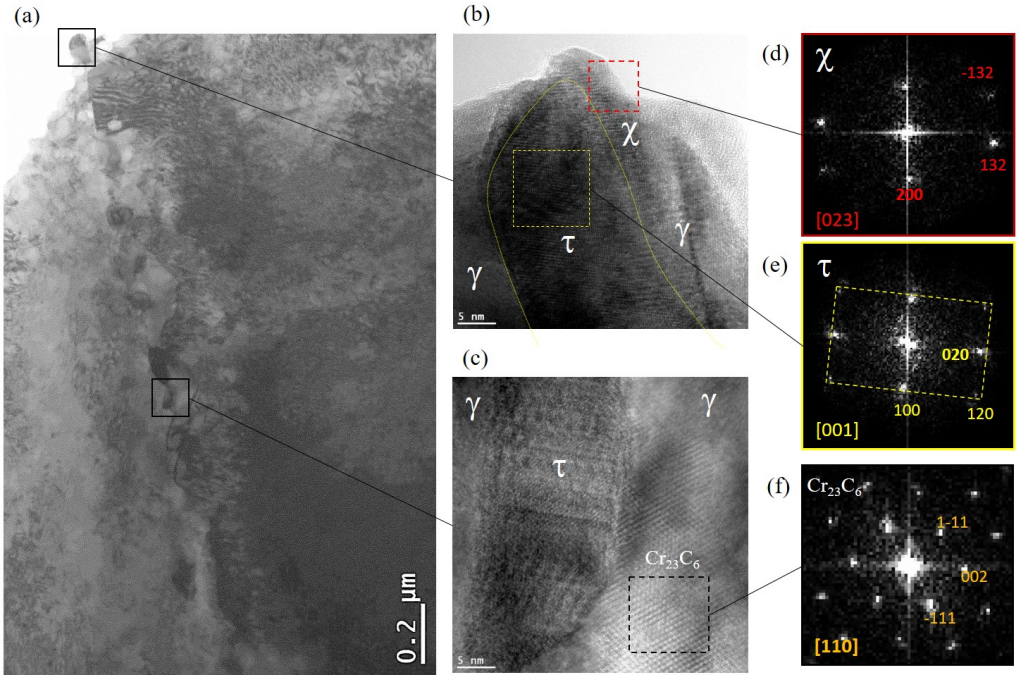

Figure 5.16: TEM analysis GB precipitates in a CT specimen made of cold-rolled state compressed at F = 25 kN and aged at 575 °C for 1470 h: (a) bright field image of a GB containing area, (b) and (c) HRTEM images of χ, τ and $Cr_{23}C_6$ precipitates along with their corresponding FFT patterns in (d), (e) and (f), respectively.

Table 5.1: Composition of the phases identified in damaged cold-rolled CT specimens measured by EDS under TEM, in %at.

Phase	Fe	Cr	Ni	Mo	C
Austenite	67.0	19.0	12.2	1.3	-
$Cr_{23}C_6$	15.6	62.5	2.4	6.8	12.6
τ	59.9	13.5	14.4	8.2	-
χ	53.6	18.5	8.1	15.6	-

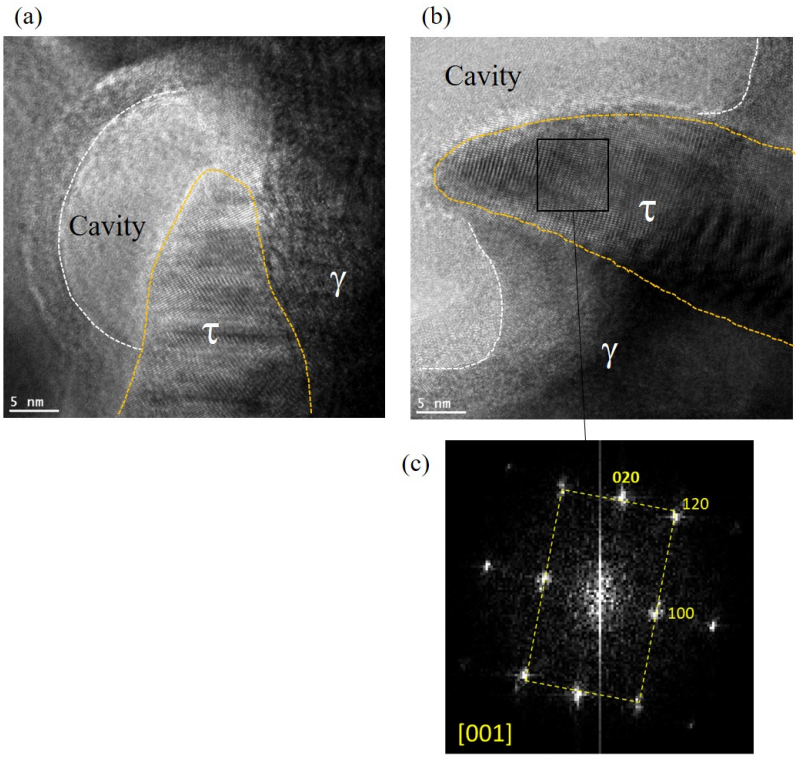

Figure 5.17: HRTEM image of cavities containing region; precipitates near cavities might correspond to *tau* phase. Sample machined from CT specimens made of cold-rolled state compressed to F = 25 kN and aged at (a) 575 °C for 1470 h and (b) 600 °C for 580 h with (c) corresponding FFT pattern of τ phase.

5.3 Single-pass welded state

To study the effect of welding on stress relaxation damage, SRC tests were carried out using welded specimens. Results for CT specimens machined from a single-pass welded plate are first presented.

First, in order to determine if the residual stress and strain generated during the welding process alone could induce stress relaxation damage for the considered ageing times and temperatures, a study of damage after the welding and without Turski compression was carried out (for both single and multi-pass states). None of the specimens showed any form of damage after ageing at 575 °C for 580 and 1470 h. The absence of damage observed for both material states confirmed that the residual stresses magnitude (below 400 MPa) and plastic strain (below 5%) induced by welding were not sufficient to allow SRC in the studied 316L(N) steel, for the chosen thermal relaxation conditions. Therefore, the Turski compression after the welding was used to generate sufficient stress and plastic strain to allow the observation of SRC in welded materials.

To induce different levels of residual stresses and strains, aiming for different damage levels, CT specimens made of single-welded state of the studied 316L(N) steel were compressed to CMODs of 1.39, 1.73, 1.85, 6.09 and 6.41 mm. After Turski compression, samples were thermally aged at 575 °C for 580 and 1470 h. Investigations of damage were carried out in the (YZ) and (XY) planes by SEM in the three weld zones (FZ, CGHAZ and HAZ) of the specimens as described in Figure 2.11. The influence of the welding microstructure, Turski compression magnitude and relaxation time on the initiation of damage is presented in the following. The nucleation sites and distribution of damage are also discussed.

5.3.1 Influence of Turski compression level (CMOD)

The optical micrographs presented in Figure 5.18 (b) and (c) show typical GB damage resulting from stress relaxation in a single-pass welded state, observed in the (YZ) plane at the notch root of a CT specimen (Figure 5.18 (a)) compressed to a CMOD of 6.09 mm and aged at 575 °C for 580 h. Multiple large cracks were observed in the CGHAZ (Figure 5.18 (c)), which were found to be initiated from the coalescence of grain boundary cavities shown in Figure 5.18 (d). In order to better characterize and understand the effect of welding on SRC, similar observations were carried out in CT specimens made of single-pass welded state compressed to other CMODs and thermally aged in other conditions.

Figure 5.19 shows typical damage found in specimens compressed to CMODs of 1.39, 1.73 and 6.41 mm, and submitted to the same heat treatment at 575 °C for 1470 h. Although other conditions of Turski compression were tested for CT specimens made of single-pass welded state (Table 2.2), these three CMODs were chosen here as they each represented a stage of SRC (isolated cavities, coalesced cavities and cracks). Cracks were observed for specimens compressed to CMODs higher than 1.73 mm, mainly in the CGHAZs below the FZ/CGHAZ boundary similarly to previous observations. Typically, a long crack along one GB in the CGHAZ of the specimen compressed to a CMOD of 1.73 mm (Figure 5.19 (b)). By significantly increasing the Turski compression loads to CMODs up to 6.41 mm, many large cracks were formed in the CGHAZ but also at the bottom of the FZ and in the HAZ (Figure 5.19 (d)).

To get a better insight of damage mechanisms, SEM observations of the most damaged region of each weld zone of each specimen were carried out. Results are shown in Figure 5.20. Figure 5.20 (a) shows that damage nature in the specimen compressed to a CMOD of 1.39 mm was slightly different for the three weld zones: CGHAZ and HAZ presented several coalesced cavities, while isolated cavities were observed within the FZ. As expected, the damage increased with CMOD increase. For the CMOD of 1.73 mm, locally higher

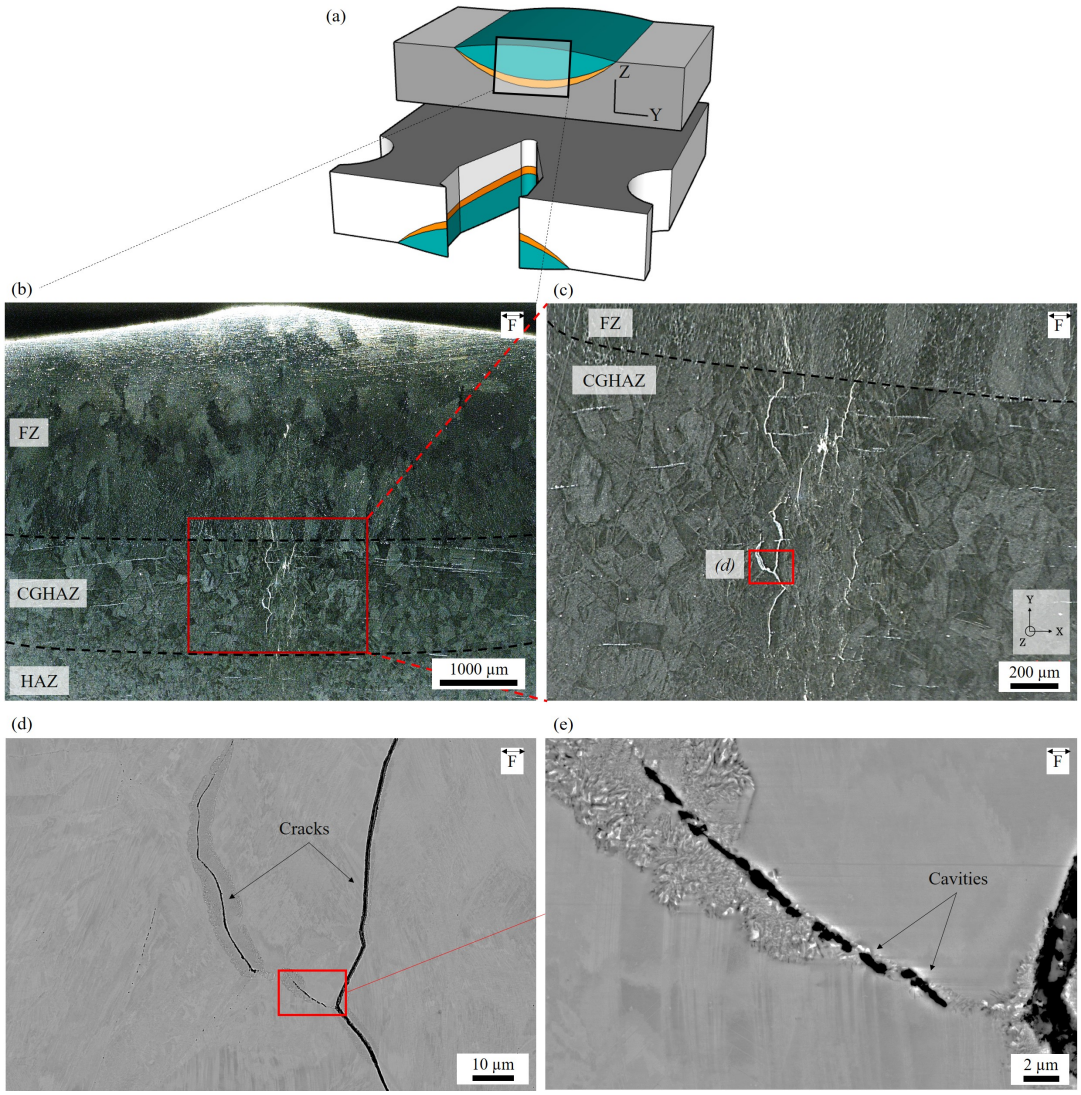

Figure 5.18: SRC damage in the (YZ) plane at the notch root of a CT specimen made of single-pass welded state, compressed to a CMOD of 6.09 mm and aged at 575 °C for 580 h with (a) location of the analysis area, (b) and (c) optical images of GB cracks, (d) and (e) SEM-BSE images of the damage.

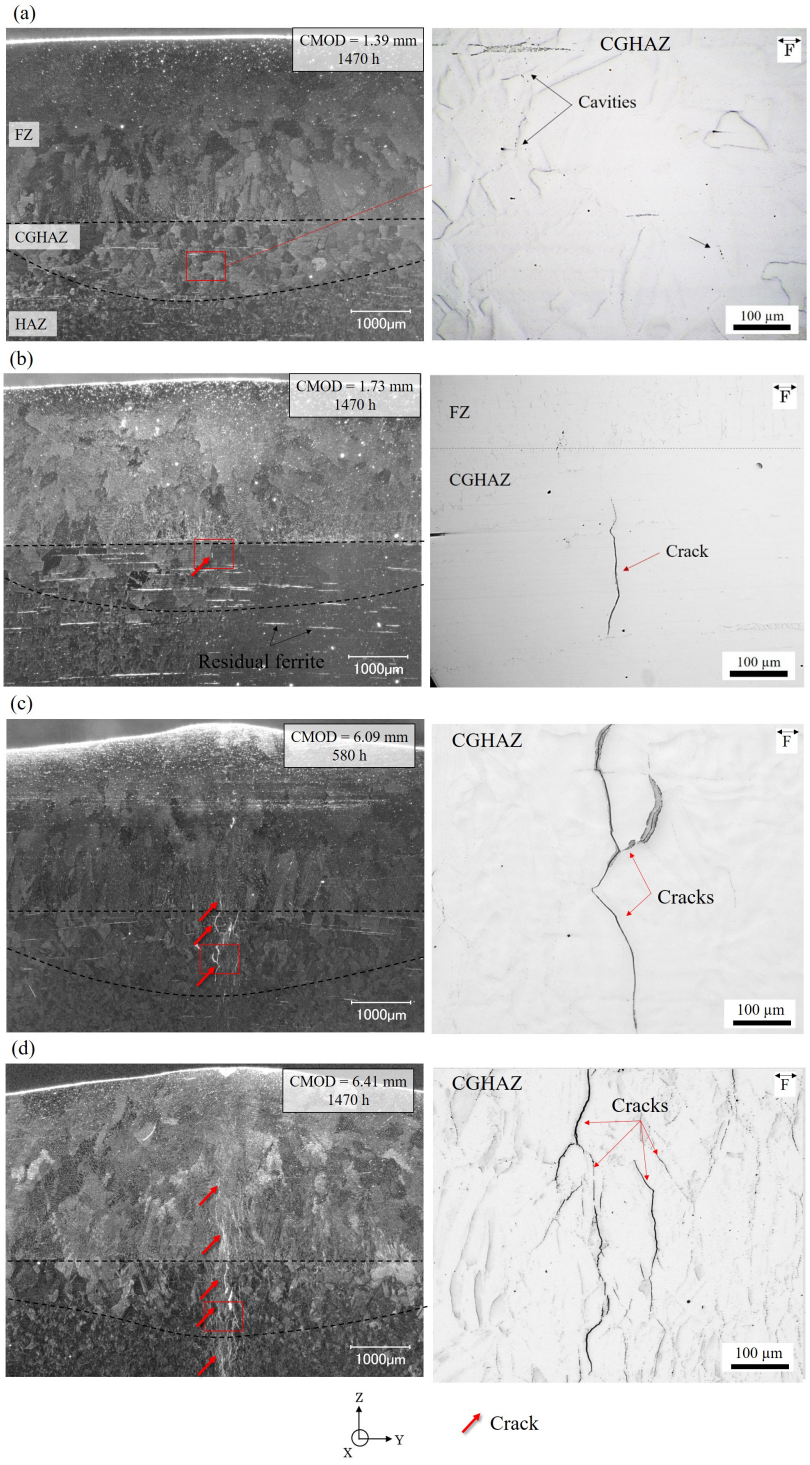

Figure 5.19: SRC damage in CT specimens made from single-pass welded state at a distance of 40 μm from the notch root in the (YZ) compressed to different maximum CMOD: (a) 1.39 mm, (b) 1.73 mm, (c) 6.09 mm (aged for 580 h) and (f) 6.41 mm, and aged at 575 °C for 1470 h (optical microscopy).

cavity density and the nucleation of a microcrack in the CGHAZ (Figure 5.20 (b)) were observed. In this specimen, measured mean length of cavities was 798 nm in the FZ, 1126 nm in the CGHAZ and 955 nm in the HAZ. Cavities width was similar in the three regions with 487 nm in the FZ, 510 nm in the CGHAZ and 451 nm in the HAZ. Asides

from larger cavities, the higher cracking hazard in the CGHAZ was the result of a lower mean distance between neighbour cavities (or higher cavity density) on a grain boundary. This induces a higher probability of cavity coalescence and thus crack nucleation. For the most compressed specimen (CMOD of 6.41 mm), cracks were observed in the three zones (Figure 5.20 (c)), with numerous larger cracks in the CGHAZ (Figure 5.19 (d)).

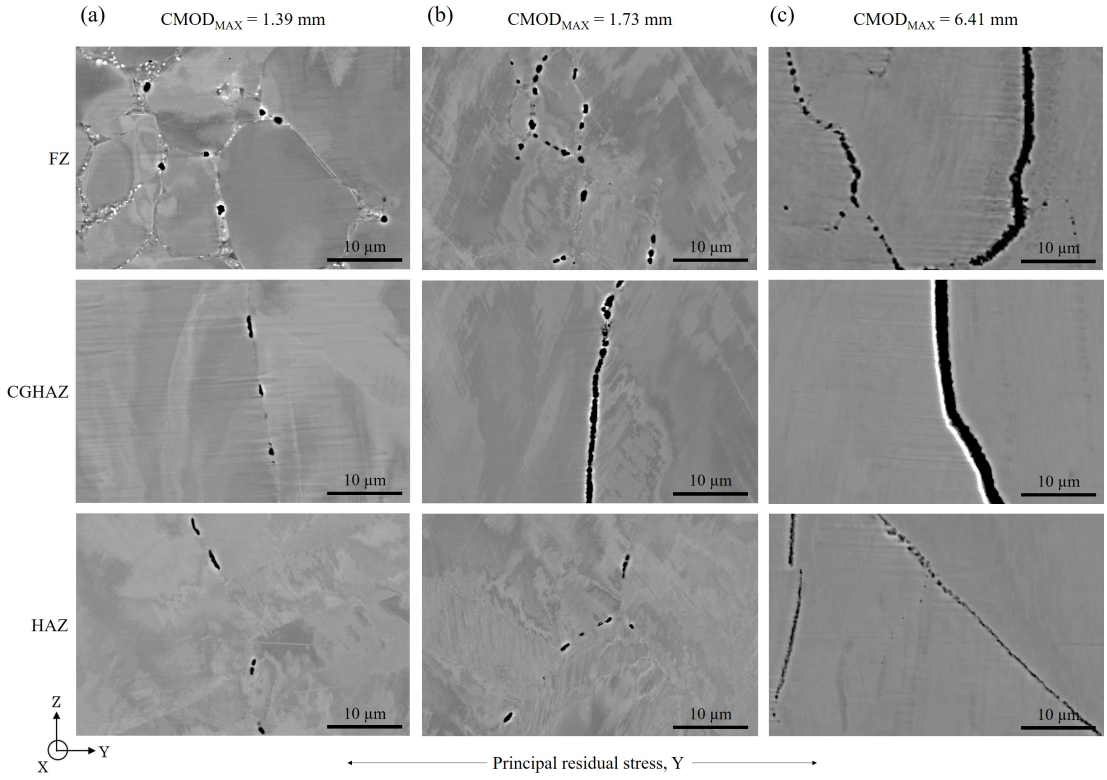

Figure 5.20: SEM observation of cavities and cracks observed in CT specimens of single-pass welded state compressed to CMODs of (a) 1.39, (b) 1.73 and (c) 6.41 mm, and heat treatment at 575 °C for 1470 h. Z axis crosses the CT sample thickness.

To quantify the damage, cavities and cracks were counted over the most damaged regions of each weld zone, for each loading condition. Figure 5.21 compares the damage distribution and number of cavities for each case. As suggested by earlier observations, the increase in CMOD highly increased the damage level, with specimens of higher CMOD presenting greater crack number. Besides, the FZ and HAZ presented more homogeneous damage distribution, while in CGHAZ damage was concentrated on few grain boundaries leading to cracks by cavity coalescence. Even though the total number of cavities was observed to be higher in the HAZ than in the CGHAZ, Turski compression to CMODs of 1.39 and 1.73 mm did not allow the observation of any crack in the HAZ. Cracks in the HAZ were only observed for the highest CMOD of 6.41 mm, with only a few of them propagating along multiple GBs (Figure 5.20 (c) and Figure 5.21 (c)). Correlations between damage analyses carried out in both (XY) and (YZ) planes and FEM simulations of Turski compression (Figure 4.14) allowed estimating stress and strain thresholds required to induce damage in the different weld zones (Table 5.2). Threshold for cavity nucleation is first discussed analysing the lesser compressed specimens (CMOD of 1.39 and 1.73 mm), while threshold for cracking is discussed using analyses carried out in highly compressed specimens.

For the least compressed specimen, first cavities were observed near the top of the FZ (weld surface) in the (YZ) plane, which corresponded to computed stress and accumulated

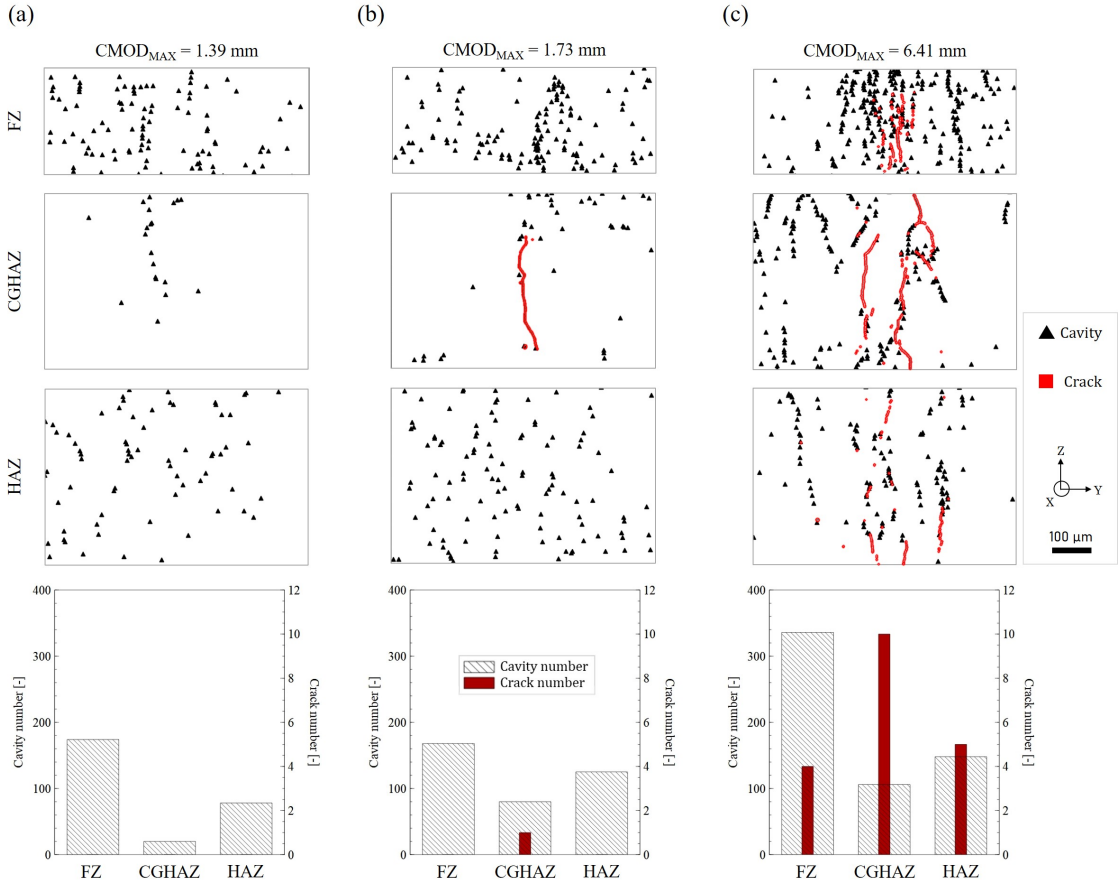

Figure 5.21: Comparison of stress relaxation damage observed in the FZ (near boundary with CGHAZ), CGHAZ and HAZ (at half-thickness) of 316L(N) steel after single-pass welding, Turski compression to CMODs of (a) 1.39 mm, (b) 1.79 mm and (c) 6.41 mm, and heat treatment at 575 °C for 1470 h.

Table 5.2: Estimation of stress relaxation cavitation and macro cracking thresholds (post-Turski compression stresses σ_{YY} and cumulated plastic strain p) for each region of the single-welded microstructure for relaxations conducted at 575 °C for 1470 h determined from analyses and FEM simulation results in the (YZ) and (XY) planes.

Weld zone	FZ		CGHAZ		HAZ	
Damage type	Cavities	Cracks	Cavities	Cracks	Cavities	Cracks
σ_{YY} [MPa]	490	720	580	600	460	900
p [%]	12	52	20	23	11	85

strain of 490 MPa and 12%, respectively. For this same CMOD, the CGHAZ was the least damaged zone, with several isolated cavities located exclusively on a few grain boundaries (Figure 5.21 (a)). Predicted stress and accumulated strain thresholds for cavity nucleation were 580 MPa and 20%, respectively. In the HAZ, investigation of damage was also carried out in the (XY) plane for CMOD of 1.73 mm, allowing determining more precise stress and strain thresholds (Figure 5.26). The characterization in this plane was facilitated by the homogeneous microstructure, as the (XY) plane is normal to the microstructure gradient induced by welding (along Z direction). The comparison of cavity number with numerical predictions of strain and residual stresses (Figure 5.26 (b)) suggested that cavities in the HAZ appeared above 460 MPa of residual stress and 11% of accumulated plastic strain.

Similarly, thresholds for crack nucleation were investigated for the three zones, by analysing highly compressed specimens. Micro-cracks in the FZ were observed only for the most compressed specimen (Figure 5.21), between the middle of the zone (at a distance of 1.9 mm from the surface) and the FZ/CGHAZ interface. First cracks observed in this zone thus corresponded to principal stresses and accumulated plastic strain thresholds of about 720 MPa and 52%, respectively. These are extreme conditions, as compared to those usually encountered in industrial applications.

In the HAZ, cracks were only observed in the specimen compressed to a CMOD of 6.41 mm. Similarly to the cavity nucleation, cracking threshold in the HAZ was estimated through additional analyses in the (XY) plane at half thickness of the specimen compressed to a CMOD of 6.41 mm for better precision. First cracks were observed at a distance of 265 μm from the notch, corresponding to calculated stress and cumulated plastic strain of 900 MPa and 85%, respectively. These values are higher than the stress SRC thresholds of 740 $\pm$ 40 MPa suggested by Pommier [45]. As discussed for specimens made of cold-rolled state (Section 5.2), it is important to remind that the method used by Pommier for quantifying damage is completely different from that of this work, and thus thresholds could not be compared properly.

In the CGHAZ, the first crack was observed in the specimen compressed to a CMOD of 1.73 mm. For this specimen, the stress and cumulated strain crack threshold in this zone was thus estimated to be 600 MPa and 23%, respectively. This low value of cracking threshold can be related to the particularly favorable microstructure: a long GB ($>$ 200 μm) located beneath the FZ/CGHAZ boundary oriented in almost normal direction to the residual tensile stress Y axis. This suggests that a GB particularly favorable to SRC located in the CGHAZ can be highly detrimental for SRC resistance. Such an effect would be less pronounced in the other two welding zones since more GBs are found there and they can accumulate thus more cavities in the same volume (detailed in Chapter 6).

These first results showed that the method adopted in this work allowed triggering SRC in heterogeneous microstructures resulting from single-pass welding of a 316L(N) steel. The observation of damage in the heterogeneous microstructures allowed identifying the weld zones most prone to SRC and allowed, for the first time, the estimation of damage nucleation thresholds of each weld zone by comparison with predicted post-Turski compression residual stresses and plastic strain. These correlation showed that cavity nucleation was most favoured in the HAZ, followed by the FZ and finally the CGHAZ. However, the cavity size and most importantly the high concentration of cavities on some GBs in the CGHAZ made it more prone to the initiation and development of cracks, if residual stresses and strain levels are sufficient. The first explanation for this behavior would be the large grain size in the CGHAZ. It is partially true because the FZ was also more prone to SRC than the HAZ, but less prone than the CGHAZ despite the larger grain size. Additional analyses are then required to properly understand these behaviors.

5.3.2 Influence of relaxation time

In order to assess the influence of relaxation time on the distribution and level of damage in the three regions of the single-pass welded state, CT specimens pre-loaded to similar CMODs (6.09 and 6.41 mm) and both heat treated at 575 °C for 580 and 1470 h, respectively, were analyzed (Figure 5.22). Globally, damage increased in all three welding zones with an increase in relaxation time. In Figure 5.22, damage is illustrated using optical image for the sake of easier visibility, however image analysis for damage quantification was still performed on SEM images, as previously.

In the FZ, optical images showed that damage mostly consisted of cavities and a few small micro-cracks (several coalesced cavities) near the FZ/CGHAZ boundary after 580 h. After 1470 h of relaxation, the number of damaged GBs and number of cavities largely increased. This resulted in a broader damaged area and in more severe damage per boundary, which was manifested by a higher number of micro cracks (Figure 5.22). By analyzing the binarized SEM images of damaged FZ, an increase of about 90% in the surface damage was observed by increasing the relaxation duration. In the CGHAZ, macro-cracks were already observed after 580 h of relaxation, but only few GBs were affected. After 1470 h, numerous grain boundaries presented micro and macro-cracks (Figure 5.22). Analysis of binarized images revealed an increase of 120% of surface damage in this zone when the relaxation time was increased to 1470 h. In the HAZ after 580 h, only few micro-cracks were observed, in addition to the many cavities, similarly to the FZ. After 1470 h, more grain boundaries were damaged. The number and length of micro-cracks also increased leading to a surface damage increase of 80%. The investigation of damage evolution as function of relaxation time revealed that macro-cracks appeared quicker in the CGHAZ than in the FZ or HAZ. Even though cracks appeared in all three regions after 1470 h, SRC occurred sooner in the CGHAZ, suggesting a favored damage growth in this zone. The evolution of surface damage for the three zones showed that the increase in damage as a function of relaxation time was the most severe in the CGHAZ, followed by the FZ and finally the HAZ. It is probable that the steeper increase in damage in the CGHAZ is due to the presence of cracks for the shortest relaxation time, favoring the nucleation and growth of additional damage. Overall, these results confirmed that the propensity to crack formation by stress relaxation was higher in the CGHAZ than in the other regions, in agreement with suggestions made from industrial observations of SRC [7, 24, 37].

5.3.3 Correlation between cavities and GOS

Previous sections allowed characterizing damage in a heterogeneous single-pass welding microstructure, thereby estimating stresses and plastic strain damage thresholds for each weld zone. In this section, additional analyses are presented aiming to understand the differences of damage observed previously.

To get a finer description of damage in the weld microstructure, cavity distribution was analyzed along both Z and Y directions of the (YZ) plane. GOS values computed from EBSD data were averaged over the zones to be used as a local measure related to the plastic strain. GOS was indeed used in rare cases in the literature to estimate deformation, as in the study of Carneiro *et al.* [216] or Keiji *et al.* [217]. Typically, Keiji *et al.* [217] showed that the average GOS and KAM increased with an increase in strain. However, the use of GOS criterion to evaluate plastic strain still remains questionable.

Simulated cumulated plastic strain field in the (YZ) plane at the notch root of the specimen of single-pass welded state compressed to a CMOD of 1.73 mm and further aged at 575 °C for 1470 h, cut at a distance X = 120 μm from the notch root is shown in Figure 5.23 (a). This revealed particularly high levels of strain at the notch centreline

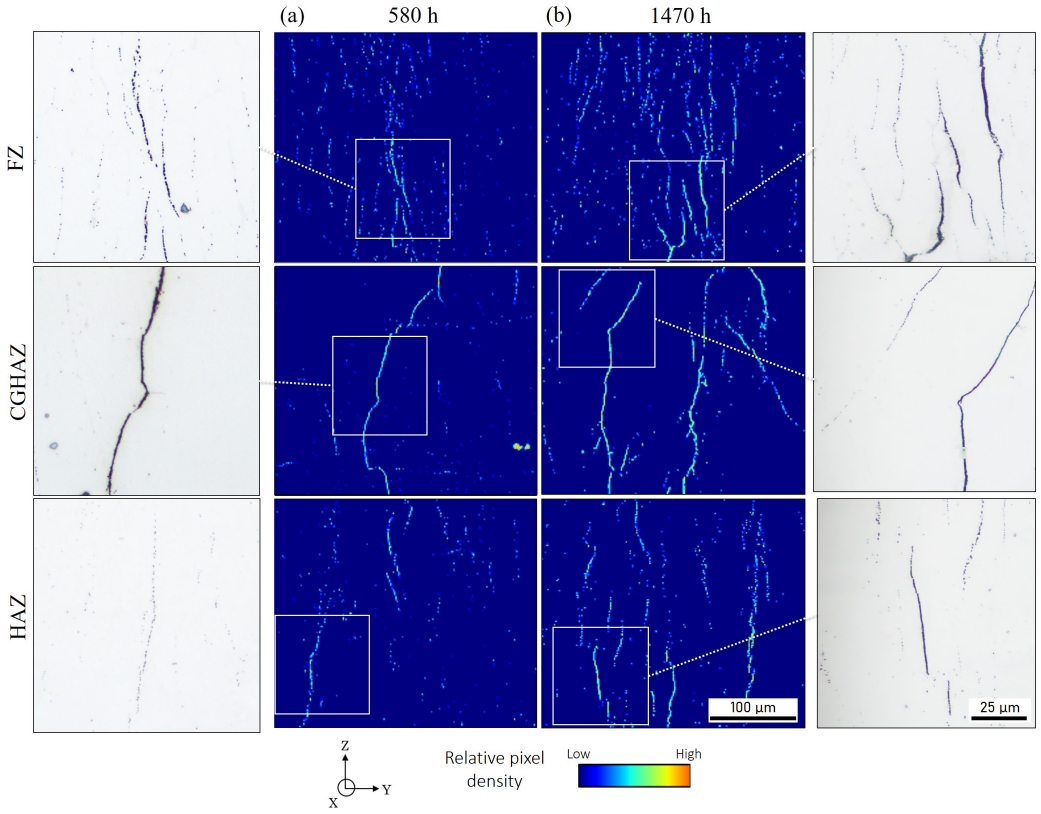

Figure 5.22: Comparison of most damaged areas of each region of the single-pass weld for stress relaxation at 575 °C during 580 h and 1470 h, for specimen pre-loaded to CMODS of 6.09 and 6.41 mm, respectively. SEM images were binarized to only show cavities and cracks.

(Figure 5.23 (b)), going from the surface of the FZ up to the mid-thickness. EBSD mapping of the region near the FZ/CGHAZ interface was carried out to compare computed plastic strain to measured grains distortion. IPF and GOS maps of this region are shown in Figure 5.23 (c) and (d), respectively. Comparison between computed plastic strain and averaged GOS revealed good correlation between these two quantities (Figure 5.23 (e)).

GOS values were further correlated to stress relaxation damage. The distribution of cavities over the weld zones of the specimen compressed to CMOD of 1.73 mm and aged at 575 °C for 1470 h is shown in Figure 5.24. Along the CT sample thickness (Z axis), the detection of cavities indicated a very heterogeneous distribution across the three weld zones whose interfaces are represented by red dashed-dotted lines in Figure 5.24 (b). According to FEM simulations (Figure 4.12), a slight progressive increase in stress and cumulated strain from the sample surface to the half-thickness should be expected. However, instead of progressive increase in cavities number from the surface towards mid-thickness, here the cavity distribution (Figure 5.24 (c)) was found to be more complex with important variations throughout the thickness, indicating a significant influence of the microstructure on damage. The number of cavities increased in the FZ towards the FZ/CGHAZ boundary (along Z axis), where the highest cavity number was found. From there, the highest damage was found at the top of the CGHAZ, and almost no cavities in the center of the CGHAZ asides a few ones located at the interfaces of residual ferrite[2] (indicated by blue arrows). A significant number of cavities was then observed again at the bottom of the

[2]Cavity nucleation sites for each zone of the weld are detailed further in Section 5.3.4 and thus not discussed here.

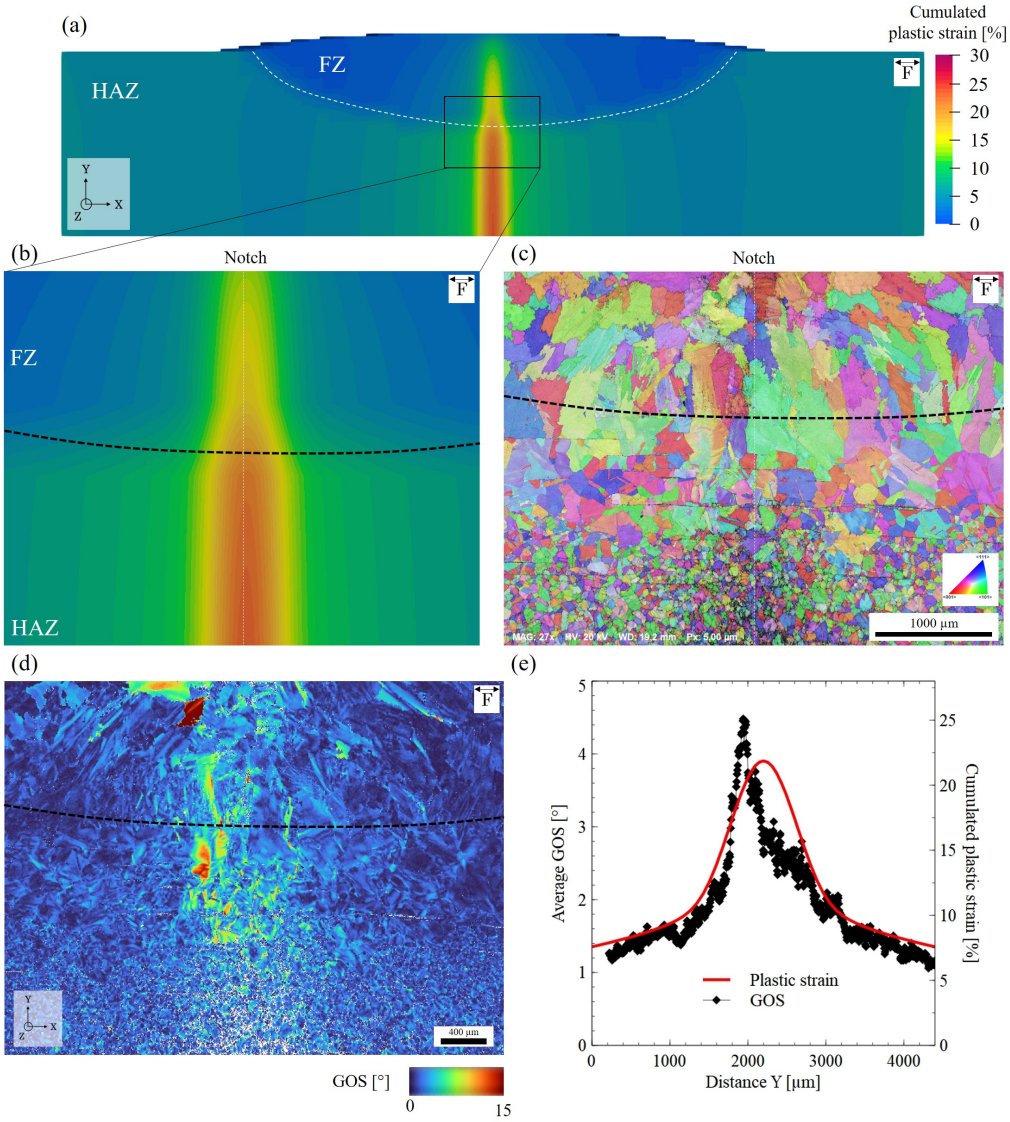

Figure 5.23: Investigation of strain at a distance X = 120 μm from the notch root in a CT specimen made from single-pass welded state compressed to a CMOD of 1.73 mm and aged at 575 °C for 1470 h, with (a) predicted post-Turski compression cumulated plastic strain in the (YZ) plane and (b) close up near the bottom of FZ, (c) IPF over IQ, (d) GOS computed from EBSD data and (e) comparison between computed plastic strain and measured GOS integrated over the whole region shown in (d). EBSD data was acquired with a step of 5 μm.

CGHAZ. The number of cavities then progressively increased towards the mid-thickness (Z = 8.25 mm), presenting a more homogeneous distribution of damage in the HAZ as compared to the two other regions (Figure 5.24 (e)). The average GOS profile integrated along the Z direction did not show a clear correlation with cavity distribution. GOS in the FZ slightly increased towards the FZ/CGHAZ boundary, reaching a peak in the CGHAZ. Throughout the CGHAZ, the GOS profile slowly decreased. As expected from the computed plastic strain evolution through thickness Z (Figure 5.24 (e)), GOS values in the HAZ at mid-thickness were higher than in the two other regions.

Increase in cavity number towards the FZ/CGHAZ boundary observed in the FZ would be probably related to the increase in stress and strain towards mid-thickness, as suggested by the FEM computations, but also to the presence of a transition region between the FZ and the CGHAZ which could results in straining incompatibilities. This increase in cavity number can be even more surprising given that in the FZ, austenite grains are smaller near the surface than near the FZ/CGHAZ boundary. Indeed, mostly equiaxed grains were present near the FZ surface, while larger columnar grains were observed near the FZ/CGHAZ boundary (Figure 3.20). A higher grain size, thus lower grain boundary density, would normally imply a lower total surface for cavity nucleation and thus lower total number of cavities. This could then sound contradictory with observations. Actually, as presented later in Section 5.3.4 for the FZ, most of the cavities were located on vermicular ferrite, thus reducing the influence of austenite grain size in the FZ. Damage in the CGHAZ was concentrated on a few grain boundaries, especially near the FZ/CGHAZ interface with more than 54% of the cavities, here being coalesced cavities, located on a single grain boundary. The more homogeneous distribution of cavities in the HAZ was favored by a higher density of GBs observed in this zone.

Cavity distribution, average GOS profile and predicted post-Turski compression stresses and strain were also plotted as a function of the Y axis (compression direction) for each weld zone (Figures 5.25 (a) to (c)). The notch centreline was indicated by grey dashed lines, corresponding to the maximum of computed post-Turski compression stresses and strain. Damage was plotted as cavity number fraction allowing better comparing the three zones in terms of distribution rather than magnitude.

These analyses showed that cavities in the FZ were relatively homogeneously distributed over the Y direction, but with an increase towards the notch centreline (Figure 5.25 (a)), consistent with the higher magnitudes of both stress and strain. The average GOS profile in the FZ showed a very good correlation with cavity distribution, with coincident peaks and global evolution over the whole zone. The CGHAZ again presented the most heterogeneous cavity distribution when compared to the two other weld zones, represented by the highest peak of cavity number (Figure 5.25 (b)). In this zone, multiple coalesced cavities forming a microcrack were observed in its centreline. The average GOS profile in the CGHAZ showed a good correlation with cavity distribution for Y $>$ 250 μm, with coincident peaks and global evolution. However, for Y $<$ 250 μm, high magnitudes of GOS were observed while very few cavities were found. Similarly to analyses in the Z direction, cavity distribution in the HAZ over the Y direction was the most homogeneous (Figure 5.25 (c)). Cavity distribution was consistent with the GOS profile, with no significant peaks in cavity number or GOS as compared to the two other zones. The total cavity number per unit area, Nc, was also estimated for each region: 11.10^{-4}, 4.10^{-4} and 6.10^{-4} mm^{-2} in the FZ, CGHAZ and HAZ, respectively. This showed the FZ was the most affected zone by cavities nucleation, followed by the HAZ and finally the CGHAZ. This is in agreement with the observations carried out in the Z direction (Figure 5.24). However, the CGHAZ was the most prone to the nucleation of cracks as it contained the only crack found in the specimen.

The comparison of GOS evolution with the cumulated plastic strain showed overall

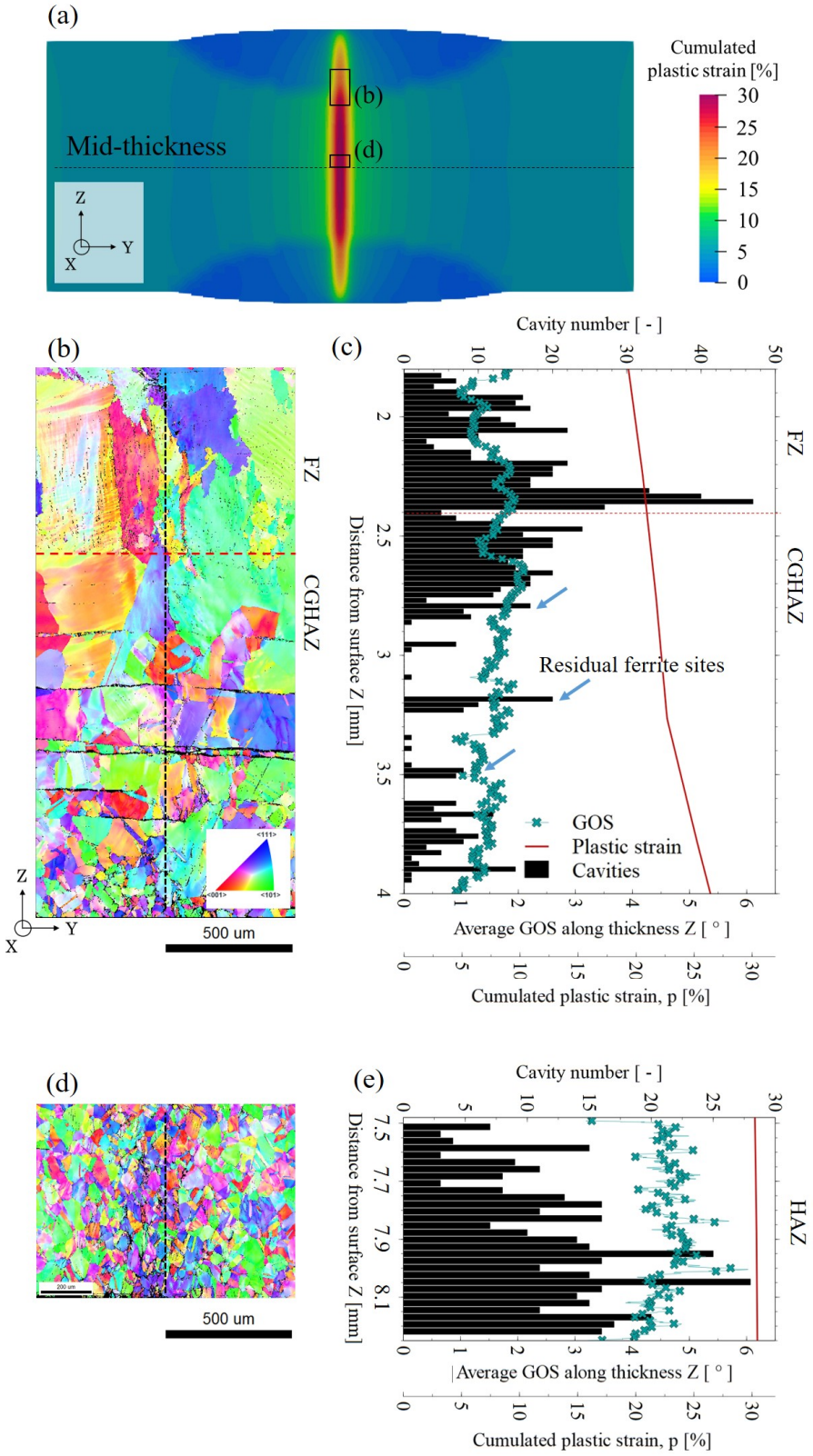

Figure 5.24: Cavity distribution near the notch centreline in a CT specimen of single-welded state compressed to a CMOD of 1.79 mm and aged at 575 °C for 1470 h: (a) predicted post-Turski compression plastic strain of the analyzed region, (b) and (d) IPF maps of the FZ-CGHAZ and HAZ (at mid-thickness) respectively, (c) and (e) cavities distribution, GOS and predicted plastic strain along the Z axis in the FZ-CGHAZ and HAZ (at mid-thickness), respectively.

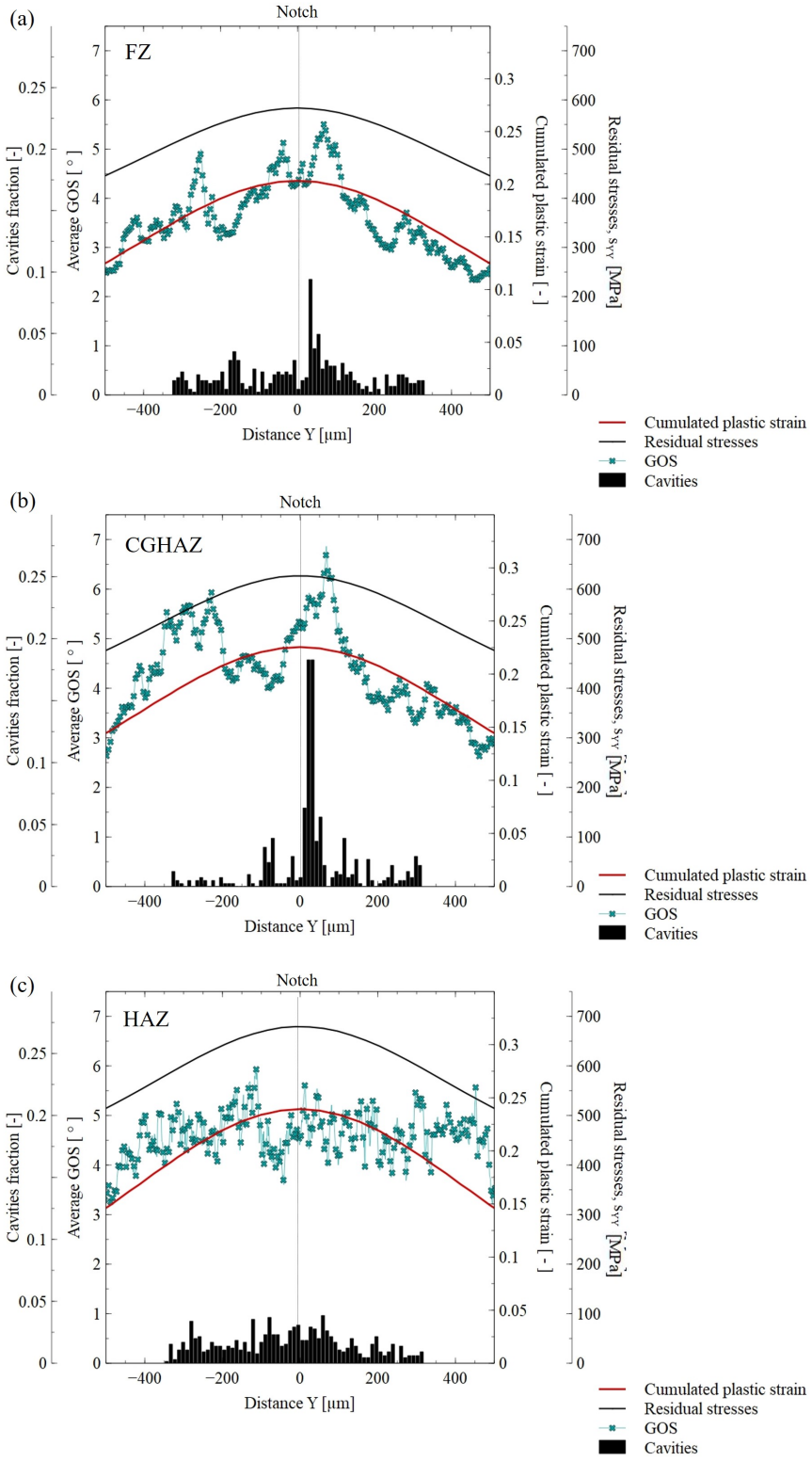

Figure 5.25: Comparison of cavities distribution, average GOS, predicted post-Turski compression cumulated plastic strain and residual stresses σ_{YY} in (a) FZ, (b) CGHAZ and (c) HAZ (at half-thickness, Z = 8.25 mm) at the notch root of a CT specimen of single-welded state pre-compressed to a maximum CMOD of 1.79 mm and further aged at 575 °C for 1470 h. Cavities in the three zones were only analyzed up to distances of 350 μm from the notch.

good correlation along the Y axis, especially in the FZ and CGHAZ. Of course, local GOS peaks observed in the FZ and CGHAZ could not be reproduced since simulations carried out in this work were based on continuum mechanical modeling.

The correlation of average GOS with cavity distribution showed that the heterogeneous distribution of damage in the FZ and CGHAZ was most probably, at least partially, related to a heterogeneous strain in these two regions induced by Turski compression. On the contrary, the homogeneous distribution of damage in the HAZ was related to a homogeneous strain over this zone.

GOS and KAM were also computed in the HAZ (mid-thickness, at Z = 8.25 mm) along the X direction to be compared to predicted residual stresses, plastic strain and the observed damage carrying out the analyses in the (XY) plane at the notch of the same specimen compressed to CMOD of 1.73 mm (Figure 5.26). Such analyses were not performed in the CGHAZ nor the FZ as it would have required partial destruction of the specimen, impeding further investigations. GOS and KAM were integrated along the X-axis averaged over a 200 μm large band as shown in Figure 5.26 (d). Evolution of both GOS and KAM values with the distance from the notch followed the evolution of the predicted cumulated plastic strain and were consistent with the cavity distribution (Figure 5.26 (b)). Results showed that along the X-axis, unlike the results obtained for the as-received state (Figure 5.6), a more continuous decrease of both strain and stresses in the HAZ allowed a continuous decrease of cavities number. This is most likely due to the initial hardening of the HAZ due to the welding (around 4%), leading to cavity distribution similar to that observed in cold-rolled state. It is worth noting, that the analysis for single-pass weld state along X-axis was carried out within distances lower than 700 μm from the notch. It cannot be completely excluded that several cavities were present beyond this limit.

5.3.4 Damage nucleation sites

Stress relaxation damage was observed to be quite different in terms of damage nature, distribution and levels in the three weld zones. Analysis of damage nucleation sites is further presented for each region of the weld regardless of the applied Turski compression load to get a better understanding of susceptibility to SRC of each weld zone.

5.3.4.1 Fusion zone

First, EBSD analysis was carried out in damaged regions of the FZ (Figure 5.27 (a)). Phase maps shown in Figure 5.27 (b) and Figure 5.28 (d) suggested the presence of ferrite, regenerated austenite, γ_R, $Cr_{23}C_6$ and σ-phase at austenite GBs and within austenite grains where the cavities were observed. The γ_R, $Cr_{23}C_6$ and σ-phases were the result of partial decomposition during thermal ageing of the vermicular ferrite initially formed upon cooling after welding (Section 3.5). Ferrite and associated phases were observed both at austenite GBs (Figure 5.28 (c)) and within austenite grains (Figure 5.27 (c)). This is in agreement with observations made by Vijayanand *et al.* [218] on creep damage in the FZ of a welded 316L(N) steel. As shown in Figure 5.28 (d), cavities were located at the interfaces between different phases, without any obvious preference between them. Most of the cavities were observed on the vermicular ferrite located within the austenite grains. Indeed, only 30% of the 456 identified cavities were located at austenite GBs, against 70% on the intragranular vermicular ferrite and associated phases (Figure 5.30). This is due to the large austenite grains in the FZ, resulting in low total GB length and thus less surface available for cavity nucleation, as compared to the numerous intragranular vermicular ferrite. Moreover, the number of GB precipitates at austenite GBs appeared to be much less, as compared to that found in the ferrite. In several damaged regions of

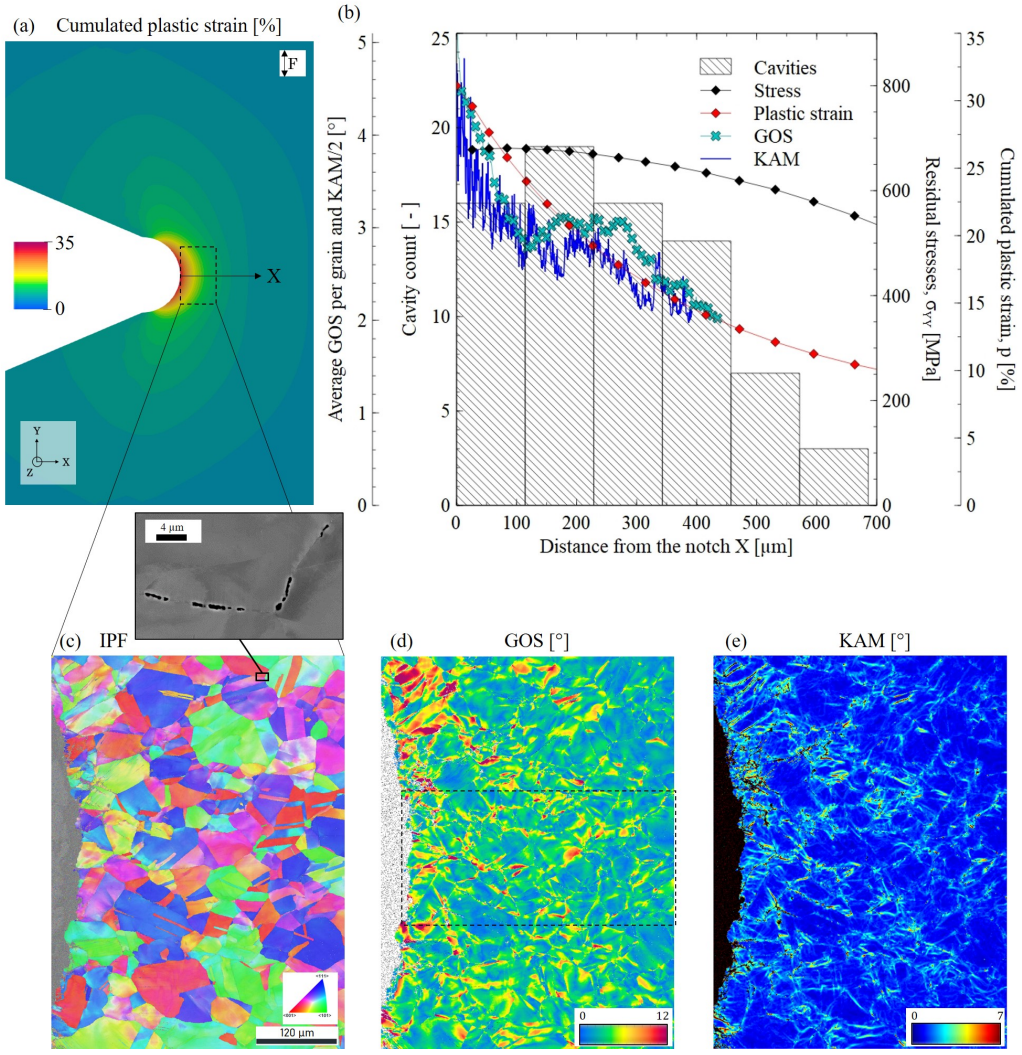

Figure 5.26: Analysis of damage in XY plane near the notch root at mid-thickness (Z = 8.25 mm) in the HAZ of single-pass welded 316L(N) steel, compressed to a CMOD of 1.73 mm and heat treated at 575 °C for 1470 h with (a) computed accumulated plastic strain field, (b) distribution of cavities compared to the residual stress σ_{YY} and accumulated plastic strain p, average GOS and KAM profiles. (c), (d) and (e) show the IPF map with a insert of SEM micrograph of GB cavities, GOS and KAM maps of the ROI, respectively, obtained from EBSD data acquired with a 550 nm step.

the FZ, austenite GBs were even completely free of cavities, partially due to the absence of GB precipitates.

As shown in Figure 5.29 for the highest CMOD of 6.41 mm, even though numerous cavities and even several micro-cracks were observed on vermicular ferrite within austenite grains, the propagation of these cracks was not observed. Instead, long cracks were rather observed at austenite GBs (Figure 5.29) suggesting an easier crack propagation at austenite GBs, even if less cracks were formed there. This is in agreement with observations of stress relaxation cracks in industrial welds by Dhooge *et al.* [6], Picker and Fraser [207] who indicated that the rare cracks observed in the weld metal (FZ) were exclusively located on austenite GBs.

5.3.4.2 Coarse grain heat affected zone

EDS maps obtained in areas with damaged GBs in the CGHAZ shown in Figure 5.31 revealed precipitates with high contents in Cr/Mo and a depletion in Fe. These precipitates had an average length of 500 nm and a very low distance between neighbours. EBSD analysis (Figure 5.32) carried out in other area with other damaged GB in the CGHAZ revealed precipitates similar to those previously found in as-received and cold-rolled state after Turski compression and ageing. TEM analyses were further carried out in specimens machined in the CGHAZ near the notch to identify the nature of the precipitates (Figure 5.33). Diffraction patterns of all GB precipitates (Figure 5.33 (b)) corresponded to the $Cr_{23}C_6$ phase. While smaller precipitates rich in Mo were observed under SEM in the single-pass welded state after Turski compression and ageing, similarly to previous states (Figure 5.37 (a)), their nature could not be confidently identified. According to the results obtained for the cold-rolled state, these Mo-rich precipitates might be R, τ and/or χ phases.

TEM analyses of damaged GBs also revealed cavities formed on the $Cr_{23}C_6$ carbides. Similarly to the cold-rolled state after Turski compression and thermal ageing, these cavities were located in between carbides (Figure 5.34 (a)) or at the tip of carbides (Figure 5.34 (b)). These cavities in CGHAZ were significantly larger than those in cold-rolled state. Very similar observations of cavities were achieved by Jiang *et al.* using TEM [219] after creep testing of a HAZ of a 310S welded joint. However, it is worth noting that the electropolishing process used for the preparation of thin foils could still have increased the size of cavities. Interestingly, TEM observations also showed accumulation of dislocations tangles near GB (Figure 5.34 (c) and (d)). According to Skelton *et al.*, these provide particularly favorable sites for cavity nucleation and growth in heat affected zones of austenitic steel weldments [220]. Moreover, the distribution of these dislocations appeared much more heterogeneous than that observed for cold-rolled state after Turski compression and thermal ageing.

EDS maps of damaged regions of the CGHAZ also revealed an increase in oxygen content in cracks relatively to the matrix. Diffusion of oxygen could have occurred after the nucleation of cracks near the notch surface exposed to ambient air. EDS profile of larger cracks in a CT specimen compressed to a CMOD of 6.41 mm shown in Figure 5.35 presented similar results, with layers of presumed chromium oxide and iron oxide observed on both sides and inside the crack, respectively. This is in agreement with results reported by Auzoux [13] for a failed superheater header (component for pipe systems) made of 316H after 50 000 h of service at 550 °C (Section 1.4).

5.3.4.3 Heat affected zone

In the HAZ, cavities were located on austenite GBs and homogeneously distributed in the entire zone. Samples were tilted to 70° under SEM using SE detector to better reveal GB

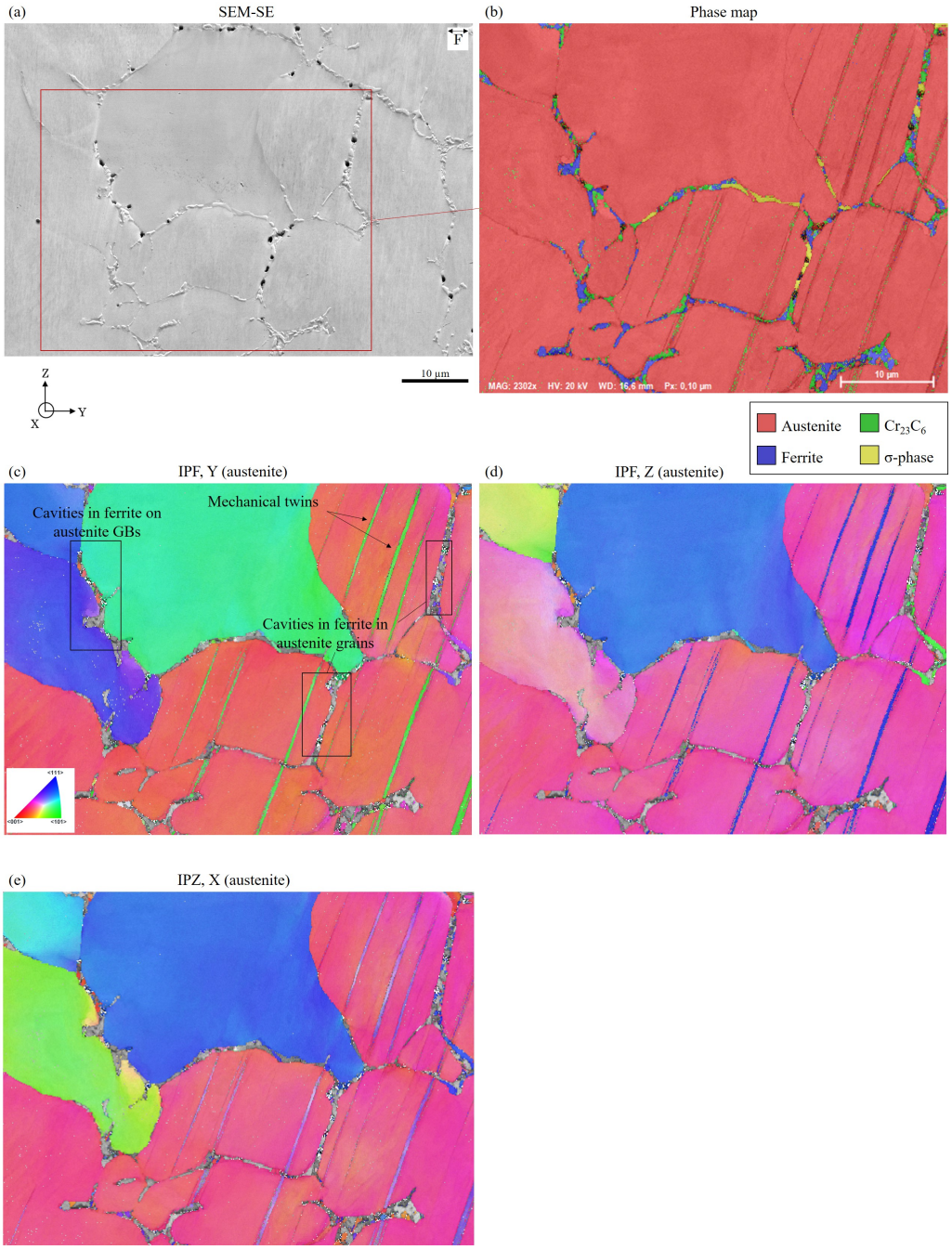

Figure 5.27: Cavities at vermicular ferrite within austenite grains and at austenite GB in the lower part of the FZ near the FZ/CGHAZ interface. Section located at X = 120 μm from the notch of a CT sample of single-pass welded state compressed up to a CMOD = 1.73 mm and aged at 575 °C for 1470 h: (a) SEM-SE, (b) phase map, and austenite IPF maps projected onto (c) Y, (d) Z and (e) X axis. A 100 nm step size was used for the acquisition.

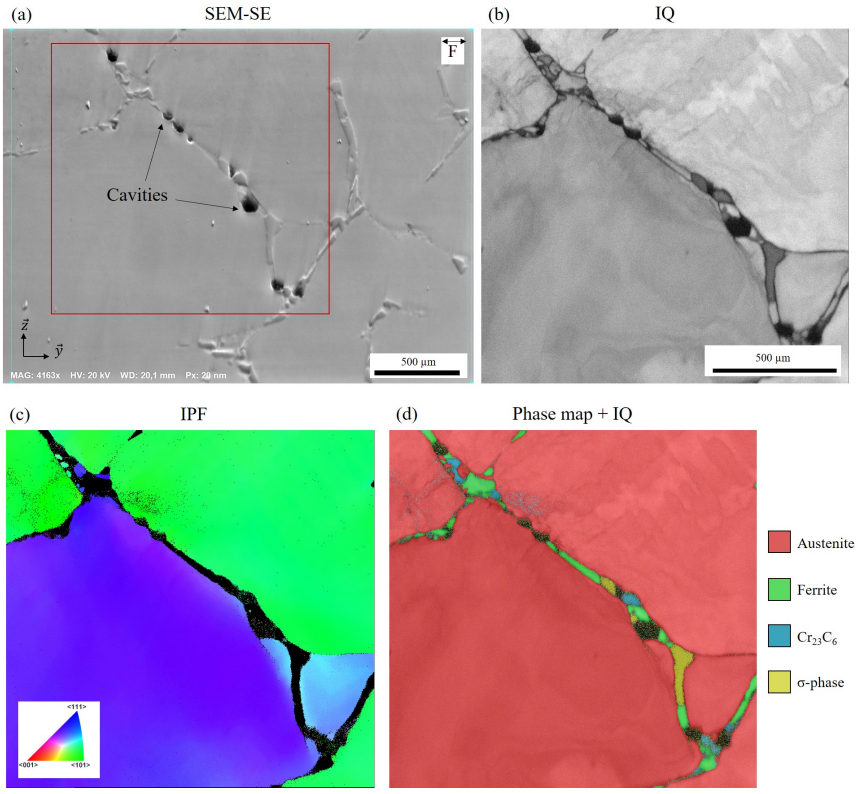

Figure 5.28: Cavities at vermicular ferrite on austenite GB in the lower part of the FZ near the FZ/CGHAZ interface. Section located at X = 120 μm from the notch of a CT sample of single-pass welded state compressed up to a CMOD = 1.73 mm and aged at 575 °C for 1470 h: (a) SEM-SE, (b) index quality map, (c) IPF map (d) phase map overlaid on the quality index images. A 20 nm step size was used for the acquisition.

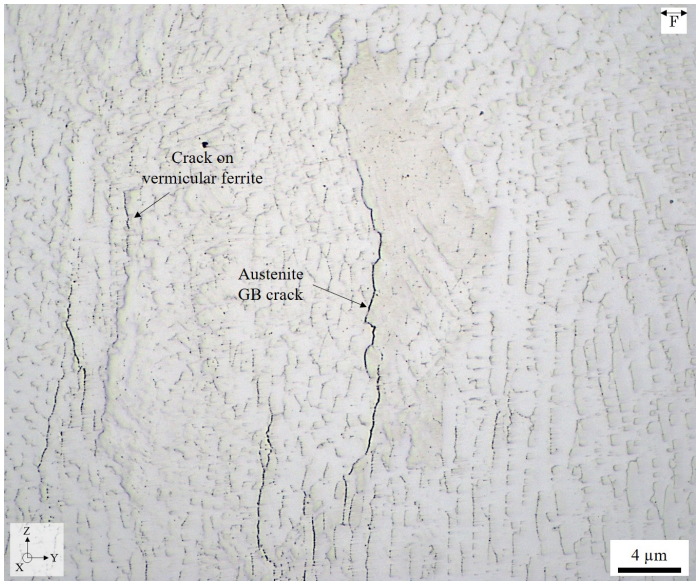

Figure 5.29: Stress relaxation damage in the FZ near the notch root of a single-pass welded sample section in the (YZ) plane after a Turski compression up to CMOD = 6.41 mm and subsequently aged at 575 °C for 1470 h (optical microscope).

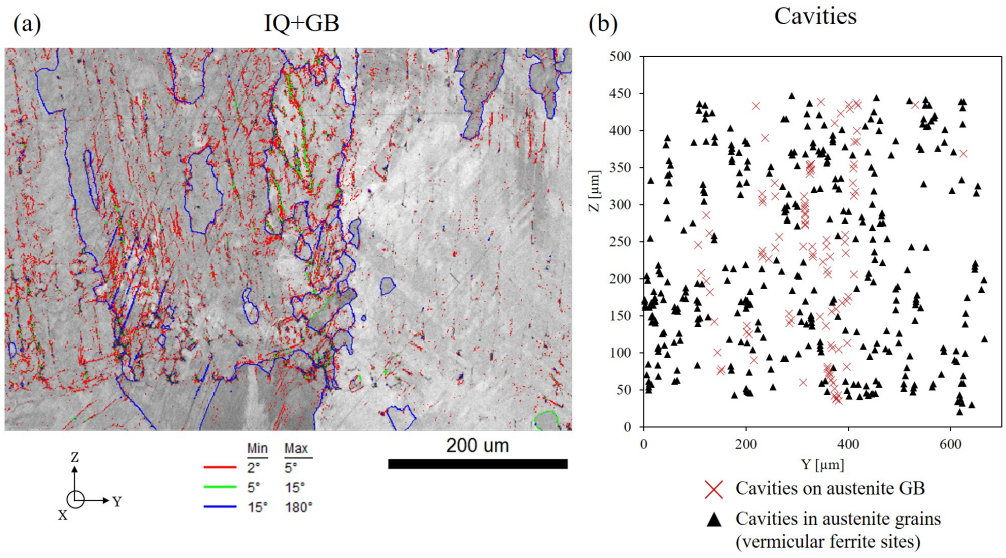

Figure 5.30: Stress relaxation damage in the FZ in a (YZ) section at a distance of 70 μm from the notch of a single-pass welded specimen compressed up to a CMOD = 1.73 mm and aged at 575 °C for 1470 h: (a) GB map over IQ (acquired with a 1 μm step) of the bottom of FZ, (b) cavity distribution of the analyzed region, located on austenite GB (red cross) and within the grains on the vermicular ferrite (black triangles).

precipitates associated to cavities, as illustrated in Figure 5.36 (a). EBSD mapping of the damaged GB was then carried out, suggesting these precipitates might be $Cr_{23}C_6$ carbides (Figure 5.36 (d)). As it is shown in the phase map, some single pixels were also identified as $Cr_{23}C_6$ phase by EBSD within the grains, but these correspond to indexation errors. The presence of precipitates was only determined correlating SE images and EBSD phase maps. The size of larger precipitates (carbides) was measured in HAZ and compared to that of those observed in the CGHAZ in a (YZ) section at X = 160 μm from the notch of a CT specimen of single-pass welded state compressed up to a CMOD = 1.73 mm and aged at 575 °C for 1470 h (Figure 5.38). The resulting sizes distribution for the two zone was very similar, with an average size of 215 nm and 228 nm in the HAZ and CGHAZ, respectively. The negligible difference in precipitate size between the two regions suggested that precipitate size was not a parameter that could explain the higher susceptibility of the CGHAZ to SRC. This is important to note since some authors in the literature [188] suggested that the higher susceptibility to cavity nucleation of large grain regions is due to a higher precipitate size, which was not observed here.

SEM-BSE images of cavities in the HAZ shown in Figure 5.37 (b) also suggested the presence of smaller Mo-rich precipitates, similarly to the as-received and cold-rolled states (Figure 5.17). These could thus correspond to the R, χ and τ phases. Similarly to the CGHAZ, the small size of these precipitates made the analysis of their nature difficult. Besides, it was difficult to conclude on relative effect of $Cr_{23}C_6$ carbides and Mo-rich precipitates on cavity nucleation.

5.3.4.4 Residual ferrite

In the HAZ and more rarely in the CGHAZ, cavities were observed in the partially decomposed residual ferrite, as shown in Figure 5.39. The fraction of cavities observed on the residual ferrite specifically in the CGHAZ was generally less than 11%. Although no further analysis was carried out, it was assumed the phases from the decomposition of residual ferrite were of the same nature as the ones determined in the as-received state.

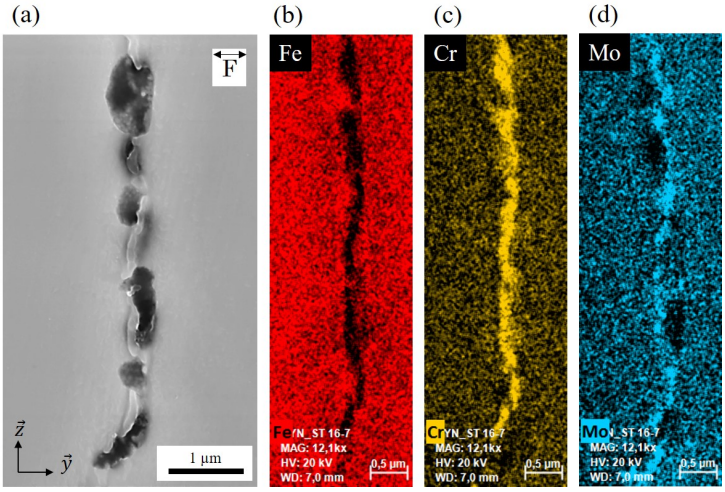

Figure 5.31: Precipitates near cavities at an austenite grain boundary in the CGHAZ. Section located at X = 120 μm from the notch of a CT sample of single-pass welded state compressed up to a CMOD = 1.73 mm and aged at 575 °C for 1470 h. (a) SEM-InLens image. EDS maps of (b) iron, (c) chromium and (d) molybdenum showing their respective qualitative distribution in the analyzed region acquired at a 7.0 mm working distance and 20 kV.

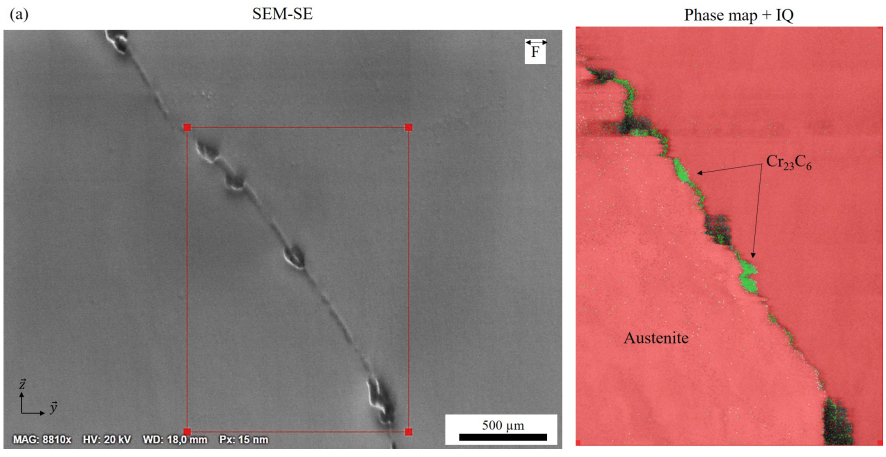

Figure 5.32: Damaged region of the CGHAZ in a single-pass welded state after Turski compression to a CMOD of 1.22 mm and aged at 575 °C for 1470 h with (a) SEM-SE captured with a 70° tilt (tilt was further corrected) and (b) phase map over on the quality index (from EBSD analysis). A 15 nm step size was used for the acquisition.

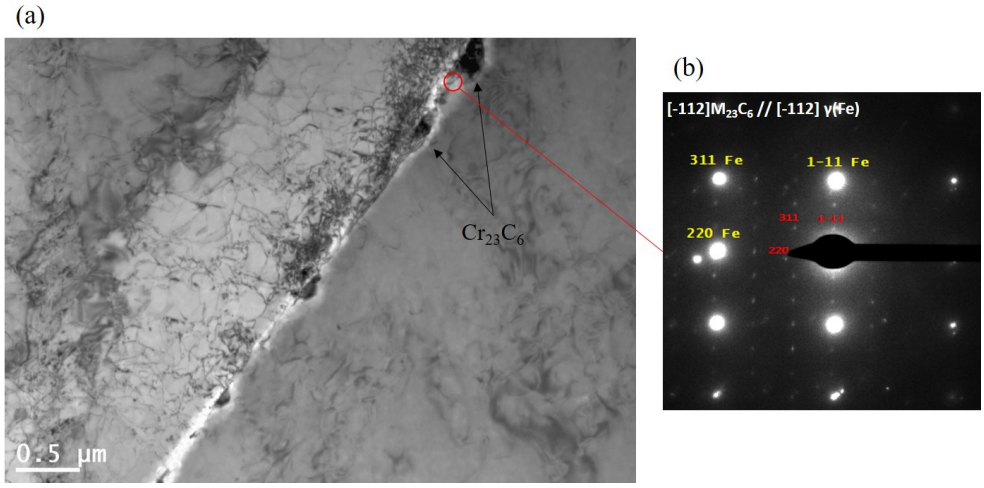

Figure 5.33: $Cr_{23}C_6$ precipitates at austenite GBs in damaged regions of the CGHAZ of a single-pass welded state after Turski compression to a CMOD of 1.73 mm and aged at 575 °C for 1470 h with (a) bright field image and (b) diffraction pattern.

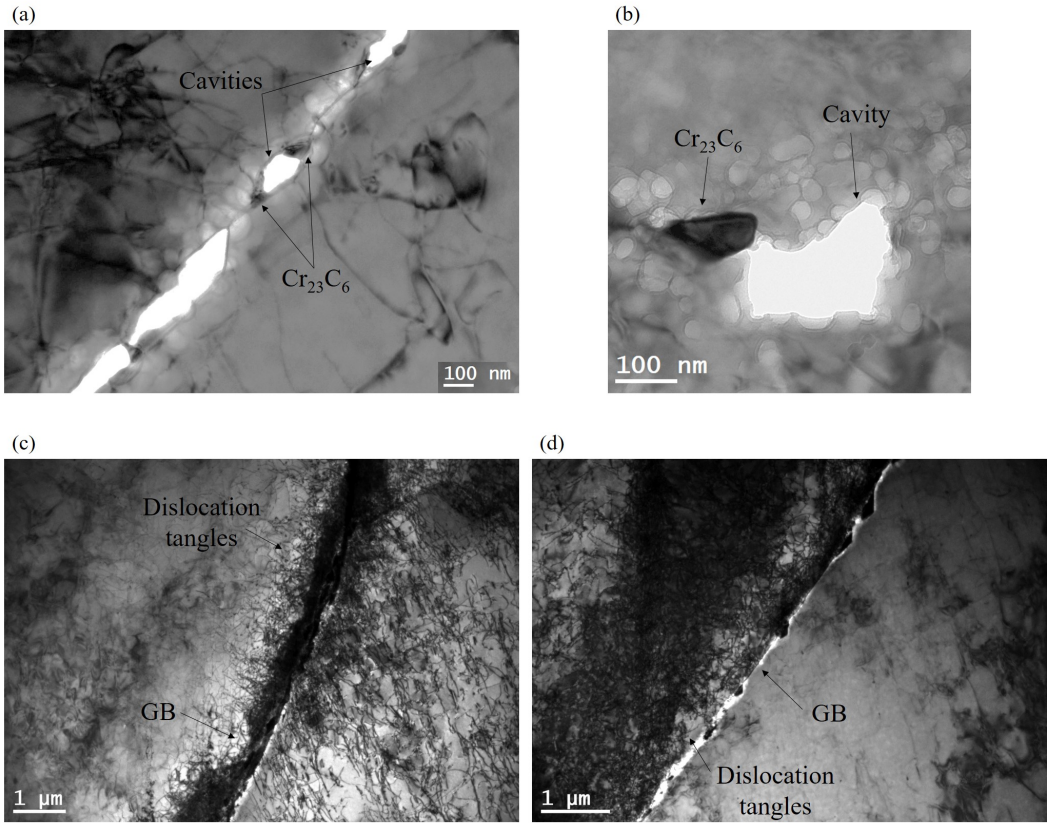

Figure 5.34: TEM images of damaged GBs in the CGHAZ of a CT specimen made from single-pass welded state compressed to a CMOD of 1.73 mm and aged at 575 °C for 1470 h with (a) and (b) cavities and $Cr_{23}C_6$ precipitates, (c) and (d) dislocations tangles at GBs.

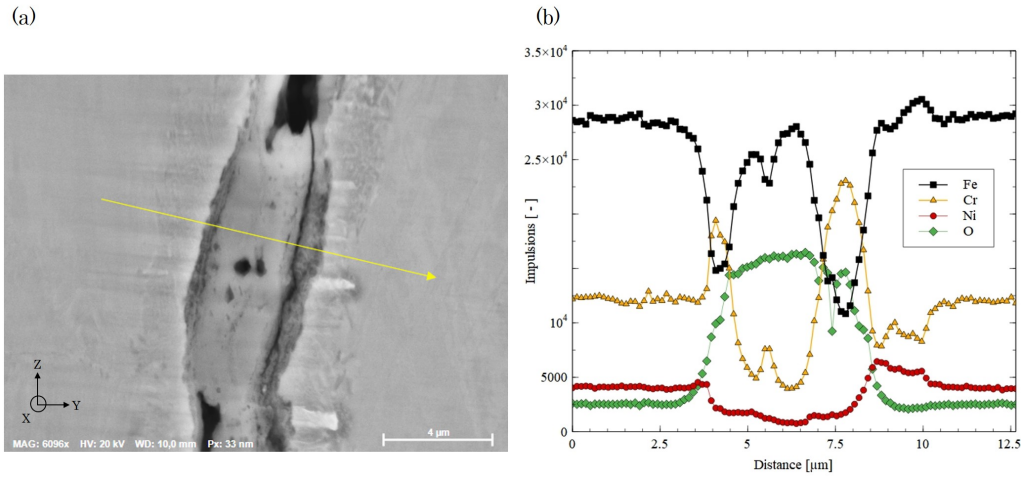

Figure 5.35: Chromium oxide layers detected in a stress relaxation crack in the CGHAZ at the notch of a single-pass welded state after Turski compression to a CMOD = 6.41 mm and ageing at 575 °C for 1470 h with (a) SEM-SE image and (b) EDS profiles of major elements.

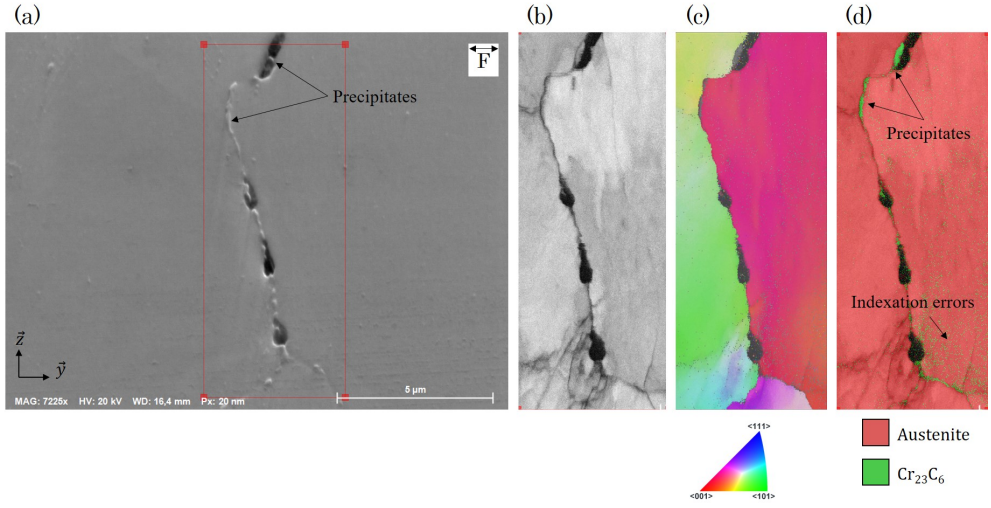

Figure 5.36: Damaged region of the HAZ in a (YZ) section at X = 160 μm from the notch of a CT specimen of single-pass welded state compressed up to a CMOD = 1.73 mm and aged at 575 °C for 1470 h: (a) SEM-SE, (b) quality index, (b) IPF in X direction of the austenite and (c) phase map overlaid on the quality index images. EBSD maps were acquired at a 70° (tilt was further corrected), 20 kV and a working distance of 16.4 mm. A 20 nm step size was used for the acquisition.

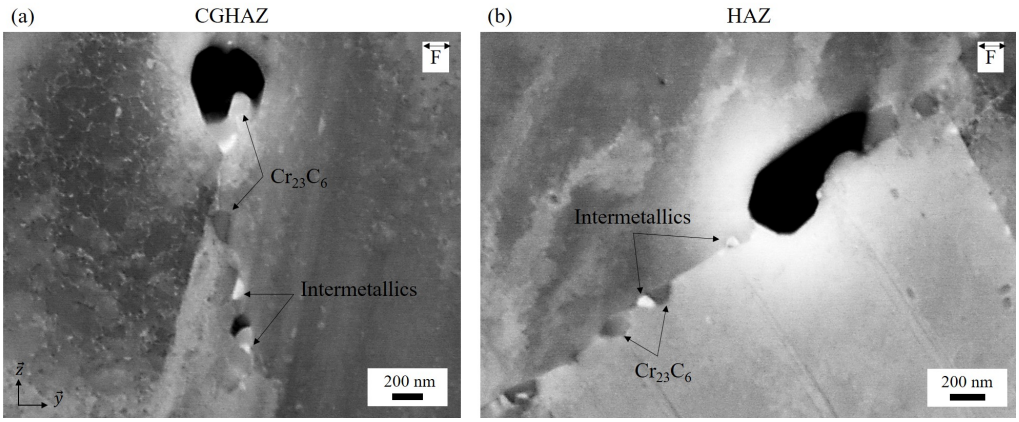

Figure 5.37: SEM-BSE images of precipitates at damaged GBs of the (a) CGHAZ and (b) HAZ of a CT specimen of single-pass welded state compressed to a CMOD of 1.22 mm and aged at 575 °C for 1470 h.

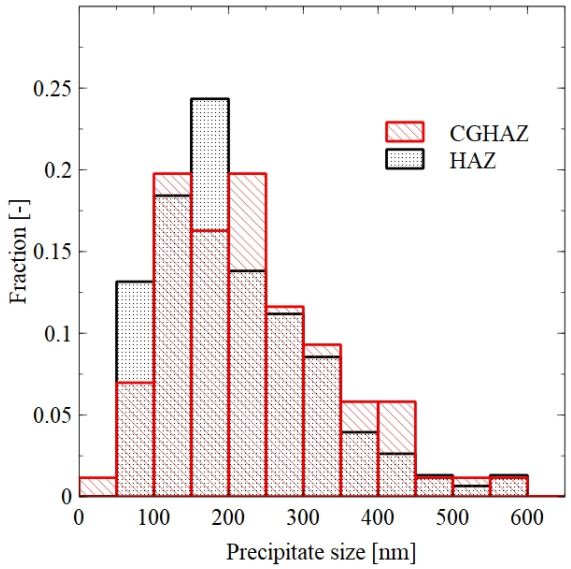

Figure 5.38: Comparison of precipitate size in the HAZ and CGHAZ measured in a (YZ) section at X = 160 μm from the notch of a CT specimen of single-pass welded state compressed up to a CMOD = 1.73 mm and aged at 575 °C for 1470 h.

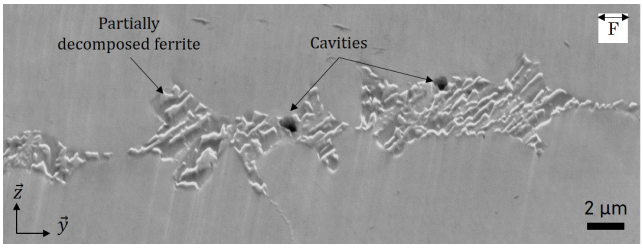

Figure 5.39: SEM-SE image of cavities located in a partially decomposed residual ferrite band in a CT specimen of single-pass welded state compressed up to a CMOD = 1.73 mm and aged at 575 °C for 1470 h. Image was captured with a 70° tilt and the tilt was further corrected.

5.4 Multi-pass welded material

In order to increase the effect of welding on SRC, a 316L(N) steel plate was welded with five passes on each face. As shown in Section 3.6, multi-pass welding allowed an increase in hardening especially in the HAZ, but also led to a more complex microstructure in the FZ and CGHAZ as compared to the single-pass weld. Similarly to single pass welded specimens, observations of as-welded multipass specimen aged at 575 °C for 1470 h did not reveal cavities. The slightly higher level of initial hardening of the HAZ in the multipass sample, as shown by the hardness measurements (Figure 3.31), did not allow for the nucleation of cavities either. As for single-pass welded material, CT specimens were then machined from multi-pass welded material to investigate SRC in this microstructure.

5.4.1 Damage analysis

CT specimens made of multi-pass welded state of the studied 316L(N) steel were compressed to CMODs of 1.82 mm and aged at 575 °C for 580 and 1470 h. Damage was further analysed in the (YZ) plane near the notch root to observe the three weld zones, as shown in Figure 5.40. The projected damage across the CT sample thickness (Z axis) is shown in Figure 5.41. No cavity was observed at the top of the FZ (Z = 0 mm) likewise to the single-pass welded state compressed to similar CMOD. However, a steep increase in cavity number was observed near the FZ/CGHAZ boundary (Figure 5.41, Z = 3.4 mm) resulting from the presence of many cavities at the bottom of the FZ (Figure 5.40 (a)). While the global number of cavities observed in this zone was high as compared to the other zones (Figure 5.41), they were relatively dispersed (Figure 5.40 (b)) hence the risk of coalescence and further cracking appeared to be relatively low.

In the CGHAZ, the total number of cavities was significantly lower but, as observed for the single-pass welded state, the cavities were localised on only few GBs of this zone near the FZ/CGHAZ boundary, with several coalesced cavities (Figure 5.40 (c) and (d)). As shown in the distribution map, many other cavities in the CGHAZ were found in the residual ferrite, which were shown to have a low effect on crack nucleation for single-pass welded state. However, the cavities at austenite GBs in this zone resulted in higher cavity density per damaged GB, making it more prone to SRC. Typically, the most damaged GB of the CGHAZ had 60% of its total length covered with cavities.

Damage and cavity distribution in the HAZ were very different from the ones observed in single-pass welded state. Although very few cavities were observed in HAZ below CGHAZ of single-pass welded state, a significant amount of cavities was noticed right below the CGHAZ of the multi-pass welded state (Figure 5.40 (a)). Moreover, multi-pass welding led to more cavities in the HAZ at mid-thickness (Z = 10.5 mm) (Figure 5.42 (a)), with several damaged GBs presenting a high cavity density, closer to the one observed in the CGHAZ (Figure 5.42 (b) and (c)). Indeed, the most damaged GB in the HAZ had 20% of the total length covered by cavities at mid-thickness of CT specimen. The level of damage in the HAZ close to that in CGHAZ in the multi-pass welded state was certainly due to the higher hardening induced by multiple welding (Figure 3.31). The higher initial plastic strain in the HAZ was certainly more favorable to cavity nucleation as compared to the FZ and CGHAZ which had still comparable hardness values to the single-pass welded state.

These results showed that while the CGHAZ remained the most prone to SRC, an increase in number of welding passes can increase the susceptibility of the HAZ to stress relaxation damage. However, despite the more complex microstructure of the FZ and CGHAZ due to the multi-pass welding, as compared to single-pass (as shown in Section 3.6), the two zones seemed to have the same impact on SRC as those after single-pass welding.

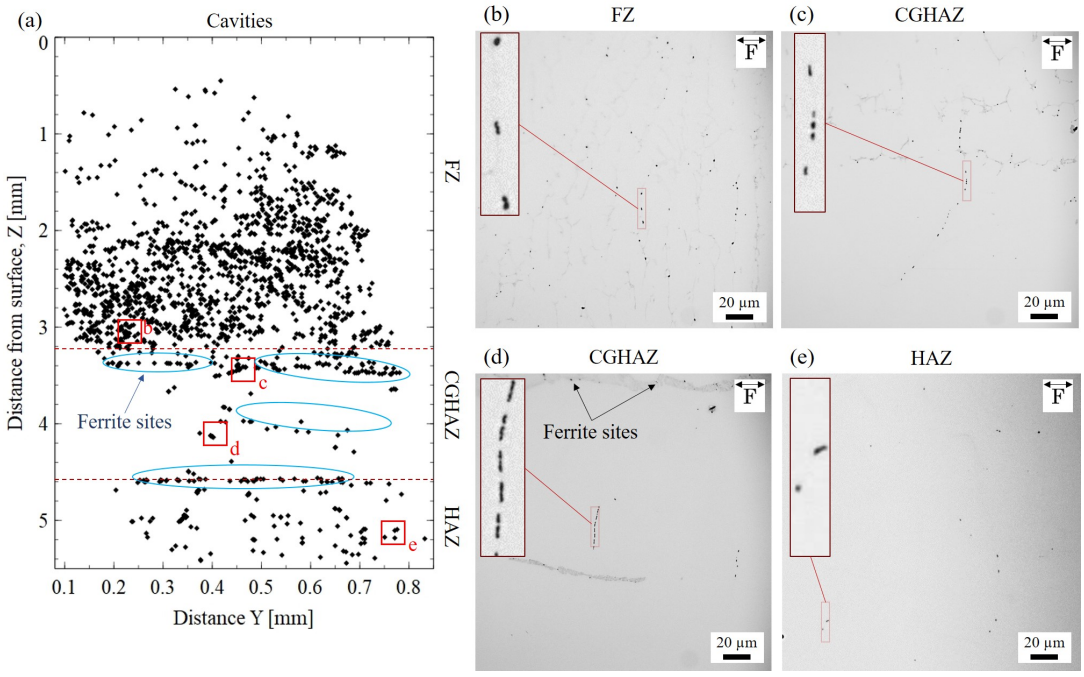

Figure 5.40: Stress relaxation damage at the notch root of a CT specimen of multi-pass welded state compressed to a CMOD of 1.82 mm and heat treated at 575 °C for 1470 h with (a) distribution of cavities and micro cracks in the FZ, CGHAZ and HAZ. Cavities located on residual ferrite are circled in blue. Maximum damage of the (b) FZ, (c)-(d) CGHAZ and (d) HAZ.

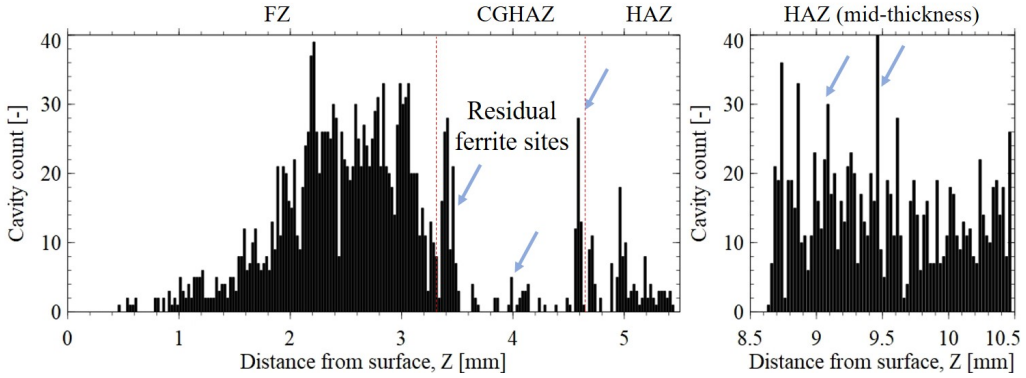

Figure 5.41: Stress relaxation damage at the notch root of a CT specimen of a multi-pass welded state compressed to a CMOD of 1.82 mm and heat treated at 575 °C for 1470 h. Cavity number was cumulated and plotted over the Z axis in the FZ, CGHAZ and HAZ.

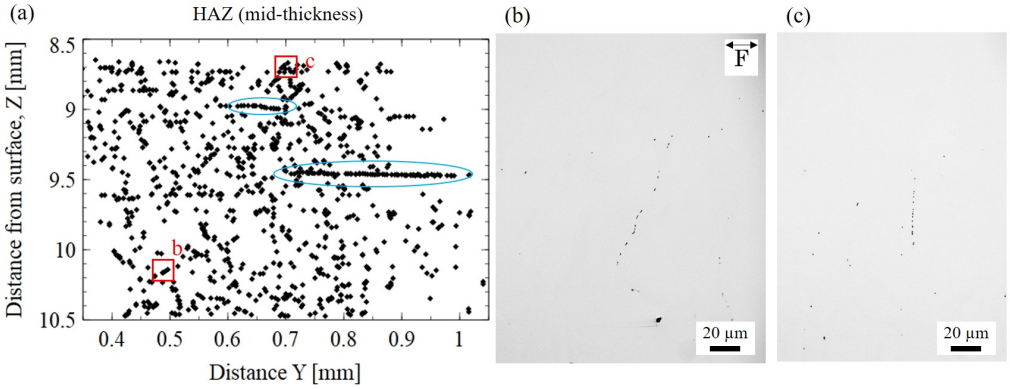

Figure 5.42: Stress relaxation damage at the notch root of a CT specimen of multi-pass welded state compressed to a CMOD of 1.82 mm and heat treated at 575 °C for 1470 h with (a) distribution of cavities and micro-cracks in the HAZ at mid-thickness. Cavities located on residual ferrite are circled in blue. Maximum damage is shown in (b) and (c).

5.4.2 Influence of relaxation time

Damage in CT specimens made of multi-pass welded material was compared after ageing for 580 and 1470 h at 575 °C . Comparison of pixel map density, representative of cavity and crack number, is shown in Figure 5.43. After 580 h of ageing (Figure 5.43 (a)), a significant number of cavities was already observed in the FZ, however they were widely dispersed at different GBs. After 1470 h, the global number of cavities in the FZ did not appear to have significantly increased (Figure 5.43 (b)). However, at some of the damaged GBs, the distance between cavities decreased as compared to ageing duration of 580 h, resulting in a higher risk for coalescence and thus cracking. In the CGHAZ after 580 h, only one GB in the whole zone was damaged but with a high density of cavities, and some coalesced cavities. In the specimen aged for 1470 h, the cavity density per damaged GB did not significantly increase, however the number of damaged GB increased, similar to observations made for the single-pass welded state (Figure 5.22). In the HAZ at mid-thickness, after 580 h of ageing the total number of cavities was higher than in the CGHAZ but lower than in the FZ, generally dispersed over the GBs. In some damaged GBs, as shown in Figure 5.43 (a), multiple but small cavities were observed close to each other. After 1470 h, the global number of cavities and the number of damaged GBs with multiple cavities in the HAZ increased, similarly to the CGHAZ.

Damage observations carried out for the multi-pass welded state showed very similar trends to observation made for single-pass welded state. Firstly, the CGHAZ was the zone with the most advanced level of damage, with highest density of cavities per damaged GB. Secondly, the damage level per GB in the CGHAZ did not increase with the relaxation time increasing, but instead damage was observed for a larger number of GBs.

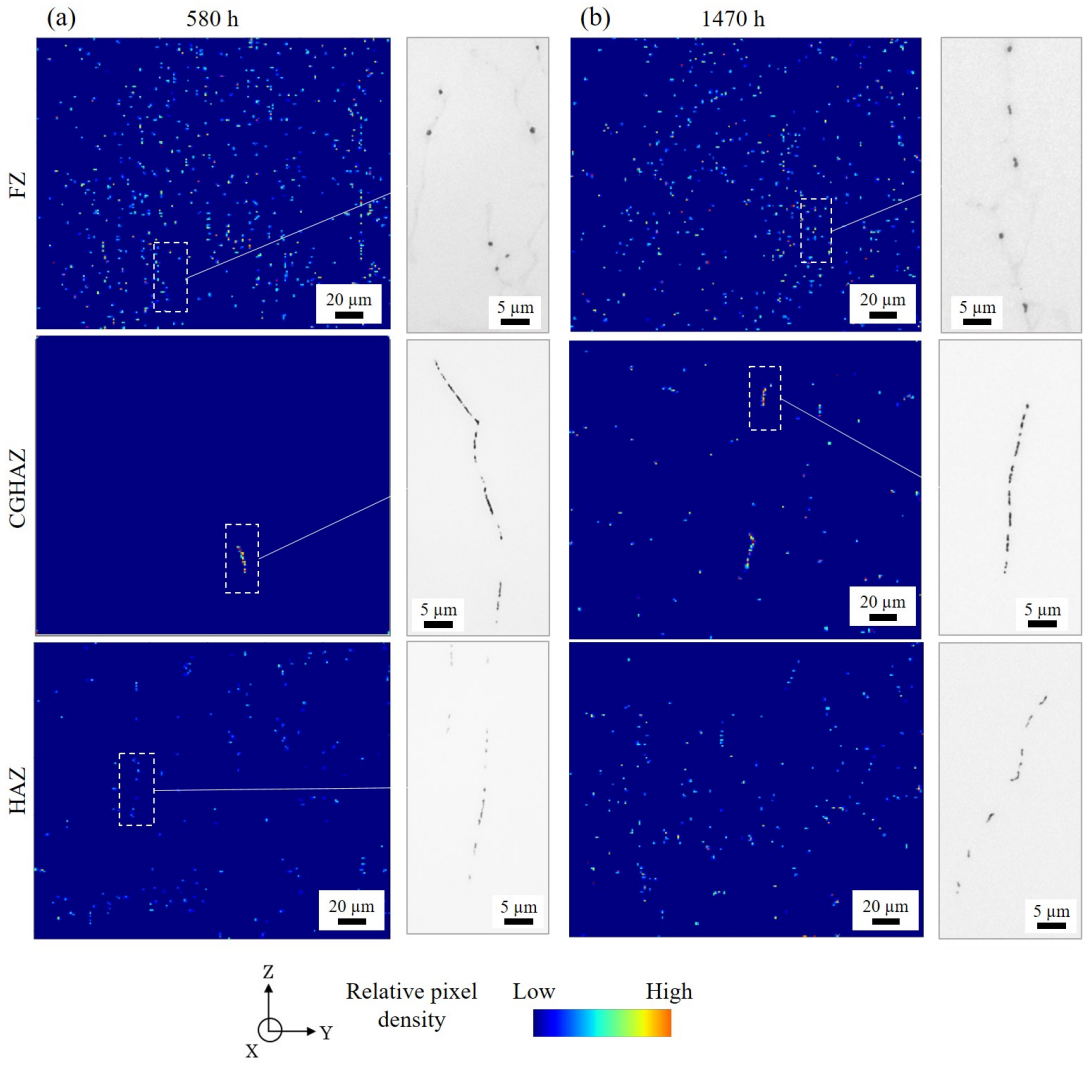

Figure 5.43: Comparison of most damaged areas of each zone of the weld of multi-pass welded state after Turski compression to CMOD of 1.82 mm, and ageing at 575 °C for 580 h and 1470 h. SEM images were binarized to only show cavities and cracks.

5.5 Cold-rolled single-pass welded state

A cold-rolled plate of 316L(N) steel was subjected to single-pass welding. Hardness measurements presented previously in Figure 3.31 showed that recovery took place due to the high temperatures induced by welding, favored by the low thickness of the plate. Therefore, very homogeneous hardening over the three weld zones was obtained.

A CT specimen machined from cold-rolled and subsequently single-pass welded material was compressed to a CMOD of 2.49 mm and aged at 575 °C for 1470 h. The most damaged region of the specimen in the (YZ) plane at the notch root is shown in Figure 5.44 (a). As compared to other material states, this specimen revealed the most heterogeneous distribution of damage among the three weld zones. The CGHAZ was the only zone with macro-cracks. Most damaged regions of the FZ, CGHAZ and HAZ are shown in Figures 5.44 (b), (c) and (d), respectively. In the FZ, no macro-crack was detected, but a few GBs presented a high density of cavities and sometimes coalesced cavities (Figure 5.44 (b)), which might form micro-cracks for longer relaxation times or higher pre-loads. In the CGHAZ, numerous micro- and macro-cracks and cavities were observed over the entire zone. Specifically, a long crack of 167 µm in length was observed right below the FZ/CGHAZ boundary (Figure 5.44 (c)). In the HAZ at mid-thickness, only a few GBs were damaged, with a very low density of cavities (Figure 5.44 (d)) as compared to the two other weld zones.

The observed damage, accounting for both cavities and cracks, was plotted across the thickness of CT sample (Z axis) (Figure 5.45 (a)). The damage distribution across the heterogeneous microstructure showed similar trends to the single-pass welded state. In the FZ, the damage level was the lowest near the CT sample surface, but highly increased near the FZ/CGHAZ boundary. The highest peaks of damage were found in the CGHAZ, with most of the damage located in the first half of the zone. This is also similar to results obtained for the single-pass welded state, where most of the damage was localised in the first quarter of the CGHAZ near the FZ/CGHAZ boundary. In the CGHAZ, several macro- and micro-cracks were observed propagating along neighbour GBs, showing a high risk of failure of the zone (Figure 5.46). Damage significantly decreased in the HAZ, similarly to observations made in the single-pass welded state. No micro-cracks were detected in this zone, and the highest peak of damage in the upper part of the HAZ was attributed to cavities formed at residual ferrite.

Similarly to the single-pass welded state, the residual ferrite bands in the CGHAZ appeared to prevent the propagation of cracks along austenite grains boundaries as illustrated in Figure 5.46 (a), red squares 1 and 2. In the case of damaged GBs without residual ferrite bands, the propagation of cracks was not restrained and were then observed along several successive GBs (Figure 5.46 (b), squares 3, 4 and 5).

Damage distribution integrated along the Y direction (Figures 5.45 (b-d)) showed a homogeneous distribution in the FZ, with no significant increase towards the notch centreline. Majority of damage in the CGHAZ was localised near the notch centreline, with three main peaks representative of the main cracks visible in Figure 5.44 (a). Damage distribution in the HAZ in this specimen appeared to be heterogeneous, with one main peak near the notch centreline. It is important to keep in mind that damage in the HAZ was very low as compared to the other regions. Therefore, confident statistical analysis of cavities distribution in HAZ was not possible.

In conclusion, differences in damage between the three weld zones were significantly higher than those observed in the single and multi-pass welded specimens.

Stress relaxation damage for the cold-rolled single-pass welded state presented similar trends to other welded states (without prior cold rolling), with the CGHAZ being the most damaged zone. However, the difference in damage between the three weld zones

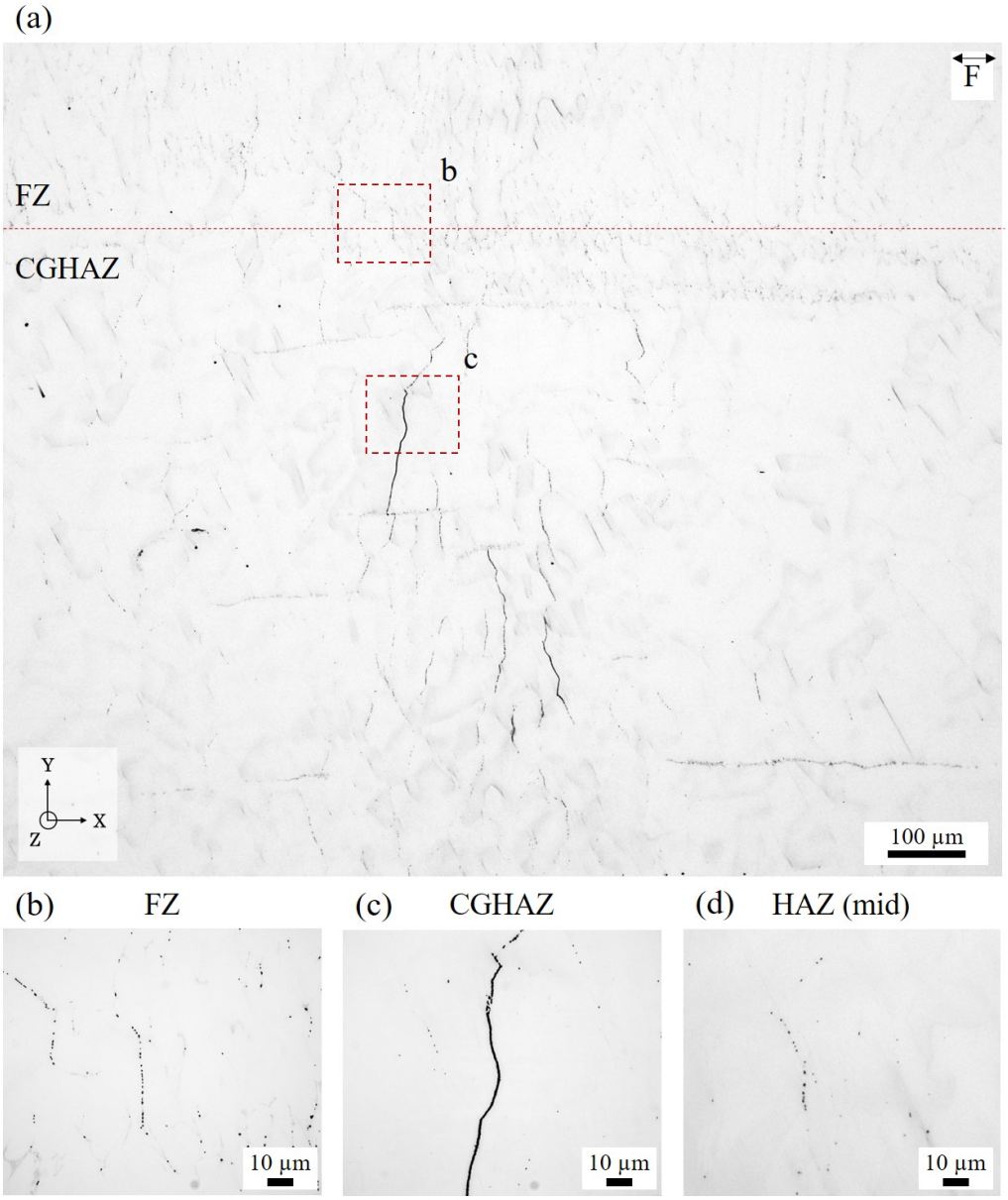

Figure 5.44: Stress relaxation damage in a (YZ) section at the notch root of a CT specimen of cold-rolled single-pass welded state compressed to CMOD = 2.49 mm and aged at 575 °C for 1470 h. (a) Macro view of the most damaged region, (b), (c) and (d) correspond to the FZ (near FZ/CGHAZ boundary), CGHAZ and HAZ (at mid-thickness), respectively.

was much more significant with prior cold-rolling. Namely, the HAZ was less affected by SRC. This is most probably because of a lower level of initial hardening in the HAZ after welding (Figure 3.31). The lower initial plastic strain in the HAZ manifestly lowered its susceptibility to cavity nucleation and growth during ageing. These results are in agreement with literature data, reporting that most cases of industrial SRC are observed in thick components [7], allowing both higher residual stresses and higher hardening.

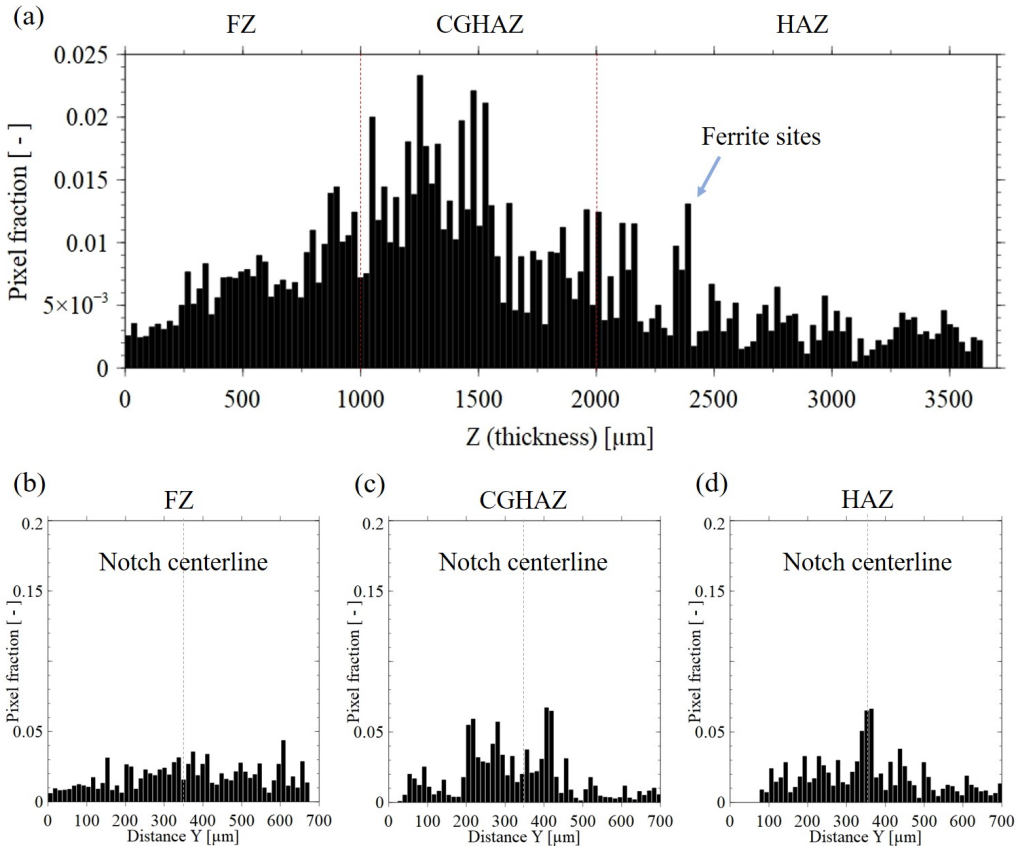

Figure 5.45: Comparison of black pixel count (representative of cavities and cracks): (a) to (c) along the Z axis corresponding to the CT specimen thickness across the three weld zones; (d) to (f) along the Y axis, for each weld zone. Cavities were observed in a (YZ) section at the notch root of a CT sample of cold-rolled single-pass welded state compressed to a CMOD of 2.49 mm and aged at 575 °C for 1470 h.

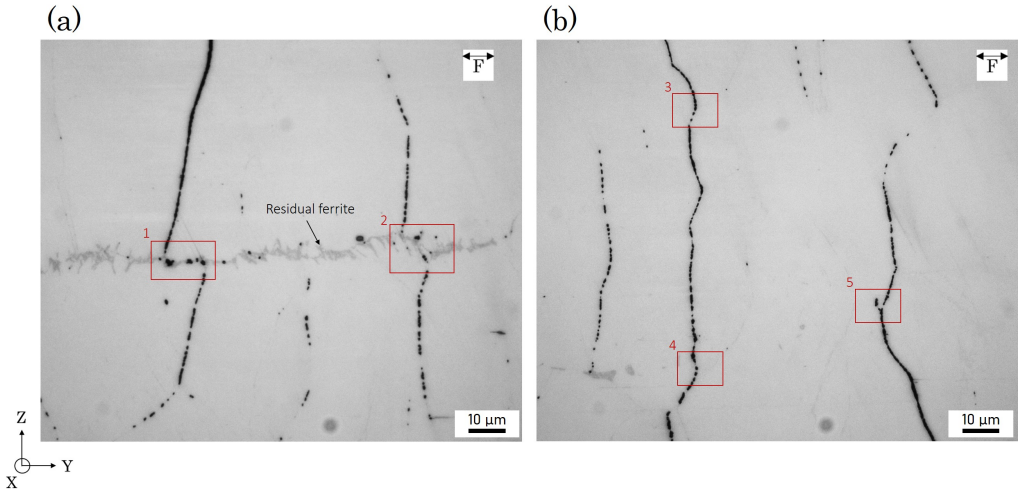

Figure 5.46: Propagation of cracks in the CGHAZ in regions (a) with and (b) without residual ferrite. Observations carried out in a (YZ) section located at X = 40 μm from the notch of a CT specimen of cold-rolled single-pass welded state compressed to a CMOD = 2.49 mm and aged at 575 °C for 1470 h.

5.6 Material with increased grain size

In all CT specimens made of single- or multi-pass welded states, CGHAZ clearly appeared to be the most prone to SRC. Specifically, the CGHAZ was shown to be more susceptible to crack nucleation than the HAZ. One of the major differences between these two zones is the grain size, which is often cited in the literature as an SRC detrimental factor. In order to better understand the lower resistance of the CGHAZ to SRC, 316L(N) steel in as-received state was subjected to heat treatment at 1300 °C to induce austenite grain growth; the resulting austenite grain size was almost five times greater than that in initial as-received state.

CT specimens made of material with increased grain size were compressed to CMODs of 2.34 and 5.62 mm and further aged at 575 °C for 1470 h. The area close to the notch root at mid-thickness of the CT sample in the (XY) plane was analysed. Observations at low magnification of the specimen compressed to a CMOD of 2.34 mm did not reveal any damage (Figure 5.47 (a)). However, two long cracks (250 μm) along two different grain boundaries were observed at the notch of the specimen compressed to a CMOD of 5.62 mm, with an additional micro-crack formed at a distance of 350 μm from the notch (Figure 5.47 (b), (d)).

Damage was further investigated at higher magnification. In the specimen compressed to a CMOD of 2.34 mm, a total of 64 cavities were observed on only 8 different GBs. Similarly to the CGHAZs in CT specimens made of single-pass welded state, damage in the material with increased grain size was localised on only a few GBs, as illustrated in Figure 5.47 (c). In the specimen compressed to a CMOD of 5.62 mm, a total of 3 cracks located on only 3 different GBs and 204 cavities on only 9 different GBs were observed. The increase in Turski compression did not seem to increase the volume of damaged material or number of damaged GBs; instead the level of damage locally increased similarly to observations of damage in CT samples made of as-received material (Section 5.1). Similarly, Lee et al. [188] showed that an increase in grain size induces a reduction of the total number of creep cavities but leads to increase in cavity density per grain.

In both specimens, cavities were observed on precipitates formed at austenite GBs similarly to other material states. In the specimen subjected to the highest Turski compression, these cavities were numerous on some GBs (Figure 5.48 (d)) with very low distance between them. On other GBs, this high density of cavities resulted in the nucleation of cracks (Figure 5.48 (c) and (e)). Some of these cracks presented similar features to damaged CGHAZ of CT made of single-pass welded state (Figure 5.35): (Fe, O)-rich and (Cr, O)-rich layers were observed inside of some cracks (Figure 5.48 (b)).

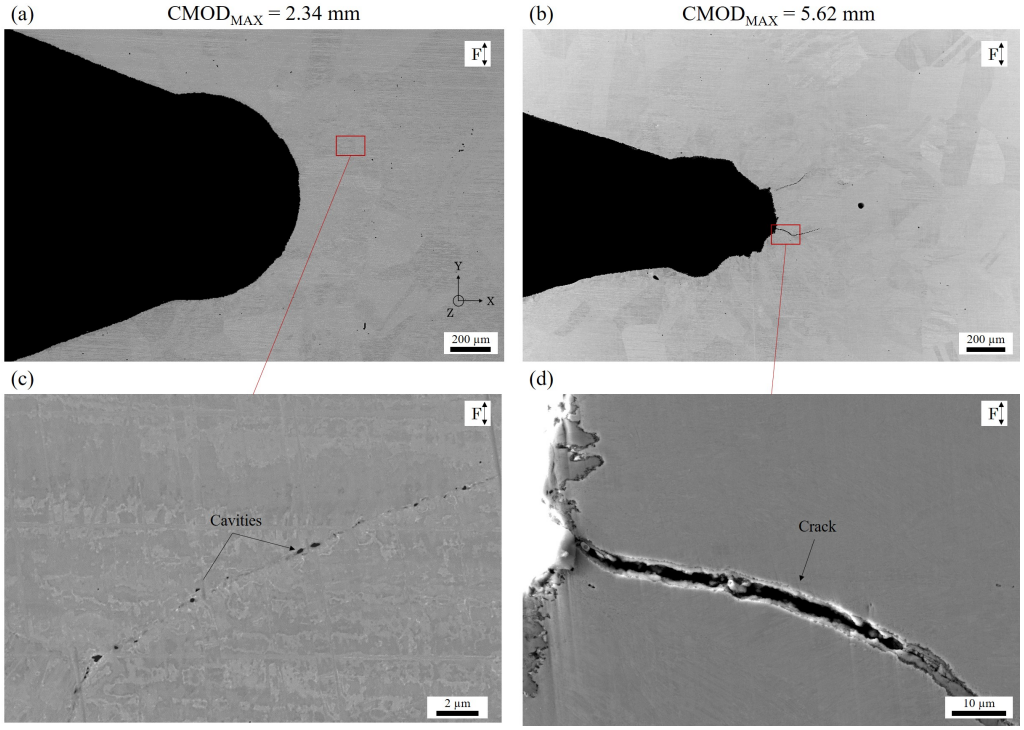

Figure 5.47: Stress relaxation damage in a (XY) section at the notch root at the mid-thickness of a CT specimen of the material with increased grain size compressed to (a) and (c) CMOD of 2.34 mm; (b) and (d) CMOD of 5.62 mm and further aged at 575 °C for 1470 h.

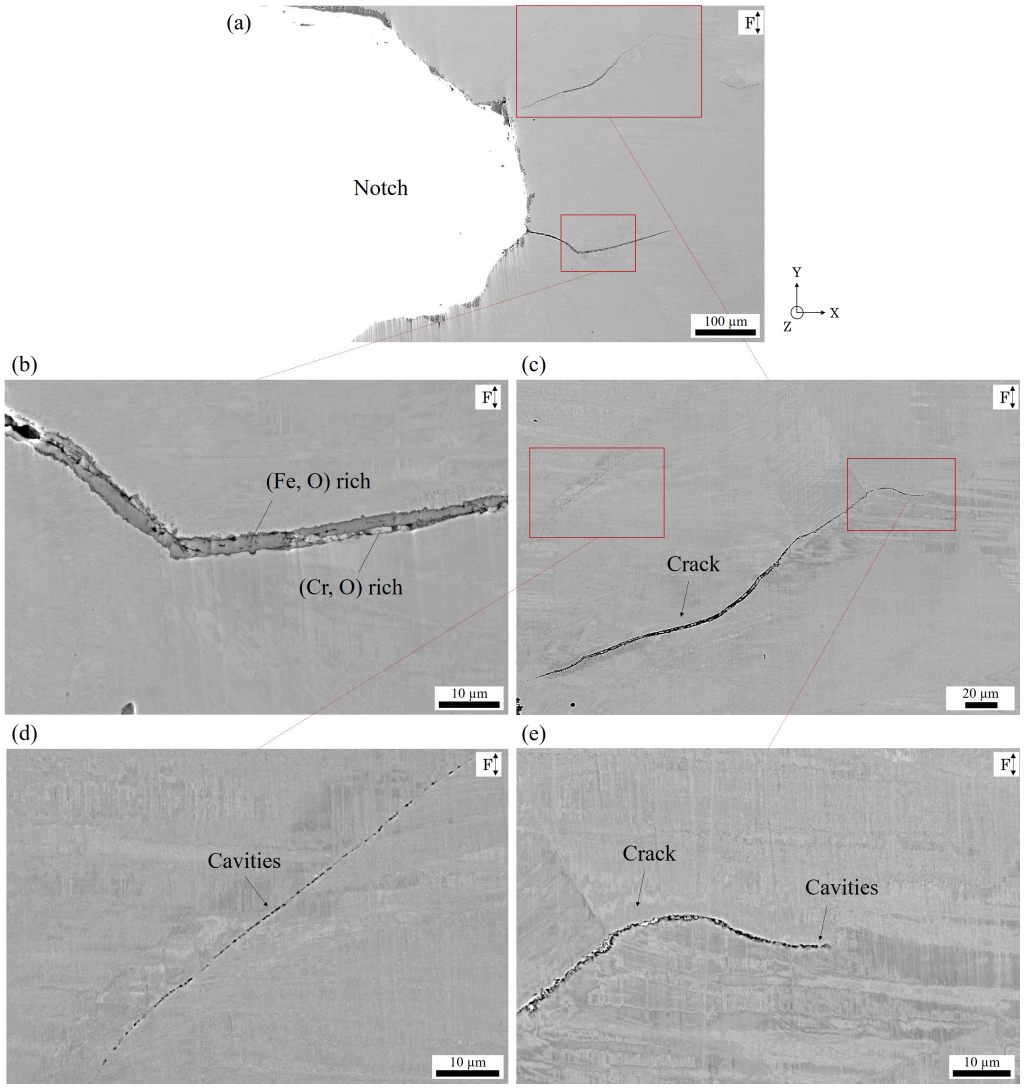

Figure 5.48: Stress relaxation damage in a (XY) section at the notch root at the mid-thickness of a CT specimen of the material with increased grain size compressed to CMOD of 5.62 mm and aged at 575 °C for 1470 h.

5.7 Comparison of SRC in the different material states

Damage distribution, magnitude and nature were compared for the different material states to get a better understanding of the SRC. It is important noting that due to the difference in mechanical properties of each material state, it was not possible to compare them in absolutely identical conditions. Therefore, comparison could only be made either using similar CMODs, residual stresses or plastic strain magnitude.

The distribution of cavity fraction and total cavity number observed in CT samples made of as-received, single-pass welded and cold-rolled states was compared in Figure 5.49. It is worth nothing that here, identification of cavities in the specimen made of cold-rolled material was carried out over a larger area than previously shown in Section 5.2 to match that of specimens made of as-received and single-pass welded states. Consequently, total cavity number of the specimen made of cold-rolled material presented here differs from numbers reported in Figure 5.9, but this does not affect previous conclusions. As-received and single-pass welded material were compressed to a CMOD of 1.73 mm and cold-rolled material to 25 kN (CMOD of 0.34 mm). Distribution of damage compared to computed residual stresses and plastic strain clearly showed the role of plastic strain: in the as-received material, plastic strain was high near the notch but quickly decreased (Figure 5.49 (a)). As a result, most of the damage (more than 50%) was localised in the near-notch root region. In the single-pass welded material, the initial hardening induced by welding (about 4%) led to higher plastic strain levels over the whole specimen (Figure 5.49 (b)). As a result, damage was still significant at 500 μm distance from the notch. In the cold-rolled state, this effect was more pronounced: high level of plastic strain (>20%) induced by cold-rolling was initially observed in the whole specimen (Figure 5.49 (c)). As a result, the distribution of damage was even more homogeneous than in the single-pass welded material and cavities could be observed up to 2 mm from the notch root. It thus appeared clearly that the initiation of damage requires first of all sufficient levels of plastic strain and then may be governed by residual stresses, which are also required to induce SRC.

Comparison of the highest damaged regions CT specimen made of as-received and single-pass welded materials are shown in Figures 5.50 (a) and (b), respectively. These also indicated that the level of damage per GB in the HAZ of the single-pass welded state was significantly higher than in the as-received state for the same CMOD. This illustrated the detrimental effect of welding on SRC. It is worth reminding that in the CT specimen made of single-pass weld compressed to a CMOD of 1.73 mm, even cracks were found in the CGHAZ (Figure 5.20 (b)).

Damage observed in CT specimen made of as-received material was also compared to that of a CT specimen made of material with increased grain size, both compressed to the same CMOD of 2.34 mm and aged at 575 °C for 1470 h. Firstly, the total number of cavities was somewhat higher in the as-received material than in the material with increased grain size, 85 against 64, respectively. This is consistent with higher total cavity number in the HAZ as compared to the CGHAZ in CT specimens made of single and multi-pass welded materials (Section 5.3 and 5.4). Secondly, spatial distribution of damage was quite different between the two material states (Figure 5.51 (a) and (b)): the number of damaged GBs in the material with increased grain size was significantly lower than in the as-received one. In the material with increased grain size, only 8 GBs were damaged, compared to 50 in the as-received material. This is also consistent with the results obtained for the single- and multi-pass welded states. At this point, results were not sufficient to conclude on the relative risk of SRC between the two material of different grain sizes. Consequently, to better characterize the influence of grain size, additional characteristics of cavities and their distribution were analysed (Figure 5.52).

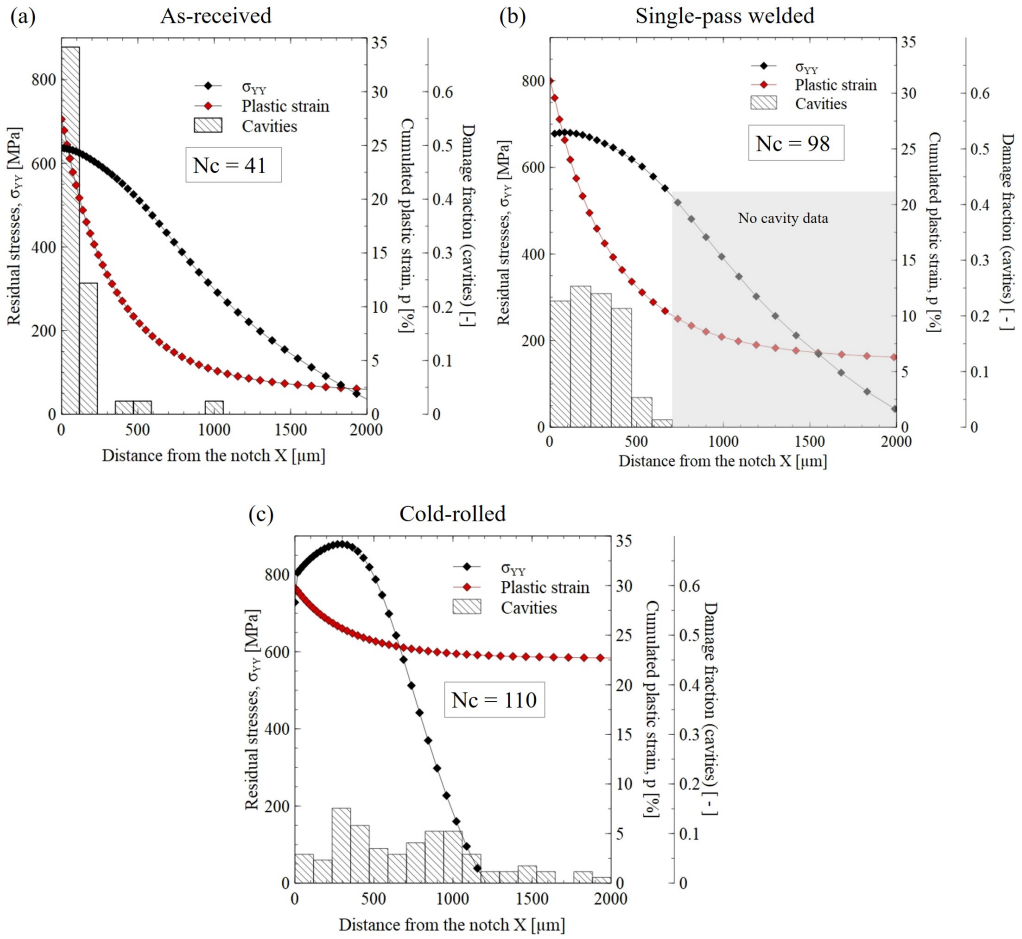

Figure 5.49: Comparison of stress relaxation cavity fraction, predicted post-Turski compression residual stresses σ_{YY} and cumulated plastic strain in a (XY) section at the notch root at the mid-thickness of CT specimens made of (a) as-received, (b) single-pass welded state compressed to a CMOD of 1.73 mm and (c) cold-rolled state compressed to 25 kN (CMOD of 0.34 mm), all aged at 575 °C for 1470 h. "Nc" stands for total cavity number.

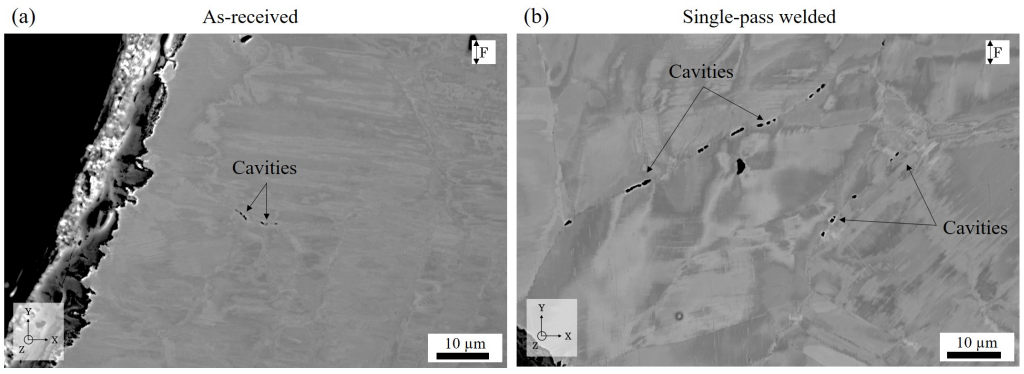

Figure 5.50: Comparison of highest stress relaxation damage in a (XY) section at the notch root at the mid-thickness of CT specimens made of (a) as-received and (b) HAZ of the single-pass welded material, both compressed to CMOD of 1.73 mm and aged at 575 °C for 1470 h.

Results showed that the average number of cavity per damaged GB was higher in the material with increased grain size (Figure 5.52 (a)). In addition, the maximum number

of cavities on one GB was significantly higher in the material with increased grain size: 21 against 2 in the as-received material. In contrast, the average cavity size was slightly larger in the as-received material (Figure 5.52 (b)), and coalesced cavities observed in the as as-received material seemed to be at a more advanced state that those observed in the material with increased grain size (Figure 5.53 (a) and (b)). This is consistent with differences observed between the CGHAZ and the HAZ of a CT specimen made of a single-pass welded material compressed to a CMOD of 1.39 mm (Figure 5.20 (a)). This is also in agreement with quantification of stresses and strain thresholds for cavity nucleation, which were estimated to be lower in the HAZ than in the CGHAZ (Table 5.2).

However, the total cavity length per damaged GB was higher in the material with increased grain size than in the as-received material (Figure 5.52 (c)). In addition, the spread of cavities, measured by the maximum GB length covered by a significant number of cavities, was higher in the material with increased grain size (Figure 5.53 (c) and (d)). As a result, in a small-grained microstructure (HAZ or as-received material), relatively large coalesced cavities could form, but they would tend to be isolated and concentrated over a small portion of GBs. In the material with increased grain size (or CGHAZ), cavities would be smaller and less coalesced in the first steps of the damage mechanism, but distributed over a much larger GB length. As it is suggested by observations carried out in CT made of welded materials, the propagation of damage over a GB is then favored in large grain materials. Lastly, it is worth noting that, while the two specimens were subjected to the same displacement during Turski compression, due to the coarser grains of the material with increased grain size, post-compression residual stresses and plastic strain are expected to be much lower as compared to those of the as-received material for the same CMOD.

In summary, these analyses showed that the favored SRC observed in the large grain material (or CGHAZ), is due to two main characteristics of cavity distribution: a favored multiplication of cavities traduced by a higher number of cavity per damaged GB, spread out over a higher GB length; and a higher total length of cavity per damaged GB. Furthermore, it is important to remember that the occurrence of a crack in a fine-grained material would be less harmful than in a coarse-grained material, since crack growth and propagation is favoured in a coarse-grained material.

In conclusion, comparison of SRC in the different material states showed that an increase in initial plastic strain and material grain size increase the risk for SRC. However, these did not entirely explain the observations made for the welded materials: while the CGHAZ was observed to be the most prone to cracking, damage in this zone was generally limited to the first quarter close to the FZ/CGHAZ border. It is very likely that the transition region between the FZ and the CGHAZ is an additional factor for the SRC sensitivity. This would also be consistent with the fact that a high concentration of damage in the FZ was found near the FZ/CGHAZ interface.

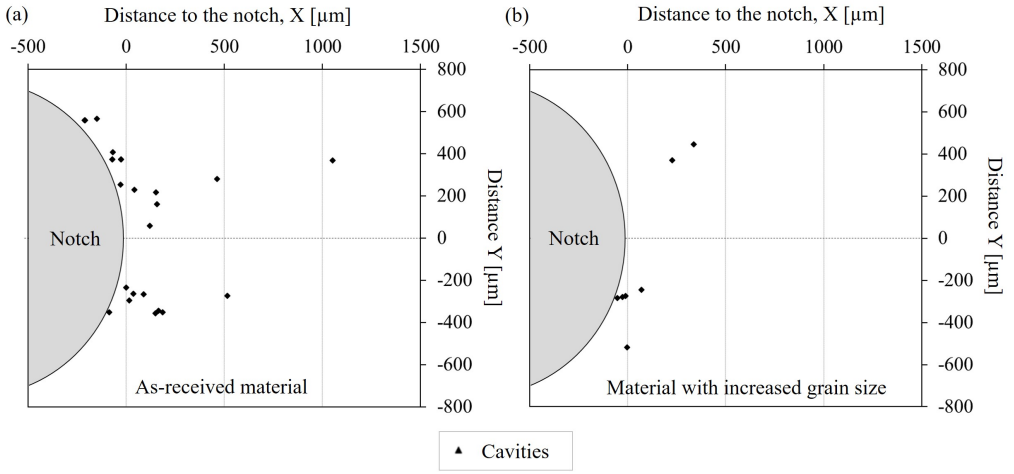

Figure 5.51: Comparison of spatial distribution of cavities in a (XY) section at the notch root at the mid-thickness of CT specimens made of (a) as-received material and (b) material with increased grain size, both compressed to CMOD of 2.34 mm and aged at 575 °C for 1470 h.

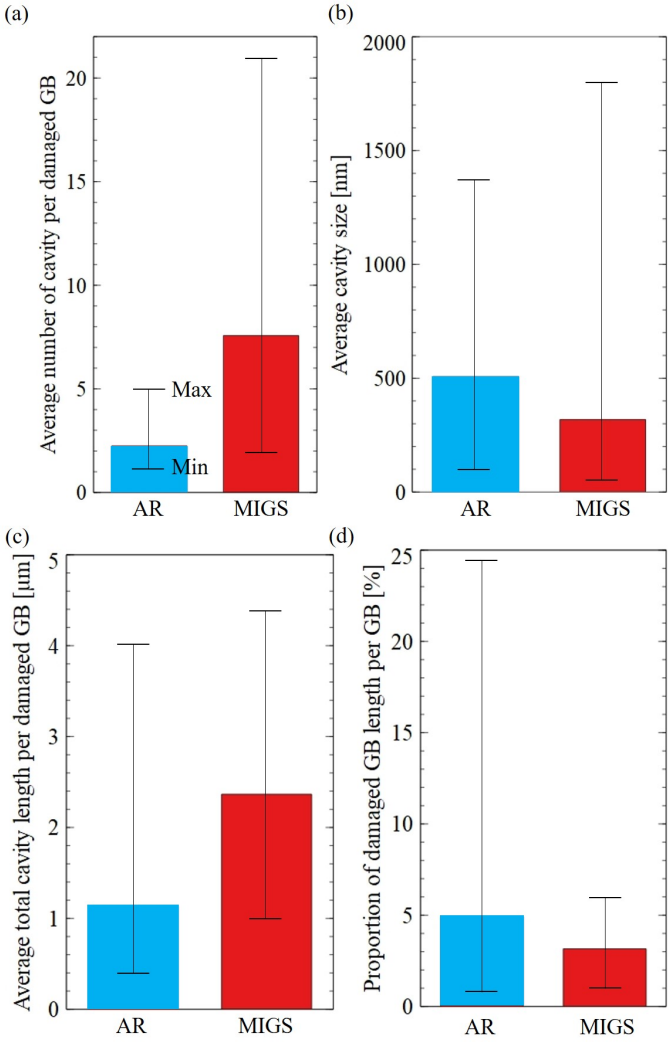

Figure 5.52: Comparison of stress relaxation cavities properties in a (XY) section at the notch root at the mid-thickness of CT specimens made of as-received (AR) material and material with increased grain size (MIGS) both compressed to CMOD of 2.34 mm and aged at 575 °C for 1470 h: (a) average cavity number per damaged GB, (b) average cavity size, (c) average total cavity length per damaged GB and (c) proportion of damaged GB length per GB. Maximum and minimum values for each quantity is also indicated.

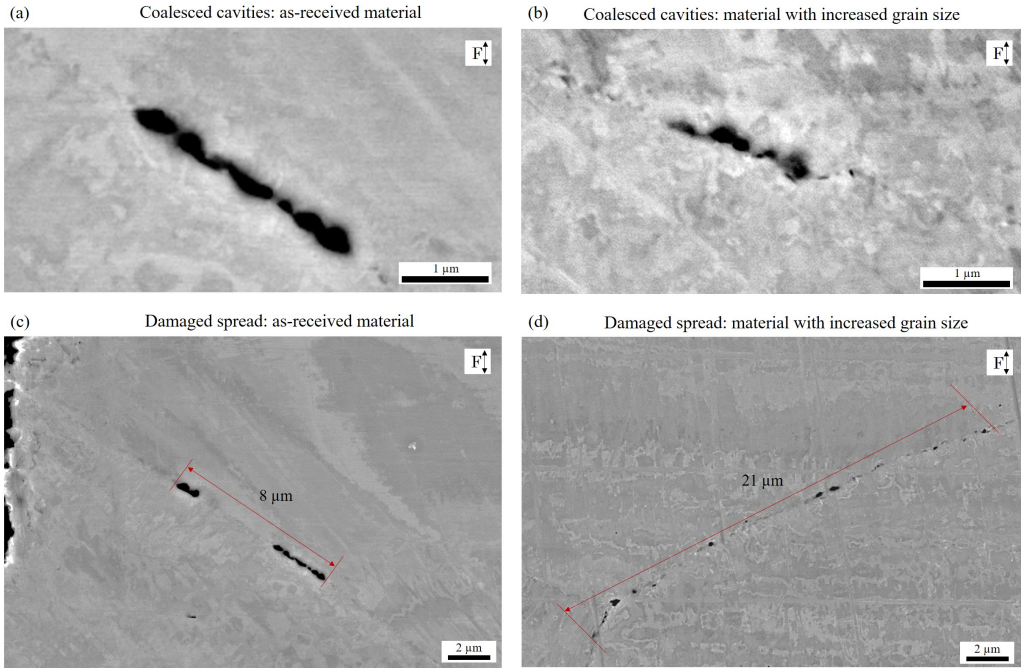

Figure 5.53: Comparison of most coalesced cavities (a, b) and highest damage spread (c, d) in a (XY) section at the notch root at the mid-thickness of CT specimens made of (a), (c) as-received material and (b), (d) material with increased grain size both compressed to CMOD of 2.34 mm and aged at 575 °C for 1470 h.

5.8 Summary of results and conclusions

To study the effect of welding on SRC in 316L(N) steel, SRC tests were carried out for as-received, cold-rolled, single-pass welded, multi-pass welded, cold-rolled welded states and material with increased grain size. A careful analysis of CT specimens for these different states after Turski compression and further heat treatment at 575, 600 °C for 580 and 1470 h allowed analysing the effect of a heterogeneous microstructure and mechanical factors (stresses, strain) on SRC.

The study of as-received state showed that it was possible to trigger stress relaxation damage in the studied 316L(N) steel by a Turski compression, inducing the required tensile residual stresses. For this state, damage was found to be in the form of creep-like GB cavities. These cavities were mostly observed to form at the interface between austenitic matrix and GB precipitates in agreement with literature data [45]. The formation of damage appeared to be primarily influenced by the level of plastic strain, at least as much as residual stresses. This is a very important result since many studies on SRC available in the literature focused on the level of residual stresses. As expected, an increase in pre-load (i.e. increase in residual stresses and plastic strain) led to an increase in damage.

Using the analysis of damage made in the cold-rolled material, the nature of GB precipitates on which cavities were observed to form during the stress relaxation could be carefully investigated. Large and small precipitates close to cavities were clearly observed using both SEM and TEM. The large precipitates, rich in C/Cr/Mo, were identified as $Cr_{23}C_6$ by electronic diffraction in agreement with literature data [45]. Smaller precipitates rich in Mo might correspond to τ and/or χ, but it was difficult to conclude on their precise nature due to their size and very small fraction. Nevertheless, these Mo-rich precipitates were believed to favor the cavity nucleation, suggested by the presence of nano-cavities observed at the tip of these precipitates. In addition, it was found that an increase in relaxation time and temperature (from 575 to 600 °C) resulted in an increase of damage. Finally, the correlation of observed damage and stress and plastic strain computed using FEM showed that higher initial plastic strain led to a larger damaged zone than in the as-received state. As a result, for cold-rolled state, the cavities were observed to form in the regions where the principal residual stress was relatively low, but the plastic strain was high due the prior cold-rolling. This again confirmed the strong influence of plastic strain on SRC.

Microscopy analysis of single and multi-pass welded states after heat treatment (without Turski compression) showed that stresses and strain induced by the welding alone were not sufficiently high to trigger SRC and hence prior Turski compression was required to induce damage for the chosen relaxation duration and temperatures. Results showed that the procedure developed in this work allowed triggering SRC in welded specimens after a Turski compression and thermal relaxation. This method thus allowed for the first time the observation and characterisation of stress relaxation damage in heterogeneous weld microstructures, in which each zone was exposed to comparable levels of stresses and plastic strain (see Section 4.3.1). For single-pass welded state, after Turski compression and ageing, the damage was heterogeneously distributed in the three weld zones, with the CGHAZ being the most prone to SRC. In the FZ, the cavities were mainly formed in the vermicular ferrite partially transformed into the $Cr_{23}C_6$, σ phase and regenerated austenite γ_R during the ageing. In the CGHAZ and HAZ, cavities were found on $Cr_{23}C_6$ precipitates and less often in residual ferrite. Cavitation appeared for lower stresses and strain levels in the FZ and HAZ than in the CGHAZ. However, crack nucleation was clearly favored in the CGHAZ as lower stresses, strain and shorter relaxation time were required for the first crack to be detected in this zone as compared to that in other weld zones. For the first time, the higher susceptibility of the CGHAZ to SRC often observed in

industrial cases could be reproduced in laboratory conditions thanks to a new approach. Particularly, the use of Turski compression allowed concluding that the differences in damage observed between the three weld zones were primarily due to the microstructure. For the first time, apparent strain estimated using GOS and KAM criteria from EBSD data was correlated to the plastic strain obtained from FEM and was correlated to GB damage. This showed that the GOS can be used as probe of global macroscopic strain, even though it has to be used with care at smaller scale due to the heterogeneous behavior of grains.

The investigation of SRC in multi-pass and cold-rolled single-pass welded states showed that the hardening induced by welding favored the nucleation and development of damage in Turski-compressed CT specimens. In the HAZ with no welding hardening (cold-rolled welded state), damage was very mild in the HAZ as compared to the CGHAZ. In the HAZ with medium level of initial hardening (single-pass welded state), damage was still lower than that in the CGHAZ but with less difference. In a HAZ with high level of initial hardening (multi-pass welded state), damage was very close to that of the CGHAZ. The reduction of component thickness or lowering the welding heat (by lowering welding power input) could then help in increasing the resistance to SRC.

For the first time, an experimental study was dedicated to the investigation of the effect of grain size on SRC. Analyses of SRC carried out in the material with increased grain size revealed that damage was significantly more localised than in the as-received state, meaning higher number of cavity per GB and lower distance between them. This is in agreement with observations made in the CGHAZs of CT specimens made of welded states. However, the increase in grain size led to smaller cavities. Therefore, it was concluded that the grain size is one of the main parameters explaining the higher susceptibility of CGHAZ to SRC, but that other factors are also involved. Typically, the FZ-CGHAZ transition region was found to be particularly detrimental for both the FZ and CGHAZ regarding their resistance to SRC. Further investigations on SRC influencing factors had thus to be carried out to better understand the lower resistance of the CGHAZ.

Chapter 6

Effect of microstructural features on SRC

Contents

Results presented in Chapter 5 showed that SRC is very heterogeneous for welded states of studied 316L(N) steel. Although damage induced by Turski compression and following heat treatment could be observed in all zones of weld microstructure, stress relaxation cracks were preferentially initiated in the CGHAZ. In addition, the analysis of SRC in CT specimen made of material with increased grain size revealed that the way GB cavities nucleated, multiplied and coalesced was different as compared to that of the as-received material. The grain size then appeared to be the main explanation for the differences in resistance to SRC observed between the HAZ and CGHAZ of the welding microstructure.

However, as discussed in the literature review on SRC (Section 1.4), other factors were suggested to explain higher susceptibility of the coarse-grained regions to SRC, such as a change in the deformation behavior, a higher linear GB density of precipitates and larger precipitates. Besides, the literature also reported microstructural factors that can favor the nucleation of cavity, in the case of stress relaxation or creep tests. Typically, Young's modulus, Schmid factor, grain boundary misorientation angle, mechanical twins, grain boundary triple points, angle formed between the grain boundary and the loading axis are cited to influence the formation of GB cavity.

Therefore, these factors are now discussed using the results of the present work to get insight into the mechanisms of SRC in the studied 316L(N) steel. It is essential noting that the study of these factors is particularly complex, because most of them are correlated. For example, grain boundary misorientation angle can be correlated to GB energy and thus to GB precipitation. The effect of each factor of weld microstructure on SRC is thus very difficult to analyse. Moreover, our methodology had limitations and might have induced uncertainties, as characterisations were performed using 2D cross-sections. Other sites prone to damage may therefore not be visible during the analysis. It is worth noting as well that the effect of Young's modulus and Schmid factor cannot be confidently analysed as the grain orientation before the relaxation could not be known: the analysis of damage was performed after compression, which induced significant plastic strain and thus an evolution of grain orientation and structure.

Therefore, based on the EBSD analyses performed on the CT specimens made of single-pass welded state and further subjected to relaxation treatment, the cavity formation was then confronted to several microstructure features: intragranular strain, mechanical twins, GB misorientation angle, GB precipitates, angle formed by a GB plane with the loading axis and GB triple points. To increase statistics, the effect of these parameters on cavity nucleation was mainly investigated using the observations carried out in HAZs of damaged specimens where more cavities was observed, their distribution was homogeneous and microstructure was similar to the CGHAZ asides from the grain size. The results could then be transposed to the CGHAZ and eventually further explain SRC in this zone. All grains analyzed in the (YZ) plan near the notch centreline were assumed to be exposed to a similar macroscopic loading for a given Turski compression condition, so their susceptibility to cavity nucleation could be compared.

6.1 Intragranular strain

It was shown in Section 5.3.3 that average grain orientation spread, or GOS, was highly correlated to the plastic strain and number of cavities formed during stress relaxation. In damaged regions of CT specimens of single-pass welded state, cavities were frequently found at GBs where at least one of the two adjacent grains had a low GOS value while being localised in a region where the mean GOS value was high. Lower GOS value would suggest lower plastic strain. This statement is of course made with the assumption that

the plastic strain revealed by the GOS is mostly due to the compression and not to relaxation of stresses. Indeed, plastic strain at the notch of the CT specimen induced by the compression was estimated to be around 30% while the strain which might be generated by relaxation is believed to be lower than 3%, according to Wortel [12].

An example of analysis of the effect of plastic strain using GOS on the presence of cavity after the relaxation treatment is shown in Figure 6.1, where the HAZ near the notch of a CT sample of single-pass welded state compressed to a CMOD of 1.73 mm and aged at 575 °C for 1470 h is investigated. The highest number of cavities in this region (indicated by white circles) was observed at the GBs between the grains 1 and 2 (Figure 6.1 (c)), having relatively low GOS levels in comparison to the rest of the region. Low strained grains surrounded by highly strained grains is a result of different initial orientations of these grains to the loading direction (i.e. different Schmid factors) which might lead to high strain and stress close to GB to accommodate this difference and, thus, earlier cavity nucleation at these GBs. In a similar way, cavities were also observed at GBs between two grains with significantly different GOS values: a GOS of 8° in grain 3 and 3° in grain 4 (Figure 6.1 (a)).

Nevertheless, as stated earlier, it was difficult to identify the effect of intergranular strain alone since it can be correlated with other factors. For instance, as cavities were observed to form between the grains 1 and 2 with low GOS levels, cavity formation could be expected as well for the grains 1 and 8 due to their GOS values; however, no cavities was observed. The absence of cavities in this case was in fact due to the absence of GB precipitates (Figure 6.1 (b)), which are necessary to the nucleation of cavities. Besides, the presence of cavities at GB between the grains 5 and 6, but also between the grains 5 and 7, was most likely due to the presence of mechanical twins in the grain 5, which also strongly favor cavity nucleation (discussed further in Section 6.3).

A similar analysis was also conducted in a weld microstructure, over the three weld zones. GOS and KAM maps of the FZ/CGHAZ/HAZ regions close to the notch of the specimen compressed to a CMOD of 1.73 mm are shown in Figure 6.2 (a) and (b), respectively. The map of GOS averaged for each grain compared to the distribution of damage (in black) showed again that the highest damage was located preferentially at a GB between grains with low GOS values (grains 2 and 3). This suggests that the average plastic strain of the grain does not influence the nucleation of cavity, but instead it is the accumulation of dislocations near GBs that creates favorable nucleation sites. Indeed, the KAM map shown in Figure 6.2 (b) revealed that, while grains 2 and 3 did not have a high GOS value, grain 3 presented high local KAM values close to grain 2. A low average GOS associated with high KAM levels in the bulk would indicate that the plastic strain within the grain was very heterogeneous. Moreover, high KAM values close to GBs suggest an accumulation of dislocations near the GB (it is worth noting that KAM reveals only geometrically necessarily dislocations and not statistically stored dislocations), thus a rise of stress near the GB, favoring cavity nucleation. This is in agreement with TEM results shown previously in Figure 5.34, where accumulation of dislocations were observed near damaged GBs of the CGHAZ. This is also in agreement with results of Unnikrishnan *et al.* [44], who found high KAM values near reheat cracks in a post service 316H header.

To further investigate the effect of intragranular strain on the presence of damage, EBSD analyses were carried out at smaller scales. Significant crystal orientation rotations near GB with cavities was often revealed by both local GOS and KAM (Figures 6.3 and 6.4). This is in agreement with results of Noel *et al.* [141] for creep cavity nucleation. Besides, a lot of the cavities were located on portions of grain boundaries where crystal rotations close to the damaged GB was observed only in one of the two grains.

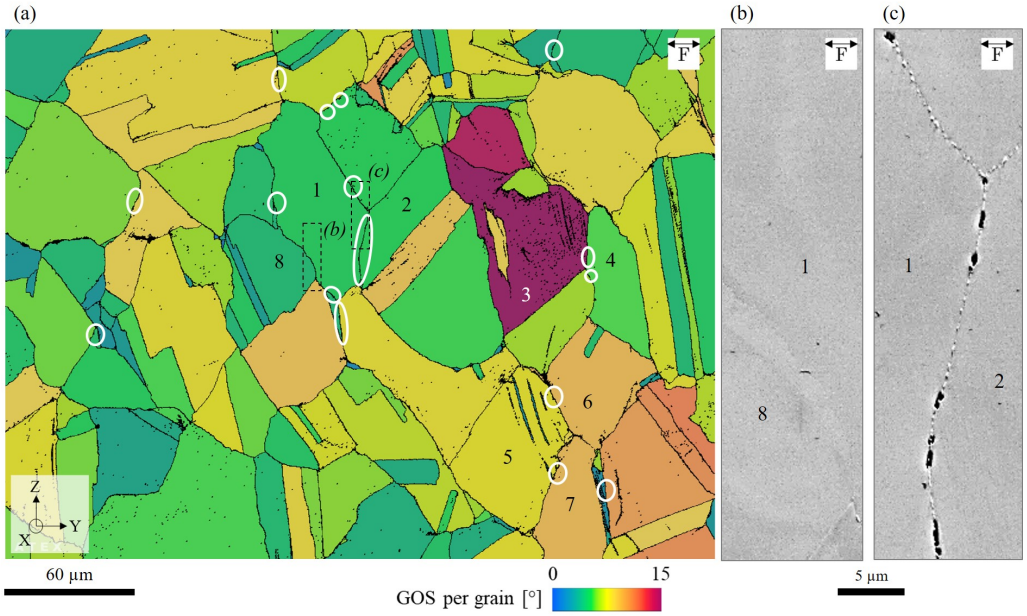

Figure 6.1: Effect of intragranular strain probed using grain orientation spread (GOS) on damage development after the relaxation treatment: (a) Average grain orientation spread map, (b) and (c) SEM-SE close-up images of GBs between grains indicated by 1 and 8 and 1 and 2 in (a), respectively. Data from EBSD maps were acquired in the (XY) plan in the HAZ at mid-thickness of a CT specimen single-pass welded state compressed to CMOD of 1.73 mm and aged at 575 °C for 1470 h.

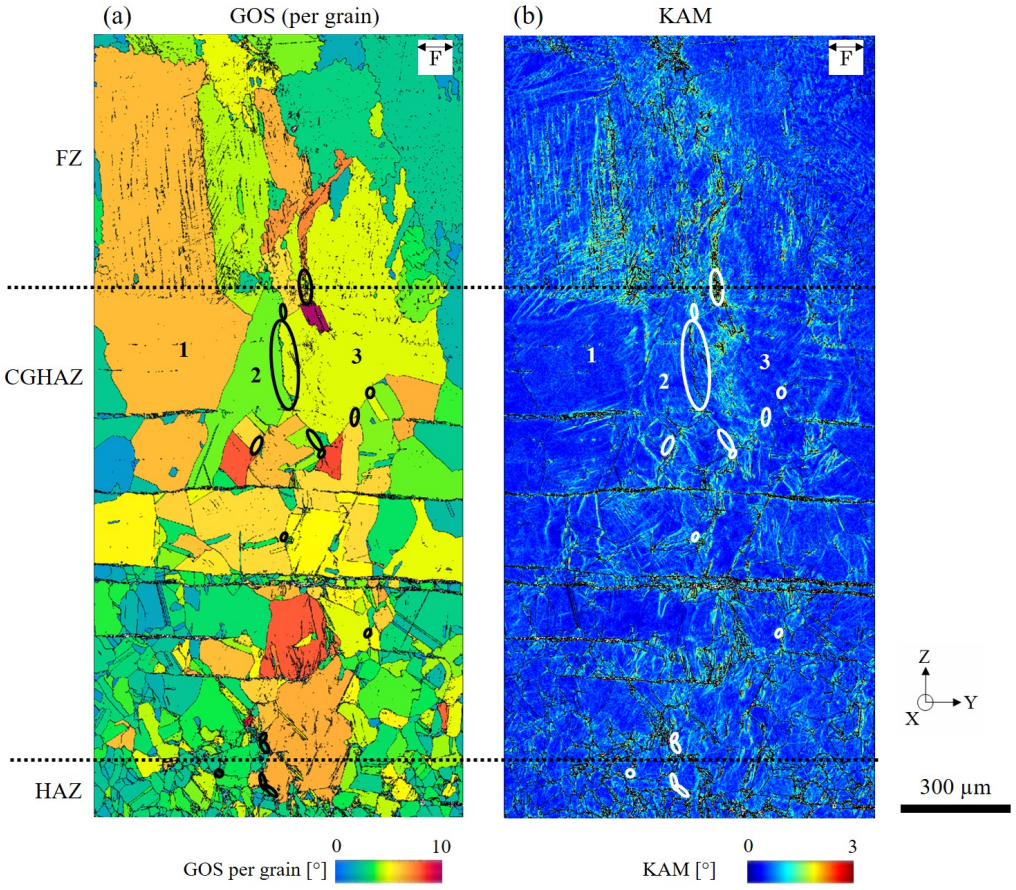

Figure 6.2: Effect of intragranular strain probed by GOS and KAM on the presence of cavities: (a) average GOS (per grain) and (b) KAM with 3 neighbours map. Data from EBSD maps were acquired in the (YZ) plan at the notch root of a specimen compressed to CMOD = 1.73 mm and subsequently aged at 575 °C for 1470 h.

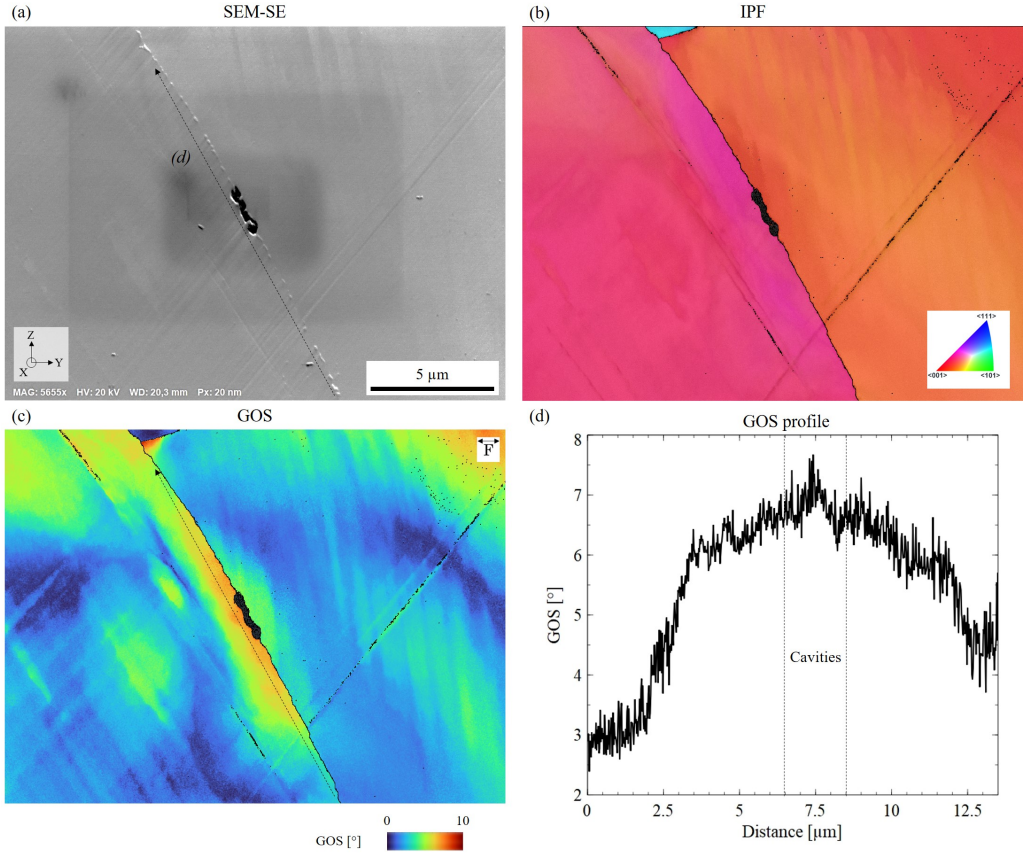

Figure 6.3: Effect of local strain probed by local GOS on the presence of cavities with (a) SEM-SE image, (b) IPF over IQ plotted in X direction, (c) local GOS and (d) GOS profile along GB with cavities. Data and image were taken in the HAZ of a specimen compressed to a CMOD = 1.73 mm and aged at 575 °C for 1470 h. EBSD was acquired with a 30 nm step.

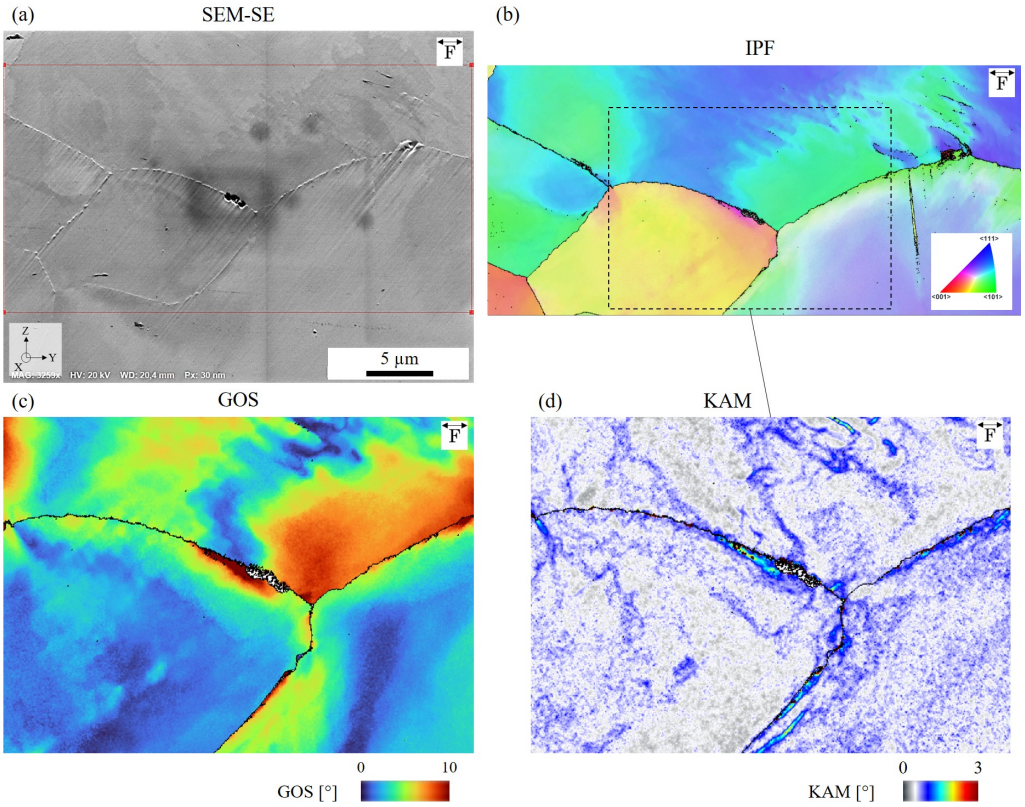

Figure 6.4: Effect of local strain probed by both GOS and KAM on the presence of cavities with (a) SEM-SE image, (b) IPF over IQ plotted in X direction, (c) local GOS and (d) KAM (third neighbour). Data and image were taken in the HAZ of a specimen compressed to a CMOD = 1.73 mm and aged at 575 °C for 1470 h. EBSD was acquired with a 30 nm step.

6.2 Grain boundary misorientation angle

Grain boundary misorientation angle corresponds to the angle due to the misorientation of crystallographic orientation of two adjacent grains. It is known to have an effect on GB energy and other GB related phenomena and was thus considered to understand the preferential nucleation of stress relaxation cavities. A total of 51 damaged GBs were analysed by EBSD. The GB maps of the damaged regions showed that cavities were preferentially located on GBs with misorientation angles comprised between 25 and 55° which corresponds to so-called high-angle GBs (Figure 6.5 (a) and (b)). The high proportion of 60° boundaries in the as-received state mostly corresponds to annealing twin boundaries. Besides, more than 95% of cavities were found to be located on random boundaries ($\Sigma > 35$ b). Particularly, $\Sigma 3$ CSL boundaries (twins) were found to be highly resistant to cavity nucleation. These observations are in agreement with results obtained by Pommier [45] for SRC in a similar steel, but also with observations for creep cavities made in 304 steels [221] and for corrosion cracking [222]. This can be explained by a lower grain boundary energy and lower extrinsic grain boundary dislocation mobility for specific boundaries (CSL) [221].

The GB precipitation of carbides also appeared to follow this trend with a majority of carbide located on boundaries with a misorientation angle comprised between 30 and 55° relatively to global distribution (Figure 6.5 (a)). High-angle random boundaries were then identified as most susceptible to both carbide precipitation and cavity nucleation probably due to their increased energy as compared to low-angle or special GBs.

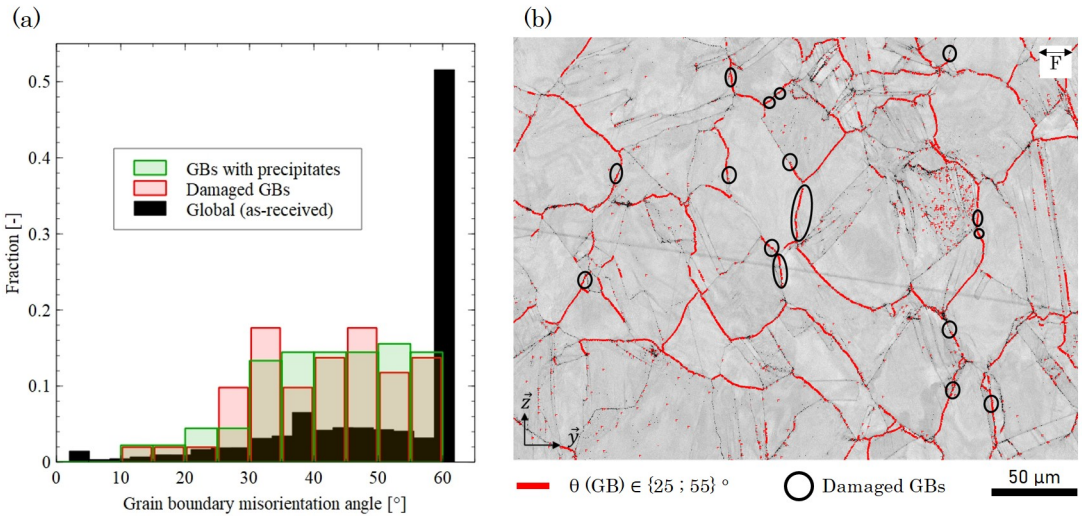

Figure 6.5: Effect of GB misorientation angle on cavity nucleation studied using EBSD data: (a) distribution of GB misorientation angle in the as-received state (black), GB with precipitates (green) and GB with cavities (red) in the HAZ of the CT specimen compressed up to CMOD of 1.73 mm aged at 575 °C for 1470 h. (b) Index quality map and GBs (red) with a misorientation angle comprised between 25° and 55°. Cavities are indicated with black circles.

6.3 Mechanical twins

Mechanical twins, or deformation twins, which are the result of high plastic straining at low temperatures, especially in FCC metals with low stacking fault energy [223], were often observed in several Turski-compressed specimens. Particularly, the number and size

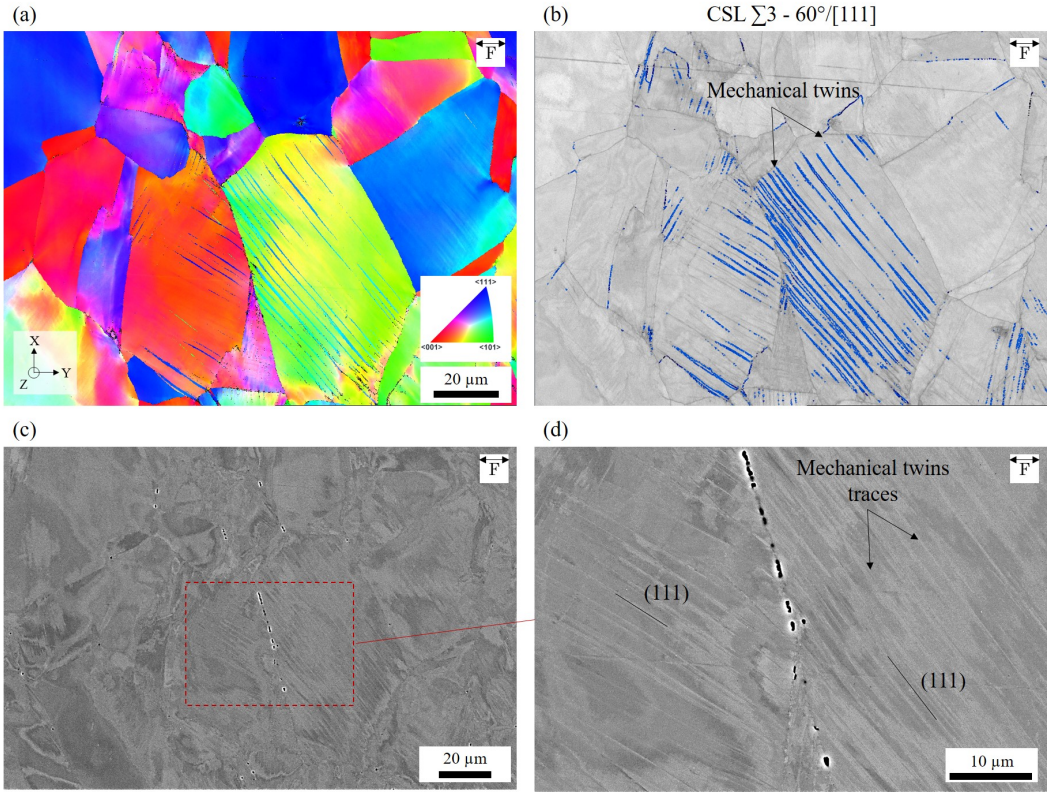

Figure 6.6: Mechanical twins observed in the HAZ close to the notch at mid-thickness of the CT specimen made of single-pass welded material compressed to a CMOD of 1.73 mm and aged at 575 °C for 1470 h, with (a) IPF map plotted in Z direction, (b) CSL Σ3 boundaries map and (c), (d) SEM-SE images of the region showing GB cavities.

of mechanical twins increased with the increase in Turski compression magnitude (increase in CMOD).

In the highest strained regions of the CT specimens (near the notch), cavities were often observed at the GBs between adjacent grains containing mechanical twins, as illustrated in Figure 6.6. Mechanical twins were found to be parallel to the (111) crystallographic planes. The mechanical twins could also be observed in BSE or SE imaging, as shown in Figure 6.6 (d).

The presence of mechanical twins actually tends to favor the nucleation of cavities by creating high local stress concentration points, especially at triple points between mechanical twin boundaries and GBs, as it was suggested by Noel *et al.* [141] for creep cavity nucleation. This is particularly true in the case of non-favourable mechanical twin transfer, as illustrated in Figure 6.7. In this case, mechanical twins were formed on the one side of the GB (in one adjacent grain), resulting in high local strain in the neighbour grain revealed by high KAM values (Figure 6.7 (c)). Such observation is in agreement with results of Zhang *et al.* [224]. It was actually proven experimentally by Abdolvand *et al.* [225] and numerically by Arul Kumar *et al.* [226] that stress fields surrounding mechanical twin tips are very high. This is particularly true for the twins tips near GBs. The regions with high local stresses created by the mechanical twins were also observed to favor intergranular precipitation amplifying the effect of mechanical twins.

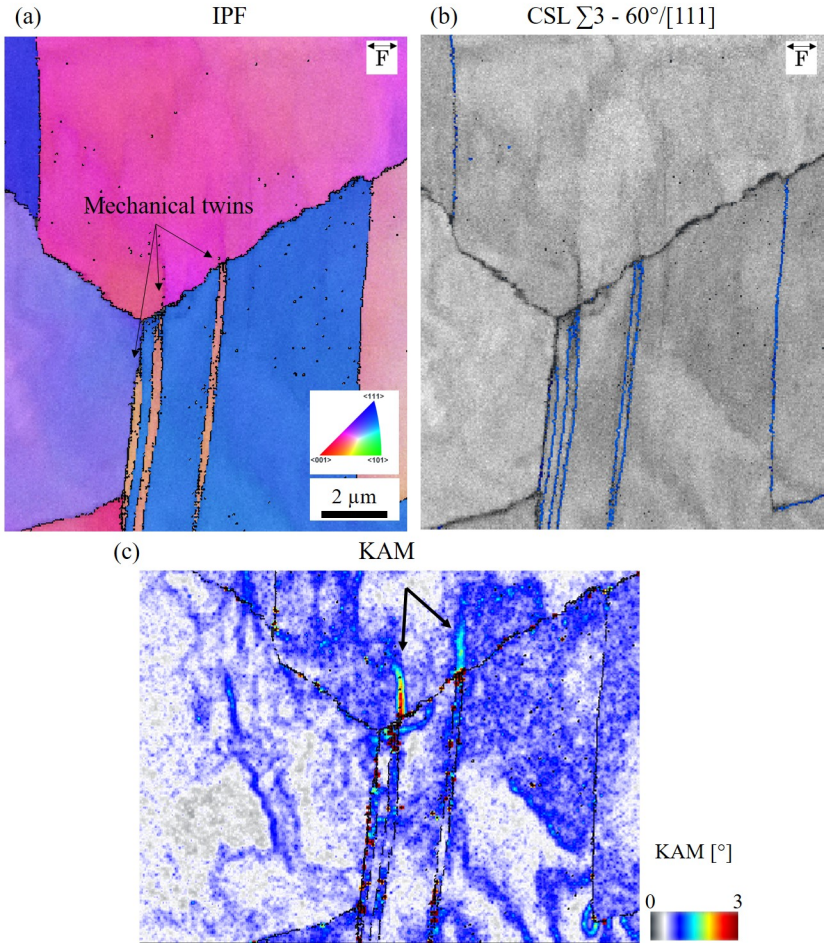

Figure 6.7: Effect of mechanical twins on local strain with (a) IPF map, (b) GB map with boundaries of angle close to 60° and (c) KAM map in the HAZ at mid-thickness of a specimen made of single-pass welded material compressed to a CMOD of 1.73 mm and aged at 575 °C for 1470 h.

6.4 Grain boundary precipitates

Analyses carried out on CT specimens after relaxation treatment (Chapter 5) showed that cavities in both HAZ and CGHAZ nucleate mostly on GB precipitates. For mild levels of damage resulting in only few cavities per damaged GBs, all of the damaged GBs contained precipitates. Similarly to creep damage, cavities formation preceding SRC is preferentially observed at GB precipitates because of the high local stress concentration due to strain mismatch between them and the austenitic matrix.

As showed by Raj [227], the morphology of GB precipitates can impact the nucleation and growth of cavities at high temperature under tensile stress. Hence, here the size of 378 precipitates located on damaged GBs was measured and compared to the size of 362 other precipitates located on non-damaged GBs in the HAZ near the notch of a CT specimen made of single-pass welded material compressed to a CMOD of 1.73 mm. This specimen was specifically chosen as many cavities were observed in the HAZ, thus a sufficient number of damaged GBs could be characterized. Specimens where HAZ contained cracks however, would not be suited for this analysis, as it could not help understanding the effect of precipitates characteristics on the onset of damage (cavity nucleation). The size of precipitates at damaged GBs was found to be slightly higher than that at non-damaged GBs with an average of 331 and 290 nm, respectively (Figure 6.8 (a)). In addition, the

number of precipitates relative to the grain boundary length (i.e. linear density of GB precipitates) was found to be slightly higher at damaged boundaries (Figure 6.8 (b)), with an average of 1.5 precipitates per damaged GB against 1.4 precipitates per non-damaged GB. This is in agreement with simulations conducted by Cui [208], who showed that stress concentration at GB precipitates was higher for a higher density of precipitates on the same grain boundary. A higher number of precipitates also induces a higher number of potential sites for cavity nucleation, and reduces the ductility in areas close to the GBs.

The size of GB precipitates and their linear density were shown to have little influence on the presence of cavities, but the impact would be too low to explain the high differences in damage observed between the CGHAZ and HAZ. Besides, as discussed in Chapter 5 precipitates size and linear density were not particularly higher in the CGHAZ than in the HAZ.

Similarly to previous factors, it was very difficult to isolate the effect of precipitates from other factors. This is illustrated in Figure 6.8 (c), where cavities were located on GBs with smaller precipitates and lower precipitate density than the neighbouring GBs. Actually, it was found that the GB with cavities showed much higher level of local GOS (Figure 6.8 (d)) and KAM (Figure 6.8 (e)) as compared to the others.

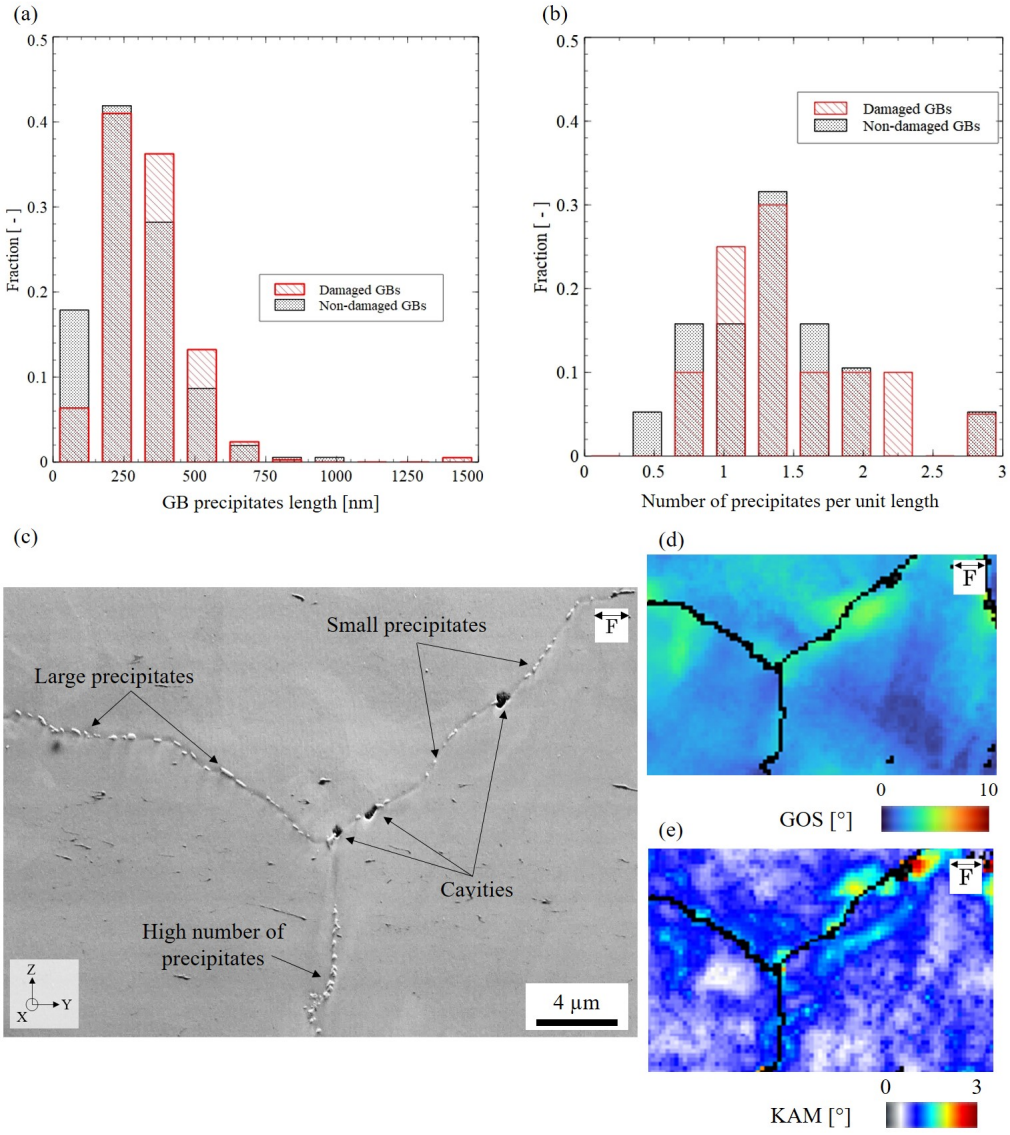

Figure 6.8: Effect of GB precipitates on cavity nucleation with (a) distribution of precipitate length located at damaged (red) and non-damaged (black) GBs, (b) precipitates per GB unit length at damaged (red) and non-damaged (black) GBs, (c) SEM-SE image of three GBs with corresponding (d) local GOS and (e) KAM maps. Data and image were taken in the HAZ of the specimen compressed to CMOD = 1.73 mm and aged at 575 °C for 1470 h.

6.5 Triple points

Grain boundary triple points (TP), either formed by three GBs or between a GB and a twin boundary, are often mentioned in the literature as sites of high local stress during straining, which then represent preferential sites for the nucleation of cavities [144]. In the present work, only 10% of observed cavities were located at triple points. Besides, a very small fraction of all the triple points was damaged. An example of a damaged TP is shown in Figure 6.10 (b). Cavities located at TPs were either shaped as wedge cracks as illustrated in Figure 6.9 (a) or similarly to grain boundary cavities (Figure 6.9 (b)). The size of cavities at triple points was similar to that at GBs (Figure 6.9 (b)), suggesting that the influence of triple point on SRC is relatively low. Even for high levels of damage

with cracks, triple points were not preferential initiation sites. Instead, triple points rather acted as obstacles to the propagation of damage along grain boundaries.

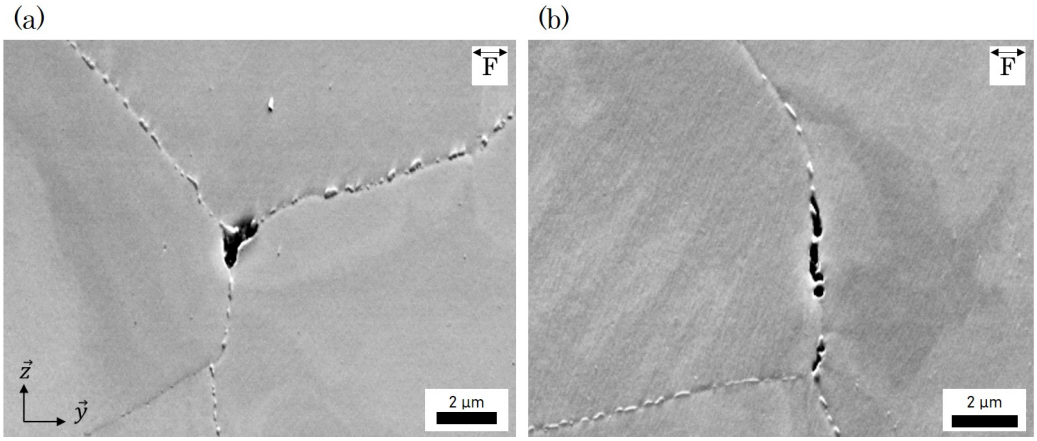

Figure 6.9: Effect of triple points on damage. (a) Wedge cavity at a grain boundary triple point and (b) cavities at a triple point and on a grain boundary. SEM-SE images in the HAZ of a CT specimen made of single-pass welded material compressed to CMOD = 1.73 mm and aged at 575 °C for 1470 h.

6.6 Grain boundary angle with the loading axis

For over 165 damaged GBs in CT made of single-pass welded material, most of observed cavities (75%) were located at GBs forming an angle with the macroscopic loading axis (Y) comprised between 60 and 90°, as shown in Figure 6.10 (a). This is in agreement with observations on SRC of Pommier [45], but also on creep and fatigue at high temperature [141, 228]. This tendency is the direct result of higher tensile stress magnitude on GBs perpendicular to principal loading direction. The proportion of cavities located on GBs forming an angle close to 45° however, was quite low (around 6%).

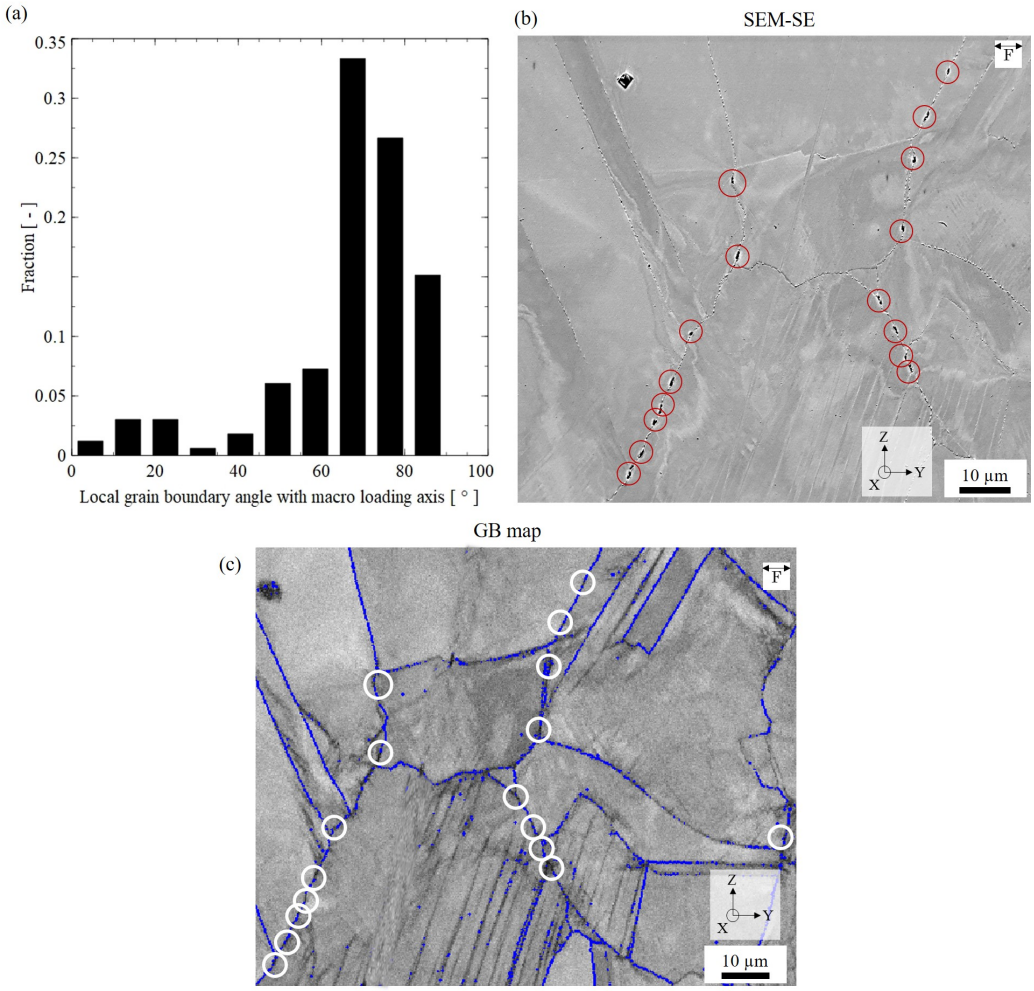

Figure 6.10: Effect of GB angle formed with loading axis (Y) with (a) distribution of GB angle with macroscopic loading axis for 165 damaged grain boundaries, (b) SEM-SE image of cavities (red circles) in a HAZ, (c) grain boundaries map with GBs in blue and cavities in white circles. Data and image were taken in the HAZ of the specimen compressed to CMOD = 1.73 mm and aged at 575 °C for 1470 h.

6.7 Summary of influencing factors

At a macroscopic scale, it was shown in Chapter 5 that SRC is first induced by the presence of tensile residual stresses and plastic strain. Besides, investigations carried out at microscopic scale showed that the presence of stress relaxation cavities is allowed by the presence of GB precipitates, in agreement with literature [45]. This chapter allowed to discuss additional factors influencing the nucleation of cavities proposed by the literature:

- A higher number, size, and density of precipitates were identified as favoring the presence of cavities but with a relatively low impact.
- The presence of cavities was also influenced by the average direction of a GB relatively to the macroscopic loading axis with a majority of damaged GB oriented between 60 and 90°.
- The misorientation angle of the GB also influenced damage with a majority of damaged GB with angles between 25 and 55°, also related to the presence of precipitates.

- Cavities were often located at GBs where at least one of the two adjacent grains presents low level of global strain, but high local variation in crystal orientation near the GBs. High distortions near GBs suggest high dislocation density favoring the rise of stresses, which is in agreement with TEM observations.
- The presence of mechanical twins was also related to higher GB damage, by creating high stress fields at the tips near GBs.

6.8 SRC in CGHAZ

Results obtained before for the HAZs were then used to understand the presence of cavities in the CGHAZs. As an example, a single pass welded state after compression to a CMOD of 1.22 mm and ageing at 575 °C for 1470 h is considered. In order to access to damage initiation mechanism in CGHAZ, the microstructure-damage relationship was characterized in the FZ/CGHGAZ/HAZ close to the notch.

IPF covering the region where all three welding zones were present is shown in Figure 6.11 (a), with the FZ a the top, CGHAZ in the middle and HAZ at the bottom. The most strained region, according to GOS per grain, is indicated in Figure 6.11 (b) by a white dashed rectangle. In this rectangle, the CGHAZ is investigated: particularly, the top of the CGHAZ close to the FZ/CGHAZ interface was analysed, as it is the region where most of damage was observed in CT made of welded materials (in Section 5.3). In addition, this region corresponds to grains with the lowest average GOS (per grain) in a highly strained region (near the notch). For this region, KAM and local GOS were plotted in Figure 6.11 (c) and (d), respectively, allowing identifying grains with highest local strains, characterized by highest values of both KAM and local GOS, again indicated by black rectangles in both figures. These maps are compared with GOS per grain of the same region and GB misorientation angle in Figures 6.11 (e) and (f), respectively: GBs most prone to SRC are GBs between grains with low GOS or with significant GOS difference and misorientation angle comprised between 25 and 55°. In the black rectangles regions, maps of angle formed between GBs and the loading axis were plotted in Figure 6.11 (g) and (h) and compared with optical images of the regions. Therefore, the most damaged GBs in CGHAZ responded to the microstructure criteria (low overall strain but strain localisation at GBs, high-angle random GBs, angle between the GB plane and loading direction between 25 and 55°) previously identified for the HAZ.

The correlation of microstructural factors proposed by the literature (either for creep or SRC) and the presence of cavities allowed to better understand the localisation of stress relaxation cavities within both the HAZ and the CGHAZ. However, these factors were not observed to be more pronounced in the CGHAZ than in the HAZ, thus they did not appear to better explain the higher susceptibility of the CGHAZ to SRC. Instead, several explanations for the localisation of damage in CGHAZs can be proposed, induced by the higher grain size of the region:

- **Lower total GB length per unit area** than in the FZ and HAZ (Figure 3.21). This directly affects the plastic strain accommodation, and results in less free surface for cavity nucleation, as it was suggested by hypotheses reported by the literature [27, 28, 37, 161]. Unlike in the FZ, cavities in the CGHAZ can only nucleate on austenite GB, asides from a few residual ferrite sites. This gives the CGHAZ even less possibility to have a homogeneous distribution of damage. While authors [3, 4, 33, 46, 139, 158, 159] also generally suggested that an increase in grain size leads to a decrease of grain boundary surface available for precipitation, an increase in precipitates number per boundary was not observed in the CGHAZ for the studied 316L(N) steel.

- **Lower fraction of GBs favorable for damage**: the fraction of austenite GBs with misorientation angle between 25 and 55°, which were observed here to be the most favorable for cavity nucleation, was lower in CGHAZ than in the FZ (Figure 3.21). This again leads to the reduction in the number of potential sites for cavity nucleation, resulting inevitably in a concentration of damage on the few sites available. At a mild state of damage, cavities nucleate only on a few GBs hence leading to higher number of cavities per damaged boundary than in the other regions (Figure 5.21 (a)). At this state, damage localization is not yet an issue. However, an increase in plastic strain, residual stress and/or relaxation time results in a rapid multiplication of cavities on the few damaged GBs already presenting a high cavity density, as observed in the material with increased grain size. Because of that, the coalescence of cavities and further development of cracks is much quicker in the

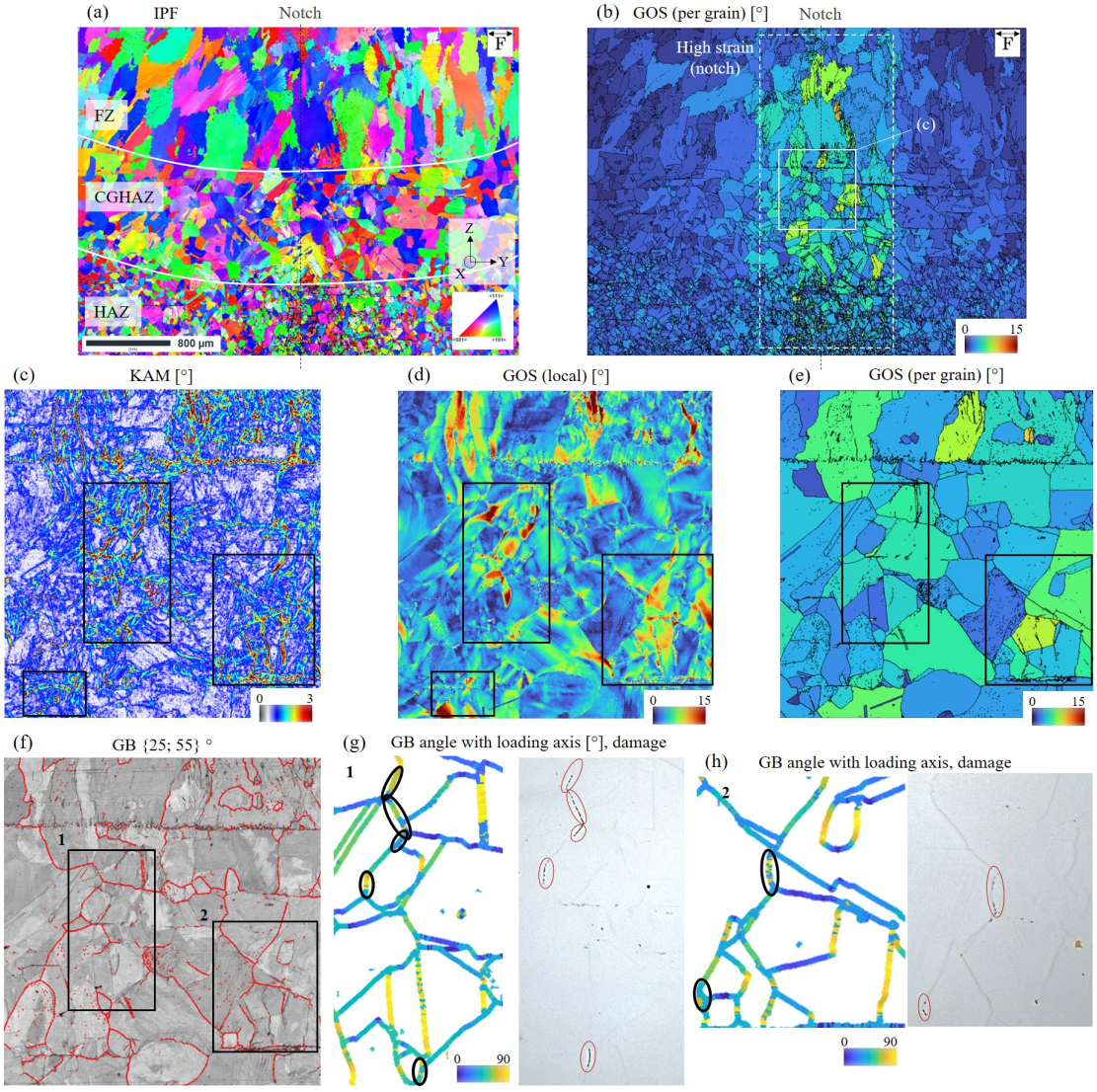

Figure 6.11: Example of identification of most damaged regions in a single pass welded specimen compressed to a CMOD of 1.22 mm and aged at 575 °C for 1470 h in the FZ/CGHGAZ/HAZ region with (a) IPF, (b) GOS per grain, (c) KAM, (d) local GOS, (e) GOS per grain, (f) GB misorientation angle comprised between 25 and 55°. GB maps with angle relative to the loading axis and corresponding GB damage observed by optical microscope are shown in (g) and (g), for the two zones indicated in (c-f).

CGHAZ (Figure 5.21 (b)).

- **Lower number of obstacles for propagation**: the lower GB density in the CGHAZ and longer GBs also favors the propagation of damage, since triple points can act as obstacles [13]. This would then result in much longer intergranular cracks, as observed in the most damaged specimens (Figure 5.21 (c)).

Besides, it was shown in Section 5.3 that the transition region between the FZ and CGHAZ was particularly prone to cavity nucleation, explaining why the damage is also localized within the CGHAZ itself. Finally, the higher number of cavities per GB length in the CGHAZ as compared to the FZ and HAZ, was also attributed to specific distribution of plastic strain:

- **Heterogeneous distribution of plastic strain**: it was shown through the GOS maps that the CGHAZ presented the most heterogeneous distribution of plastic strain contributing to stress localization favoring damage localization.
- **Higher dislocation density near GBs**: TEM analyses also showed accumulation of dislocations tangles together with precipitates at GB areas in the CGHAZs, known to facilitate cavity nucleation and further cracking [13], as illustrated in Figure 5.34. Due to the high plastic strain during Turski compression, EBSD analyses suggested that grains tended to be oriented preferentially along specific direction in which dislocations glide and thus pile near GBs is favored.

For the first time, an extensive investigation accounting for both mechanical and microstructural aspects was carried out to get a better understanding of the susceptibility of weld zones in the 316L(N) steel. Several detrimental mechanisms and associated factors proposed by the literature were then confronted to results obtained in this work, concluding that grain size was the major factor responsible for the susceptibility of the CGHAZ to SRC. This study thus strongly emphasised the need to avoid grain coarsening during welding as much as possible by tuning process parameters, but also to avoid exposing region of microstructures transition to loads during service.

Overview of results and conclusions

The main objectives of this work were (*i*) to develop an approach to observe and characterize stress relaxation cracking in the welded 316L(N) steel (*ii*), to characterize the influence of welding on SRC by identifying weakest region and comparing the results to homogeneous material states and finally (*iii*) to assess the mechanical and microstructural factors influencing the SRC phenomenon.

To meet these objectives, multiple material states were tested to better comprehend the influence of welding and of thermo-mechanical pre-treatments on SRC. To this end, as-received, cold-rolled, material with increased grain size, single and multi-pass welded, cold-rolled single-pass welded materials were investigated. CT specimens were then machined from these states and further subjected by a Turski compression, consisting in a compression and subsequent unload, in order to introduce controlled levels of residual stresses and plastic strain. To estimate residual stresses and further choose relevant loading conditions regarding SRC threshold suggested by the literature, 3D FEM simulations of the compression test were carried out using an elastic-plastic model and meshes accounting the microstructures of the different specimens. It has been numerically shown that the welding residual stresses originally present in the CT specimens were largely redistributed during the Turski compression, which then allowed to subject all three weld zones to comparable levels of residual stresses and pre-strains. Residual stresses in the specimens were then relaxed through thermal treatments at 575 and 600 °C for 580 and 1470 h. The resulting damage was analyzed by electron microscopy (SEM, TEM) and quantified by image analysis tools.

Microstructures of each state prior to and after thermal ageing were investigated to study microstructure evolution without the influence of residual stresses and strain induced by the compression used for SRC tests. Characterization of the microstructure evolution of the thermally aged as-received and cold-rolled states revealed the precipitation of the $Cr_{23}C_6$ carbide at austenite GBs, accompanied by smaller Mo-rich intermetallics phases which might correspond to χ and τ phases. Precipitation was observed to be faster in the cold-rolled material. Investigations carried out in the single-pass, multi-pass and cold-rolled single-pass welded states revealed a complex microstructure with three main regions: the fusion zone (FZ), the coarse grain heat affected zone (CGHAZ) and the heat affected zone (HAZ). In the CGHAZ and HAZ after thermal ageing, precipitates of the $Cr_{23}C_6$ and intermetallics phases were also observed at austenite grain boundaries. In the FZ, vermicular ferrite formed during welding was further decomposed after thermal ageing into a complex distribution of $Cr_{23}C_6$, χ, σ phases and regenerated austenite.

The relaxation cracking tests carried out with CT specimens made of as-received, cold-rolled and material with increased grain size states revealed damage similar to that observed after creep, with the nucleation of intergranular cavities preferentially at $Cr_{23}C_6$ carbides identified by TEM. Smaller Mo-rich phase precipitates were also observed on these carbides, which probably favored cavity nucleation. An increase in residual stresses,

plastic strain and relaxation time induced an increase in the level of damage. Besides, it was found that relaxation at 600 °C induced higher damage than at 575 °C. Besides, an increase in grain size was found to lower the fraction of damaged GBs but to increase the damage level per damaged GB. The correlation of the cavity distribution with computed residual stresses and plastic strain obtained from 3D FE showed that damage was driven by both plastic strain and maximal principal stresses. Specifically, cavities were observed in highly strained regions and low stresses but less often in highly stressed regions with low plastic strain.

The SRC study conducted in the welded samples without pre-compression revealed that the levels of stresses and strains induced by the welding were insufficient to allow SRC in the welded 316L(N) steel. This confirmed the high resistance of the 316L(N) steel to SRC. Relaxation tests with prior compression resulted in damage in the welded materials, with a very heterogeneous distribution directly induced by the heterogeneous microstructure. Particularly, the CGHAZ was found to be the most prone to SRC, as cracks were found in this region. In the FZ, the majority of the damage was found near the FZ/CGHAZ interface with the highest number of cavities per unit area among the three regions. These cavities were mainly located on the vermicular ferrite precipitated during the cooling of the weld. In the HAZ, the damage was distributed homogeneously, similar to the non-welded specimens. The most heterogeneous distribution of damage was observed in the CGHAZ, with only a small fraction of the GBs containing cavities/cracks. As a result, the lowest number of cavities was observed in the CGHAZ as compared to the FZ and HAZ. However, the high concentration of cavities in the CGHAZ presented a higher risk for cracking than the FZ and HAZ: lower stresses, strain and shorter relaxation time were required for the first crack to form in the CGHAZ as compared to that in other weld zones. Typically, cracks nucleated in the CGHAZ for 23% and 28% lower stresses and plastic strain than in the HAZ, respectively. These results thus showed that the CGHAZ is the most prone to SRC, and that this susceptibility is mostly due to the microstructure.

In order to understand the particular susceptibility of CGHAZ to SRC, analyses of microstructure parameters which might lead to SRC were conducted. The results showed that aside from stresses and strain, the nucleation of the cavities was mostly influenced by the GB precipitates (number, size and density), the orientation of the GB plane with respect to the loading axis, the GB misorientation angle and by low intragranular plastic strain levels (estimated by EBSD) in the highly strained regions. To a lesser extent, the presence of mechanical twins increased the number of cavities. Surprisingly, none of these parameters was observed to be more present in CGHAZ than in other welding zones. The low resistance of CGHAZ to SRC was hence attributed to several factors related to the higher grain size of the zone. First, the lower number of GBs in the region induced a considerable decrease of the number of potential sites favorable to cavity nucleation, thus favoring damage concentration during nucleation. In addition, the heterogeneous distribution of plastic strain in the CGHAZ and the apparent accumulation of dislocations (from TEM and at least geometrically necessarily dislocations, according to KAM from EBSD) near the GBs of this zone, favoring stress concentration at GB precipitates, appeared to be detrimental to the CGHAZ resistance to SRC. Particularly, it seemed that the nucleation of damage was less favored in the CGHAZ than in the other zones, however, the growth and propagation of damage was highly favored in this zone. Finally, the transition region between the FZ and CGHAZ also appeared to be detrimental to the resistance of weld microstructures to SRC.

The estimation of cavity nucleation and stress relaxation cracking thresholds for each zone of the weld microstructure achieved in this work can be further used in laboratory or industrial conditions for precise determination of SRC hazard in a weld joint. By a thermo-mechanical simulation of the welding process, the location of the different weld

zones can be deducted from thermal fields. Then, residual stresses and plastic strain can be estimated for each region. Finally, using the thresholds determined in this work, the precise location of SRC hazard can be estimated. Such approach could significantly help designing weld joints and ensure the safety of structures, especially for nuclear applications.

The study of SRC in 316L(N) specimens first showed that the 316L(N) steel has a high resistance to SRC as compared to other steels. Furthermore, the results showed that even in equivalent mechanical conditions, the high susceptibility of CGHAZ to SRC was still observed. Evaluation of the microstructural factors influencing the occurrence of damage revealed that the overall grain size of the whole zone was responsible for the localization of the damage, and therefore the increased risk of cracking. The reduction in the risk of welded parts is therefore closely linked to the reduction in the size of the CGHAZ, but also to the grain size.

Perspectives

The investigation of the effect of welding on stress relaxation cracking in 316L(N) steel has answered numerous questions, but there are several areas of the study that could be further developed to improve the understanding and prediction of the phenomenon.

First, the estimation of residual stresses. Experimental measures of residual stresses in single-pass welded material and in compressed CT specimens were tried by X-ray diffraction method but did not lead to relevant results due to high stress gradients. In order to improve confidence in the mechanical model and eventually improve simulations accuracy, additional measurements of residual stresses should be considered, for instance using synchrotron diffraction. In addition, estimations of residual stresses and strain were performed using a macroscopic model whereas part of the SRC phenomenon occurs at a microscopic scale. The use of a mechanical model accounting for microscopic effects could then provide additional information.

Secondly, SRC testing of specimens made of welded materials carried out in this work could be completed using specimens made of material welded with filler metal, which was not considered here. A study could then be dedicated to investigate and compare the effect of different filler metals and different weld configurations (butt joint, corner joint) on SRC. Besides, SRC testing of material with increased grain size provided explanations for the susceptibility of the CGHAZ to SRC, particularly the effect of grain size. However, additional SRC tests of material with increased grain size with intermediate levels of pre-compression to those studied in this work could be considered to better understand the chronological stages of SRC in a coarse grain region. Similarly, SRC tests of material with increased grain size could be performed with intermediate time of relaxation and other grain sizes.

One of the main drawbacks of the present study is that the analyses were carried out post-mortem. For this reason, it was very difficult to evaluate the contribution of each factor separately and to correctly describe the chronological stages of damage nucleation. To address these issues, new approaches could be developed for in-situ SEM or TEM damage testing using micro-tensile machines. In this idea, two methods can be considered:

- The first approach would be to use mini-tensile specimens machined from a welded plate, containing one of the three welded zones, or all three in the same specimen. These specimens would then be mounted in a heated specimen holder in an SEM (or TEM), and then subjected to a relaxation test in temperature by applying a constant strain. This first approach would allow observing the first stages of cavity nucleation, but the time needed to observe first cavities is uncertain. Also, the method can be very difficult as it is complex to know which regions of the specimens to analyse, i.e. to priory know where the damage will appear first. Finally, it could be very difficult reaching SRC stress thresholds using this method.

- The second approach would be to produce CT specimens machined from the welded material, to compress and relax them to nucleate damage as it was done in this work. Mini-tensile specimens could then be machined from the notch of these specimens

and mounted on a heated micro-tensile machine in SEM or TEM. In this case, it would be easy to identify already damaged grain boundaries, and to observe the nucleation of new cavities or the propagation mechanisms of the damage in these regions. This approach is simpler than the first one and ensure the observations of damage, but would not allow observing the first stages of cavity nucleation.

In this study, the computed stresses and strain resulting from the compression were correlated to the observed damage, which allowed estimating damage thresholds for each microstructure. In addition, several microstructural factors influencing damage nucleation were identified. It would then be very interesting to design simulations for damage prediction that could take into account all of these parameters. In the literature, two main approaches for simulating damage are generally found. The first method uses a macroscopic approach, and the second a local one (microscopic):

- Pommier [45] used a macroscopic and phenomenological approach to simulate stress relaxation damage, originated from Yoshida *et al.* [229] work, used to describe creep damage. In this approach, the intergranular damage evolution is a function of the principal stress and the equivalent viscoplastic strain rate ε_p. This model has the advantage of being relatively simple, with few parameters. Damage prediction can thus be calculated quickly, knowing conditions such as initial pre-strain, residual stress, relaxation time and temperature. As a result, the model uses material and temperature-dependent parameters, and only allows predicting damage based on prior experimental observations. An additional issue with this approach is that it considers that damage is mainly driven by stress relaxation magnitudes, while results in this work showed that plastic strain also has a major role. Besides, the model being relatively simple, it does not take into account many factors influencing damage nucleation and development. Because of that, it would be difficult to account for the effect of precipitates characteristics (nature, size, shape, density, precipitation kinetics), grain size and microstructural heterogeneity on damage.

- A more local approach can be adopted when simulating GB damage, by considering the nucleation of cavities at grain boundaries over time, as it was done for creep damage modelling in various materials [208, 211, 230–232]. This approach can account for the grain size, grain orientation, GB misorientation, GB angle with loading axis, the presence of precipitates and their characteristics. This local microscopic approach allows reproducing more precisely the damage mechanisms, which can thus help understanding the experimental observations in welded components but also better predict the regions most susceptible to cavity nucleation within a heterogeneous microstructure. The biggest drawback of such an approach is the complexity of the model, which needs a significantly higher number of parameters and longer computation time than the phenomenological approach. Besides, because of the higher number of parameters, the number of experimental data needed for adjusting model parameters is also higher.

Ideally, simulations of stress relaxation cracking in a complex microstructure such as resulting from welding would use both approaches. Premises of calculations in this sense were started in the framework of this study but could not be completed. Such simulations should be multi-scale, with consideration of macroscopic displacements of the specimen, down to the stress concentration at GB precipitates. Typically, the simulations were constructed in three main steps:

- Prediction of stresses and strain fields in the CT specimen, with a mesh and model parameters accounting for the heterogeneous microstructure.

- Projection of the mechanical boundary conditions on a mesh processed from an EBSD map of a weld microstructure. Open source tools such as MTEX software [233] can typically be used to construct an FEM mesh from EBSD acquisitions. Then, a polycrystalline mechanical model such as found in the works of Huang [187] for predicting creep in a 316L(N) steel can be used to estimate local stresses and plastic strain in function of crystallographic orientation.
- Lastly, GB precipitates could be added in the mesh to better represent the SRC mechanism. However, this would add considerable complexity to the simulations for large regions (hundreds of grains). Instead, it would be wiser to project mechanical boundaries computed from the larger EBSD map on smaller regions (two or three grains), with a finer mesh and computing stresses/strain accounting for the presence of GB precipitates.

The main drawback of this approach is the simplification in 2D of a 3D problem. 2D assumptions, plane strain or plane stress, would thus have to be made and may probably not be relevant for SRC phenomenon. This shows that the choice and development of a approach/model for simulating SRC at all scales would be very difficult, hence strongly simplifying assumptions would need to be made.

Bibliography

[1] F. Dalle, M. Blat-Yrieix, S. Dubiez-Le Goff, C. Cabet, and Ph. Dubuisson. Conventional austenitic steels as out-of-core materials for generation IV nuclear reactors. In *Structural Materials for Generation IV Nuclear Reactors*, pages 595–633. Elsevier, 2017.

[2] Jinggang Qin, Yu Wu, Klaus-Peter Weiss, Zhixiong Wu, and Laifeng Li. Mechanical test on the iter tf jacket. *Cryogenics*, 52(7):336 – 339, 2012.

[3] Rishi Kant and john dupont. Stress relief cracking susceptibility in high temperature alloys. *Welding Journal*, 98:29s–49s, 02 2019.

[4] L. K. Poole. The incidence of cracking in welding type 347 steels. *Journal of Welding*, 32:403s–4l2s, 08 1953.

[5] J.C. Lippold. Solid-state cracking. In *Welding Metallurgy and Weldability*, pages 130–212. John Wiley & Sons, Inc, November 2014.

[6] A. Dhooge and A. Vinckier. Reheat cracking—a review of recent studies. *International Journal of Pressure Vessels and Piping*, 27(4):239–269, 1987.

[7] JOHN LANCASTER. The reliability of welded structures and process plant. In *Handbook of Structural Welding*, pages 375–430. Elsevier, 1992.

[8] J.C. Lippold and D.J. Kotecki. *Welding Metallurgy and Weldability of Stainless Steels*. Wiley, 2005.

[9] Robert Weber, Bruce Somers, and Eric Kaufmann. Low-carbon, age-hardenable steels for use in construction: A review. *USACERL Technical Report 96/104*, page 53, 09 1996.

[10] Henrik Stahl, Gaylord Smith, and Sophie Wastiaux. Strain-age cracking of alloy 601 tubes at 600 °c. *Practical Failure Analysis*, 1(1):51–54, 02 2001.

[11] Y. Cètre. *La corrosion dans l'industrie chimique: Enjeux-Impact*. EDP sciences, 2021.

[12] J.C. van Wortel. Relaxation cracking in the process industry, an underestimated problem, Dec 1998.

[13] Q. Auzoux. Effect of pre-strain on creep of three aisi 316 austenitic stainless steels in relation to reheat cracking of weld-affected zones. *Journal of Nuclear Materials*, 400(2):127 – 137, 2010.

[14] Z. Feng, Y. Gao, Y. Yang, and W. Zhang. Microstructure and mechanism based lifetime predictions in src of ss347 weldment under complex thermomechanical conditions. *Proceedings, evaluation of welding issues in high nickel and stainless steel alloys for advanced energy systems*, 2021.

[15] H. Cerjak, Peter Mayr, Fujio Abe, TU Kern, and R Viswanathan. Creep strength of welded joints of ferritic steels. *Creep-Resistant Steels*, pages 472–503, 03 2008.

[16] G.A. Young, Thomas Capobianco, M.A. Penik, B.W. Morris, and J.J. McGee. The mechanism of ductility dip cracking in nickel-chromium alloys. *Welding Journal (Miami, Fla)*, 87:31–s, 02 2008.

[17] R. M. Curran and A. W. Rankin. Austenitic Steels in High-Temperature Steam Piping. *Transactions of the American Society of Mechanical Engineers*, 79(6):1398–1409, 08 1957.

[18] Magali Chabaud Reytier. *Étude de la fissuration différée par relaxation d'un acier inoxydable austénitique stabilisé au titane*. PhD thesis, ENSMP, 1999. Thèse de doctorat dirigée par Pineau, André Sciences et techniques ENSMP 1999.

[19] Zhenzhen Yu, Timothy Pickle, Yu Hong, Judith Vidal, and Chad Augustine. Cracking risk mitigation in molten salt 347h ss hot tank welds. *American solar energy society solar 20-20*, 2020.

[20] B. Michel, M. T. Cabrillat, P. Allegre, and E. Pluyette. Intergranular reheat cracking in 304 h components . experiments and damage evaluation. In *Transactions, SMiRT 16, Washington DC*, 2001.

[21] R. Loots. Susceptibility of service exposed creep resistant materials to reheat cracking during repair welding. *University of Pretoria*, 2003.

[22] H. Van Wortel. Control of relaxation cracking in austenitic high temperature components. *VeMet conference*, 2009.

[23] *Fabricating Nickel Alloys To Avoid Stress Relaxation Cracking*, volume All Days of *NACE CORROSION*, 03 2007. NACE-07421.

[24] Alfred Dhooge. Survey on reheat cracking in austenitic stainless steels and ni base alloys. *Welding in The World*, 41:206–219, 1998.

[25] E Barbareschi, P Guarnone, A Giostra, and M Zappaterra. High temperature failure of expansion joints due to stress relaxation cracking. *Conference: Materials Science and Technology 2009*, 2009.

[26] French corrosion Society CEFRACOR. Corrosion in oil and gas industries high temperature working group. *Workshop on relaxation cracking of stainless steels, EUROCORR*, 2010.

[27] Muhammad Hussain, Abrar Hussain, and Intizar Hussain. Evaluation of stress relaxation cracking on 800ht pigtails of the steam reformer. *Journal of Failure Analysis and Prevention*, 18, 04 2018.

[28] American Petroleum Institute (API). Damage mechanisms affecting fixed equipment in the refining industry. *ANSI/API RECOMMENDED PRACTICE 571 THIRD EDITION*, 2019.

[29] J. Siefert, J. Shingledecker, and L. Tapasvi. Stress relaxation cracking (srxc) and strain induced precipitation hardening (siph) failures. *DOE sCO2 Cross-Cutting Team Workshop: Evaluation of Welding Issues in High Nickel and Stainless Steel Alloys for Advanced Energy Systems*, 2020.

[30] S. J. Norton. Development of a gleeble based test for post weld heat treatment cracking in nickel alloys. *Ohio State University*, 2002.

[31] Shreeneet Rathi and Nanasaheb Gurule. *Study and development of a computer assistance in selection of fatigue design recommendations for welded joints.* PhD thesis, Indian Institute of Technology Bombay, 04 2014.

[32] E. J. Galda A. W. Pense and G. T. Powell. Stress relief cracking in pressure vessel steels. *Weld J. (Miami)*, 50 (8):374–378–s, 1971.

[33] A. Dhooge, R.E. Dolby, J. Sebille, R. Steinmetz, and A.G. Vinckier. A review of work related to reheat cracking in nuclear reactor pressure vessel steels. *International Journal of Pressure Vessels and Piping*, 6(5):329–409, 1978.

[34] L. G. Liljestrand, M. Aucouturier, G. Östberg, and P. Lindhagen. Formation of microcracks during stress-relief annealing of a weldment in pressure vessel steel of type A508 C1 2. *Journal of Nuclear Materials*, 75(1):52–67, July 1978.

[35] D A Canonico. Significance of reheat cracks to the integrity of pressure vessels for light-water reactors. *U.S. Nuclear Regulatory Commission Office of Nuclear Regulatory Research, Technical Report*, 3 1977.

[36] C D Lundin and S Mohammed. Effect of welding conditions on transformation and properties of heat-affected zones in lwr (light-water reactor) vessel steels. *The University of Tennessee*, 11 1990.

[37] Norman Bailey. 6 - reheat cracking. In Norman Bailey, editor, *Weldability of Ferritic Steels*, Woodhead Publishing Series in Welding and Other Joining Technologies, pages 170–179. Woodhead Publishing, 1994.

[38] J.G. Nawrocki, J.N. DuPont, C.V. Robino, J.D. Puskar, and Arnold Marder. The mechanism of stress-relief cracking in a ferritic alloy steel. *Welding Journal (Miami, Fla)*, 82:25/S–35/S, 02 2003.

[39] Thanh (QC) Nguyen Le. Re-heat cracking in creep resistance steel.

[40] Han sang Lee, Jine sung Jung, Doo soo Kim, and Keun bong Yoo. Failure analysis on welded joints of 347h austenitic boiler tubes. *Engineering Failure Analysis*, 57:413–422, 2015.

[41] S. Soundararajan. Stress relaxation cracking of tp 347h ss flange weld joints on reactor charge heater manifold in propane de-hydrogenation unit. *EUROCORR*, 2019.

[42] Indhumathi Dayalan, Prashant Frank Crasta, Sritam Pradhan, and Renu Gupta. A review on stress relaxation cracking in austenitic stainless steel. In *Proceedings of International Conference on Intelligent Manufacturing and Automation*, pages 427–434. Springer Singapore, 2020.

[43] S He, H Shang, A Fernández-Caballero, A D Warren, D M Knowles, P E J Flewitt, and T L Martin. The role of grain boundary ferrite evolution and thermal aging on creep cavitation of type 316h austenitic stainless steel. *Materials Science and Engineering: A*, 807, March 2021.

[44] Rahul Unnikrishnan, Shirley Northover, Hedieh Jazaeri, and P. Bouchard. Investigating plastic deformation around a reheat-crack in a 316h austenitic stainless steel weldment by misorientation mapping. *Procedia Structural Integrity*, 2:3501–3507, 06 2016.

[45] H. Pommier, E.P. Busso, T.F. Morgeneyer, and A. Pineau. Intergranular damage during stress relaxation in aisi 316l-type austenitic stainless steels: Effect of carbon, nitrogen and phosphorus contents. *Acta Materialia*, 103:893–908, 2016.

[46] Y. Ito and M. Nakanishi. Study of stress relief cracking in welding low alloy steels. *The Sumitomo Search*, 7:27–36, 1972.

[47] M. Turski, P.J. Bouchard, A. Steuwer, and P.J. Withers. Residual stress driven creep cracking in aisi type 316 stainless steel. *Acta Materialia*, 56(14):3598 – 3612, 2008.

[48] Steven E. Hughes and Clifford Matthews. *A Quick Guide to Welding and Weld Inspection*. ASME Press, 01 2009.

[49] V.S. Hewitson, A.W. Pryce, and London United States. Office of Naval Research. Branch Office. *European scientific notes: ESN 32-4, 30 April 1978*. Office of Naval Research Branch Office, 1979.

[50] Sandeep Anand. Types of steel – classification of steel. `https://www.weldingandndt.com/types-of-steel-classification-of-steel/`.

[51] Sankara Papavinasam. Chapter 3 - materials. In Sankara Papavinasam, editor, *Corrosion Control in the Oil and Gas Industry*, pages 133 – 177. Gulf Professional Publishing, Boston, 2014.

[52] Michael F. McGuire. Chapter 6 - austenitic stainless steels. In *Stainless Steels for Design Engineers*. ASM International, 2008.

[53] R.P. Singh, S.E. Zorrilla, S.K. Vidyarthi, R. Cocker, and K. Cronin. Dairy plant design, construction and operation. In Paul L.H. McSweeney and John P. McNamara, editors, *Encyclopedia of Dairy Sciences (Third Edition)*, pages 239–252. Academic Press, Oxford, third edition edition, 2022.

[54] K. Cronin and R. Cocker. Plant and equipment | materials and finishes for plant and equipment. In John W. Fuquay, editor, *Encyclopedia of Dairy Sciences (Second Edition)*, pages 134–138. Academic Press, San Diego, second edition edition, 2011.

[55] B.P. Somerday and C. San Marchi. 3 - hydrogen containment materials. In Gavin Walker, editor, *Solid-State Hydrogen Storage*, Woodhead Publishing Series in Electronic and Optical Materials, pages 51–81. Woodhead Publishing, 2008.

[56] T. Michler. Austenitic stainless steels. In *Reference Module in Materials Science and Materials Engineering*. Elsevier, 2016.

[57] Erich Folkhard. *Welding Metallurgy of Austenitic Stainless Steels*, pages 197–222. Springer Vienna, 1988.

[58] AFCEN. Rcc-mrx, regles de conception et de construction des materiels mecaniques des installations nucleaires. *RCC-MRx-2012*, 2012.

[59] Abdullah Sinjlawi, Junjie Chen, Ho-Sub Kim, Hyeon Bae Lee, Changheui Jang, and Sanghoon Lee. Role of residual ferrites on crevice scc of austenitic stainless steels in pwr water with high-dissolved oxygen. *Nuclear Engineering and Technology*, 52(11):2552–2564, 2020.

[60] Liang Chen, Jian Lu Shang, Yan Zhang Liu, Jian Guang Zhao, and Ping Zhu. Effect of solution treatment on microstructure and properties of slm 316l stainless steel for nuclear power field. In *Materials and Technology of Clean Energy*, volume 999 of *Materials Science Forum*, pages 56–63. Trans Tech Publications Ltd, 7 2020.

[61] Schaeffler. A.L. Constitution diagram for stainless steel weld metal. *Metal Progress*, 56(11):680–680B, 1949.

[62] DeLong C. J. Long. The ferrite content of austenitic stainless steel weld metal. *Welding Journal*, 52(7):281–297, 1973.

[63] A Ben Rhouma, T Amadou, H Sidhom, and C Braham. Correlation between microstructure and intergranular corrosion behavior of low delta-ferrite content aisi 316l aged in the range 550-700 c. *Journal of Alloys and Compounds*, 708:871–886, 2017.

[64] Yiting Cui. *Etude numérique et expérimentale de l'endommagement de fluage à long terme dans les aciers inoxydables austénitiques.* Theses, Université Pierre et Marie Curie - Paris VI, December 2015.

[65] RCC-MRx. Règles de conception et de construction des matériels mécaniques des installations nucléaires. *AFCEN*, 131, 2012.

[66] Behnam Sadeghi, Hassan Sharifi, Mahdi Rafiei, and Morteza Tayebi. Effects of post weld heat treatment on residual stress and mechanical properties of gtaw: The case of joining a537cl1 pressure vessel steel and a321 austenitic stainless steel. *Engineering Failure Analysis*, 94:396 – 406, 2018.

[67] R. Stickler B. Weiss. Phase instabilities during high temperature exposure of 316 austenitic stainless steel. *Metallurg. Trans.*, 3:851–866, 1972.

[68] A. F. Padilha and P. R. Rios. Decomposition of austenite in austenitic stainless steels. *ISIJ International*, 42(4):325–327, 2002.

[69] T. Sourmail. Precipitates in creep resistant austenitic stainless steels (review). *Materials Science and Technology*, 17:0267–0836, 2001.

[70] Angelo Fernando Padilha, Ronald Lesley Plaut, and Paulo Rangel Rios. Stainless steel heat treatment. *Steel Heat Treatment*, pages 706–751, 2006.

[71] Ronald Lesley Plaut, Clara Herrera, Doris Maribel Escriba, Paulo Rangel Rios, and Angelo Fernando Padilha. A Short review on wrought austenitic stainless steels at high temperatures: processing, microstructure, properties and performance. *Materials Research*, 10:453 – 460, 12 2007.

[72] Mathieu Dutour Sikirić, Olaf Delgado-Friedrichs, and Michel Deza. Space fullerenes: a computer search for new Frank–Kasper structures. *Acta Crystallographica Section A*, 66(5):602–615, Sep 2010.

[73] B.S. Murty, J.W. Yeh, and S. Ranganathan. Chapter 7 - intermetallics, interstitial compounds and metallic glasses in high-entropy alloys. In B.S. Murty, J.W. Yeh, and S. Ranganathan, editors, *High Entropy Alloys*, pages 119–131. Butterworth-Heinemann, Boston, 2014.

[74] Charlotte Bonneau and Michael O'Keeffe. Intermetallic crystal structures as foams. beyond frank–kasper. *Inorganic chemistry*, 54, 09 2014.

[75] A. Proult and P. Donnadieu. A simple description of the alpha-manganese (a12) structure derived from defect studies. *Philosophical Magazine Letters*, 72(5):337–344, 1995.

[76] Maribel Saucedo-Muñoz and Victor Lopez-Hirata. Effect of precipitation on cryogenic toughness of n-containing austenitic stainless steels after aging. *In book: Austenitic Stainless Steels - New Aspects*, 2017.

[77] Girolamo Costanza, Andrea Sili, and Maria Elisa Tata. Weldability of austenitic stainless steel by metal arc welding with different shielding gas. *Procedia Structural Integrity*, 2:3508–3514, 2016. 21st European Conference on Fracture, ECF21, 20-24 June 2016, Catania, Italy.

[78] Klas Weman. The weldability of steel. In *Welding Processes Handbook*, pages 191–206. Elsevier, 2012.

[79] Ramazan Yilmaz and Huseyin Uzun. Mechanical properties of austenitic stainless steels welded by gmaw and gtaw. *Journal of Marmara for Pure and Applied Sciences*, 18, 01 2002.

[80] Makhlouf Hamide. *Numerical modelling of steel arc welding*. Theses, École Nationale Supérieure des Mines de Paris, July 2008.

[81] BY T. P. S. Gill, M. Vijayalakshmi, J. B. Gnanamoorthy, and Karthik Anantha Pg admanabhan. Transformation of delta-ferrite during the postweld heat treatment of type 316 l stainless steel weld metal transformation kinetics are rationalized on the basis of " normalized equivalent chromium content ". In *Welding research supplement*, 1986.

[82] Unknown. Tig welding – method and application. `https://www.electro-cal.com/weld-processes.html`. Accessed: 2020.

[83] Z. Śloderbach and J. Pająk. Determination of ranges of components of heat affected zone including changes of structure / określenie zakresów składowych strefy wpływu ciepła uwzględniając zmiany struktury. *Archives of Metallurgy and Materials*, 60, 12 2015.

[84] Lee Aucott. *Mechanism of solidification cracking during welding of high strength steels for subsea linepipe*. PhD thesis, University of Leicester, 08 2015.

[85] Xiaogang Li, Kejian Li, Zhipeng Cai, and Jiluan Pan. A review of austenite memory effect in haz of b containing 9% cr martensitic heat resistant steel. *Metals - Open Access Metallurgy Journal*, 9:1233, 11 2019.

[86] Ravit Silverstein, Dan Eliezer, and Thomas Boellinghaus. Hydrogen-trapping mechanisms of tig-welded 316l austenitic stainless steels. *Journal of Materials Science*, 53, 07 2018.

[87] Y. Balram, T. V. Vardhan, B. S. Babu, G. V. Ramana, and Ch. Preethi. Thermal stress analysis of aisi 316 stainless steels weldments in tig and pulse tig welding processes. *Materials Today: Proceedings*, 19, 2019.

[88] Nicolas Coniglio, Alexandre Mathieu, Olivier Aubreton, and Christophe Stolz. Weld pool surface temperature measurement from polarization state of thermal emission. *Quantitative InfraRed Thermography Journal*, 13(1):83–93, 2016.

[89] S. Lampman and ASM International. *Weld Integrity and Performance: A Source Book Adapted from ASM International Handbooks, Conference Proceedings, and Technical Books*. ASM Handbook Series. ASM International, 1997.

[90] H. Inoue, T. Koseki, S. Ohkita, and M. Fuji. Formation mechanism of vermicular and lacy ferrite in austenitic stainless steel weld metals. *Science and Technology of Welding and Joining*, 5(6):385–396, 2000.

[91] Mahmoud Saied. *Experimental and numerical modeling of the dissolution of delta ferrite in the Fe-Cr-Ni system : application to the austenitic stainless steels*. PhD thesis, Université Grenoble Alpes, May 2016.

[92] Yu Fan, Ke Wang, Xinyu Wang, Xinyuan Cao, Tingguang Liu, Long Xin, and Yonghao Lu. Microstructures and mechanical properties of the fusion zone of 316l-316ln stainless steel multi-pass gas tungsten arc welded joint. *Journal of Materials Science*, 56, 10 2021.

[93] H.N. Farneze, S.S.M. Tavares, J.M. Pardal, R.F. [do Nascimento], and H.F.G. [de Abreu]. Degradation of mechanical and corrosion resistance properties of aisi 317l steel exposed at 550°c. *Engineering Failure Analysis*, 61:69 – 76, 2016. 6th International Conference on Engineering Failure Analysis.

[94] D. P. Fairchild. A study concerning intercritical haz microstructure and toughness in hsla steels. *Welding Journal*, 1991.

[95] Muhd Faiz Mat, Yupiter H. P. Manurung, Yusuf Olanrewaju Busari, Mohd Shahriman Adenan, Mohd Shahar Sulaiman, Norasiah Muhammad, and Marcel Graf. Experimental analysis on grain growth kinetics of ss316l austenitic stainless steel. *Journal of Mechanical Engineering (JMechE)*, 18(3), 2021.

[96] Navid Moslemi, Norizah Redzuan, Norhayati Ahmad, and Tang Hor. Effect of current on characteristic for 316 stainless steel welded joint including microstructure and mechanical properties. In *Procedia CIRP*, volume 26, pages 560–564, 12 2015.

[97] Nilesh Kumar, Rajiv S. Mishra, and John A. Baumann. Chapter 1 - introduction. In Nilesh Kumar, Rajiv S. Mishra, and John A. Baumann, editors, *Residual Stresses in Friction Stir Welding*, pages 1–4. Butterworth-Heinemann, Boston, 2014.

[98] Xingzhong Liang and Pedro E.J. Rivera-Díaz del Castillo. Neutron diffraction. In Francisca G. Caballero, editor, *Encyclopedia of Materials: Metals and Alloys*, pages 695–702. Elsevier, Oxford, 2022.

[99] Nadhira Nasir, Mohammad Khairul Azhar Abdul Razab, Sarizam Mamat, and M.I. Ahmad. Review on welding residual stress. *ARPN Journal of Engineering and Applied Sciences*, 11:6166–6175, 05 2016.

[100] F. Kandil, D Lord, and Antony Fry. A review of residual stress measurement methods a guide to technique selection. *NPL Materials Centre, MATC(A)O4 Report*, 2001.

[101] P. Colegrove, C. Ikeagu, A. Thistlethwaite, S. Williams, T. Nagy, W. Suder, A. Steuwer, and T. Pirling. Welding process impact on residual stress and distortion. *Science and Technology of Welding and Joining*, 14(8):717–725, 2009.

[102] Ahmed Elmesalamy, J.A. Francis, and L. Li. A comparison of residual stresses in multi pass narrow gap laser welds and gas-tungsten arc welds in aisi 316l stainless steel. *International Journal of Pressure Vessels and Piping*, 113:49–59, 2014.

[103] S.T. Selvamani, S. Velmurugan, V. Balasubramanian, and K. Palanikumar. Effects of heat distribution during cold metal transfer arc welding on galvanized steel using volumetric heat source model. *Journal of Materials Research and Technology*, 9(5):10097–10109, 2020.

[104] Koichi Masubuchi. Analysis of welded structures: Residual stresses, distortion and their consequences. In *Analysis of Welded Structures*, pages 1–59. Elsevier, 1980.

[105] U. Zerbst. Application of fracture mechanics to welds with crack origin at the weld toe—a review. part 2: welding residual stresses. residual and total life assessment. *Welding in the World*, 64, 11 2019.

[106] Yashar Javadi, Mahmood Hasani, and Seyedali Sadeghi. Investigation of clamping effect on the welding sub-surface residual stress and deformation by using the ultrasonic stress measurement and finite element method. *Journal of Nondestructive Evaluation*, 34(1), January 2015.

[107] M. Choobi, Mohammad Haghpanahi, and M. Sedighi. Investigation of the effect of clamping on residual stresses and distortions in butt-welded plates. *Scientia Iranica*, 17:387–394, 09 2010.

[108] L. Tall. Heat input thermal and residual stresses in welded structural plates. *Fritz Laboratory Reports*, 1962.

[109] H. E. Coules. Contemporary approaches to reducing weld induced residual stress. *Materials Science and Technology (United Kingdom)*, 29:4–18, 01 2013.

[110] Segun Adedayo and M. Adeyemi. Effect of preheat on residual stress distributions in arc-welded mild steel plates. *Journal of Materials Engineering and Performance*, 9:7–11, 02 2000.

[111] Y.C. Lin and K.H. Lee. Effect of preheating on the residual stress in type 304 stainless steel weldment. *Journal of Materials Processing Technology*, 63(1):797 – 801, 1997.

[112] Stéphane Godin, Denis Thibault, and Jean Benoît Lévesque. An experimental comparison of weld-induced residual stresses using different stainless steel filler metals commonly used for hydraulic turbines manufacturing and repair. *Materials Science Forum*, 768-769:628–635, September 2013.

[113] Jonas Hensel. Mean stress correction in fatigue design under consideration of welding residual stress. *Welding in the World*, 64, 01 2020.

[114] Iing Farihin Yunasz, Agus Ismoyo, Rizki Iskandar, and Arbi Dimyati. Residual stress measurements on the tig weld joint of 57fe15cr25ni austenitic steel for structural material applications by means x-ray diffraction techniques. *Makara Journal of Technology*, 21:49, 08 2017.

[115] Tsuyoshi Shiozaki, Yoshikiyo Tamai, and Toshiaki Urabe. Effect of residual stresses on fatigue strength of high strength steel sheets with punched holes. *International Journal of Fatigue*, 80:324–331, 2015.

[116] Hitoshi Soyama, Christopher R. Chighizola, and Michael R. Hill. Effect of compressive residual stress introduced by cavitation peening and shot peening on the improvement of fatigue strength of stainless steel. *Journal of Materials Processing Technology*, 288:116877, 2021.

[117] Christopher B. Smith and Rajiv S. Mishra. Chapter 4 - case study of aluminum 5083-h116 alloy. In Christopher B. Smith and Rajiv S. Mishra, editors, *Friction Stir Processing for Enhanced Low Temperature Formability*, pages 19–124. Butterworth-Heinemann, Boston, 2014.

[118] Guillal Abdelkader, Noureddine Abdelbaki, Mohamed Gaceb, and Bettayeb Mourad. Effects of martensite-austenite constituents on mechanical properties of heat affected zone in high strength pipeline steels-review. *Chemical Engineering Transactions*, 70, 08 2018.

[119] S. Kozuh, M. Gojic, and L. Kosec. Mechanical properties and microstructure of austenitic stainless steel after welding and post-weld heat treatment. *Kovove Materialy*, 47:253–262, 01 2009.

[120] Rafal Molak, Krystian Paradowski, Tomasz Brynk, Lukasz Ciupinski, Zbigniew Pakiela, and K.J. Kurzydłowski. Measurement of mechanical properties in a 316l stainless steel welded joint. *International Journal of Pressure Vessels and Piping*, 86:43–47, 01 2009.

[121] M. Gaier, H.-T. Lin, Z.N. Farhat, and K.P. Plucknett. Precipitation hardenable tic-steel cermets. *Wear*, 477:203804, 2021. 23rd International Conference on Wear of Materials.

[122] Seong-Hyeong Lee, Hye-Sung Na, Kyong-Woon Lee, Jeong-Yong Lee, and Chung Yun Kang. Effect of austenite-to-ferrite phase transformation at grain boundaries on pwht cracking susceptibility in cghaz of t23 steel. *Metals*, 8(6), 2018.

[123] et al. H. Suzuki. Stress relief cracking. *Welding Metallurgy, Sanpo Pub Inc.*, 1978. In book : Complete Book of. Welding-Series 1, Sanpo Publications Inc.

[124] T. R. Simes, S. G. Mellor, and D. A. Hills. A note on the influence of residual stress on measured hardness. *The Journal of Strain Analysis for Engineering Design*, 19(2):135–137, 1984.

[125] Harald Aarbogh, Makhlouf Hamide, Hallvard Fjaer, Asbjorn Mo, and Michel Bellet. Experimental validation of finite element codes for welding deformations. *Journal of Materials Processing Technology*, 210, 10 2010.

[126] Ahmad AS, Wu Y, and Nie L. Gong H. Finite element prediction of residual stress and deformation induced by double-pass tig welding of al 2219 plate. *Materials*, 12(14):2251, 2019.

[127] R. Pamnani, M. Vasudevan, T. Jayakumar, P. Vasantharaja, and K.C. Ganesh. Numerical simulation and experimental validation of arc welding of dmr-249a steel. *Defence Technology*, 12(4):305 – 315, 2016.

[128] S. Feli, M. Aaleagha, Mehrdad Foroutan, and Ehsan Farahani. Finite element simulation of welding sequences effect on residual stresses in multipass butt-welded stainless steel pipes. *Journal of Pressure Vessel Technology*, 134:011209, 02 2012.

[129] M. Bibby J. Goldak, A. Chakravarti. A new finite element model for welding heat sources. *Metallurgical Transactions*, 15:229–305, 1984.

[130] L. Bertini A. Chiocca, F. Frendo. Evaluation of heat sources for the simulation of the temperature distribution in gas metal arc welded joints. *Metals*, 9:1142, 2019.

[131] Kimiya Hemmesi and Majid Farajian. Numerical welding simulation as a basis for structural integrity assessment of structures: Microstructure and residual stresses. In *Residual Stress Analysis on Welded Joints by Means of Numerical Simulation and Experiments*. InTech, May 2018.

[132] Karim Agrebi, Asma Belhadj, and Mahmoud Bouhafs. Three-dimensional numerical simulation of a gas tungsten arc welding process. *International Journal of Technology*, 10:689, 07 2019.

[133] Lionel Depradeux. *Simulation numérique du soudage - Acier 316L : validation sur cas tests de complexité croissante*. PhD thesis, INSA Lyon, 2004.

[134] Se Hwang, Janghyun Lee, Sung-Chan Kim, and K. K. Viswanathan. Numerical simulation of welding residual stress distribution on t-joint fillet structure. *International Journal of Ocean System Engineering*, 2, 05 2012.

[135] Diogo Almeida, Rui Martins, and João Cardoso. Numerical simulation of residual stresses induced by tig butt-welding of thin plates made of aisi 316l stainless steel. *Procedia Structural Integrity*, 5:633–639, 12 2017.

[136] Dean Deng and Hidekazu Murakawa. Numerical simulation of temperature field and residual stress in multi-pass welds in stainless steel pipe and comparison with experimental measurements. *Computational Materials Science*, 37:269–277, 09 2006.

[137] Jing Zheng, Ayhan Ince, and Lanqing Tang. Modeling and simulation of weld residual stresses and ultrasonic impact treatment of welded joints. *Procedia Engineering*, 213:36 – 47, 2018. 7th International Conference on Fatigue Design, Fatigue Design 2017, 29-30 November 2017, Senlis, France.

[138] *Modelization of the Strain Memory Effect on the Cyclic Hardening of 316 Stainless Steel*, 1979.

[139] R. Thomas Jr. Haz cracking in thick sections of austenitic stainless steels. *Welding Journal*, 63:24–32, 1984.

[140] M.E. Kassner. Chapter 1 - fundamentals of creep in materials. In M.E. Kassner, editor, *Fundamentals of Creep in Metals and Alloys (Third Edition)*, pages 1–6. Butterworth-Heinemann, Boston, third edition edition, 2015.

[141] Philip Noell, Jay Carroll, Joseph Michael, and Brad Boyce. In-situ high-resolution ebsd characterization of creep cavitation in ofhc copper. *Department of Energy's National Nuclear Security Administration*, 2019.

[142] A. H. Chokshi. Cavity nucleation and growth in superplasticity. *Materials Science and Engineering*, A, 410:95–99, 2005.

[143] Q. Xu. Development of advanced creep damage constitutive equations for low cr alloy under long-term service. *Doctoral thesis, University of Huddersfield*, 2016.

[144] M. Ashby. Boundary defects, and atomistic aspects of boundary sliding and diffusional creep. *Surface Science, 31, 498-542*, 1972.

[145] Q. Auzoux. Fissuration en relaxation des aciers inoxydables austénitiques - influence de l'écrouissage sur l'endommagement intergranulaire. *Mécanique [physics.med-ph]., École Nationale Supérieure des Mines de Paris*, 2008.

[146] Gao Wenhua, Chen Kai, Guo Xianglong, and Zhang Lefu. Fracture toughness of type 316ln stainless steel welded joints. *Materials Science and Engineering: A*, 685, 12 2016.

[147] R. W. Emerson and R. W. Jackson. The plastic ductility of austenitic piping containing welded joints at 1200 °f. *Welding Journal*, pages 89–a–104–s, 02 1957.

[148] H. Pommier. Stress relaxation cracking in aisi 316l-type austenitic stainless steels. *Ecole Nationale Supérieure des Mines de Paris*, 2015.

[149] A. Siefert, , and J.M. Tanzosh. Stress relaxation cracking literature review. *EPRI Conference*, 2010.

[150] Hans Wortel. Control of relaxation cracking in austenitic high temperature components. *NACE - International Corrosion Conference Series*, 01 2007.

[151] A.S Grot. Microstructural stability of titanium–modified type 316 and type 321 stainless steel. *Metall. Trans., A*, 6A(11):2023–2030, 1975.

[152] Kyohei Nomura and Keiji Kubushiro. Evaluation of reheat cracking susceptibility in high strength austenitic stainless steels. *MATERIALS TRANSACTIONS*, 63(6):877–882, 2022.

[153] M. R. James. Relaxation of stress an overview. In *Advances in Surface Treatments, 1st ed.*, volume 4 - Residual Stresses, page 349–365. Pergamon Press, 1987.

[154] Younger R.N., Haddrill D.M, and Backer R.G. Post-weld heat treatment of high-temperature austenitic steels. *Journal of Iron and Steel Institute*, pages 693–698, 1963.

[155] Pickering F.B. Irvine K.J., Murray J.D. The effect of heat-treatment and microstructure on high-temperature ductility of 18%cr-12%ni-1%nb steels. *Journal of Iron and Steel Institute*, pages 166–179, 1960.

[156] Backer R.G. Haddrill D.M. Heat affected zone cracking in thick section austenitic steels during post-weld heat treatment. *2nd Commonwealth Welding Conference, London*, pages 103–108, 1965.

[157] R. A. Swift and H. C. Rodgers. Embrittlement of 21cr-1mo steel weld metal by postweld heat treatment. *Welding Journal*, 52:145–s to 153–s, 172–s, 1973.

[158] Leijun Li and R.W. Jr. Stress relaxation study of haz reheat cracking in type 347 stainless steel. *Welding Journal (Miami, Fla)*, 79:137–s, 06 2000.

[159] Isaratat Phung-On. *An investigation of reheat cracking in the weld heat affected zone of type 347 stainless steel.* PhD thesis, The Ohio State University, December 2007.

[160] J.E. Indacochea and G.S. Kim. Reheat cracking studies on simulated heat-affected zones of crmov turbine rotor steels. *JMEP*, 5:353–364, 1996.

[161] BY E. F. Nippes and Jean-Pierre Balaguer. A study of the weld heat-affected zone toughness of 9 % nickel steel although thermal cycling reduces cryogenic impact toughness and upper shelf energy , astm specifications are still exceeded. In *Welding research supplement*, 2013.

[162] Hyun Je Sung, Nam Hoe Heo, and Sung-Joon Kim. Difference in reheat cracking susceptibility of 2.25cr-w and 9cr-w heat-resistant steels. *ISIJ International*, 57(7):1268–1272, 2017.

[163] H.U. Hong, B.S. Rho, and S.W. Nam. Correlation of the m23c6 precipitation morphology with grain boundary characteristics in austenitic stainless steel. *Materials Science and Engineering: A*, 318(1):285 – 292, 2001.

[164] Y.J. Jin, H. Lu, C. Yu, and J.J. Xu. Study on grain boundary character and strain distribution of intergranular cracking in the cghaz of t23 steel. *Materials Characterization*, 84:216–224, 2013.

[165] GC Hasson and C Goux. Interfacial energies of tilt boundaries in aluminium. experimental and theoretical determination. *Scripta metallurgica*, 5(10):889–894, 1971.

[166] H Miura, M Kato, and T Mori. Temperature dependence of the energy of cu [110] symmetrical tilt grain boundaries. *Journal of materials science letters*, 13(1):46–48, 1994.

[167] Chandra Prakash, Hongsuk Lee, Milad Alucozai, and Vikas Tomar. An analysis of the influence of grain boundary strength on microstructure dependent fracture in polycrystalline tungsten. *International Journal of Fracture*, 199(1):1 – 20, 2016.

[168] Bin Tang, Li Jiang, Rui Hu, and Qi Li. Correlation between grain boundary misorientation and m23c6 precipitation behaviors in a wrought ni-based superalloy. *Materials Characterization*, 78:144 – 150, 2013.

[169] Hellstroem. Steel in the chemical industry. *Steel congress*, 7:9–11, 1968.

[170] R.A. Stevens M. C. Coleman, D.A. Miller. Integrity of high temperatures welds proceedings. *Int. Conf. Nottingham*, 1998.

[171] Lawrence Osoba, Abdul Khan, and Samson Adeosun. Cracking susceptibility after post-weld heat treatment in haynes 282 nickel based superalloy. *ACTA METALLURGICA SINICA-ENGLISH LETTERS*, 26:747–753, 12 2013.

[172] R. Thamburaj, w. Wallace, and J. A. Goldak. Post-weld heat-treatment cracking in superalloys. *International Metals Reviews*, 28(1):1–22, 1983.

[173] Hans van Wortel. Control of relaxation cracking in austenitic high temperature components. *NACE-07423*, 2007.

[174] J. Borland. Cracking tests for assessing weldability. *Br. Weld. J.*, page 623–637, 1960.

[175] M. W. Spindler. The multiaxial creep ductility of austenitic stainless steels. *Fracture of Engineering Materials*, 27(4):273–281, 2004.

[176] Maxwell Calder Trent. *"Development and Use of a Simple Test Method to Evaluate Reheat Cracking Sensitivity in the Weld Deposit Region of a Submerged Arc Weld.* PhD thesis, University of Tennessee, 2012.

[177] C.D. Lundin, T.P.S. Gill, C.Y.P. Qiao, Y. Wang., and K.K. Khane. *Carbon equivalence and weldability of micro alloyed steels.* U.S. Coast Guard Headquarters., 1991.

[178] Mariappan K, Vani Shankar, and Bhaduri A. K. Comparative evaluation of tensile properties of simulated heat affected zones of p91 steel weld joint. *Materials at High Temperatures*, 37:114 – 128, 2020.

[179] Li Zhang, Kai Wang, Yu Huang, Chi Xu, and Jin Chen. Method and criteria to evaluate reheat cracking susceptibility. *Welding Journal*, 99:175–183, 06 2020.

[180] Nobuhiko Saito, Nobuyoshi Komai, and Keita Hashimoto. Evaluation of stress relaxation cracking susceptibility in alloy 617 for advanced usc boilers. *International Journal of Pressure Vessels and Piping*, 168:183–190, 2018.

[181] Xiaopeng Xiao, Dianzhong Li, Yiyi Li, and Shanping Lu. Microstructural evolution and stress relaxation cracking mechanism for super304h austenitic stainless steel weld metal. *Journal of Materials Science and Technology*, 100:82–90, 2022.

[182] P.J. Bouchard, P.J. Withers, S.A. McDonald, and R.K. Heenan. Quantification of creep cavitation damage around a crack in a stainless steel pressure vessel. *Acta Materialia*, 52(1):23–34, January 2004.

[183] T. L. Burnett, R. Geurts, H. Jazaeri, S. M. Northover, S. A. McDonald, S. J. Haigh, P. J. Bouchard, and P. J. Withers. Multiscale 3d analysis of creep cavities in aisi type 316 stainless steel. *Materials Science and Technology*, 31(5):522–534, 2015.

[184] Hedieh Jazaeri, P. Bouchard, Michael Hutchings, Abdullah Mamun, and Richard Heenan. Study of creep cavitation through creep life. In *Conference: 13th International Conference on Creep and Fracture of Engineering Materials and StructuresAt: Toulouse, France*, 05 2015.

[185] Hedieh Jazaeri, P. Bouchard, Michael Hutchings, Abdullah Mamun, and Richard Heenan. Study of cavities in a creep crack growth test specimen. *Procedia Structural Integrity*, 2:942–949, 12 2016.

[186] Hedieh Jazaeri, P. John Bouchard, Michael T. Hutchings, Mike W. Spindler, Abdullah A. Mamun, and Richard K. Heenan. An investigation into creep cavity development in 316h stainless steel. *Metals*, 9(3), 2019.

[187] Liang Huang. *Micromechanical simulation and experimental investigation of the creep damage of stainless austenitic steels.* Theses, Université Pierre et Marie Curie - Paris VI, December 2017.

[188] Yo Lee, Dae Kim, Dok Lee, and Woo Ryu. Effect of grain size on creep properties of type 316ln stainless steel. *Metals and Materials International - MET MATER INT*, 7:107–114, 04 2001.

[189] Cheng Ma, Qunjia Peng, Jinna Mei, En-Hou Han, and Wei Ke. Microstructure and corrosion behavior of the heat affected zone of a stainless steel 308l-316l weld joint. *Journal of Materials Science and Technology*, 34(10):1823–1834, 2018.

[190] Yo Seob Lee, Dae Whan Kim, Dok Yol Lee, and Woo Seog Ryu. Effect of grain size on creep properties of type 316ln stainless steel. *Metals and Materials International*, 7(2):107–114, April 2001.

[191] X.L. Wang, Y.R. Nan, Z.J. Xie, Y.T. Tsai, J.R. Yang, and C.J. Shang. Influence of welding pass on microstructure and toughness in the reheated zone of multi-pass weld metal of 550mpa offshore engineering steel. *Materials Science and Engineering: A*, 702:196–205, 2017.

[192] B. Beausir and J.-J. Fundenberger. Analysis tools for electron and x-ray diffraction. *ATEX-software, Université de Lorraine - Metz*, 2017.

[193] Stuart I. Wright, Matthew M. Nowell, and David P. Field. A review of strain analysis using electron backscatter diffraction. *Microscopy and Microanalysis*, 17(3):316–329, 2011.

[194] Moses and John Olafenwa. Imageai, an open source python library built to empower developers to build applications and systems with self-contained computer vision capabilities, mar 2018–.

[195] Anass Assadiki, Vladimir A. Esin, Miguel Bruno, and Rémi Martinez. Stabilizing effect of alloying elements on metastable phases in cast aluminum alloys by calphad calculations. *Computational Materials Science*, 145:1–7, 2018.

[196] Test methods for determining average grain size.

[197] ASM Handbook Committee. *Properties and Selection: Irons, Steels, and High-Performance Alloys*. ASM International, 01 1990.

[198] J Brooks, J Williams, and A Thompson. Microstructural origin of the skeletal ferrite morphology of austenitic stainless steel welds. Technical report, Sandia National Labs., Livermore, CA (USA), April 1982.

[199] E.G. Astafurova, M.S. Tukeeva, G.G. Zakharova, E.V. Melnikov, and H.J. Maier. The role of twinning on microstructure and mechanical response of severely deformed single crystals of high-manganese austenitic steel. *Materials Characterization*, 62(6):588–592, 2011.

[200] Grong O. *Metallurgical modelling of welding*. Maney Publishing, 1997.

[201] Yunlu Jiang, Ying Kan, and Huaining Chen. Heterogeneous microstructure-induced creep failure responses in various sub-zones of modified 310s welded joints. *Metals*, 12:116, 01 2022.

[202] V. D. Vijayanand, J. Ganesh Kumar, P. K. Parida, V. Ganesan, and K. Laha. Studies on creep deformation and rupture behavior of 316ln SS multi-pass weld joints fabricated with two different electrode sizes. *Metallurgical and Materials Transactions A*, 48(2):706–721, November 2016.

[203] Finite element code developed by the cea, (french atomic energy commission), cast3m:www-cast3m.cea.fr. `http://www-cast3m.cea.fr`. Accessed: 2020.

[204] J. L. Chaboche. A review of some plasticity and viscoplasticity constitutive theories. *International Journal of Plasticity*, 24(10):1642 – 1693, 2008. Special Issue in Honor of Jean-Louis Chaboche.

[205] M.C. Smith, P.J. Bouchard, M. Turski, L. Edwards, and R.J. Dennis. Accurate prediction of residual stress in stainless steel welds. *Computational Materials Science*, 54:312–328, 2012.

[206] Toshiyuki Miyazaki and Toshihiko Sasaki. X-ray residual stress measurement of austenitic stainless steel based on fourier analysis. *Nuclear Technology*, 194, 04 2016.

[207] C. Picker and A.S. Fraser. Experience of cracking in austenitic stainless components of the uk prototype fast reactor. *International Journal of Pressure Vessels and Piping*, 65(3):283–293, 1996. Fracture in Austenitic Components.

[208] Y. Cui. Etude numérique et expérimentale de l'endommagement de fluage à long terme dans les aciers inoxydables austénitiques. *Matériaux. Université Pierre et Marie Curie - Paris VI*, 2015.

[209] M. Mizouchi, Yoshihiro Yamazaki, Yoshiaki Iijima, and Koji Arioka. Low temperature grain boundary diffusion of chromium in sus316 and 316l stainless steels. *Materials Transactions*, 45:2945–2950, 2004.

[210] M.E. Kassner and Troy Hayes. Creep cavitation in metals. *International Journal of Plasticity*, 19:1715–1748, 10 2003.

[211] M. F. Ashby R. Raj. Integranular fracture at elevated temperature. *Acta Metallurgica*, 1975.

[212] R.G Fleck, D.M.R Taplin, and C.J Beevers. An investigation of the nucleation of creep cavities by 1 mv electron microscopy. *Acta Metallurgica*, 23(4):415–424, 1975.

[213] William E. Luecke, Sheldon M. Wiederhorn, Bernard J. Hockey, Ralph F. Krause Jr., and Gabrielle G. Long. Cavitation contributes substantially to tensile creep in silicon nitride. *Journal of the American Ceramic Society*, 78(8):2085–2096, 1995.

[214] Maxime Sauzay and Mohamed Ould Moussa. Prediction of grain boundary stress fields and microcrack initiation induced by slip band impingement. In Davide Bigoni, Angelo Carini, Massimiliano Gei, and Alberto Salvadori, editors, *Fracture Phenomena in Nature and Technology*, pages 215–240, Cham, 2014. Springer International Publishing.

[215] *Identification et caractérisation d'une nouvelle phase intermétallique formée dans un acier inoxydable austéno-ferritique Z3CND22-05*, 07 1991.

[216] Íris Carneiro and Sónia Simões. Recent advances in ebsd characterization of metals. *Metals*, 10(8), 2020.

[217] Keiji KUBUSHIRO, Yohei SAKAKIBARA, and Toshihiro OHTANI. Creep strain analysis of austenitic stainless steel by sem/ebsd. *Journal of the Society of Materials Science, Japan*, 64(2):106–112, 2015.

[218] V. D. Vijayanand, M. Vasudevan, P. Parameswaran V. Ganesan, K. Laha, and A. K. Bhaduri. Creep deformation and rupture behavior of single- and dual-pass 316ln stainless-steel-activated tig weld joints. *Metallurgical and Materials Transactions*, pages 2804–2814, 2016.

[219] Yunlu Jiang, Ying Kan, and Huaining Chen. Heterogeneous microstructure-induced creep failure responses in various sub-zones of modified 310s welded joints. *Metals*, 12(1), 2022.

[220] R.P. Skelton, I.W. Goodall, G.A. Webster, and M.W. Spindler. Factors affecting reheat cracking in the haz of austenitic steel weldments. *International Journal of Pressure Vessels and Piping*, 80(7):441–451, 2003. Creep crack growth in components.

[221] J. Don and S. Majumdar. Creep cavitation and grain boundary structure in type 304 stainless steel. *Acta Metallurgica*, 34(5):961–967, 1986.

[222] V.Y. Gertsman and S.M. Bruemmer. Study of grain boundary character along intergranular stress corrosion crack paths in austenitic alloys. *Acta Materialia*, 49(9):1589–1598, 2001.

[223] D. J. H. Cockayne, M. L. Jenkins, and I. L. F. Ray. The measurement of stacking-fault energies of pure face-centred cubic metals. *Philosophical Magazine*, 24(192):1383–1392, December 1971.

[224] Zhenbo Zhang, Zhibiao Yang, Song Lu, Allan Harte, Roberto Morana, and Michael Preuss. Strain localisation and failure at twin-boundary complexions in nickel-based superalloys. *Nature Communications*, 11(1), sep 2020.

[225] Hamidreza Abdolvand and Angus J. Wilkinson. Assessment of residual stress fields at deformation twin tips and the surrounding environments. *Acta Materialia*, 105:219–231, 2016.

[226] M. Arul Kumar, I.J. Beyerlein, and C.N. Tomé. Effect of local stress fields on twin characteristics in hcp metals. *Acta Materialia*, 116:143–154, 2016.

[227] Rishi Raj. Nucleation of cavities at second phase particles in grain boundaries. *Acta Metallurgica*, 26(6):995–1006, 1978.

[228] A Gittins. Stability of grain boundary cavities in copper. *Nature*, 214:586–587, 1967.

[229] M. Yoshida, C. Levaillant, R. Piques, and A. Pineau. Quantitative study of intergranular damage in an austenitic stainless steel on smooth and notched bars. *High Temperature Fracture Mechanisms and Mechanics*, pages 3–21, 1987.

[230] R. G. Faulkner Y. F. Yin. Creep damage and grain boundary precipitation in power plant metals. *Materials Science and Technology*, 2013.

[231] L. Huang, M. Sauzay, Y. Cui, and P. Bonnaille. Theoretical and experimental study of creep damage in alloy 800 at high temperature. *Material Science and Engineering*, 2021.

[232] J-D. Hu, F.-Z. Xuan, C.-J. Liu, and B. Chen. Modelling of cavity nucleation under creep-fatigue interaction. *Mechanics of Materials*, 156, 2021.

[233] Florian Bachmann, Ralf Hielscher, and Helmut Schaeben. Grain detection from 2d and 3d ebsd data—specification of the mtex algorithm. *Ultramicroscopy*, 111(12):1720–1733, 2011.

[234] Rishi Kant. Stress relief cracking susceptibility in high temperature alloys. *Thesis, Lehigh University*, 2018.

Appendix A

Literature review on stress relaxation cracking

Name	Developed by	Test conditions	Outputs	Pros	Cons
Advanced 4-point bend test	B. Kuhn, C. Ullrich, H. Tschaffon, T. Beck, L. Singheiser	1. 4-point contact fixture on a servo-hydraulic machine. 2. Notched sample with CGHAZ treatment around notch. 3. Heated to test temperature with constant bend radius throughout test. 4. Sample fractured at liquid N temperature.	1. Variation of load with time. 2. Crack growth (crack length vs. temperature/ time) and 3. Cracking propensity (final crack length vs. initial loads)	1. Simulates development of residual stress in welds with rise in temperature. 2. Load vs. time plot represents stress relaxation characteristic of alloys. 3. Uniform strain is applied on the sample thus failure to occur at weakest section in sample.	1. Cannot rank samples that do not crack. 2. Ductility cannot be measured as samples fractured at liquid N temperature.
3-Point Bend test	Van Wortel	1. Weld sample 2. loaded in 3-point bend test rig. 3. Heated to test temperature, stress is applied. 4. If no cracking observed, 2nd loading cycle is done to initiate cracking. 5. Analysis of sample	Same as 4-point bend test	1. Simulates development of residual stress in welds with rise in temperature. 2. Load vs. time plot represents stress relaxation characteristic of alloys.	1. Center of sample is max strained; thus, failure may not necessarily be at the weakest section in sample. 2. Difficult to compare ductility of plate samples

Figure A.1: SRC bending testing methods [234].

Sr.	Name of Test	Developed by	Test conditions	Outputs	Pros	Cons
3	Gleeble (Strain to failure)	DSI	1. CGHAZ heat treatment done on sample and cooled to room temperature 2. Heated to PWHT temperature, stress (order of yield stress) applied at PWHT temperature. 3. Displacement locked.	1. Time to failure 2. Elongation and ductility 3. Stress vs. time plot	1. Very high heating rates 2. High accuracy in strain measurement 3. Simple tests 4. Stress relaxing character of sample can be studied on a constraint sample.	1. Highly expensive. 2. Very small hot zone is obtained i.e. sample area with peak programmed temperature.
4	Controlled Heat Rate Test (CHRT)		1. Standard tensile test samples on a UTM with clamshell furnace attachment. 2. At temperature, sample is pulled to failure.	1. Reduction in area, 2. percent elongation, 3. fracture mode are the outputs. 4. Yield strength (0.2 offest).	1. Simple, inexpensive 2. Does not need skilled labor 3. Good test for pass/ fail type test.	1. Does not consider stress relaxation in sample. 2. Very high heating rates cannot be achieved. 3. HAZ samples from welds are to be taken.

Figure A.2: SRC tension type testing methods [234].

Sr.	Name of Test	Developed by	Test conditions	Outputs	Pros	Cons
5	Restraint test	Turski	1. Compact tension test specimen are prepared. 2. Samples used in both aged and annealed condition. 3. Compressive prestrain applied, leading to residual compressive stress 4. PWHT in furnace. 5. Notch roots examined for cracks.	1. Crack length	1. Simple test. 2. Does not need sophisticated equipment 3. Crack length is quantified.	1. Does not include stress relaxation measurement. 2. Quantifiable output is only crack length which is not obvious.
6	Weldability testing	S.A David, ORNL	1. Sheet disc sample prepared 2. Circumferential weld is done at 35 mm and 22.3 mm diameter. 3. Sample is flipped, to weld on both sides. 4. On both sides, outer weld is done first. 5. analysis of sample: Pass if no cracks; failed if cracks at both welds and Moderately susceptible if cracks only near inside weld	Pass/ fail i.e. cracks appear or not.	1. Good pass/ fail test for sheet samples.	1. For thin sheet samples 2. No quantitative outputs.
7	C-ring	Lundin	1. Welds are performed 2. Cylindrical shells are cut out of dimension, length 0.75"X OD 1" X ID 0.75". Notch applied on sample. 3. Deflection is estimated using ASTM G-38 4. Deflected sample is put to PWHT 5. Analysis of sample.	Pass/ fail i.e. cracks appear or not.	1. Good pass/ fail test for SRC testing. 2. Test can be standardized as it is compliant to ASTM standard. 3. SRC susceptibility of different areas on weld can be obtained.	1. High machining cost 2. many variables that means not good reproducibility. 3. Does not give a quantitative output.
8	Borland Test		1. Two members are welded perpendicular to each other. 2. Oblique member sits inside a grove on the base member and sides are welded. 3. Joint is PWHT'ed in furnace 4. Analysis of sample	Pass/ fail i.e. cracks appear or not.	1. Good pass or fail criteria. 2. Perpendicular bending induces high constraint in weld.	1. Making welds with good reproducibility is expensive. 2. No quantitative output.

Figure A.3: SRC constraint type testing methods [234].

Appendix B

Characterization of the material states

B.1 Single-pass welded material

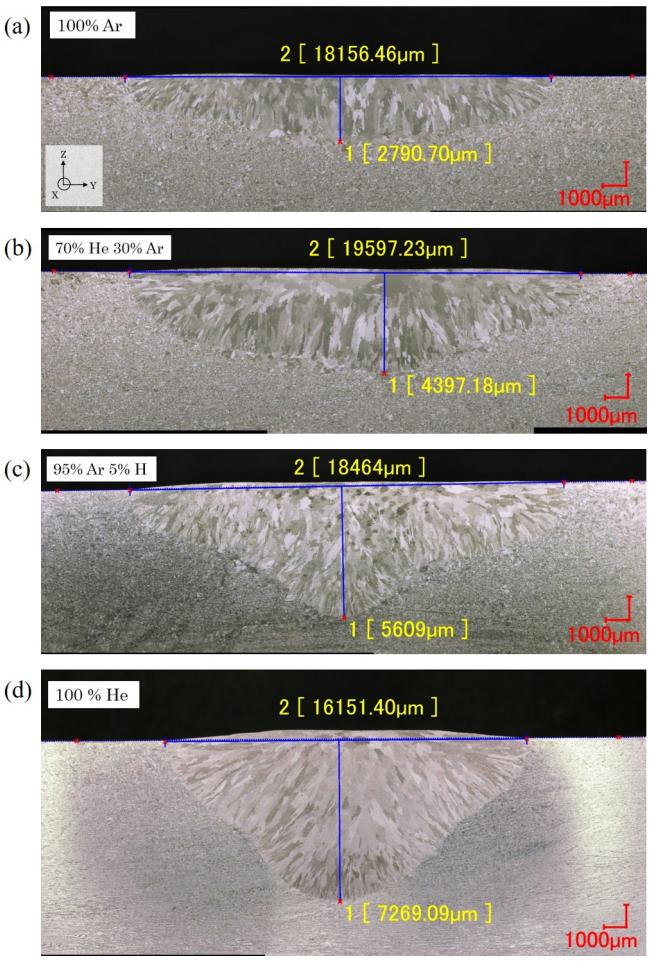

Figure B.1: Macrographic cross-section images of the single-pass welded sheet sections using a gas mix of (a) 100% Ar, (b) 70% He and 30% Ar, (c) 95% Ar and 5% H_2, (d) 100% He. Samples were priory etched with an acid attack to reveal the microstructure.

B.2 Cold-rolled single-pass welded material

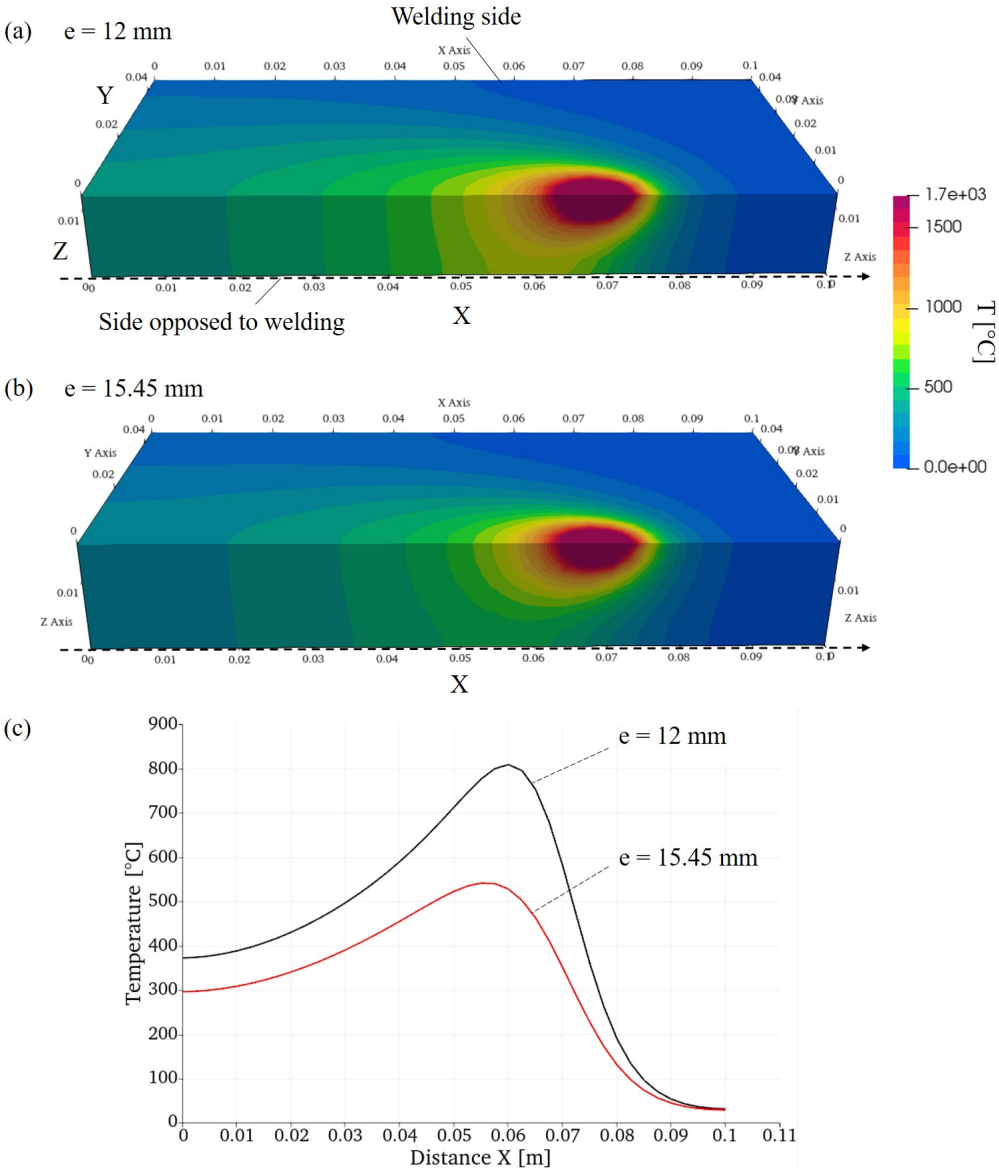

Figure B.2: FEM simulation of temperature during GTA welding of a 316 steel plate using 'soudage4' test case available on Cast3M software wesbite [203], considering plates with thickness of (a) 12 mm and (b) 15.45 mm. (c) Temperature profiles along the X axis for both cases, displaying peak temperatures along the side of the plates opposed to welding side. Welding torch displacement rate was set to 60 mm/min. Both convection and conduction were accounted for. All dimensions are in meters, or indicated if otherwise. Only half of the plates were considered for simulations, due to the symmetry of the problem (relative to the XZ plane).

RÉSUMÉ

Depuis les années 1950, de nombreux cas de fissuration intergranulaire ont été observés dans des joints d'acier soudés, après plusieurs mois ou années de service en température sans sollicitation mécanique. Grâce aux nombreuses études qui ont été menées sur la problématique, la rupture de ces composants a pu être expliquée par la relaxation des contraintes résiduelles de soudage, la présence d'écrouissage dans les zones affectées et par la précipitation de phases aux joints de grains lors de son utilisation en service. Ce phénomène, appelé Fissuration en Relaxation (FeR), a alors motivé des campagnes d'études pour l'évaluation de la résistance de différentes nuances d'aciers et ainsi prévenir les risques de rupture des joints soudés. En raison de la complexité du phénomène, la plupart de ces études ont été réalisées en utilisant des échantillons avec des microstructures homogènes représentatives des zones affectées par le soudage, considérées comme les plus sensibles à la FeR. Dans ce travail, des éprouvettes de type CT (pour Compact-Tension) ont été usinées à partir de tôles d'acier 316L(N) soudées, puis comprimées et déchargées afin d'introduire des contraintes résiduelles et des pré-déformations de manière controlée. Ainsi, l'effet sur la FeR des microstructures hétérogènes comparables à celles des joints soudés industriels a pu être étudié. Une procédure expérimentale spécifique a été développée pour analyser la FeR à des températures proches des températures de service, tout en faisant varier les forces motrices de la FeR telles que le niveau de contraintes résiduelles, de déformation, le temps et température de relaxation. L'étude de FeR dans les éprouvettes comportant des soudures a révélé une distribution très hétérogène de l'endommagement, directement induite par l'hétérogénéité de la microstructure. Particulièrement, la zone affectée thermiquement à gros grains des matériaux soudés est apparue comme la zone la plus sensible à la FeR. Les mécanismes, localisation, distributions d'endommagement ont été caractérisés pour chaque condition par microscopie électronique, et ce, à différentes échelles. La confrontation des niveaux d'endommagement observés aux estimations de contraintes résiduelles obtenues par simulation numérique a alors permis d'estimer des seuils de FeR pour chaque zone de la microstructure soudée.

MOTS CLÉS

Acier austénitique inoxydable AISI 316L(N), soudage, fissuration en relaxation, contraintes résiduelles, endommagement intergranulaire, cavités, précipités, éprouvette CT

ABSTRACT

Since the 1950s, many cases of intergranular cracking have been observed in welded steel joints after several months or years of service at temperature without mechanical loading. Numerous studies reported that the failure of these components could be explained by the relaxation of residual stresses induced by the welding, the presence of work hardening in the weld microstructure and by grain boundary precipitation during the service. This phenomenon, called Stress Relaxation Cracking (SRC), has motivated research aiming to evaluate the resistance of different steel grades. Due to the complexity of SRC, most of these studies have been carried out using specimens with homogeneous microstructures representative of the zones affected by welding, considered to be the most prone to SRC. In this work, Compact-Tension (CT) specimens were machined from welded plate made of 316L(N) steel and subjected to compression followed by unloading to introduce residual stresses and pre-strain in a controlled manner. Thereby the effect of heterogeneous microstructures comparable to those of industrial weld joints on SRC could be assessed. A specific experimental procedure was developed to test SRC at temperatures close to service ones, while varying SRC driving forces such as residual stress, strain, relaxation time and temperature. The study of SRC in specimens made of welds revealed a very heterogeneous distribution of damage, directly caused by the heterogeneity of the microstructure. In particular, the coarse-grained heat-affected zone of welded materials appeared to be the most prone to SRC. The damage mechanisms, location and distributions were characterised for each condition by electron microscopy at different scales. The correlation of the observed damage levels with the estimations of residual stress obtained by numerical simulation then allowed the estimation of SRC thresholds for each zone of the weld microstructure.

KEYWORDS

AISI 316L(N) austenitic stainless steel, welding, stress relaxation cracking, residual stress, intergranular damage, cavities, precipitates, CT specimen